

**The Evolutionary Pathways of Tidal Disruption Events:  
from Stars to Debris Streams, Accretion Disks, and  
Relativistic Jets**

by

**E. R. Coughlin**

B.S., Lehigh University, 2011

M.S., University of Colorado at Boulder, 2013

A thesis submitted to the  
Faculty of the Graduate School of the  
University of Colorado in partial fulfillment  
of the requirements for the degree of  
Doctor of Philosophy  
Department of Astrophysical and Planetary Sciences

2016

This thesis entitled:  
The Evolutionary Pathways of Tidal Disruption Events: from Stars to Debris Streams, Accretion  
Disks, and Relativistic Jets  
written by E. R. Coughlin  
has been approved for the Department of Astrophysical and Planetary Sciences

---

Prof. Mitchell C. Begelman

---

Prof. Philip J. Armitage

---

Prof. Andrew J. Hamilton

---

Prof. Mark Rast

---

Prof. Oliver DeWolfe

Date \_\_\_\_\_

The final copy of this thesis has been examined by the signatories, and we find that both the content and the form meet acceptable presentation standards of scholarly work in the above mentioned discipline.

Coughlin, E. R. (Ph.D., Astrophysics)

The Evolutionary Pathways of Tidal Disruption Events: from Stars to Debris Streams, Accretion  
Disks, and Relativistic Jets

Thesis directed by Prof. Mitchell C. Begelman

Tidal disruption events, which occur when a star is destroyed by the gravitational field of a supermassive black hole, are unique probes of the inner regions of galaxies. In this thesis we explore various stages of the tidal disruption process, in an attempt to relate the observable signatures of tidal disruption events to the properties of the disrupted star and the black hole. We use numerical techniques to study the long-term evolution of the debris streams produced from tidal disruption events, showing that they can be gravitationally unstable and, as a result of the instability, fragment into small-scale, localized clumps. The implications of this finding are discussed, and we investigate how the thermodynamic properties of the gas comprising the stream affect the nature of the instability. We derive an analytic model for the structure of tidally-disrupted, stellar debris streams, and we compare the predictions of our model to numerical results. We present a model for the accretion disk that forms from a tidal disruption event when the accretion rate surpasses the Eddington limit of the supermassive black hole, showing that these disks are puffed up into quasi-spherical envelopes that are threaded by bipolar, relativistic jets. We compare the predictions of this model to observations of the jetted tidal disruption event **Swift** J1644+57. Finally, we derive, from the relativistic Boltzmann equation, the general relativistic equations of radiation hydrodynamics in the viscous limit, which characterize the interaction between radiation and matter when changes in the fluid over the photon mean free path are small. Our results demonstrate that, in contrast to previous works, a radiation-dominated fluid does in fact possess a finite bulk viscosity and a correction to the comoving energy density. Using the general relativistic equations of radiation hydrodynamics in the viscous limit, we present two models to describe the interaction between a relativistic jet launched during a tidal disruption event and its surroundings. These models show

that regions of very large shear that arise between the fast-moving outflow and the surrounding envelope possess fewer scatterers and a harder photon spectrum, meaning that observers looking “down the barrel of the jet” infer vastly different properties of the outflow than those who look off-axis.

## Dedication

This thesis is dedicated to my wonderful wife Sarah and all of her sass.

## Acknowledgements

First I would like to thank my advisor, Mitch Begelman, for taking me on as one of his students. In addition to providing crucial insights at various stages of the projects contained in this thesis, he has been thoroughly supportive of my research endeavors and, especially during my first year as a graduate student, provided me the time necessary to learn the subject matter that comprises my work. By giving me the (guided) freedom to pursue my own lines of reasoning and thought he has been fundamental to my growth as a scientist.

I would also like to thank Chris Nixon and Phil Armitage, with whom I have had numerous enlightening conversations about astrophysics. They have also been invaluable to the numerical aspects of my research, and they contributed significantly to the improvement of my disc golf game through the countless rounds we played at Valmont.

Without the love and support of my parents, Kathleen Harley and Robert Coughlin, none of this would have been possible, and to them both I am eternally grateful. By allowing me to pursue my dreams they have made this thesis a reality. My grandparents Richard and Joan Huber (Gingop and Ganga) have been inspirational to much of my work; they serve as two role models against whom I measure my success as a human being. My in-laws, Robert and Tina Berger, have been incredibly loving and kind to me since the day we first met (c. March 2006) and have always supported me (and haven't complained too openly about the fact that I stole their daughter and took her to Colorado). I'd also like to thank my stepdad, Glenn Harley, for making the 27-hour drive out to Colorado with me, encouraging me in my academic pursuits, and being a great role model.

The friends I met at the University of Colorado made graduate school a fun and enjoyable experience. I had innumerable great times with my housemates, Chris Fowler, Katy Goodrich, Jen Kulow, and Eddy Barratt (and, at an earlier epoch, Matt McJunkin and Seth Jacobson). I thank Greg Salvesen and Susanna Kohler for enlivening the office, generating fruitful discussions, and adorning my wall with pictures of youthful Mitch. I am grateful to Grant Buckingham, Devin Silvia, Jordan Mirocha, and Marek Slipski for the great times we had playing ultimate.

Finally, last but in no way least, I thank my wife Sarah Coughlin for not only tolerating me since we met in high school, but for being the supportive, encouraging partner I needed throughout the completion of this thesis. During my time in graduate school she never once doubted me (even if I did) and kept me sane. Without her none of this would have been possible.

## Contents

<b>Chapter</b>	
<b>1</b>	<b>1</b>
<b>2</b>	<b>11</b>
2.1	11
2.2	13
2.3	15
2.4	16
2.5	21
<b>3</b>	<b>25</b>
3.1	25
3.2	27
3.2.1	29
3.2.2	32
3.3	37
3.3.1	37
3.3.2	38
3.4	47
3.4.1	52
3.5	55

3.5.1	Fragmentation . . . . .	55
3.5.2	Fallback rate features . . . . .	57
3.5.3	Clump fates . . . . .	61
3.5.4	Entropy . . . . .	62
3.6	Summary and conclusions . . . . .	63
<b>4</b>	<b>On the Structure of Tidally-disrupted Stellar Debris Streams</b>	<b>68</b>
4.1	Introduction . . . . .	68
4.2	Velocity distribution . . . . .	69
4.2.1	Self-similar velocity profile . . . . .	69
4.2.2	Radial positions . . . . .	73
4.3	Stream width . . . . .	79
4.3.1	Quasi-hydrostatic width . . . . .	80
4.3.2	Shear dominated . . . . .	81
4.3.3	Approximate, full solution . . . . .	82
4.4	Density . . . . .	83
4.5	Density scalings and fragmentation conditions . . . . .	91
4.5.1	Marginally bound material . . . . .	91
4.5.2	Unbound material . . . . .	93
4.5.3	Bound material and overall scalings . . . . .	95
4.6	Discussion . . . . .	97
4.6.1	The neglect of angular momentum . . . . .	98
4.6.2	Comparison with Kochanek (1994) . . . . .	99
4.6.3	To fragment or not to fragment? . . . . .	103
4.6.4	A more realistic entropy prescription . . . . .	106
4.7	Summary and conclusions . . . . .	110

<b>5</b>	<b>Hyperaccretion During Tidal Disruption Events: Weakly Bound Debris Disks and Jets</b>	<b>113</b>
5.1	Introduction . . . . .	113
5.2	Zero-Bernoulli accretion model . . . . .	117
5.2.1	Gyrentropic flow . . . . .	119
5.2.2	Self-similar solutions . . . . .	120
5.3	ZEBRA models of TDE debris disks . . . . .	122
5.4	Jet properties and temporal evolution . . . . .	128
5.4.1	Inner regions of the accretion disk . . . . .	128
5.4.2	Accretion rate and jet power . . . . .	137
5.4.3	Time-dependent analysis . . . . .	138
5.4.4	<b>Swift</b> J1644+57 . . . . .	156
5.5	Discussion and conclusions . . . . .	159
<b>6</b>	<b>The General Relativistic Equations of Radiation Hydrodynamics in the Viscous Limit</b>	<b>164</b>
6.1	Introduction . . . . .	164
6.2	Relativistic Boltzmann equation . . . . .	168
6.3	Diffusion approach to the transport equation . . . . .	171
6.4	Relativistic, diffusive equations of radiation hydrodynamics . . . . .	177
6.5	Perturbation analysis . . . . .	182
6.6	Discussion and Conclusions . . . . .	189
<b>7</b>	<b>Viscous boundary layers of radiation-dominated, relativistic jets. I. The two-stream model</b>	<b>195</b>
7.1	Introduction . . . . .	195
7.2	Governing equations . . . . .	198
7.3	Two-stream boundary layer . . . . .	200
7.3.1	Basic setup . . . . .	201
7.3.2	Boundary layer equations . . . . .	201
7.3.3	Self-similar approximation . . . . .	203

7.3.4	Solutions . . . . .	207
7.4	Discussion . . . . .	215
7.5	Summary and conclusions . . . . .	218
<b>8</b>	<b>Viscous boundary layers of radiation-dominated, relativistic jets. II. The free-streaming jet model</b>	<b>221</b>
8.1	Governing equations . . . . .	223
8.2	Jetted boundary layer . . . . .	225
8.2.1	Self-similar approximation . . . . .	228
8.2.2	Solutions . . . . .	236
8.3	Discussion . . . . .	242
8.3.1	Comparative notes between the two-stream model (Chapter 7) and the free-streaming jet model . . . . .	248
8.4	Summary and conclusions . . . . .	250
<b>9</b>	<b>Conclusions</b>	<b>253</b>
	<b>Bibliography</b>	<b>256</b>
	<b>Appendix</b>	
<b>A</b>	Non-self-similar ZEBRA solutions	<b>264</b>
<b>B</b>	Non-zero Bernoulli parameter	<b>267</b>

## Tables

Table

## Figures

### Figure

- 1.1 A diagram illustrating the tidal disruption process. The dashed line gives the orbit of the center of mass of the star, and the arrows indicate the center of mass velocity. 3
- 1.2 A schematic of the self-intersection process that occurs during tidal disruption events. Here  $\alpha$  is the angle between the orientation of the pericenter of the incoming debris and that of the outgoing debris, equal to  $\alpha \simeq 10^\circ$  for typical parameters, which is the result of the general relativistic advance of periapsis. . . . . 6
- 2.1 The star at the time of disruption (top, left), where the colors indicate the column density and distances are measured in units of tidal radii ( $\simeq 7 \times 10^{12}$  cm =  $100R_\odot$ ), 0.835 hours after periapsis (top, right; the top two figures coincide with the bottom-left panels of Figure 4 a) and b), respectively, of Lodato et al. 2009.), and 5.38 days (middle, left), 15 days (middle, right), 22.4 days (bottom, left) and 1 month (bottom, right) after disruption. The red, dashed curves on the bottom two rows indicate the analytic predictions. . . . . 17
- 2.2 The computed density of the stream (solid, black curve), the analytic prediction (red, solid curve; equation 3.10), and the density at which self-gravity becomes important (red, dashed curve; equation 2.1) as functions of  $r$  (spherical distance from the hole) at 22.4 days from the point of disruption. Points above the red, dashed curve are self-gravitating. The numerical solution extends to smaller radii because the star at the time of disruption is not spherical (see also Lodato et al. 2009). . . . . 18

2.3	The fallback rate in solar masses per year calculated from the simulation (black, solid curve) and the analytic prediction (red, dashed curve) as functions of time in years. The temporal shift between the numerical solution and the analytic prediction is from the stellar distortion at the time of disruption (see text for further details). The variability at late times is due to the accretion of clumps formed in the self-gravitating stream. The variability starts about 2 years after disruption; however, this timescale depends upon the details of the TDE and its environment, and therefore may be shorter. . . . .	19
2.4	The density two years after disruption and, in the insets, close-ups of the fragments that forms along the stream. . . . .	20
2.5	The ratio $h/R_J$ , $h$ being the smoothing length and $R_J$ the Jeans radius, as a function of density at a time when the first clumps start to form. . . . .	23
3.1	The initial configuration of the star under the impulse approximation when $\beta \simeq 1$ (this figure is not drawn to scale). The dashed curve traces out the orbit of the center of mass, which is assumed to be parabolic. The Cartesian coordinates are indicated by the diagram immediately below the black hole (which is indicated by the black circle), $z$ being out of the plane in a right-handed sense. The spherical-polar coordinates are labeled $r$ and $\phi$ on the diagram, and $\theta$ is measured out of the plane of the orbit from the $z$ -axis (for the above figure that focuses on the $x$ - $y$ plane, $\theta = \pi/2$ ). . . . .	30

- 3.2 The streams of debris formed from the tidal disruption of a solar-type star by a  $M_h = 10^6 M_\odot$  hole situated at the origin. Each color represents a different time, the earliest (blue points closest to the origin) being at  $t = 100 r_t^{3/2} / \sqrt{GM_h} \simeq 1.84$  days from disruption, the latest (yellow points) at  $t = 2200 r_t^{3/2} / \sqrt{GM_h} \simeq 40.6$  days from disruption. The time in between neighboring streams is  $300 r_t^{3/2} / \sqrt{GM_h} \simeq 5.53$  days. The black hole (not drawn to scale) is indicated by the black circle near the origin. While the radial positions of the gas parcels match well those from numerical analyses (see Figure 1 of Chapter 2), the width obtained from equations (3.1) – (3.3) is significantly overestimated (the numerical solutions, had we shown them, would have amounted to lines plotted overtop of the streams in Figure 2). This finding suggests that self-gravity is important for keeping the stream confined in the transverse direction. . . . . 33
- 3.3 Four snapshots of the in-plane evolution of the gas parcels comprising the edge of the star at the time of disruption; for these figures we chose a  $10^6 M_\odot$  hole and a solar-like star. The particles comprising the front of the star at the time of disruption have been colored blue, while the back has been colored orange. The arrows indicate the direction of motion of the center of mass. The bottom, left-hand panel shows that, at a time of roughly an hour after disruption, the front and back of the stream merge and thereafter trade places. The impulse approximation thus leads to a caustic – where the debris streams form a two-dimensional surface – which occurs roughly an hour after disruption. . . . . 34
- 3.4 The star at the time of disruption for an adiabatic index of  $\gamma = 1.5$  (top, left),  $\gamma = 5/3$  (top, right),  $\gamma = 1.8$  (bottom, left) and  $\gamma = 2$  (bottom, right). The configuration has clearly been altered from its original, spherical shape, showing that the tidal force does not act exactly as an impulse as was assumed in Section 2. The central density is also higher for smaller  $\gamma$ , which is predicted from the original stellar profile. . . . 39

- 3.5 The stream at a time of 2.53 days from pericenter for an adiabatic index of  $\gamma = 1.5$  (top, left),  $\gamma = 5/3$  (top, right),  $\gamma = 1.8$  (bottom, left) and  $\gamma = 2$  (bottom, right). The stream thickness decreases dramatically and the fans become less pronounced as  $\gamma$  increases. . . . . 40
- 3.6 Four snapshots of the average stream density (the average density of all particles at a given radius  $r$ ) as a function of  $r$  for the  $\gamma = 5/3$  run. Initially the density remains smooth throughout the stream; however, by about a day after the disruption, the density structure has developed a more complicated nature, consisting of a central peak that is narrower than is predicted analytically and two shoulders. . . . . 43
- 3.7 The average density (same as Figure 6) as a function of  $r$  for  $\gamma = 1.5$  (top, left panel),  $\gamma = 5/3$  (top, right panel),  $\gamma = 1.8$  (bottom, left panel), and  $\gamma = 2$  (bottom, right panel) at a time of 2.53 days after disruption (see Figure 3.5 for the shape of the streams at this time). The black, solid curves give the numerical solutions, while the red, dashed curves show the analytic predictions. It is apparent that larger adiabatic indices correspond to an enhanced amount of variability in the density along the stream, while a smaller adiabatic index results in more extended wings (this is also apparent from the tidal fans in the edges of the streams in Figure 3.5.) . . . . . 44
- 3.8 The maximum density along the stream as a function of time with  $\gamma = 5/3$  ( $n = 1.5$ ); the numerical solution is given by the black, solid curve, and the analytical solution (equation 3.18) is given by the red, dashed curve. A time of zero here corresponds to the time at which the star reaches the tidal radius. The time at which the numerically-obtained density starts to decrease is slightly earlier than the analytic one, suggesting that the time at which the star is “disrupted” is actually pre-periapsis. The first bump in the numerical solution, which occurs after a couple of hours, indicates where the pancake starts to augment the maximum density. At late times, both solutions follow the approximate power-law decline  $\rho \propto t^{-1.8}$ . . . . . 45

- 3.9 The maximum density as a function of time for  $\gamma = 1.5$  (black, solid curve),  $\gamma = 5/3$  (red, dashed curve),  $\gamma = 1.8$  (green, long-dashed curve), and  $\gamma = 2$  (blue, dotted curve). It is apparent that the initial perturbation induced by the pancake is induced sooner for larger  $\gamma$ , and the oscillation timescale of the perturbation is shorter for larger  $\gamma$ . . . . . 46
- 3.10 The particle distributions from an  $N$ -body simulation, where the initial conditions were taken from the  $\gamma = 5/3$  run at periapsis, at 37 minutes (left panel), 50 minutes (middle panel), and 62 minutes (right panel) post-disruption. The red particles comprised the back of the star at the time of disruption, while the black constituted the front of the star. This Figure demonstrates that a caustic – where the front and back of the stream merge to form an infinitely thin line – still occurs in the presence of realistic initial conditions. However, as mentioned in the text, the outermost layers of the star that are stripped earlier (and therefore violate the frozen-in condition) do not undergo this compression; this is evidenced from the fact that the “fans” present in this figure undergo no distortion in terms of their color. The central panel corresponds to the point at which the width of the stream has reached a minimum, the half-width being  $H \simeq 0.1 r_t$ . . . . . 50
- 3.11 The average density as a function of  $r$  for the unaltered,  $\gamma = 5/3$  run (solid, black curve) and the run that avoids the caustic (dashed, red curve), both at a time of 2.53 days (the same time as in Figure 3.7). This Figure shows that the pancake amplifies the anomalous density structures along the stream, effectively enhancing the ability of self-gravity. . . . . 54
- 3.12 The stream from the  $\gamma = 2$  run (top panel) and a closeup view of the stream (bottom panel), showing the clumps that have formed throughout the majority of the stream, both at a time of 5.69 days after disruption. . . . . 56

- 3.13 The fallback rate computed for the  $\gamma = 1.5$  (black curve) and  $\gamma = 5/3$  (red curve) runs. The purple curve is the canonical  $t^{-5/3}$  fallback rate for reference. It is apparent that the return time of the most bound material is earlier for smaller  $\gamma$ , which is related to the amount of distortion imparted to the star at the time of disruption. At late times, the accretion of clumps that have formed in the  $\gamma = 5/3$  stream causes the fallback rate to deviate significantly from the mean (the small amount of deviation present in the  $\gamma = 1.5$  run is numerical noise). . . . . 58
- 3.14 The fallback rate for the  $\gamma = 1.8$  run (green, solid curve) and the analytic prediction (blue, dashed curve). We see that the numerical solution is larger than the analytic one by an order of magnitude, and the fallback of bound clumps causes significant deviation from the average,  $t^{-5/3}$  fallback at times greater than about 6 months from disruption. . . . . 59
- 4.1 The solution to equation (4.4) passing through the critical point  $f(2/3) = 1$  (blue, solid curve). The approximate solution given by  $f = -1 + 1/\xi$ , which matches the asymptotic limits of the true solution, is shown by the red, dashed, curve. . . . . 72
- 4.2 A comparison between the self-similar (red, dashed curves) and numerical (black points) radial velocity profiles, both normalized to the speed of light, for the debris stream produced by the disruption of a solar-like star by a  $10^6 M_\odot$  black hole. The numerical solution was taken from the simulation in Chapter 2. The different curves represent the stream at different times, with each curve corresponding to, from left to right, 11, 30, 60, 120, 180, 300, 451, and 601 days since disruption. . . . . 74

4.3 A log-log plot of the difference in velocity normalized to the speed of light, i.e.,  $\Delta v/c \equiv (v_n - v_{ss})/c$ , where  $v_n$  is the numerically-obtained radial velocity and  $v_{ss}$  is the analytic solution (equation 4.2), for the same times chosen in Figure 4.2 (i.e., the dark blue set of points is 11 days after disruption, the light yellow set of points is 601 days after disruption, and each set of points in between corresponds to the appropriate curve in Figure 4.2). As discussed in Section 6.1, the small discrepancies shown here can plausibly be attributed to the neglect of angular momentum in the self-similar solution. . . . . 75

4.4 The analytic solution for the density when self-gravity dominates the shear of the black hole (equation 4.45), shown in the left panel, and when the shear dominates the self-gravity of the stream (equation 4.46), shown in the right panel, as functions of  $r$  for the disruption of a solar-like star by a  $10^6 M_\odot$  SMBH. We assumed isentropic gas with  $\gamma = 5/3$  and entropy calculated for solar-like parameters ( $S = 2.48 \times 10^{14}$  [cgs]; Hansen et al. 2004). The different colors correspond to different times, with the earliest time being  $2500 \times r_t^{3/2}/\sqrt{2GM_h} \simeq 32$  days after disruption (left-most, dark blue curve), the latest being  $47500 \times r_t^{3/2}/\sqrt{2GM_h} \simeq 620$  days after disruption (right-most, light blue curve), and each curve differing from the previous one by  $7500 \times r_t^{3/2}/\sqrt{2GM_h} \simeq 98$  days. . . . . 86

4.5 The numerical solution for the density when self-gravity dominates the shear of the black hole (the solution to equation 4.41 with  $H$  given by equation (4.30),  $\partial r/\partial \mu$  calculated numerically, and  $\partial M/\partial \mu$  calculated numerically from equation (4.43) with  $n = 1.5$ ), shown in the left panel, and when the shear dominates the self-gravity of the stream (the solution to equation 4.41 with  $H$  given by equation (4.33),  $\partial r/\partial \mu$  calculated numerically, and  $\partial M/\partial \mu$  calculated numerically from equation (4.43) with  $n = 1.5$ ), for the same parameters and times chosen in Figure 5.3. . . . . 86

- 4.6 The numerical solution for the density that adopts the piecewise behavior for  $H$  (equation 4.34) so that the density is shear dominated in regions where  $\rho < M_h/(2\pi r^3)$  and self-gravity dominated where  $\rho > M_h/(2\pi r^3)$ , for the same parameters and times chosen in Figure 5.3. The yellow, dashed line shows the curve  $M_h/(2\pi r^3)$ . . . . . 89
- 4.7 A particle plot of the density in the stream  $\rho$  in units of  $\text{g} / \text{cm}^3$  as a function of  $r$  in tidal radii at a time of 57 days post-disruption. The red points are from the simulation used in Chapter 2, the black points are from an identical simulation but with  $10^7$ , as opposed to  $10^6$ , particles, and the green, dashed curve shows the function  $M_h/(2\pi r^3)$  – the approximate dividing line between the shear and self-gravity dominated solutions. . . . . 90
- 4.8 The quantity  $q = d \ln(\rho r^3) / d \ln t$  as a function of  $\mu$  when  $\gamma = 5/3$ ,  $M_h = 10^6 M_\odot$ , the progenitor is solar, and the gas is isentropic; the flow is assumed to be self-gravity dominated in the left-hand panel and shear-dominated in the right-hand panel. The different curves show different times, with the blue curve at  $1000 \times r_t^{3/2} \sqrt{2GM_h} \simeq 13$  days after disruption, the brown curve at  $11000 \times r_t^{3/2} \sqrt{2GM_h} \simeq 143$  days after disruption, and each curve differs from the next closest curve by  $2000 \times r_t^{3/2} \sqrt{2GM_h} \simeq 26$  days (e.g., the yellow curve is 26 days after the blue curve, the green curve is 26 days after the yellow curve, etc.). The range of the  $y$ -axis was set to the same values for each plot for ease of comparison. Fluid elements in the stream follow vertical lines from one curve to the next. . . . . 96
- 4.9 A schematic of the debris stream, not drawn to scale, returning to the black hole under the approximations set out in our analysis (left drawing) and a more realistic distribution that accounts for the finite angular momentum of the hole (right drawing). This shows that, as the material gets very close to the hole, the tidal compression becomes a tidal shear that serves to decrease the density. . . . . 100

4.10	A log-log plot of the stream width, $H$ , in units of solar radii at the marginally-bound location along the stream as a function of Lagrangian distance (i.e., moving with the marginally-bound portion of the stream) from the SMBH. The black, solid curve shows the solution from the same simulation performed in Chapter 2 (i.e., a solar-like star destroyed by a $10^6 M_\odot$ SMBH) but with $10^7$ particles, while the red, dashed curve shows the analytic prediction $H/R_\odot \propto (r/r_t)^{1/2}$ (the constant of proportionality was set to 0.33). . . . .	102
5.1	The value of $q$ obtained for $\gamma = 4/3$ (blue, solid) and $\gamma = 5/3$ (red, dashed) as we vary the left-hand side of equation (5.19). . . . .	127
5.2	The self-consistent model (equation (5.22)) for the angular momentum (blue, solid), the self-similar model (red, dashed), and the psuedo-Newtonian distribution (black, dotted). Here we've set $q = 1.5$ , $\gamma = 4/3$ , the abscissa is in units of Schwarzschild radii, and the angular momentum is normalized by $\sqrt{GM_h r_s}$ . . . . .	131
5.3	Solutions for the density in the non-self-similar (blue, solid) and self-similar (red, dashed) limits. Here $q = 1.5$ , $\gamma = 4/3$ , the x-axis is in units of Schwarzschild radii, and the density is measured in units such that $\rho_0 (r_s/r_0)^{-q} = 1$ , i.e., the red, dashed curve is simply $(r/r_s)^{-2.2}$ . . . . .	133
5.4	The mass contained within $r$ for the angular momentum given in equation (5.22) (blue, solid) and that for the self-similar model (red, dashed). The parameters are the same as those in Figure 5.3, with the same normalization for the density. . . . .	134
5.5	The angular momentum contained within $r$ for the self-consistent model (blue, solid) and the self-similar solution (red, dashed). The parameters and normalization are the same as those in Figure 5.3. . . . .	135
5.6	A schematic of the star at the time of disruption to illustrate the geometry. Note that $r = \eta R_*$ . . . . .	141

- 5.7 The solution for  $q(t)$  with a solar progenitor ( $M_* = 1 M_\odot$ ,  $R_* = 1 R_\odot$ ,  $\gamma_* = 5/3$ ), a radiation pressure-dominated gas ( $\gamma = 4/3$ ),  $M_h = 10^5 M_\odot$ ,  $y = 1$ ,  $\delta = 0.05$ ,  $\chi = 5$ , and three different  $q_0$ , indicated by the legend. As one can see, the initial conditions quickly become irrelevant to the long-term behavior of the solutions. . . . . 144
- 5.8  $q(t)$  for a radiation-dominated gas ( $\gamma = 4/3$ ) and a variety of black hole masses. Here  $y = 0.5$ ,  $\delta = 0.05$ ,  $\chi = 5$ ,  $q_0 = 3/2$ ,  $\gamma_* = 5/3$ ,  $M_* = 1 M_\odot$ , and  $R_* = 1 R_\odot$ . The legend displays the black hole mass in units of solar masses. We see that initially  $q$  falls off very rapidly, which is a consequence of initial conditions. However, the initial conditions stop having a major effect early in the evolution of the system, and  $q$  then decreases less rapidly. . . . . 145
- 5.9 The mass contained in the ZEBRA as a function of time for the same parameters as those in Figure 5.8. The mass quickly increases initially, owing to the fact that the fallback rate exceeds the accretion rate. However, as both rates decrease for later times, the mass levels off to a nearly constant value. . . . . 146
- 5.10 The jet luminosity, normalized to the Eddington luminosity of the black hole, for the same parameters as those in Figure 5.8 with an efficiency  $\epsilon = 0.1$ . Initially the luminosity is very super-Eddington, decaying to only mildly super-Eddington at later times. . . . . 147
- 5.11 The black hole accretion rate, given by equation (5.26), in solar masses per year for  $q_0 = 1$  (blue, solid curve) and for  $q_0 = 2$  (red, dashed curve) to illustrate where the solutions have converged; the parameters are the same as those in Figure 5.8 and the black hole has a mass  $M_h = 10^5 M_\odot$ . We have also plotted the fallback rate, shown by the black, dotted curve, to illustrate how the two accretion processes compare. It is apparent from this figure that they match each other closely, and that after about 4 years, the black hole accretion rate exceeds the fallback rate. . . . . 149
- 5.12 The effective temperature as a function of time for different black hole masses. The fiducial parameters are the same as those in Figure 5.8. . . . . 151

- 5.13 The black hole accretion rate (blue, solid curve) and the fallback rate (red, dashed curve) for  $M_0 = 0.1 \times M_\odot/2$ ,  $M_h = 10^5 M_\odot$ ,  $m = 2$ , and otherwise the same parameters as in Figure 5.8, plotted on a log-log scale. The accretion rate follows a shallower power-law than the fallback rate, causing the former to exceed the latter for times greater than about 0.5 years. . . . . 154
- 5.14 The power-law of the accretion rate, which we defined as  $m_{acc}$ , as a function of the power-law index of the fallback rate is shown by the blue, solid curve. The value of  $m_{acc}$  is determined by performing a best-fit to the black hole accretion rate between  $t = 0.2$  and 1.5 years, during which time the accretion rate, for all values of  $m$ , is well-described by a power-law. We have also plotted  $m$  for comparative purposes (red, dashed curve). We see that  $m_{acc}$  is always less than  $m$ . For small values of  $m$ , the relationship between  $m_{acc}$  and  $m$  is roughly an offset, linear one. As  $m$  becomes larger, however,  $m_{acc}$  displays a more nonlinear behavior, and the difference between the two power-law indices becomes larger. . . . . 155
- 7.1 The function  $f_\xi$ , which is the normalized  $z$ -component of the four velocity, in terms of the parameter  $\tilde{\alpha} \propto y/\sqrt{z}$ , for  $\mu = 1$  and a number of jet Lorentz factors, as indicated by the legend. As we can see, the thickness of the velocity boundary layer, in terms of  $\tilde{\alpha}$ , is nearly independent of  $\Gamma_j$ . . . . . 208
- 7.2 The variation of the normalized density, given by  $g$ , as a function of  $\tilde{\alpha}$  for the same parameters as those chosen for Figure 7.1. The density remains below its asymptotic value over a slightly larger range of  $\tilde{\alpha}$  for higher  $\Gamma_j$ , and the decrease in density within the boundary layer is consistent with the findings of Arav & Begelman (1992). The density formally equals zero at  $\tilde{\alpha} = 0$ ; however, because  $g$  approaches zero at a very slow rate (recall  $g(\xi) \propto -1/\ln \xi$ ), it appears from the Figure, which only samples a finite number of points around  $\tilde{\alpha} = 0$ , that the density remains positive and larger for smaller  $\Gamma_j$ . . . . . 209

- 7.3 The solution to equation (7.27),  $h$ , which is the normalized number density of photons, for the same set of parameters as those chosen in Figure 7.1. The number density of photons is seen to roughly track the number density of scatterers. Because the energy density of the radiation remains constant across the layer, the energy per photon increases in the boundary layer. . . . . 210
- 7.4 The solution for the normalized  $z$ -component of the four-velocity ( $f_\xi$ ) for  $\Gamma_j = 25$  and three different values of  $\mu$ , as indicated by the legend. The velocity profile does not differ much as  $\mu$  increases beyond 1, but for smaller values of  $\mu$  the boundary layer widens noticeably. . . . . 212
- 7.5 The function  $g$ , which is the rest-frame number density of scatterers, for the same parameters as in Figure 7.4. For smaller values of  $\mu$ , the density is significantly reduced from its asymptotic value over a larger range in  $\alpha$ . . . . . 213
- 7.6 The solution to equation (7.27), which gives the number density of photons observed in the comoving frame, for the same set of parameters as in Figure 7.4. The radiation number density roughly follows that of the scatterers. . . . . 214
- 8.1 The behavior of  $f_\xi$ , which is the normalized  $z$ -component of the four-velocity, with  $\xi$  for  $\zeta = 4$  (blue, solid curve),  $\zeta = 10$  (purple, dot-dashed curve), and  $\zeta = 25$  (red, dashed curve). As expected, the curves are all coincident when  $\xi \ll 1$  and  $\xi \gg 1$ , with a non-self-similar transition (one that depends on  $\zeta$ ) in between those two limits. 233
- 8.2 The function  $g$ , which is approximately the inverse of the lab-frame density, plotted with respect to  $\xi$  for the same set of  $\zeta$  chosen in Figure 8.1. As was true for  $f_\xi$ ,  $g$  is approximately self-similar close to and far from the jet, with the deviation from self-similarity in the trans-relativistic region being apparent but small. . . . . 234

- 8.3 The normalized  $z$ -component of the four-velocity ( $f_\xi$ ) for  $\mu = 1$  and  $\zeta = 4, 10,$  and  $25$  (the solid, blue curve, the dot-dashed, purple curve, and the dashed, red curve, respectively), which, for  $z \simeq z_0$ , correspond to  $\Gamma_j = 4, 10,$  and  $25$ . We see that the width of the boundary layer is nearly unchanged as we alter the value of  $\zeta$ . . . . . 238
- 8.4 The normalized fluid-frame density of scatterers for the same set of parameters used in Figure 8.3. For all solutions the number density of scatterers approaches zero as we near the center of the jet. We see that the average number density of scatterers within the boundary layer is lower for larger Lorentz factors. . . . . 239
- 8.5 The normalized number density of photons for the same set of  $\zeta$  used in Figure 8.3. The photon number density closely follows that of the scatterers. . . . . 240
- 8.6 The  $y$ -component of the three-velocity normalized by  $\sqrt{2/(9\rho'_0\kappa z_0)}$  (see equation (8.42)) for the same set of parameters used in Figure 8.3. For positive  $\tilde{\alpha}$ , each solution is initially positive and reaches a relative maximum before approaching a negative constant, which shows that the flow expands outwards near the center of the jet and entrains ambient material far from the axis. . . . . 241
- 8.7 The function  $f_\xi$ , which is the normalized  $z$ -component of the four-velocity, for  $\zeta = 10$  and  $\mu = e'/\rho'_0 = 0.1, 1,$  and  $10$ , which correspond to the blue, solid curve, the purple, dot-dashed curve, and the red, dashed curve, respectively. Increasing the value of  $\mu$ , we see, has little effect on the solution, while decreasing  $\mu$  drastically widens the boundary layer. . . . . 243
- 8.8 The normalized density of scatterers for the same values of  $\mu$  chosen in Figure 8.7. The mean value of the density decreases as  $\mu$  decreases. . . . . 244
- 8.9 The normalized number density of photons for the same set of  $\mu$  chosen in Figure 8.7. This figure demonstrates, as we saw in Figure 8.5, that the density of photons tracks that of the scatterers. . . . . 245

- 8.10 The  $y$ -component of the three-velocity, normalized by  $\sqrt{2/(9\rho'_0\kappa z_0)} \sim \delta$ , for the same set of  $\mu$  chosen in Figure 8.7. We see that the relative maximum increases for smaller  $\mu$ . . . . . 246

# Chapter 1

## Introduction

Of the numerous predictions of Einstein’s general theory of relativity, perhaps the most profound is that of a black hole – a region of spacetime so severely warped by the presence of mass that not even light can propagate freely. Initially regarded as mathematical curiosities that were of little physical relevance, black holes are now considered fundamental to many seemingly-distinct aspects of astronomy and play central roles in the evolution of the Universe. Furthermore, a supermassive black hole (SMBH), with a mass in excess of  $\sim 10^5 M_\odot$ , is now thought to reside at the center of nearly every galaxy.

Some of these galactic SMBHs reveal themselves through the intense emission of radiation across many wavelengths and thereby fall into the class of active galactic nuclei (AGN; e.g., Krawczynski & Treister 2013). While these AGN come in a variety of observational flavors – quasars (e.g., Warren & Hewett 1990), Seyfert galaxies (e.g., Maiolino & Rieke 1995), and radio galaxies (e.g., Begelman et al. 1984), to name a few – the underlying physical mechanism generating the luminous output is thought to be the same and arises from the accretion of material onto a SMBH. However, galaxies harboring AGN are in the minority (at least as we see them today), and the central regions of most galaxies remain quiescent and give no indication of the gravitational monster that lies within.

When studying these quiescent galaxies, astronomers are usually forced to rely on empirical laws such as the  $M-\sigma$  (Ferrarese & Merritt, 2000; Gebhardt et al., 2000) and Magorrian (Magorrian et al., 1998) relations to infer information about the black hole at the galactic center. These laws

relate the SMBH mass to the velocity dispersion ( $M$ - $\sigma$  relation) or the mass (Magorrian relation) of the galactic bulge. One important caveat is that, while these laws seem to yield tight and reliable correlations over a fairly wide range in black hole mass, it is unclear whether they can be applied to every galaxy. Indeed, a more direct probe of the central region of a quiescent galaxy would not only yield useful information about the properties of the black hole at its center, it would also generate an independent constraint on the validity of the  $M - \sigma$  and Magorrian relations.

Tidal disruption events (TDEs) provide one such probe by igniting brief periods of AGN-like activity in otherwise-quiescent galaxies, thereby illuminating their central SMBHs. These events occur when a star is tidally shredded by the SMBH at the center of a galaxy. Specifically, when a star of mass  $M_*$  and  $R_*$  is far away from a SMBH of mass  $M_h$  (but still within the sphere of influence of the hole), the star can effectively be treated as a point mass and the magnitude of the gravitational field it experiences is simply  $f_g = GM_h/r^2$ , where  $r$  is the instantaneous distance between the center of mass of the star and the SMBH. However, the finite stellar radius becomes important as the star nears the SMBH, with the side of the star closer to the hole feeling a stronger force than the side that is farther away. This differential force across the stellar diameter – the **tidal force** – scales as  $f_t = 2GM_hR_*/r^3$  and stretches the star along  $r$ , perturbing its original, assumed-spherical structure. If the distance between the center of mass of the star and SMBH continues to decrease, the magnitude of the tidal force can actually exceed the self-gravity of the star,  $f_{sg} \simeq GM_*/R_*^2$ , resulting in its destruction. The radius at which the stellar self-gravity equals the tidal force, the **tidal radius**, is given by  $r_t \simeq R_* (M_h/M_*)^{1/3}$ , and defines the approximate location at which the star will be destroyed by the gravitational field of the SMBH (the numerical factor, of order unity, that enters this equation depends on the precise properties of the star; Guillochon & Ramirez-Ruiz 2013). This process (and the complex gravitational and thermodynamical processes that ensue; see below) is known as a tidal disruption event, and the reader is referred to Figure 1.1 for a rough schematic that illustrates the interaction.

TDEs have been studied for decades, with the earliest investigations attempting to elucidate the rates at which they should occur. The pioneering work of Frank & Rees (1976), who studied

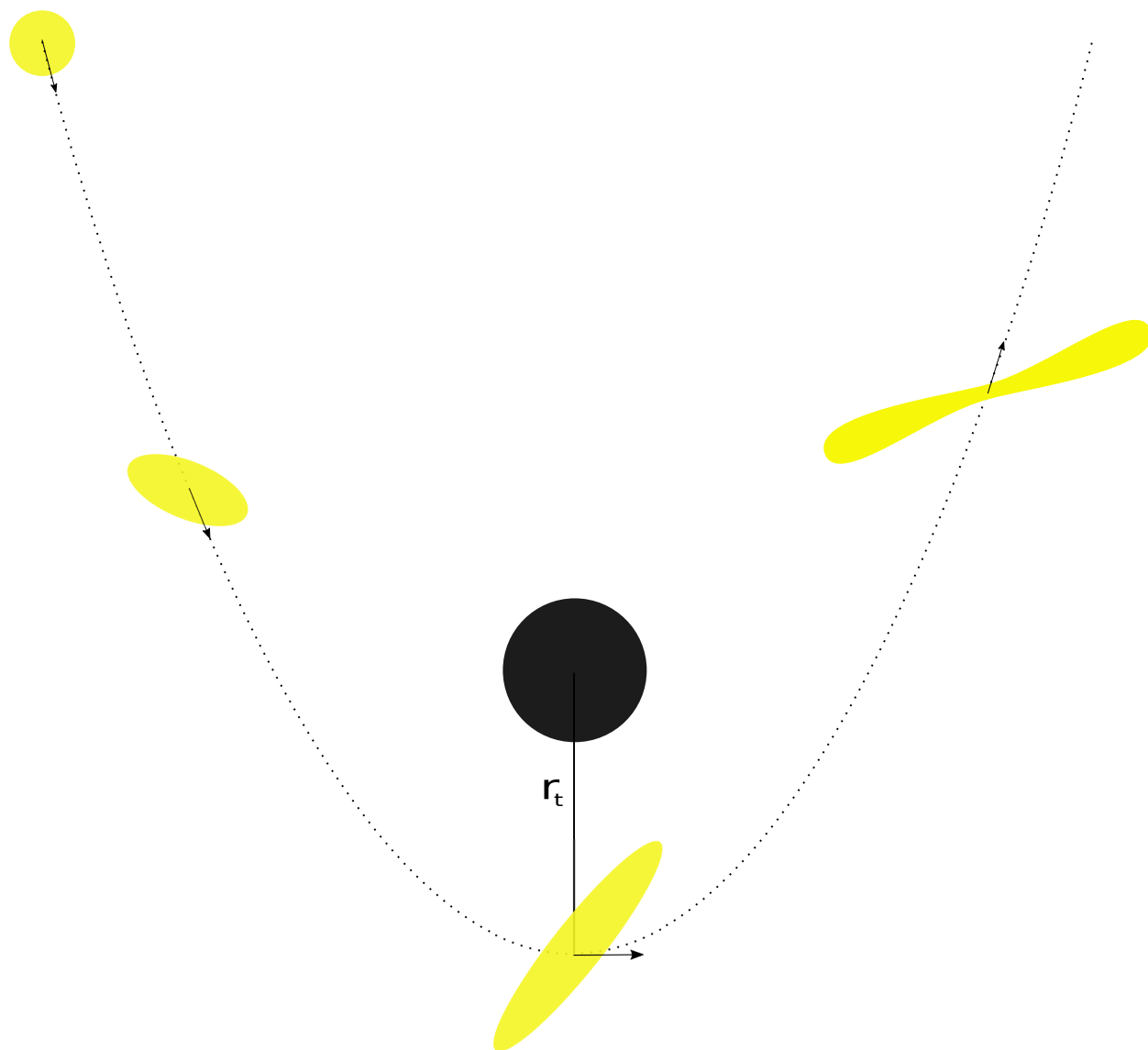


Figure 1.1: A diagram illustrating the tidal disruption process. The dashed line gives the orbit of the center of mass of the star, and the arrows indicate the center of mass velocity.

the process by which stars are scattered into the loss cone of orbits that plunge within the tidal sphere of the SMBH at the center of a galaxy, demonstrated that this rate should be approximately  $10^{-4} - 10^{-5}$  disruptions per galaxy per year. Since then, others have refined these estimates by performing numerical simulations and accounting for uncertainties concerning the low-mass end of the SMBH distribution (Brockamp et al., 2011; Stone & Metzger, 2014). The tidal disruption rate of a supermassive black hole binary has also been calculated, and could be as high as  $10^{-1}$  per galaxy per year (Chen et al., 2009); such a high rate then has notable consequences for future surveys, such as the Large Synoptic Survey Telescope (LSST), that are predicted to observe thousands to millions of galaxies (Ivezic et al., 2008).

In addition to calculating the rates of TDEs, much work has been done on the tidal disruption process itself and the fate of the disrupted debris. Early studies showed that the tidal potential of the SMBH generates a range in the binding energy (i.e., the sum of the kinetic and potential energies) of the disrupted material (Lacy et al., 1982). If the center of mass of the star is on a parabolic orbit, which should be true to a high degree of accuracy considering that most stars scattered into the loss cone come from very far distances from the SMBH (Frank & Rees, 1976), then this range in energies implies that roughly half of the material is bound to the black hole (negative binding energy) while the other half is unbound (positive binding energy) (Rees, 1988). Thus, half of the disrupted debris will recede to large (but finite) distances from the black hole before eventually returning to the point of disruption, while the other half will escape from the black hole at some terminal velocity, which scales approximately as  $v_\infty \simeq v_{esc} (M_h/M_*)^{1/6}$ ; here  $v_{esc} = \sqrt{2GM_*/R_*}$  is the escape velocity from the surface of the tidally-disrupted star. For the fiducial encounter between a solar-like star (i.e., one with a solar mass and a solar radius) and a  $10^6 M_\odot$  SMBH, the most bound material takes about a month to return to the point of disruption, while the escape velocity of the most unbound debris is on the order of a few percent the speed of light. Furthermore, while the initial stage of the fallback of material to the SMBH may depend on the specific details of the encounter (Lodato et al., 2009), asymptotically the rate at which debris returns to pericenter should scale as  $t^{-5/3}$ ,  $t$  being the time since disruption (Phinney 1989, but

see Guillochon & Ramirez-Ruiz 2013), and this feature has been seen in all TDEs observed so far (Komossa, 2015).

Despite the fact that the star is “tidally shredded” by the SMBH, the disruption process itself is relatively gentle (see, however, Carter & Luminet 1983, Bicknell & Gingold 1983, and Guillochon et al. 2009 for the scenario in which the star plunges deep inside the tidal radius, where the encounter can be more violent). After passing through the tidal radius, the star is stretched into a long thin debris stream (Chapter 2). In general, the gas parcels comprising this stream evolve under the gravitational influence of the black hole in the radial direction, with self-gravity being important for confining the stream in its transverse extent (Kochanek 1994, Chapters 2 – 4). Because of the tidal potential mentioned above, half of this stream escapes from the influence of the black hole.

So far, little if any of the disruptive encounter presents observable evidence of its occurrence (but see Kasen & Ramirez-Ruiz (2010) for a discussion of recombination transients that may provide weak optical signals on the order of weeks after disruption, and Guillochon et al. (2015) and Chen et al. (2015) for an analysis of the debris remnants that may mimic supernova remnants). However, the bound portion of the debris stream – the half of the disrupted star that eventually returns to the point of disruption – can generate a substantial luminous flare across a number of wavelengths. In particular, as material returns to the SMBH, it is compressed vertically and horizontally; this compression can then generate a shock that heats the gas and dissipates kinetic energy (Rees, 1988; Evans & Kochanek, 1989). Furthermore, after material passes through pericenter for a second time, its orbit is rotated through a general relativistic precession angle that amounts to approximately  $10^\circ$  for a solar-like star disrupted by a  $10^6 M_\odot$  SMBH (this also assumes that the pericenter distance of the star was equal to the tidal radius at the time of disruption; Rees 1988). As this debris recedes from the black hole for a second time, it will thus impact the portion of the debris stream still making its way to the black hole (see Figure 1.2). This intersection will also serve to deplete the kinetic energy of the debris at the expense of heating it viscously (see Piran et al. 2015 for a discussion of the observable signals generated at this stage of the TDE).

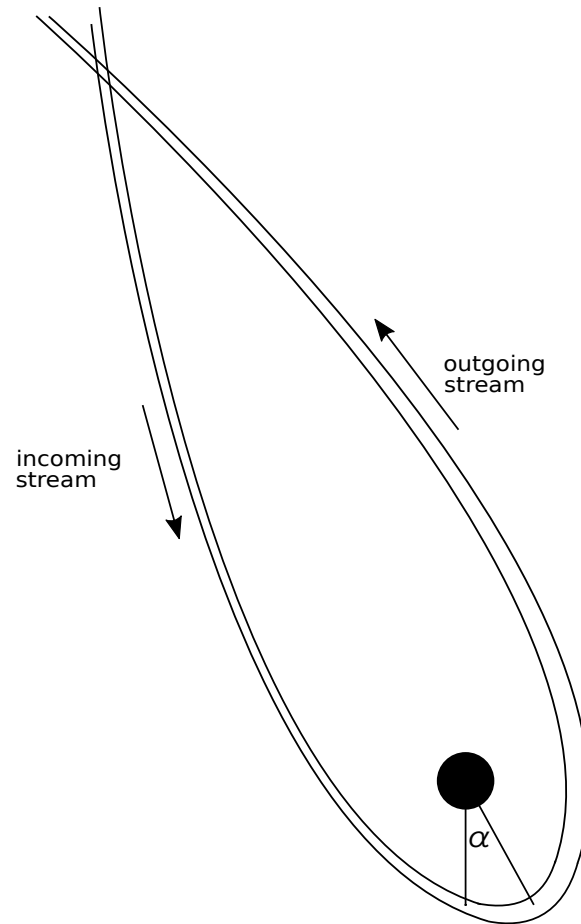


Figure 1.2: A schematic of the self-intersection process that occurs during tidal disruption events. Here  $\alpha$  is the angle between the orientation of the pericenter of the incoming debris and that of the outgoing debris, equal to  $\alpha \simeq 10^\circ$  for typical parameters, which is the result of the general relativistic advance of periastron.

Through non-ideal interactions such as these, the bound debris from a TDE will generally dissipate its ordered kinetic energy, ultimately resulting in material moving closer to the SMBH. If the gas continues to lose its energy efficiently, then material will be rapidly funneled onto the SMBH, releasing a large amount of radiation in the process. Through such a sequence of events, the bound portion of the debris stream should give rise to an intense period of accretion onto the black hole, continuing as material from the debris stream returns to the pericenter of the original star and forming an accretion disk around the SMBH. Early predictions generally found that the spectra of these accretion disks should peak in the optical/UV (Cannizzo et al., 1990; Ulmer, 1999; Lodato & Rossi, 2011), with the lightcurve tracking the initial fallback rate for years before transitioning to a viscous-like accretion phase (Lodato & Rossi, 2011). These predictions are generally in agreement with observations (Komossa, 2015), though there have been a few surprises (see below).

An intriguing feature of the early stages of the accretion process concerns the rate at which material is consumed by the SMBH. Specifically, if the black hole mass is less than roughly  $10^7 M_{\odot}$  (and the disrupted star is solar-like), then, assuming that the rate at which material returns to pericenter closely mimics the accretion rate onto the black hole, one can show in a straightforward manner that the accretion rate onto the SMBH is super-Eddington for months to years (Strubbe & Quataert 2009, 2011, Chapter 5). During this super-Eddington phase, when the isotropic radiation pressure associated with the accretion luminosity exceeds the gravitational pull of the black hole, material may be blown off in a large-scale wind (Strubbe & Quataert, 2009), the disk may “spread” to account for the high luminous output and redistribution of angular momentum (Shen & Matzner, 2014), or the debris may be heated to the point where the accretion disk becomes quasi-spherical (Loeb & Ulmer 1997, Chapter 5).

One of the most profound aspects of tidal disruption events, from theoretical and observational standpoints alike, is that they can be responsible for launching collimated, fast-moving (i.e., on the order of the speed of light) outflows of gas. While these **relativistic jets** are encountered in other seemingly-distinct astrophysical phenomena including, but not limited to, radio galaxies (e.g., Begelman et al. 1984), gamma-ray bursts (GRBs; e.g., Woosley 1993; MacFadyen & Woosley 1999;

Woosley & Bloom 2006), and Herbig-Haro objects (Reipurth & Bally, 2001), they were completely unexpected from TDEs (but see the prescient analysis of Giannios & Metzger 2011) prior to the discovery of the event **Swift** J1644+57 (hereafter J1644; Bloom et al. 2011; Burrows et al. 2011; Cannizzo et al. 2011; Levan et al. 2011; Zauderer et al. 2011). When it originally triggered the burst alert telescope (BAT) onboard the **Swift** satellite, J1644 was a source of hard X-rays and soft gamma-rays that was thought to be an ordinary GRB. However, continued monitoring with the X-ray telescope (XRT) also onboard the **Swift** satellite showed that its level of activity continued well past the normal threshold of GRB duration, with emission measured by the XRT extending beyond 500 days after the initial detection (compared to the standard 1-10 second duration of long GRBs). Observations in the radio with very long baseline interferometry (VLBI) also showed that J1644 was simultaneously a strong source of radio emission, with radio observations yielding a non-zero detection long after the cessation of the X-ray emission (see Zauderer et al. 2013 for the long-term evolution of the radio emission). The X-ray lightcurve also exhibited an approximately power-law decay,  $L_X \propto t^{-\alpha}$ , with  $1 \lesssim \alpha \lesssim 2.5$ .

Ultimately, the extremely long duration, power-law decline of the X-ray emission (with power-law index consistent with the theoretically-expected value of 5/3), proximity to the nucleus of an identified host galaxy, and coincident (spatially and temporally) radio emission led observers and theorists alike to interpret J1644 as the first-observed, jetted TDE. The luminosity of the source was unequivocally super-Eddington by orders of magnitude (Zauderer et al., 2011), which has been the invoked explanation for the presence of the relativistic jet (though the mechanism responsible for launching and collimating the jet remains elusive and polemical; see Tchekhovskoy et al. 2014 and Chapters 7 and 8). Since the discovery of J1644, two other sources – **Swift** J2058+05 (Cenko et al., 2012) and **Swift** J2111-28 (Brown et al., 2015) – have also been found that are qualitatively (and quantitatively, to a lesser extent) similar to J1644. It thus appears that relativistic jets make an appearance in a small subclass of TDEs, specifically those that are super-Eddington in nature.

Following the order-of-events picture of TDEs generated above, this thesis is organized to tell the evolutionary history of a tidal disruption event – from the formation of the tidally-disrupted

debris stream, to the development and evolution of the accretion disk, and finally to the behavior of the relativistic jets that can be launched from these systems. Perhaps not surprisingly, this chronological order was not the order in which the research was done, with the projects on the debris streams (Chapters 2 – 4) done most recently and the project on the accretion disks (Chapter 5) done first. However, to preserve the readability of the thesis, we follow the history that makes sense from a nature-oriented, as opposed to an academic, standpoint. We note, however, that opting to do will result in earlier parts of the thesis referencing later parts.

The first three chapters of this thesis describe the dynamical evolution of the debris streams generated from TDEs. In particular, Chapter 2 presents the findings of an analytical and numerical investigation that considers the self-gravity of tidally-disrupted debris streams, showing that these streams can be gravitationally unstable and form small-scale, gravitationally-bound “clumps.” In Chapter 3 we investigate how the gravitational stability of these streams is affected by the thermodynamic properties of the gas, and we show that stiffer equations of state result in decreased stability. Chapter 4 gives a predominantly analytic treatment of these debris streams, deriving approximate expressions for their velocity structure, density profile, and stability criteria, and the results are compared to the simulations performed in Chapter 2.

In Chapter 5 we consider the next stage of the tidal disruption process, and develop a new model to describe the structure of the accretion disks that form during the super-Eddington phase of accretion that ensues from some TDEs. This ZERo-BERnoulli Accretion, or ZEBRA, picture postulates that the debris forming the disk absorbs energy liberated during the accretion process until it conforms to a weakly-bound (zero-Bernoulli) state. Using the zero-Bernoulli prescription, we find self-similar expressions for the density, pressure, and angular momentum profiles of the disk. We make comparisons to the event **Swift** J1644 and we show that our model is consistent with observations if the black hole that powered this event has a mass of  $\sim 10^5 M_\odot$ .

Finally, the last three chapters describe the evolution of the jets launched from these systems, the energy and momentum of these jets dominated by the radiation released during the accretion process. Chapter 6 presents a derivation of the general relativistic equations of radiation hydrody-

namics in the viscous limit, which describe how anisotropies in a radiation field transfer energy and momentum between a relativistic jet and its surroundings. We show, in contrast to previous works, that the radiation-viscous stress tensor contains a non-zero bulk viscosity and a correction to the comoving energy density. In Chapters 7 and 8 we use these equations in a boundary layer form, the boundary layer assumption stating that the transition between the jet and its surroundings is confined to a thin layer (on the order of the square root of the photon mean free path), and derive two models for the structure of the jets launched from tidal disruption events. These models show that regions of large shear that develop between the fast-moving outflow and the static ZEBRA envelope are characterized by fewer scatterers and, hence, a lower optical depth and a harder photon spectrum.

Chapter 2 was published in original form in the *Astrophysical Journal Letters*, Volume 808, Issue 1, Letter 11 (6 pp.). Chapter 3 was published in original form in the *Monthly Notices of the Royal Astronomical Society*, Volume 455, Issue 4, pages 3612 – 3627. Chapter 4 was published in original form in the *Monthly Notices of the Royal Astronomical Society*, Volume 459, Issue 3, pages 3089 – 3103. Chapter 5 was published in original form in the *Astrophysical Journal*, Volume 781, Issue 2, Article Id. 82 (17 pp.). Chapter 6 was published in original form in the *Astrophysical Journal*, Volume 797, Article Id. 103 (13 pp.). Chapter 7 was published in original form in the *Astrophysical Journal*, Volume 809, Issue 1, Article Id. 1 (9 pp.). Chapter 8 was published in original form in the *Astrophysical Journal*, Volume 809, Issue 1, Article Id. 2 (10 pp.).

## Chapter 2

### Gravitationally Unstable Streams

#### 2.1 Introduction

When a star comes within a supermassive black hole's (SMBH) tidal radius  $r_t \simeq R_*(M_h/M_*)^{1/3}$ , where  $R_*$  and  $M_*$  are the stellar radius and mass, respectively, and  $M_h$  is the black hole mass, the tidal force exerted by the hole across the star is sufficient to overcome its self-gravity, resulting in its destruction. Early studies of these tidal disruption events (TDEs) demonstrated that roughly half of the disrupted stellar debris is bound to the black hole (Lacy et al., 1982; Rees, 1988), meaning that it will eventually return to the tidal radius, dissipate energy through shocks (Evans & Kochanek, 1989; Kochanek, 1994; Guillochon et al., 2014b), and form an accretion disk. The resulting accretion power is then capable of producing a highly luminous event, and many have already been detected (Komossa & Greiner, 1999; Gezari et al., 2008; Burrows et al., 2011; Cenko et al., 2012; Bogdanović et al., 2014).

Considerations of the star at the time of disruption show that the rate at which the bound, tidally-stripped material returns to the hole decreases as  $t^{-5/3}$  (Phinney, 1989), and early simulations supported this estimate (Evans & Kochanek, 1989). More recently, authors investigated the consequences of the stellar composition on the rate of return (Lodato et al., 2009), illustrating that the early fallback stages have a more complex temporal behavior that depend on the density stratification. Guillochon & Ramirez-Ruiz (2013) showed that the pericenter distance can have dramatic effects on the rate of return of debris. General relativistic Lense-Thirring (Stone & Loeb, 2012) and apsidal (Bonnerot et al., 2016) precession and recompression shocks (Guillochon et al.,

2014b) have also been investigated.

Most of the recent work on TDEs has been performed with the aid of numerical simulations. For example, Guillochon et al. (2014b) used a grid code (see also Shiokawa et al. 2015) to follow the evolution of the tidally disrupted debris from the initial encounter with the black hole to its eventual return to pericenter, while Bonnerot et al. (2016) used a smoothed particle hydrodynamics (SPH) code to achieve the same feat (see also Hayasaki et al. 2015). In these cases, however, the set of parameters used to model the tidal disruption was somewhat unphysical – Guillochon et al. (2014b) used a  $10^3 M_\odot$  black hole when following the return of the debris to the pericenter radius, while Bonnerot et al. (2016) used a more tightly bound stellar progenitor ( $e = 0.95$  for their most parabolic simulation,  $e$  being the stellar eccentricity). Both of these choices were made to reduce the computational cost at the expense of reality. Instead, a more likely mass for an SMBH is  $10^5 - 10^8 M_\odot$ , and the infalling star is initially so far from the hole that its orbit is effectively parabolic ( $e \simeq 1$ ).

A full TDE with realistic parameters has not yet been modeled because of the extreme set of spatial and temporal scales. In spite of these difficulties, we present the first simulation that has resolved the full duration of a TDE with a solar progenitor on a parabolic orbit, the periapsis of which coincides with the tidal radius, and a  $10^6 M_\odot$  SMBH. The simulation runs from well before the initial tidal interaction to long after the most bound debris returns to pericenter, corresponding to roughly ten years after disruption. This enables us to calculate explicitly the rate of return of tidally stripped debris to the black hole, demonstrating the effects of self-gravity which dominate that of the hole when the material is near apoapsis. In section 2 we provide analytic formulae for the shape and density distribution of the stream as it recedes from the hole, and we develop arguments which suggest the dominance of self-gravity over the tidal field of the hole at large radii. In section 3 we describe the initial conditions and numerical method used to simulate the encounter. Section 4 presents the results of the simulations and their analysis. We conclude and discuss further implications of our findings in section 5.

## 2.2 Self-gravity

The forces acting on the debris are self-gravity, the tidal shear across the width of the stream, and pressure. If we consider a small volume within the stream of length  $\delta R$  and mass  $\delta M$ , then the self-gravity of the stream dominates the tidal field if

$$\rho_0 \gtrsim \frac{3}{2\pi} \frac{M_h}{r^3}, \quad (2.1)$$

where  $\rho_0 = 3\delta M/(4\pi\delta R^3)$ .

We can calculate when this condition is satisfied by approximating the stream as a circular cylinder of width  $H$ . In this case, the differential amount of mass  $dM$  contained in the stream is

$$dM = \pi H^2 \rho dx, \quad (2.2)$$

where  $x$  is the length measured along its center. If the specific energy distribution of the gas is frozen in at disruption, then the curve traced out by  $x$  is a function solely of the position of a given gas parcel when the star is at pericenter, which we will denote by  $R_p = \mu R_*$ , with  $-1 \leq \mu \leq 1$ . Modeling the star as a polytrope (Hansen et al., 2004), the differential amount of mass contained in  $d\mu$  is (Chapter 5)

$$\frac{dM}{d\mu} = \frac{1}{2} M_* \xi_1 \frac{\int_{\mu\xi_1}^{\xi_1} \Theta(\xi)^n \xi d\xi}{\int_0^{\xi_1} \Theta(\xi)^n \xi^2 d\xi}, \quad (2.3)$$

where  $n$  is the polytropic index of the gas,  $\Theta(\xi)$  is the solution to the Lane-Emden equation and  $\xi_1$  is the first root of  $\Theta(\xi)$ .

We can parametrize  $x$  by the functions  $r(\mu)$  and  $\theta(\mu)$ , where  $r$  and  $\theta$  are solutions to the equations of motion of a test particle in the Newtonian gravity of the hole:

$$r = \frac{\ell^2}{GM_h} \frac{1}{1 + e \cos \theta}, \quad (2.4)$$

$$r^2 \dot{\theta} = \ell. \quad (2.5)$$

Here  $\ell$  and  $e$  are the specific angular momentum and eccentricity, respectively, of the gas parcel with position  $\mu$ , and are given by

$$\ell = \sqrt{2GM_h r_t} (1 - \mu q^{-1/3}), \quad (2.6)$$

$$e = 1 - 2\mu q^{-1/3}, \quad (2.7)$$

where  $q \equiv M_h/M_*$ . We have assumed here that the gas parcels initially move with the center of mass of the star and  $\beta = r_t/r_p = 1$ . By numerical integration of equation (2.5) we can determine  $\theta(\mu)$ , and  $r(\mu)$  is then found by using that result in equation (2.4).

The infinitesimal distance along the curve is  $dx = d\mu \sqrt{(r')^2 + r^2(\theta')^2}$ , where primes now denote differentiation with respect to  $\mu$ . Using this result and equation (2.3) in equation (2.2) gives

$$\rho = \frac{M_* \xi_1}{2\pi H^2 \sqrt{(r')^2 + r^2(\theta')^2}} \frac{\int_{\mu\xi_1}^{\xi_1} \Theta(\xi)^n \xi d\xi}{\int_0^{\xi_1} \Theta(\xi)^n \xi^2 d\xi}. \quad (2.8)$$

Using this equation in condition (2.1) gives the range in  $\mu$  over which self-gravity dominates the tidal shear.

The pressure of the material can also resist self-gravity. However, even if a small overdensity of radius  $\delta R$  and mass  $\delta M$  is pressure-supported, it must satisfy the Jeans condition  $\delta R \lesssim c_s \sqrt{\pi/(\rho G)}$ . If  $\delta R$  exceeds this value, any perturbation will cause material to clump around  $\delta M$ .

Finally, the local velocity gradient can potentially stabilize the stream. The divergence of the velocity decreases the density within the stream on a timescale  $\tau_{div} \simeq 1/(\nabla \cdot v)$ . If  $\tau_{div} \gtrsim \tau_{ff}$ , where  $\tau_{ff} \simeq \delta R^{3/2}/\sqrt{G\delta M}$  is the local free-fall time, self-gravity will overcome the stabilizing effect of the divergence of the flow.

By balancing the tidal shear and self-gravity in the transverse direction, Kochanek (1994) found that  $H \propto r^{1/4}$  for a  $\gamma = 5/3$  equation of state. We will use this when considering how the density (equation 3.10) varies with  $r$  (see Figure 2.2).

### 2.3 Simulation setup

To test our analytical reasoning above and the canonical  $t^{-5/3}$  fallback rate, we now employ three dimensional hydrodynamic simulations. We use the SPH code PHANTOM (Price & Federrath, 2010; Lodato & Price, 2010) to simulate the tidal encounter. PHANTOM was designed for running high resolution hydrodynamic simulations with complex geometries (Nixon et al., 2012a,b; Martin et al., 2014b,a; Nealon et al., 2015), and is therefore well suited to studying TDEs.

For our simulations we model the black hole as a Newtonian sink particle situated at the origin. Self-gravity of the stellar material is modeled using a k-D tree alongside an opening angle criterion, calculating directly the forces arising over short distances (Barnes & Hut, 1986). The opening angle for the simulations presented here was 0.5 (we ran an additional simulation with a more accurate opening angle of 0.3 and found negligible differences with the run presented here). The gas retains a polytropic equation of state, i.e., only adiabatic energy gains and losses are included (we also performed simulations with shock heating and, with our parameters, found negligible differences; see also Lodato et al. 2009).

We initialized our runs by placing  $10^6$  particles in the configuration of a  $\gamma = 5/3$  polytrope; this is achieved by first placing the particles on a close-packed sphere. This configuration is then stretched to achieve the correct polytropic density distribution, the resulting polytrope then placed at a distance of  $10 r_t$  from the hole with its center of mass on a parabolic orbit, its location at periapsis equal to the tidal radius (equations (2.4) and (2.5) with  $\ell = \sqrt{2GM_h r_t}$  and  $e = 1$ ). The distance of  $10 r_t$  allows the initial configuration time to relax before interacting with the black hole.

Here we are primarily interested in exploring the effects of self-gravity on the stream evolution, and so we include self-gravity at all stages of the simulation. We are also interested in comparing the theoretical rate of return of bound material (not necessarily equal to the accretion rate onto the black hole),  $\dot{M}_{\text{fb}} \propto t^{-5/3}$ , with that inferred from the simulation. Therefore, once the disrupted debris is beyond periapsis, the accretion radius of the black hole, initially well inside the tidal radius, is extended to  $r_{\text{acc}} \simeq 3 r_t$  ( $\simeq 120 R_g$ ). Once the bound material returns to the point of

disruption, it is removed from the simulation.

## 2.4 Results

The top, left panel of Figure 2.1 shows the density of the debris stream at periapsis, while the top, right is 0.84 hours after disruption; these reproduce Figure 4 of Lodato et al. (2009). The bottom four show, from left to right and top to bottom, 5.38 days, 15 days, 22.4 days and one month after disruption. The red curves indicate the analytic predictions; the fact that they provide good fits to the data means that the particles approximately trace out Keplerian orbits in the potential of the black hole.

The black points in Figure 2.2 show the density distribution along the stream at  $t = 22.4$  days after disruption; the solid, red curve gives the analytic prediction (equation (3.10) with  $H = R_\odot(r/r_t)^{1/4}$ ) and the dashed, red curve is the density at which the self-gravity of the debris and the tidal field of the hole are equal along the stream (the right-hand side of equation (2.1); self-gravity dominates for points above this curve). The wings present in the simulated values, which were also found by other authors (Lodato et al., 2009), are due to the fact that the shape of the star at the time of disruption is not spherical (see the left-most panel of Figure 2.1).

Figure 2.3 shows the rate of return of material to pericenter,  $\dot{M}_{fb}(t)$ , from the simulation (solid, black curve) and the analytic solution (red, dashed curve). The analytic estimate was determined by using equation (2.3) and the fact that  $\mu(t) = (t/T)^{-2/3}$ , where  $T = 2\pi M_h / (M_* \sqrt{GM_h})(R_*/2)^{3/2}$  (Chapter 5). The time at which material returns to pericenter is slightly earlier than that predicted analytically, a consequence of the tidal distortion at the time of disruption (see Figure 2.3). The asymptotic scaling  $\dot{M}_{fb} \propto t^{-5/3}$  is closely followed by the numerical solution at late times, reaffirming that the gas parcels follow approximately Keplerian motion. In our simulation, half of the bound material is accreted by about one year – shortly after the peak in the fallback rate.

Figure 2.3 also shows that the fallback rate quasi-periodically deviates from the  $t^{-5/3}$  law at late times. This scatter is due to the fact that the stream fragments, forming small gravitationally bound clumps that enter the accretion radius at discrete times, and is **not** simply numerical noise.

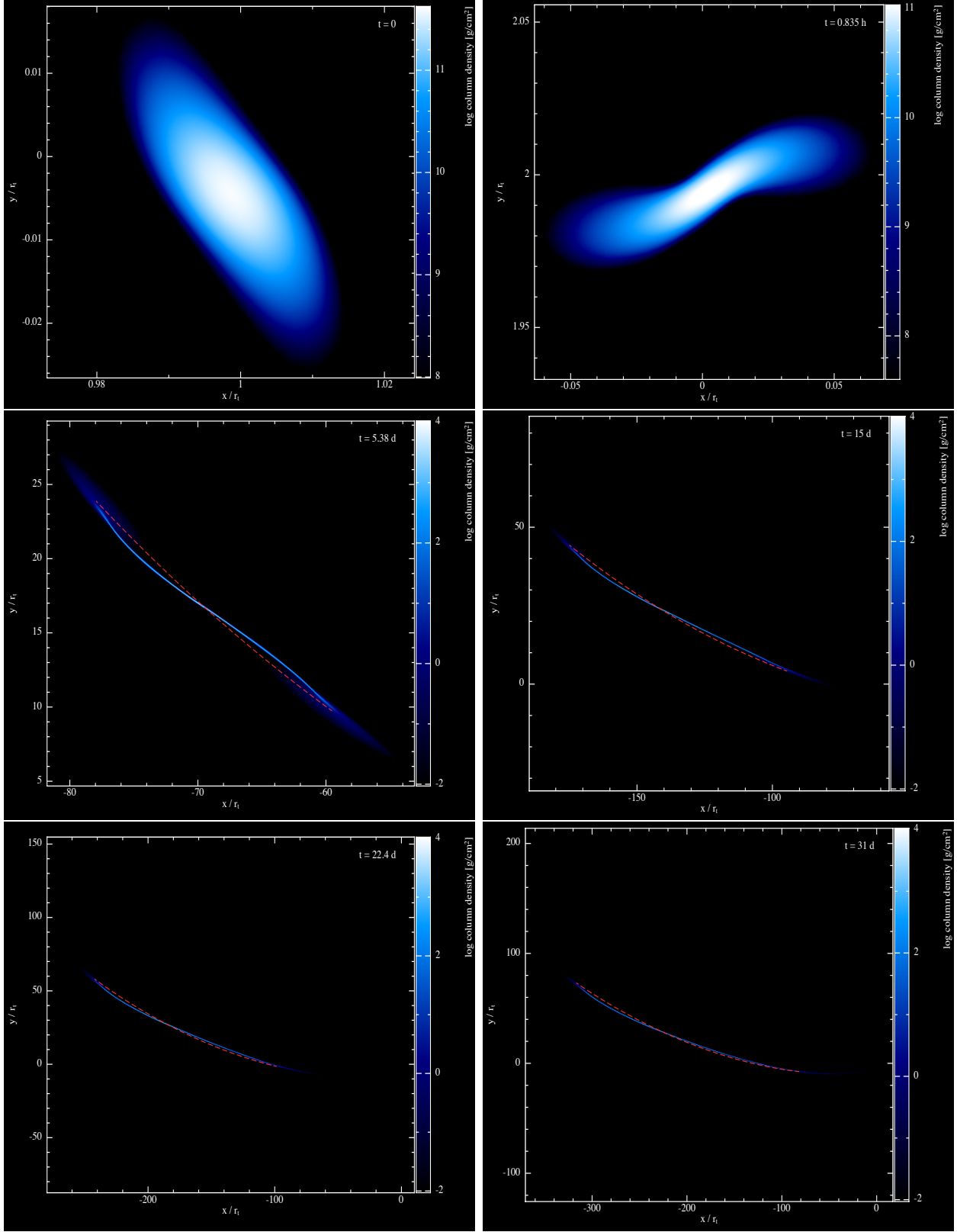


Figure 2.1: The star at the time of disruption (top, left), where the colors indicate the column density and distances are measured in units of tidal radii ( $\simeq 7 \times 10^{12}$  cm =  $100R_{\odot}$ ), 0.835 hours after periapsis (top, right; the top two figures coincide with the bottom-left panels of Figure 4 a) and b), respectively, of Lodato et al. 2009.), and 5.38 days (middle, left), 15 days (middle, right), 22.4 days (bottom, left) and 1 month (bottom, right) after disruption. The red, dashed curves on the bottom two rows indicate the analytic predictions.

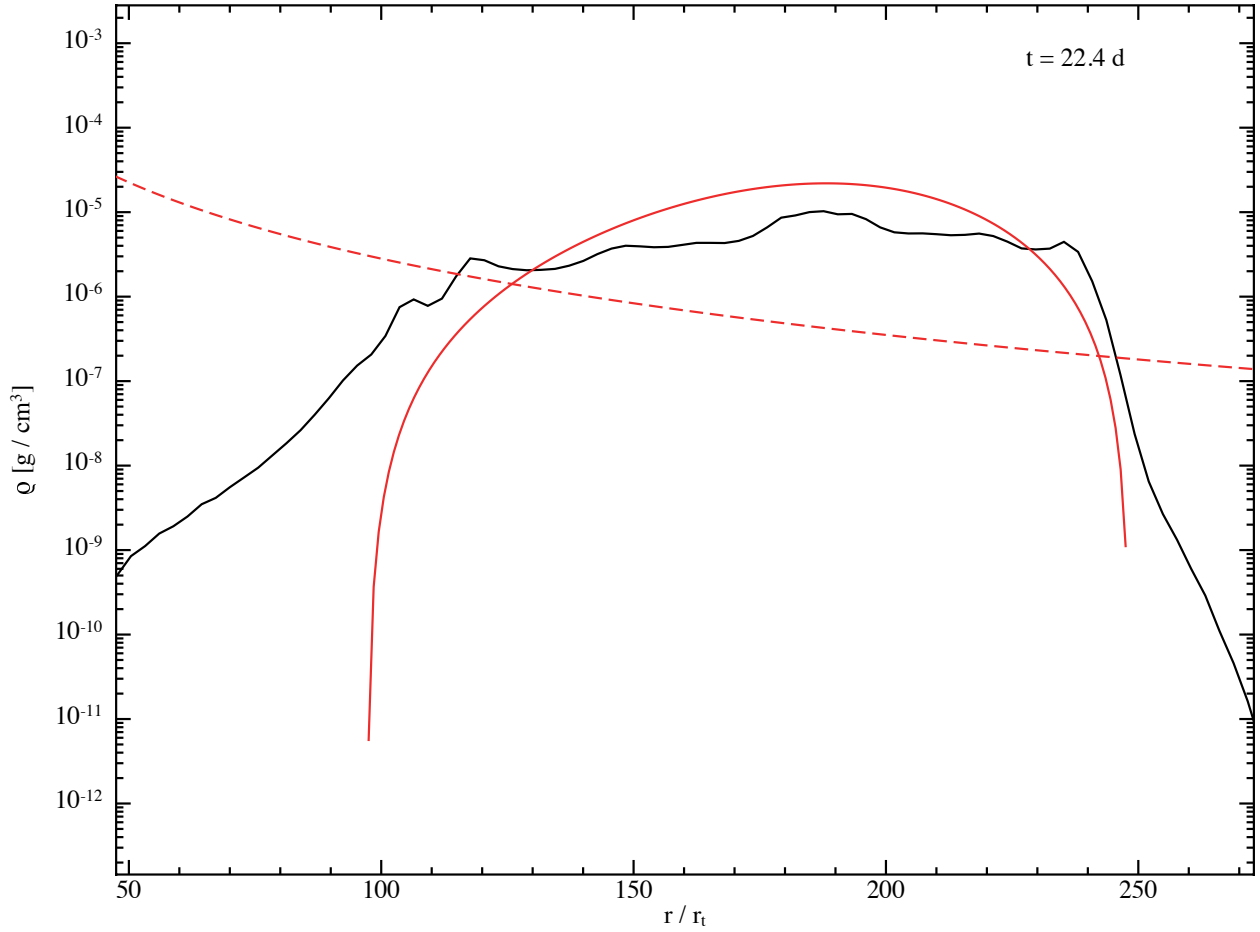


Figure 2.2: The computed density of the stream (solid, black curve), the analytic prediction (red, solid curve; equation 3.10), and the density at which self-gravity becomes important (red, dashed curve; equation 2.1) as functions of  $r$  (spherical distance from the hole) at 22.4 days from the point of disruption. Points above the red, dashed curve are self-gravitating. The numerical solution extends to smaller radii because the star at the time of disruption is not spherical (see also Lodato et al. 2009).

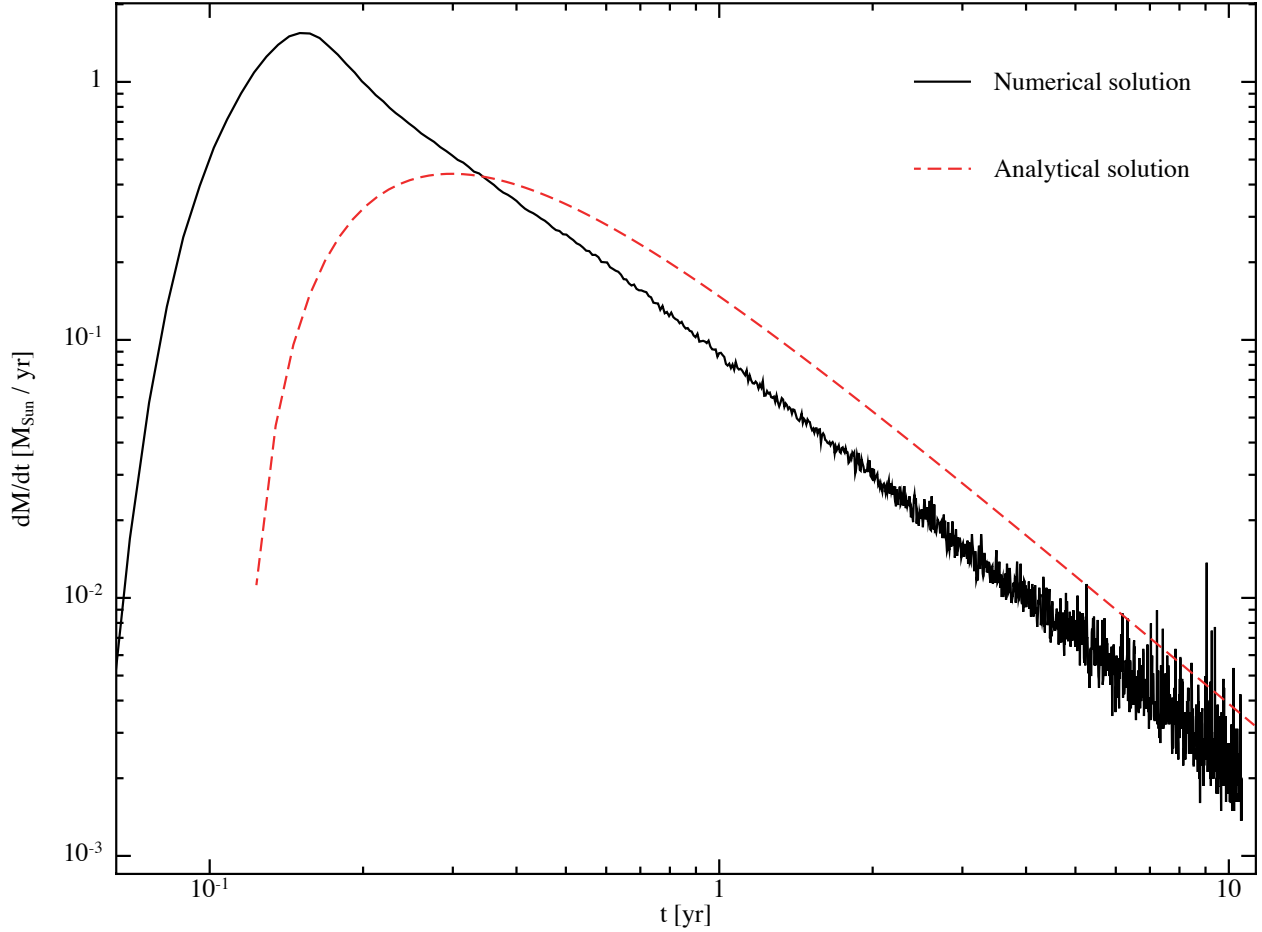


Figure 2.3: The fallback rate in solar masses per year calculated from the simulation (black, solid curve) and the analytic prediction (red, dashed curve) as functions of time in years. The temporal shift between the numerical solution and the analytic prediction is from the stellar distortion at the time of disruption (see text for further details). The variability at late times is due to the accretion of clumps formed in the self-gravitating stream. The variability starts about 2 years after disruption; however, this timescale depends upon the details of the TDE and its environment, and therefore may be shorter.

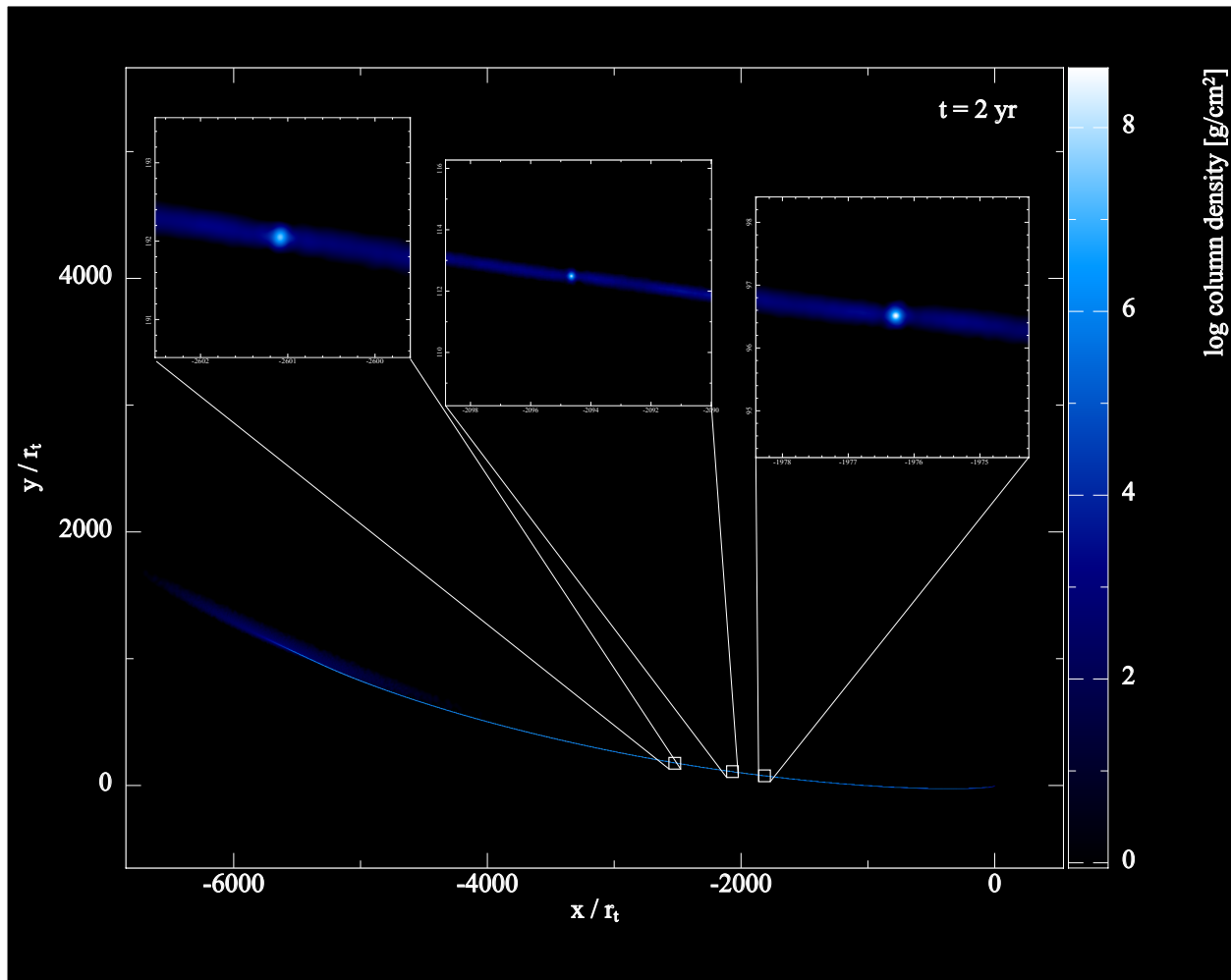


Figure 2.4: The density two years after disruption and, in the insets, close-ups of the fragments that forms along the stream.

To emphasize this point, Figure 2.4 shows the stream two years after disruption and insets that focus on clumps near the center of the stream.

## 2.5 Discussion and conclusions

We have presented the results of a TDE in which a solar mass star (with its pericenter at the tidal radius and its center of mass on a parabolic orbit) was disrupted by a  $10^6 M_\odot$  black hole. Contrary to past investigations, we resolved the full duration of the TDE – from the initial encounter between the undisturbed star and the hole to long after the most bound, tidally-stripped debris has returned to periapsis. When finished, more than 90% of the bound material was accreted. Crucially, we are the first to follow this long-term evolution for a solar mass star on a parabolic orbit around an SMBH.

The two main aims of this paper are (1) to determine the effects of self-gravity on the stream far from the black hole (see Figures 2.3 and 2.4), and (2) to compare the rate of return of bound material to the analytic estimates (Figure 2.3). The fiducial rate  $\dot{M}_{fb} \propto t^{-5/3}$  was determined by assuming that the specific energy distribution of the material was frozen in at the time of disruption. However, the self-gravity of the material, which is important at large distances from the hole (Section 2), has the potential to alter the specific energy distribution (see also Guillochon & Ramirez-Ruiz 2013). It is therefore necessary to resolve the full disruption process with self-gravity included at every step to determine the true rate of return.

Our simulations demonstrate that the fallback rate of debris closely mimics the theoretically-predicted one, the biggest discrepancy arising from the return time of the most tightly bound material. Therefore, the material, in agreement with intuition, follows approximately Keplerian orbits about the hole. Interestingly, however, we also found that the fallback rate at late times tends to over and under-estimate the  $t^{-5/3}$  law, a feature that is due to the fragmentation of the stream into gravitationally-bound clumps. When one of these clumps is accreted, the fallback rate spikes above its average value, while the rate is reduced when the lower density debris between clumps returns to periapsis.

We have shown analytically and numerically (see equation (2.1) and Figure 2.2) that the local self-gravity of the stream dominates the tidal field of the hole at large radii. We also find that the pressure within the sphere of the center inset of Figure 2.4 is  $p \simeq 10^3$  dyn/cm<sup>2</sup>. Conversely, the pressure necessary for maintaining hydrostatic equilibrium is  $p_{eq} \simeq GM\rho/R \simeq 4\pi G\rho^2 R^2/3$ , where the radius of the clump in Figure 2.4 is  $R \simeq 0.3r_t (= 30R_\odot)$  and the density is  $\rho \simeq 10^{-6}$  g/cm<sup>3</sup>, which gives  $p_{eq} \simeq 10^6$  dyn/cm<sup>2</sup>. Finally, the computed divergence of the velocity just outside the clump gives a divergence timescale of  $\tau_{div} \simeq 1/(\nabla \cdot v) \simeq 10^7$  s, while the infall timescale is  $\tau_{ff} \simeq 1/\sqrt{G\rho} \simeq 4 \times 10^6$  s. This shows that gas pressure and the local shear of the stream are also incapable of overcoming self-gravity.

The tidal field of the hole, gas pressure, and the local velocity shear are all incapable of supporting the clump in Figure 2.4 against its own self-gravity. This finding suggests that the original stream was gravitationally unstable, and small perturbations resulted in its fragmentation. For the results presented here, these perturbations are induced by the discreteness of the numerical method. To substantiate this claim, we ran the simulation with  $10^4$  and  $10^5$  particles and found that clumps formed sooner with decreasing particle number. However, our pressure smoothing length, equal to the gravitational smoothing length, was always at least as small as the Jeans radius  $R_J = c_s \sqrt{\pi/(G\rho)}$  (see Figure 2.5); the collapse was therefore always resolved (Truelove et al., 1997; Bate & Burkert, 1997). Additionally, the first clumps in the simulation presented here form around a month after disruption; at this time, the smoothing length at the center of the stream is roughly 0.1 times the width of the stream, meaning that the forces are clearly resolved at this time (see also Figure 5, which shows that the collapse itself is also resolved). Finally, we note that our SPH simulations are not susceptible to artificial fragmentation (Hubber et al., 2006), and our results demonstrate that any physical perturbation imposed on a stream that satisfies (2.1) is unstable to collapse.

To further investigate the instability of the stream, we performed additional runs with  $10^5$  and  $10^6$  particles and seeded the initial distribution of debris with a small, but resolved, perturbation. In these cases, clumps formed at almost the exact same time with nearly identical masses. Therefore,

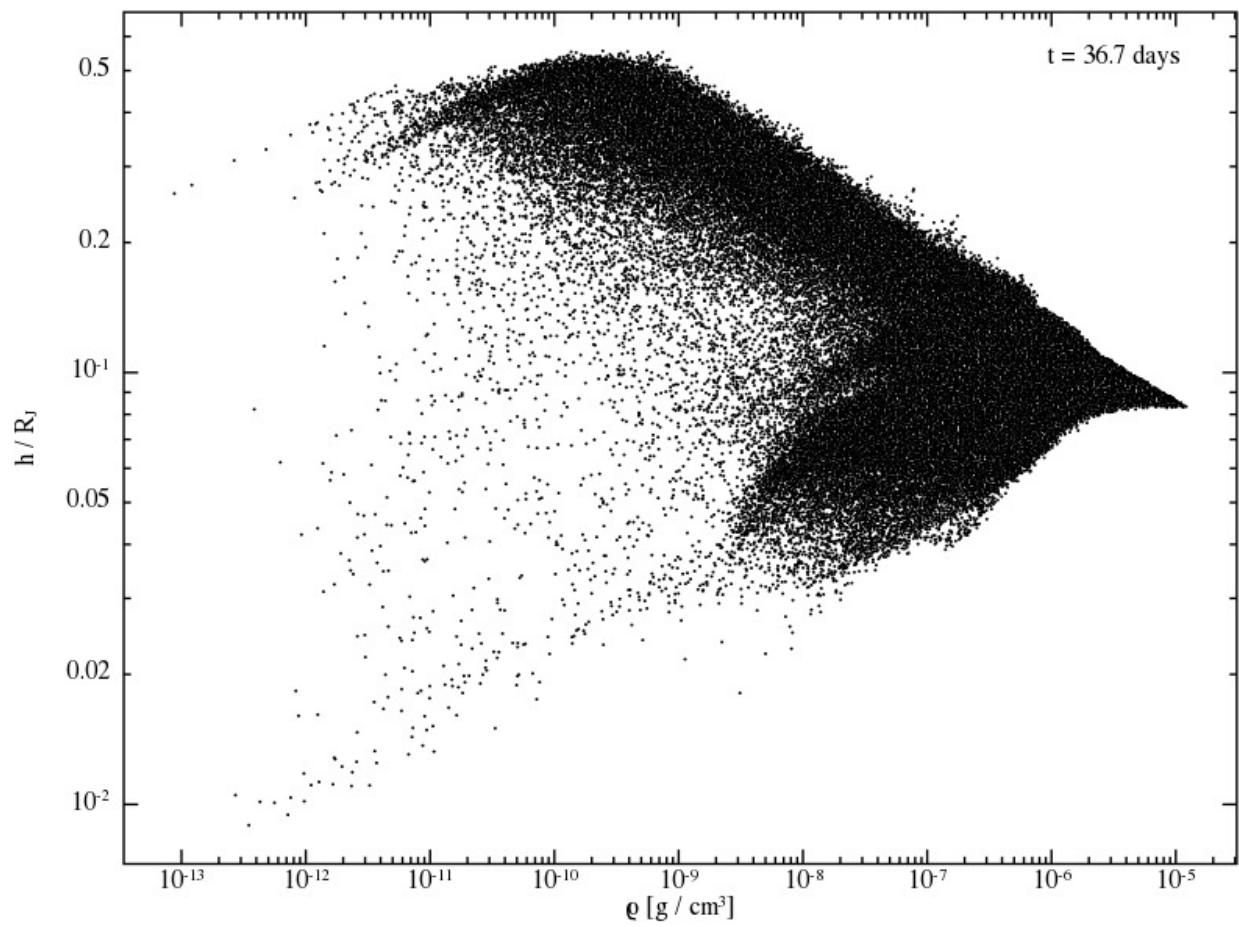


Figure 2.5: The ratio  $h/R_J$ ,  $h$  being the smoothing length and  $R_J$  the Jeans radius, as a function of density at a time when the first clumps start to form.

a resolved noise field imposed on top of the otherwise smooth distribution of stellar debris results in converged fragmentation. This finding further supports the fact that the stream is gravitationally unstable, and any small physical perturbation to the distribution of the debris will cause it to fragment. We will present a more complete analytical and numerical analysis of the gravitational stability of the stream in a future publication.

Real, fragmentation-inducing perturbations could be caused by a number of physical processes. For example, the interaction of the debris with any material surrounding the hole, the density distribution of which is neither necessarily smooth nor homogeneous, could cause local deformities within the stream. In light of this, the variability in the light curve of the event **Swift** J1644+57 (Burrows et al., 2011; Levan et al., 2011; Zauderer et al., 2011), the recently-observed, jetted TDE, could be interpreted as abrupt changes to the accretion rate induced by the fallback of bound clumps. This notion is supported by the lack of any ultraviolet and optical emission from the event, which is indicative of a large amount of dust present in the circumnuclear environment (Burrows et al., 2011); interactions between the stream and this natal environment could have initiated early fragmentation of the stream, causing variability in the fallback rate on a timescale commensurate with observations.

Finally, we note that while the mass contained in the fragments in Figure 2.4 is  $\delta M \simeq 0.005 M_{\odot}$ , there is a range of clump masses. Therefore, we suggest that the object G2 – the clump of material observed near the galactic center (Burkert et al., 2012) – and other such clouds, could have been produced by the tidal disruption of a star in the recent past. Guillochon et al. (2014a) reached a similar conclusion; their clump, however, was formed by fluid instabilities generated through the interaction of a stream of debris with an ambient medium. Here, on the other hand, self-gravity causes the stream to fragment.

## Chapter 3

### Post-periapsis Pancakes: Sustenance for Self-gravity in Tidal Disruption Events

#### 3.1 Introduction

A supermassive black hole of mass  $M_h$  can tidally destroy a star of mass  $M_*$  and radius  $R_*$  if the star comes within the tidal radius  $r_t \simeq R_*(M_h/M_*)^{1/3}$  of the hole. In this scenario, called a tidal disruption event (TDE), the star is shredded into a stream of debris. The properties of the debris and its ultimate fate have been studied for decades, both analytically and numerically, and the observational predictions generated from these studies have been tested.

Early analyses of TDEs showed that, due to the differential gravitational potential of the black hole, half of the disrupted debris that was closer to the hole at the time of disruption is bound to the black hole, while the other half is unbound (Lacy et al., 1982; Rees, 1988). The half that is bound will eventually return to the black hole, circularize, and form an accretion disk. The properties and observational signatures of this accretion disk have been investigated by many authors (e.g., Cannizzo et al. 1990; Loeb & Ulmer 1997; Strubbe & Quataert 2009, 2011; Lodato & Rossi 2011; Guillochon et al. 2014b; Shen & Matzner 2014). The power radiated during the accretion process is enough to generate a highly luminous event, and some of these events have already been observed (Bade et al., 1996; Komossa & Greiner, 1999; Halpern et al., 2004; Levan et al., 2011; Cenko et al., 2012; Bogdanović et al., 2014; Komossa, 2015).

Phinney (1989) showed analytically that the rate at which the debris returns to the black hole decreases with time as  $\dot{M}_{fb} \propto t^{-5/3}$ . This feature, coupled with the longevity of the signature, is the observational “smoking gun” of a TDE. Many of the recently-observed TDE candidates exhibit

a lightcurve that decreases in a manner commensurate with this power-law rate (Bloom et al., 2011; Zauderer et al., 2011; Cenko et al., 2012; Gezari et al., 2012; Bogdanović et al., 2014; Brown et al., 2015).

To investigate the complex hydrodynamical interactions that take place during TDEs, many authors have resorted to numerical simulations. Early smoothed-particle hydrodynamics (SPH) calculations supported the analytic estimates of Rees (1988) and Phinney (1989), showing that the distribution of specific energies calculated not long after the time of disruption generates a fallback rate that scales as  $\dot{M}_{fb} \propto t^{-5/3}$  (Evans & Kochanek, 1989). More recently, Lodato et al. (2009) elucidated the effects of the structure of the progenitor star on the disruption process, demonstrating that the early stages of the fallback depend on the properties of the star. Guillochon & Ramirez-Ruiz (2013) investigated how the impact parameter  $\beta \equiv r_t/r_p$ ,  $r_p$  being the pericenter distance of the stellar progenitor, alters the nature of the event, and found that shallower impact parameters often result in the survival of a bound stellar core. Finally, Hayasaki et al. (2013), Bonnerot et al. (2016), Hayasaki et al. (2015), and Shiokawa et al. (2015) have looked into the effects of general relativity on the stream, showing how apsidal and Lense-Thirring precession can alter the formation of the disk that forms when the tidally-disrupted debris returns to pericenter.

In Chapter 2 we demonstrated that, when a solar-like star with a  $\gamma = 5/3$  adiabatic equation of state is disrupted by a  $10^6 M_\odot$  hole, self-gravity can be important for determining the stream properties during its late evolution (see also Kochanek 1994 and Guillochon et al. 2014b for a discussion of self-gravity). In particular, they showed that the tidal influence of the black hole becomes sub-dominant to the self-gravity of the debris, which results in the late-time fragmentation of the stream into gravitationally-bound clumps. These clumps then return to the original pericenter at discrete times, causing the fallback rate of the material to fluctuate about the  $t^{-5/3}$  average.

An important question arising from the results of Chapter 2 is: when is the self-gravitational nature of the stream revived post-disruption? As the tidal shear and the self-gravity of the star equal one another at the tidal radius, one might suspect that the self-gravity of the debris is most influential at late times. Indeed, it is during this late evolution that we found in Chapter 2 that

the stream gravitationally fragments. As we will show here, however, the self-gravity of the debris can affect the stream evolution soon after the star passes through periapsis (on the order of hours for the tidal disruption of a solar-like star by a  $10^6 M_\odot$  hole). We find that the star experiences compressive forces in the orbital plane, which lead to the formation of a post-disruption pancake, similar to the one found by Carter & Luminet (1982) but oriented orthogonal to the orbital plane of the progenitor. This in-plane recompression then augments the importance of self-gravity, resulting in perturbations on top of the stream that can induce early recollapse. (We note that we will be considering TDEs in which the star is completely destroyed, and hence these results should not be confused with those of Guillochon & Ramirez-Ruiz 2013 who, in certain cases, found surviving stellar cores for impact parameters less than one.)

In Section 2 we present an analytical analysis of the stream under the impulse approximation, which assumes that the star maintains hydrostatic balance until it reaches the tidal radius. We demonstrate that, even when the pericenter distance and the tidal radius are approximately coincident, a caustic – a location where the orbits of the gas parcels comprising the stream collapse to a two-dimensional surface – occurs shortly after the star is disrupted. Section 3 presents numerical simulations that demonstrate the effects of this caustic, and specifically shows how it can modify the density structure of the stream for times long after disruption. We present a discussion of the results of our simulations in Section 4 and consider the astrophysical implications of our findings in Section 5. We conclude and summarize in Section 6.

### 3.2 The impulse approximation

Many authors (e.g., Carter & Luminet 1983; Rees 1988; Lodato et al. 2009; Stone et al. 2013) have considered the disruption process from a simplified, analytic standpoint. While an analytic approach almost certainly misses many of the intricacies associated with the realistic problem, it has the advantage of being able to characterize the bulk processes that take place during the interaction. Furthermore, it is able to elucidate the manner in which those processes depend on the properties of the progenitor star and the black hole, which provide useful observational

diagnostics. Here we discuss the impulse approximation, which assumes that the star is able to maintain hydrostatic balance until it reaches the tidal radius and it is thereafter disrupted, i.e., the pressure and self-gravity of the material are negligible after the star has passed through the tidal radius.

Carter & Luminet (1982, 1983) considered the case where the pericenter distance of the star,  $r_p$ , is well inside the tidal radius of the hole (their affine star model; see also Stone et al. 2013 for an alternative approach to analytically modeling this scenario). For these high- $\beta$  encounters, where  $\beta \equiv r_t/r_p$  is the impact parameter, the impulse approximation can be applied early on in the tidal disruption process. Because of the component of the tidal force that acts orthogonally to the orbital plane of the star, the gas parcels comprising the top and bottom of the stellar envelope undergo effective freefall, forming an infinitely thin plane, or caustic, at the pericenter radius (the location of the caustic is actually slightly after the pericenter, only equaling the pericenter distance for  $\beta \rightarrow \infty$ ; Bicknell & Gingold 1983). This “pancaking” effect was then thought to be capable of igniting thermonuclear fusion via the triple- $\alpha$  process, resulting in the detonation of the star. However, studies showed that the shocks near pericenter resulted in lower densities and pressures in the stellar core than those predicted by Carter & Luminet (1982), meaning that the triple- $\alpha$  process is unlikely to be initiated in these encounters (though some fusion via the CNO cycle may occur; Bicknell & Gingold 1983).

On the other hand, when  $\beta \simeq 1$ , the star can retain its unperturbed structure for much longer. In this case, one can approximate the star as being spherical, with every gas parcel moving with the center of mass, until the pericenter is reached. Here we will focus on this case, not only because it has not been treated as thoroughly as the  $\beta \gg 1$  scenario, but also because it has interesting consequences for the disrupted material soon after the pericenter distance is reached. Later in this paper, we will relax the assumptions made by this model with three dimensional hydrodynamic simulations.

### 3.2.1 Equations

Once the star passes through the tidal radius, the pressure and self-gravity of the gas parcels are assumed negligible, implying that they follow Keplerian orbits in the potential of the black hole. The equations of motion that describe these orbits are given by

$$r^2 \sin^2 \theta \dot{\phi} = \ell, \quad (3.1)$$

$$r^4 \dot{\theta}^2 + \frac{\ell^2}{\sin^2 \theta} = k^2, \quad (3.2)$$

$$\frac{1}{2} \left( \dot{r}^2 + \frac{k^2}{r^2} \right) - \frac{GM}{r} = \epsilon, \quad (3.3)$$

where dots denote differentiation with respect to time,  $r(t)$ ,  $\theta(t)$ , and  $\phi(t)$  are the respective radial, polar, and azimuthal coordinates of the gas parcel under consideration, and  $M$  is the mass of the black hole. Here  $\ell$ ,  $k$ , and  $\epsilon$  are constants of integration, the first two being projections of the specific angular momentum, while the last is the specific energy.

Setting the impact parameter to  $\beta \equiv r_t/r_p = 1$ , the point at which equations (3.1) – (3.3) become valid occurs when the star reaches pericenter. We will let the orbit of the stellar progenitor be confined to the  $xy$ -plane, with the periapsis on the positive- $x$  axis and the location of the black hole at the origin. The center of mass of the star will also trace out a parabolic orbit. The impulse approximation then means that the star retains its unperturbed (assumed-spherical) structure until it reaches pericenter, so that the initial conditions we will use for equations (3.1) – (3.3) will be those depicted by Figure 3.1. Note that the entire star initially shares the velocity of the center of mass, which is along the positive- $y$  axis at pericenter.

With the setup given by Figure 3.1 in mind, we will define the initial position of a given fluid element that comprises the star by the coordinates  $(r_i, \theta_i, \phi_i)$ . Since the entire star moves with the center of mass, the velocity of every fluid element is given by  $\dot{z}_i = \dot{x}_i = 0$ ,  $\dot{y}_i = \sqrt{2GM_h/r_t}$ .

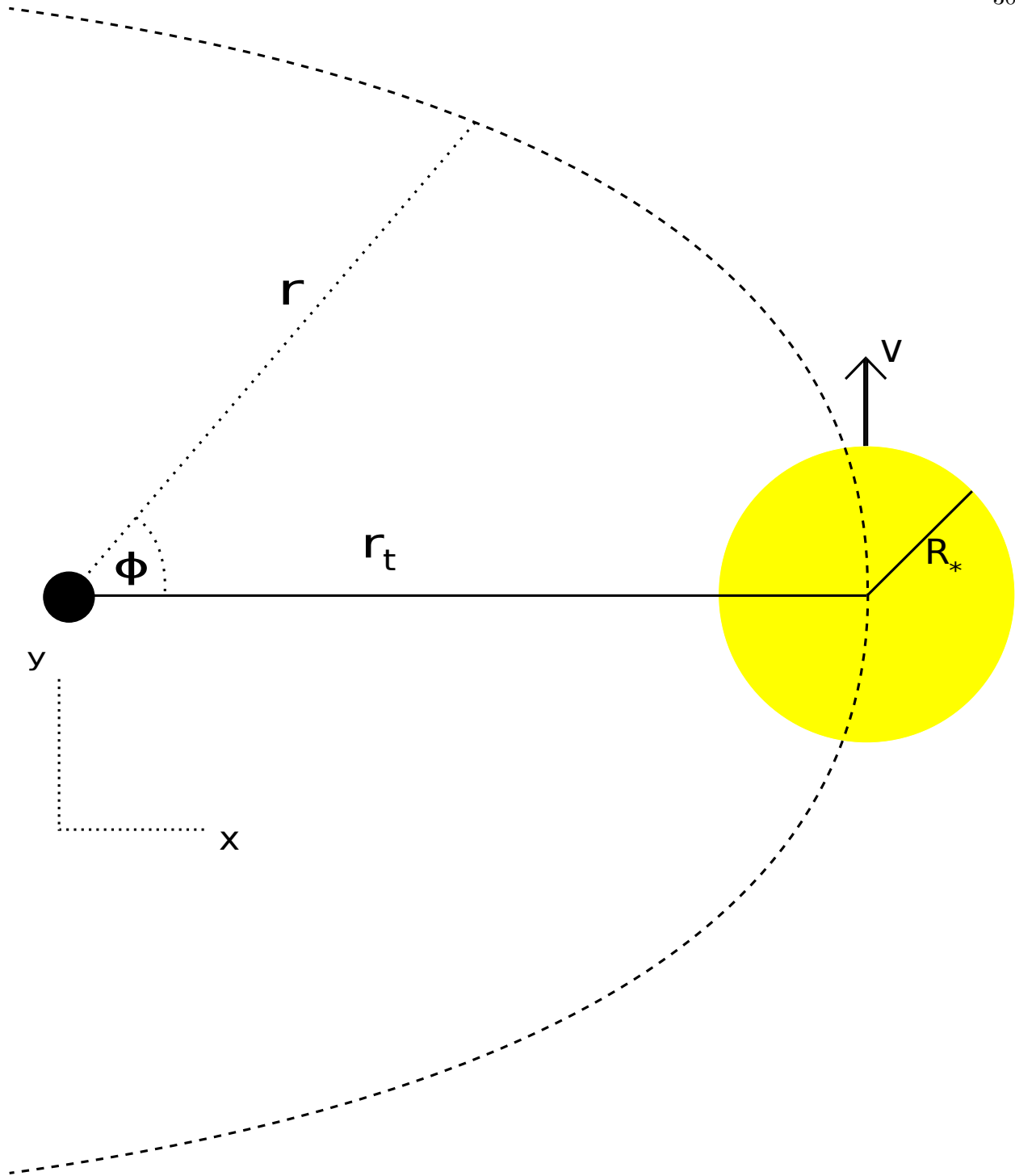


Figure 3.1: The initial configuration of the star under the impulse approximation when  $\beta \simeq 1$  (this figure is not drawn to scale). The dashed curve traces out the orbit of the center of mass, which is assumed to be parabolic. The Cartesian coordinates are indicated by the diagram immediately below the black hole (which is indicated by the black circle),  $z$  being out of the plane in a right-handed sense. The spherical-polar coordinates are labeled  $r$  and  $\phi$  on the diagram, and  $\theta$  is measured out of the plane of the orbit from the  $z$ -axis (for the above figure that focuses on the  $x$ - $y$  plane,  $\theta = \pi/2$ ).

Transforming these conditions into spherical coordinates via the transformations  $z = r \cos \theta$ ,  $y = r \sin \theta \sin \phi$ ,  $x = r \sin \theta \cos \phi$ , we find

$$\dot{r}_i = \sqrt{\frac{2GM_h}{r_t}} \sin \theta_i \sin \phi_i, \quad (3.4)$$

$$\dot{\theta}_i = \frac{1}{r_i} \sqrt{\frac{2GM_h}{r_t}} \cos \theta_i \sin \phi_i, \quad (3.5)$$

$$\dot{\phi}_i = \frac{1}{r_i} \sqrt{\frac{2GM_h}{r_t}} \frac{\cos \phi_i}{\sin \theta_i}, \quad (3.6)$$

and using these expressions in equations (3.1) – (3.3) gives

$$\ell = r_i \sqrt{\frac{2GM_h}{r_t}} \sin \theta_i \cos \phi_i, \quad (3.7)$$

$$k = r_i \sqrt{\frac{2GM_h}{r_t}} \sqrt{\cos^2 \phi_i + \cos^2 \theta_i \sin^2 \phi_i}, \quad (3.8)$$

$$\epsilon = \frac{GM_h}{r_t} \left( 1 - \frac{r_t}{r_i} \right). \quad (3.9)$$

Equation (3.9) shows that gas parcels with initial positions inside the tidal radius are bound ( $\epsilon < 0$ ), while those outside are unbound ( $\epsilon > 0$ ), which is what we expect.

In addition to its position, we will also be interested in the density of the stream. As was demonstrated in Chapter 2, the density structure can be determined by considering the star at the time of disruption and assuming that the specific energies of the gas parcels are frozen in thereafter. Making the additional assumption that the stream is a circular cylinder of cross-sectional radius  $H$ , then we can show that the azimuthally-averaged density along the stream varies as (see Chapter 2)

$$\rho = \frac{M_* \xi_1}{2\pi H^2 \sqrt{(r')^2 + r^2(\phi')^2}} \frac{\int_{\mu\xi_1}^{\xi_1} \Theta(\xi)^n \xi d\xi}{\int_0^{\xi_1} \Theta(\xi)^n \xi^2 d\xi}, \quad (3.10)$$

where  $M_*$  is the mass of the disrupted star,  $n = 1/(\gamma - 1)$  is the polytropic index of the gas,  $\Theta(\xi)$  is the solution to the Lane-Emden equation and  $\xi_1$  is the first root of  $\Theta(\xi)$  (Hansen et al., 2004). Here  $\mu$  is the dimensionless position of a gas parcel from the center of the star at the time of disruption, i.e.,  $\mu = R_p/R_*$ , where  $R_p$  is the radial position of the gas parcel. Primes on the functions  $r$  and  $\phi$  denote differentiation with respect to  $\mu$ . We will return to the question of what determines  $H$  in Section 3.2.

### 3.2.2 Solutions

With equations (3.7) – (3.9) and the initial positions of the gas parcels, we can numerically integrate equations (3.1) – (3.3) to determine the temporal evolution of the debris stream.

Figure 3.2 shows the solution to equations (3.1) – (3.3) with the relevant initial conditions for a TDE between a solar-type star and a  $10^6 M_\odot$  hole. The first time (closest set of blue points) is 1.84 days after disruption, while the longest, yellow set of points is 40.6 days after disruption, and coincides roughly with the time at which the most bound material has returned to pericenter. Intermediate streams are shown at intervals of 5.53 days. We find overall good qualitative and quantitative agreement between the radial positions of these solutions and the solution to the full problem – making no assumption about the negligible nature of pressure and self-gravity – obtained using numerical simulations (see, e.g., the red curves in Figure 1 of Chapter 2).

However, we find disagreement between the width of the stream obtained from equations (3.1) – (3.3) and that from the simulations, the former being significantly wider than the latter. This discrepancy is due to the fact that self-gravity plays a crucial role in determining the width of the stream (Chapter 2). In other words, the  $H$  that appears in equation (3.10) is not simply determined by the free expansion of the parcels in the gravitational potential of the hole (see equation (3.17) below, which shows how  $H$  depends on the density of the stream in the limit that hydrostatic balance is upheld in the transverse direction).

The approximate point at which the self-gravity of the stream becomes important can, however, be gleaned from the solutions to equations (3.1) – (3.3). Figure 3.3 shows the evolution of

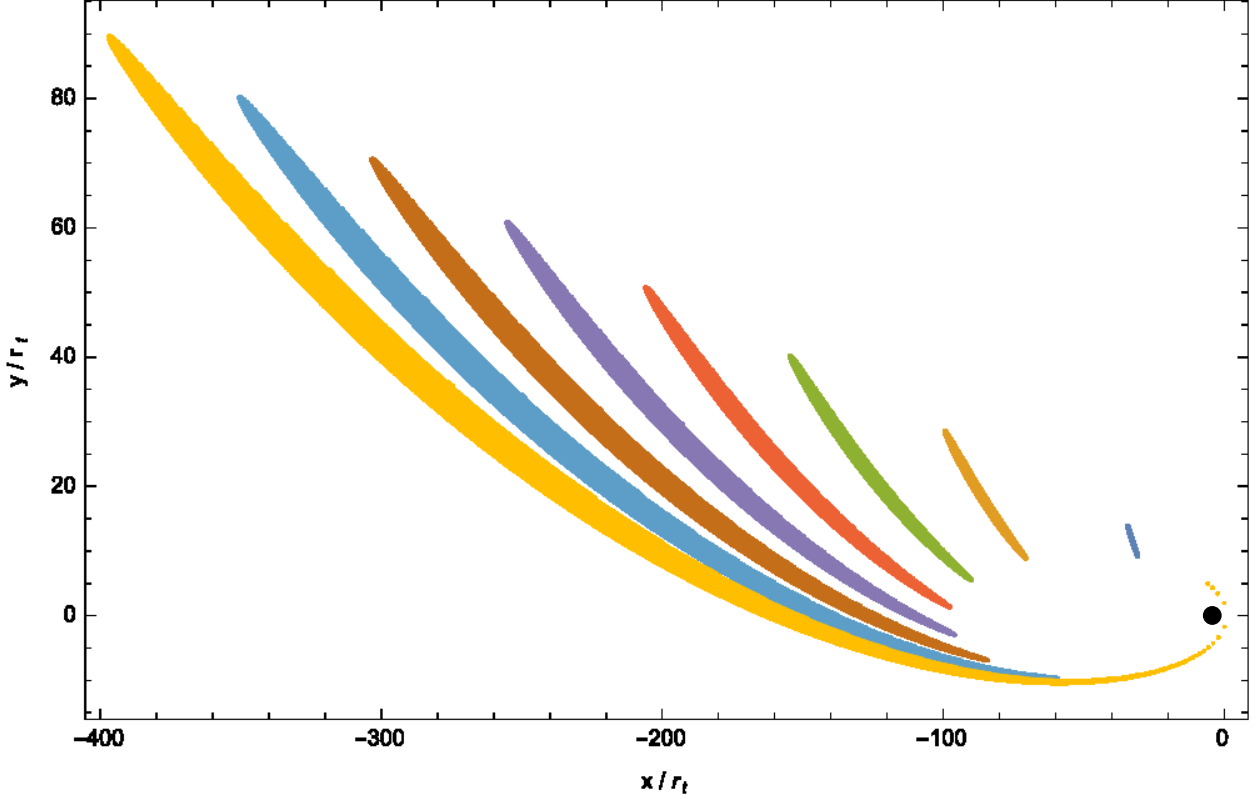


Figure 3.2: The streams of debris formed from the tidal disruption of a solar-type star by a  $M_h = 10^6 M_\odot$  hole situated at the origin. Each color represents a different time, the earliest (blue points closest to the origin) being at  $t = 100 r_t^{3/2} / \sqrt{GM_h} \simeq 1.84$  days from disruption, the latest (yellow points) at  $t = 2200 r_t^{3/2} / \sqrt{GM_h} \simeq 40.6$  days from disruption. The time in between neighboring streams is  $300 r_t^{3/2} / \sqrt{GM_h} \simeq 5.53$  days. The black hole (not drawn to scale) is indicated by the black circle near the origin. While the radial positions of the gas parcels match well those from numerical analyses (see Figure 1 of Chapter 2), the width obtained from equations (3.1) – (3.3) is significantly overestimated (the numerical solutions, had we shown them, would have amounted to lines plotted overtop of the streams in Figure 2). This finding suggests that self-gravity is important for keeping the stream confined in the transverse direction.

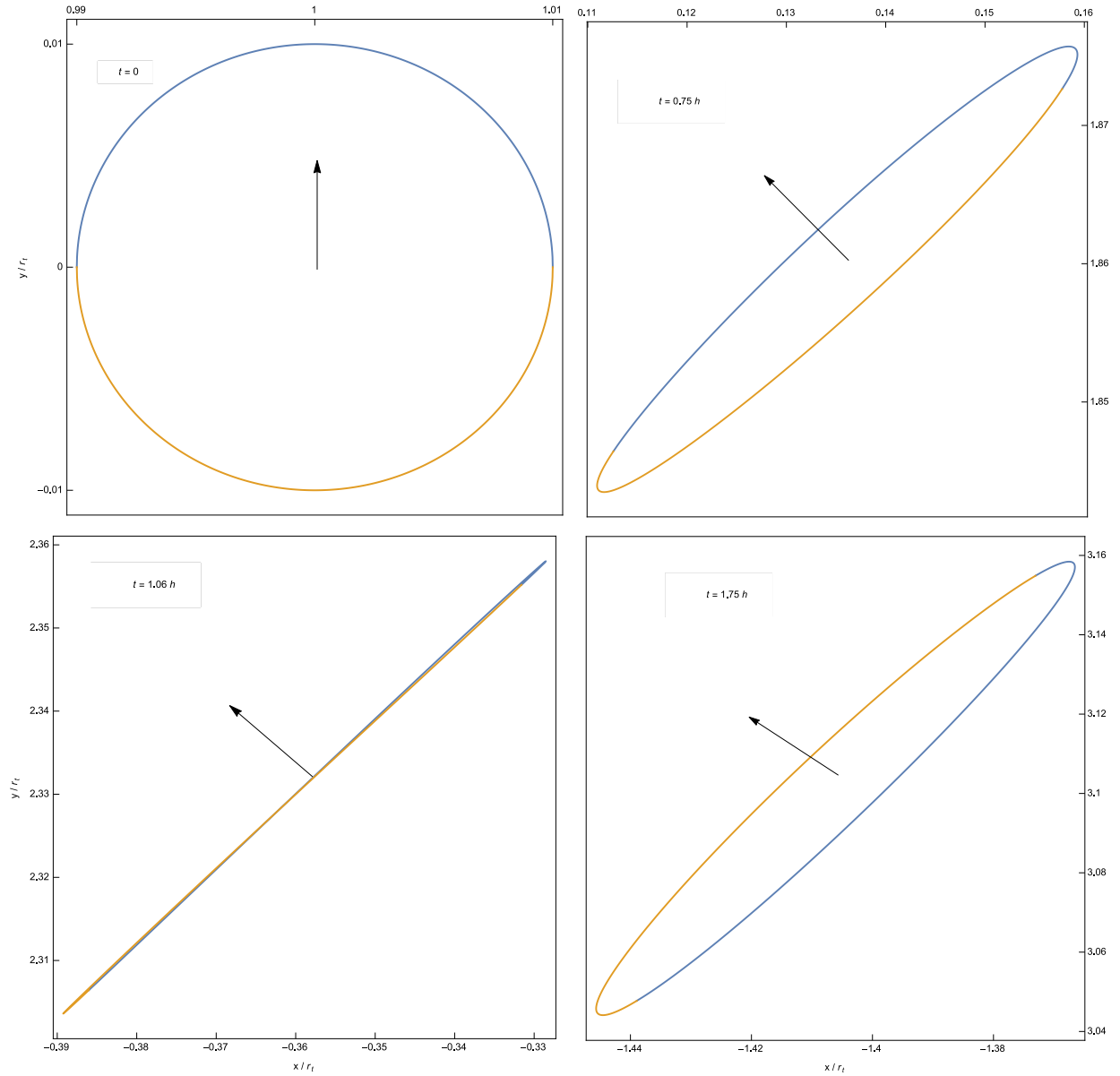


Figure 3.3: Four snapshots of the in-plane evolution of the gas parcels comprising the edge of the star at the time of disruption; for these figures we chose a  $10^6 M_\odot$  hole and a solar-like star. The particles comprising the front of the star at the time of disruption have been colored blue, while the back has been colored orange. The arrows indicate the direction of motion of the center of mass. The bottom, left-hand panel shows that, at a time of roughly an hour after disruption, the front and back of the stream merge and thereafter trade places. The impulse approximation thus leads to a caustic – where the debris streams form a two-dimensional surface – which occurs roughly an hour after disruption.

the in-plane edge of the stream at four different times for the disruption of a solar-type star by a  $10^6 M_\odot$  hole. The front of the stream (the fluid parcels comprising the leading edge of the polytrope at the time of disruption) has been colored blue, the back has been colored orange, and the arrow indicates the instantaneous direction of motion of the center of mass. This figure demonstrates that, roughly an hour after disruption, the leading and trailing edges of the stream form a caustic – a point where the two-dimensional, in-plane surface of the stream collapses to a one-dimensional line – and thereafter trade places, the front becoming the back and the back becoming the front.

The tidal stream thus exhibits a “perpendicular pancake” shortly after disruption, the perpendicular aspect referring to the fact that the orientation of the pancake is orthogonal to the orbital plane of the debris. This pancake is analogous to but distinct from the one found by Carter & Lummett (1982), who noted that the top and bottom of the star flatten to a point of infinite density at the tidal radius for high- $\beta$  encounters. Here, however, the compressive motions occur in the orbital plane.

The existence of the pancake encountered here can ultimately be attributed to the initial conditions: from Figure 3.1, it is apparent that the parcels along the line passing through the center of the star and perpendicular to the orbital plane all have their periapses at  $\phi = 0$ . Those constituting the leading edge of the star, however, have already passed through their periapses, while the periapses of the parcels comprising the back of the star have not yet been reached. From the conservation of angular momentum (3.1), the front of the star is therefore decelerating at the time of disruption while the back is accelerating, which causes the two to cross at a certain location. Specifically, if we differentiate equation (3.1) with respect to time, set  $\theta = \pi/2$  and use equation (3.4), we find

$$\ddot{\phi}_i = -\frac{4GM_h}{r_i^2 r_t} \sin \phi_i \cos \phi_i, \quad (3.11)$$

which shows that gas parcels with  $\phi_i > 0$  are decelerating in the  $\phi$  direction, while those with  $\phi_i < 0$  are accelerating. Investigating this equation further, we see that the differential acceleration

across the star at the time of disruption is

$$\Delta\ddot{\phi} \simeq -\frac{4GM_h}{r_i^2 r_t} \Delta\phi, \quad (3.12)$$

where  $\Delta\phi$  is the angle subtended by the star. Geometrically  $\Delta\phi \simeq 2R_*/r_t$ , which yields, after setting  $r_i \simeq r_t$ ,

$$|\Delta\ddot{\phi}| \simeq \frac{32\pi G\rho_*}{3} \left(\frac{M_h}{M_*}\right)^{-1/3}, \quad (3.13)$$

where  $\rho_* = 3M_*/(4\pi R_*^3)$  is the average stellar density. This expression shows that the change in acceleration from the front of the star to the back depends primarily on the properties of the progenitor, though the inverse dependence on black hole mass shows that the effect should be amplified for smaller-mass SMBHs.

During a realistic  $\beta \simeq 1$  tidal encounter, the star will not retain perfect spherical symmetry until reaching its pericenter. In particular, the outer, low-density material comprising the envelope will be more easily stripped, resulting in an elongated, ellipsoidal configuration. However, the higher-density core will be able to better maintain its structure. Therefore, while considering the entire star as spherical and moving with the center of mass at the time of disruption is likely too simplistic for the physical problem, those initial conditions are perhaps reasonable for the central regions.

Furthermore, the non-zero pressure of the gas will prevent the development of a true caustic. On the contrary, the convergence of the Keplerian orbits will increase the pressure and density until it reaches an approximate equilibrium. However, the stretching of the stream in the radial direction will cause the density to decrease, which will likewise result in a more drastic lowering of the pressure if the gas follows an adiabatic equation of state. The ability of the pressure to resist the caustic will thus decrease with time, making it possible for the perpendicular pancake to alter the nature of the debris stream.

The precise time at which the caustic occurs as it has been presented here depends only on

the gravitational field of the black hole. In reality, the self-gravity of the steam would serve to alter the precise nature of the pancake. However, we expect that self-gravity would only serve to enhance the focusing of the orbits and potentially generate the caustic at a slightly earlier time.

In the next section we present simulations that address the complexity of the full problem. As we will see, the numerical solutions do exhibit interesting behavior near the time at which equations (3.1) – (3.3) predict the existence of a caustic, and this behavior is imprinted on the stream for much later times.

### 3.3 Numerical simulations

To test whether or not the caustic discussed in the previous section affects realistic  $\beta \simeq 1$  tidal encounters, we now employ numerical simulations that allow the star to evolve in the tidal field of the hole pre-periapsis and include the effects of pressure and self-gravity at all times.

#### 3.3.1 Simulation setup and initial conditions

We use the SPH code PHANTOM (Price & Federrath, 2010; Lodato & Price, 2010) to simulate the tidal disruption of a solar-type star (one with a solar mass and a solar radius) by a  $10^6 M_\odot$  black hole. PHANTOM is a highly efficient code and is especially useful for astrophysical problems involving complex geometries and a large range of spatial and temporal scales. For other applications of this code, see, e.g., Nixon et al. (2012a,b); Martin et al. (2014b,a); Nealon et al. (2015).

In our simulations the star is initially assumed to be a polytrope with polytropic index  $\gamma$  (Hansen et al., 2004). The correct, polytropic density profile is obtained by first placing  $10^6$  particles in a close-packed sphere, then stretching that sphere to obtain a good approximation to the exact solution.

We place the polytrope at a distance of  $10 r_t$  from the hole, with the center of mass on a parabolic orbit. The distance at periapsis is equal to the tidal radius ( $\beta = 1$ ). Every gas parcel composing the star initially moves with the center of mass when the star is at  $10 r_t$ , and the length of time taken to traverse the distance to the hole is sufficient to allow the polytrope to relax. The

adiabatic index of the gas is always equal to the initial, polytropic index of the star.

Self-gravity is included at all stages of the TDE, and is employed via a k-D tree (Gafton & Rosswog, 2011) alongside an opening angle criterion, the latter employing a direct summation method for the gravitational forces between neighboring particles (Price & Monaghan, 2007). The simulations presented here used an opening angle of 0.5 (we have run simulations with smaller opening angles and found negligible differences; see Chapter 2). Shock heating was not included for the runs presented here, though we have done tests in which it was included and found only negligible differences. We also do not account for non-adiabatic cooling; the gas therefore retains its polytropic equation of state throughout the TDE.

We ran four different simulations, each identical to the next except in the adiabatic index used for the gas. Specifically, we chose  $\gamma = 1.5, 5/3, 1.8,$  and  $2$ , and thus our parameter space agrees with that chosen by Lodato et al. (2009) except for  $\gamma = 2$ . While adiabatic indices greater than  $5/3$  are difficult to realize physically in stellar progenitors (though they may be appropriate for planets; Faber et al. 2005; Li et al. 2002), we included these cases to highlight the presence of the caustic and to compare to Lodato et al. (2009).

### 3.3.2 Results

Figure 3.4 shows the star at the time of disruption, with each panel corresponding to a different adiabatic index. As was commented upon in Section 2, the fact that the tidal force does not act impulsively means that the polytrope is already distorted when it reaches its periapsis, and this distortion is apparent from the figure. We also see that the central density is higher for lower  $\gamma$ , which is a general feature of polytropes.

Figure 3.5 shows the disrupted stream 2.53 days after disruption for the four different adiabatic indices. In this case it is evident that a larger adiabatic index corresponds to a thinner, denser stream. This result may seem counterintuitive, as one might expect the higher-density core of the lower- $\gamma$  polytropes to result in a denser stream. However, if one assumes that pressure and self-gravity are the two dominant terms controlling the width of the stream, which is a reasonable

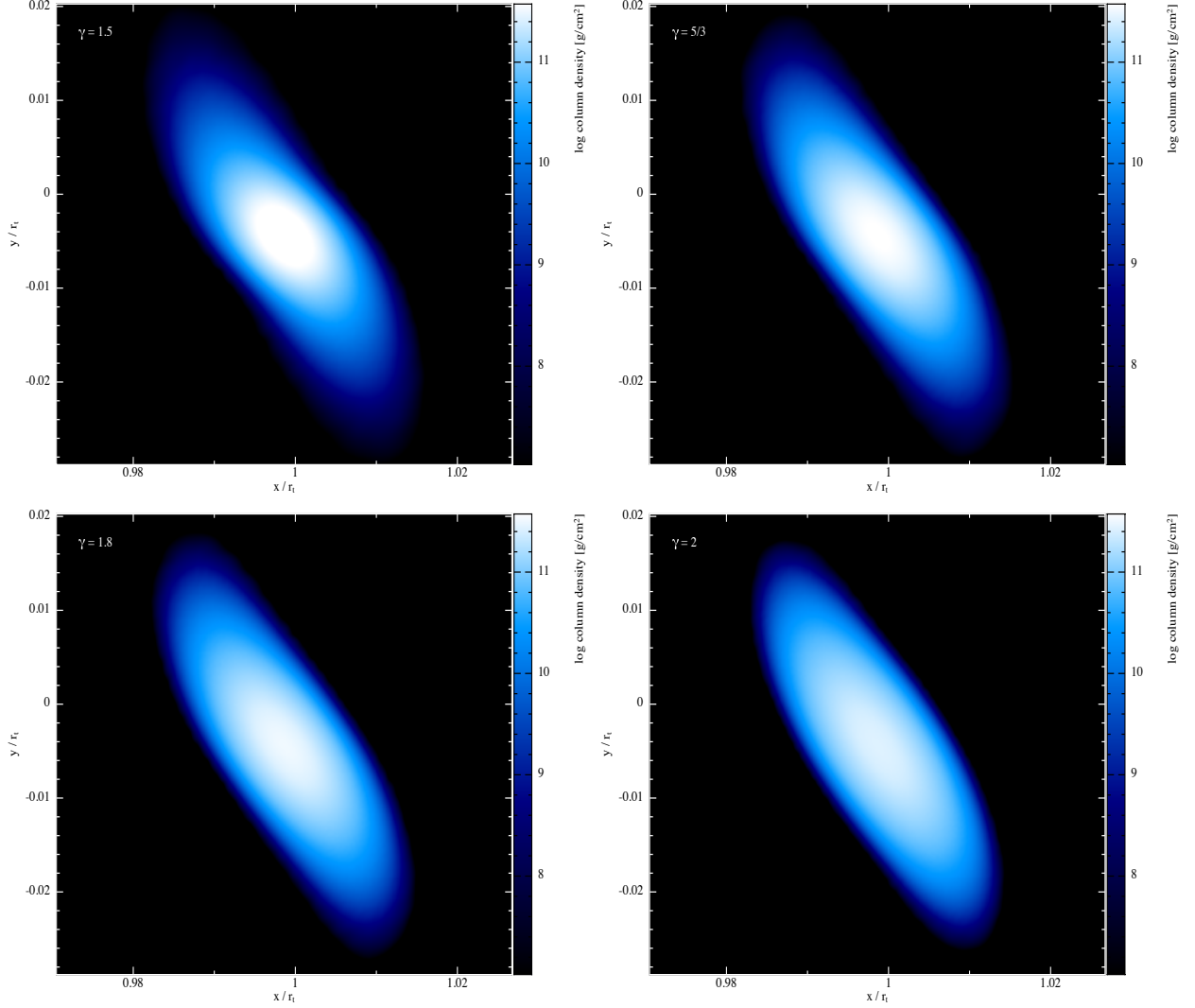


Figure 3.4: The star at the time of disruption for an adiabatic index of  $\gamma = 1.5$  (top, left),  $\gamma = 5/3$  (top, right),  $\gamma = 1.8$  (bottom, left) and  $\gamma = 2$  (bottom, right). The configuration has clearly been altered from its original, spherical shape, showing that the tidal force does not act exactly as an impulse as was assumed in Section 2. The central density is also higher for smaller  $\gamma$ , which is predicted from the original stellar profile.

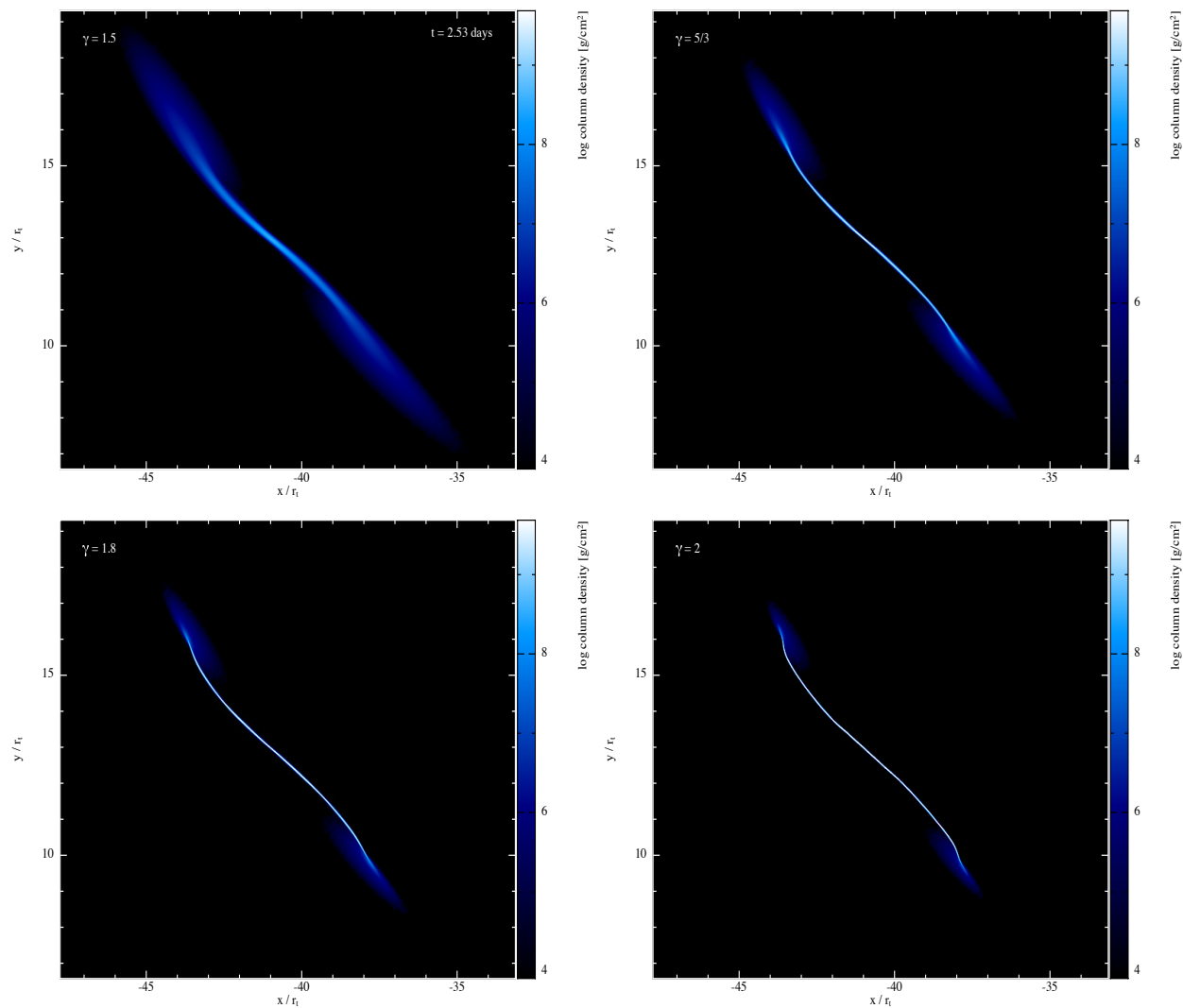


Figure 3.5: The stream at a time of 2.53 days from pericenter for an adiabatic index of  $\gamma = 1.5$  (top, left),  $\gamma = 5/3$  (top, right),  $\gamma = 1.8$  (bottom, left) and  $\gamma = 2$  (bottom, right). The stream thickness decreases dramatically and the fans become less pronounced as  $\gamma$  increases.

assumption because of the nature of the perpendicular pancake, then the transverse structure of the stream is governed by the equation of hydrostatic equilibrium:

$$\frac{1}{\rho} \frac{\partial p}{\partial s} = -\frac{\partial \phi_{sg}}{\partial s}, \quad (3.14)$$

where  $\phi_{sg}$  is the gravitational potential due to the self-gravity of the debris and  $s$  is the transverse distance from the center of the stream. Furthermore, if the variation in the self-gravitational potential along the radial direction of the stream is small, which is a good approximation toward the center of the stream owing to its approximately symmetric nature and only breaks down when we approach its radial extremities, then the Poisson equation reads

$$\frac{1}{s} \frac{\partial}{\partial s} \left( s \frac{\partial \phi_{sg}}{\partial s} \right) = 4\pi G \rho. \quad (3.15)$$

Using this equation in conjunction with equation (3.14), we find that the equation of hydrostatic equilibrium becomes

$$\frac{1}{s} \frac{\partial}{\partial s} \left( \frac{s}{\rho} \frac{\partial p}{\partial s} \right) = -4\pi G \rho. \quad (3.16)$$

With the polytropic equation of state  $p \propto \rho^\gamma$ , dimensional analysis of this equation shows that the cross-sectional radius of the stream varies as

$$H \propto \rho^{\frac{\gamma-2}{2}}, \quad (3.17)$$

where here  $\rho$  is the density at the center of the stream. The precise constant of proportionality depends on the entropy of the gas and the numerical solution to equation (3.16).

It is ultimately the scaling given by equation (3.17) that tends to outweigh the presence of a higher-density core for smaller  $\gamma$ . Also, if we use this expression for  $H$  in equation (3.10), then the density along the stream varies as

$$\rho = \rho_m \left( \frac{1}{\sqrt{(u')^2 + u^2(\phi')^2} \int_0^{\xi_1} \Theta(\xi)^n \xi^2 d\xi} \int_{\mu\xi_1}^{\xi_1} \Theta(\xi)^n \xi d\xi \right)^n, \quad (3.18)$$

where  $\rho_m$  is a normalization constant, chosen such that the density equals the correct, central stellar density at the time of disruption, and  $u \equiv r/r_t$ .

The density along the stream already exhibits a number of interesting features well before 2.53 days. To exemplify this point, Figure 3.6 shows the average radial density (i.e., the average density of all particles at a given radius  $r$ ) along the stream for the  $\gamma = 5/3$  run at times of  $t = 6.14, 9.57, 13.0,$  and  $19.8$  hours after disruption. Initially the density distribution along the curve is smooth, and matches well the distribution obtained if the original polytrope is stretched in one dimension (equation 3.18). However, at later times the density adopts a more intricate structure, exhibiting a sharper peak at the center of the stream and “shoulders,” evident from the bottom-right panel of Figure 3.6, that are not predicted analytically.

Figure 3.7 shows the average density along the stream for the four different adiabatic indices at 2.53 days after disruption (the black curves are the numerical solutions, while the red, dashed curves give the analytic estimate that results from equation 3.18). This Figure demonstrates that the small-scale density fluctuations that develop along the stream at later times are intensified for larger  $\gamma$ . It is evident that lower adiabatic indices show relatively smooth variations in the density, and retain an approximately symmetric structure about the center of the stream. For larger polytropic indices, however, the scale at which perturbations develop along the stream decreases and the perturbations themselves become more erratic in amplitude and position. It is also clear that a smaller adiabatic index results in more material at smaller and larger radii than would be predicted analytically, and these “fans” are also apparent from Figure 3.5. This results from the fact that polytropes with smaller  $\gamma$  have lower-density envelopes, those envelopes being more easily stripped at early times.

To determine when the density of the debris stream starts to exhibit the anomalous, small-scale structure that is apparent in Figures 3.6 and 3.7, Figure 3.8 shows the maximum density along the stream as a function of time; the black, solid curve indicates the numerical solution, while the red, dashed curve gives the analytic prediction (equation 3.18). Aside from slightly over-predicting its magnitude, the analytic solution matches the numerical one well, which shows that the stream

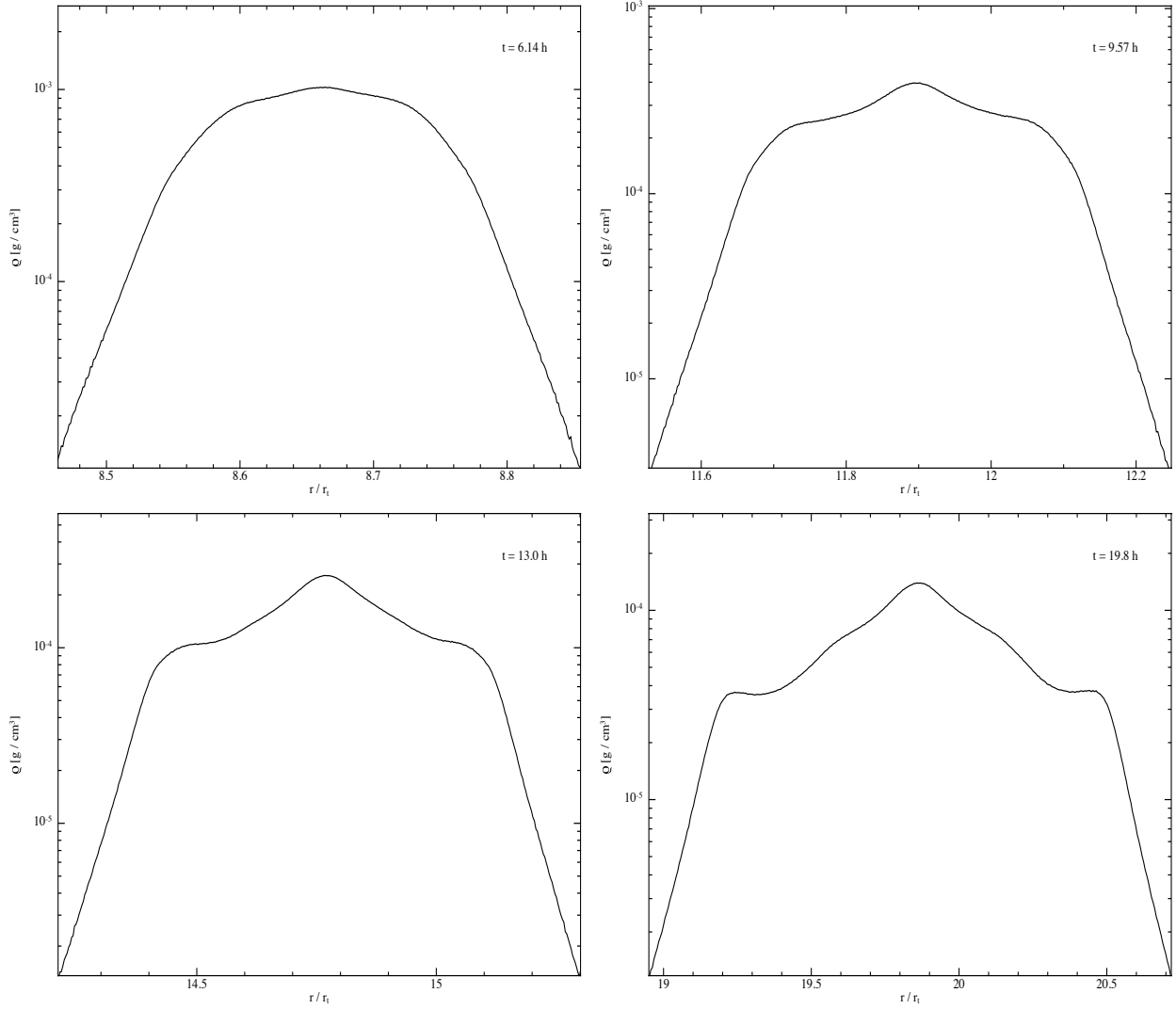


Figure 3.6: Four snapshots of the average stream density (the average density of all particles at a given radius  $r$ ) as a function of  $r$  for the  $\gamma = 5/3$  run. Initially the density remains smooth throughout the stream; however, by about a day after the disruption, the density structure has developed a more complicated nature, consisting of a central peak that is narrower than is predicted analytically and two shoulders.

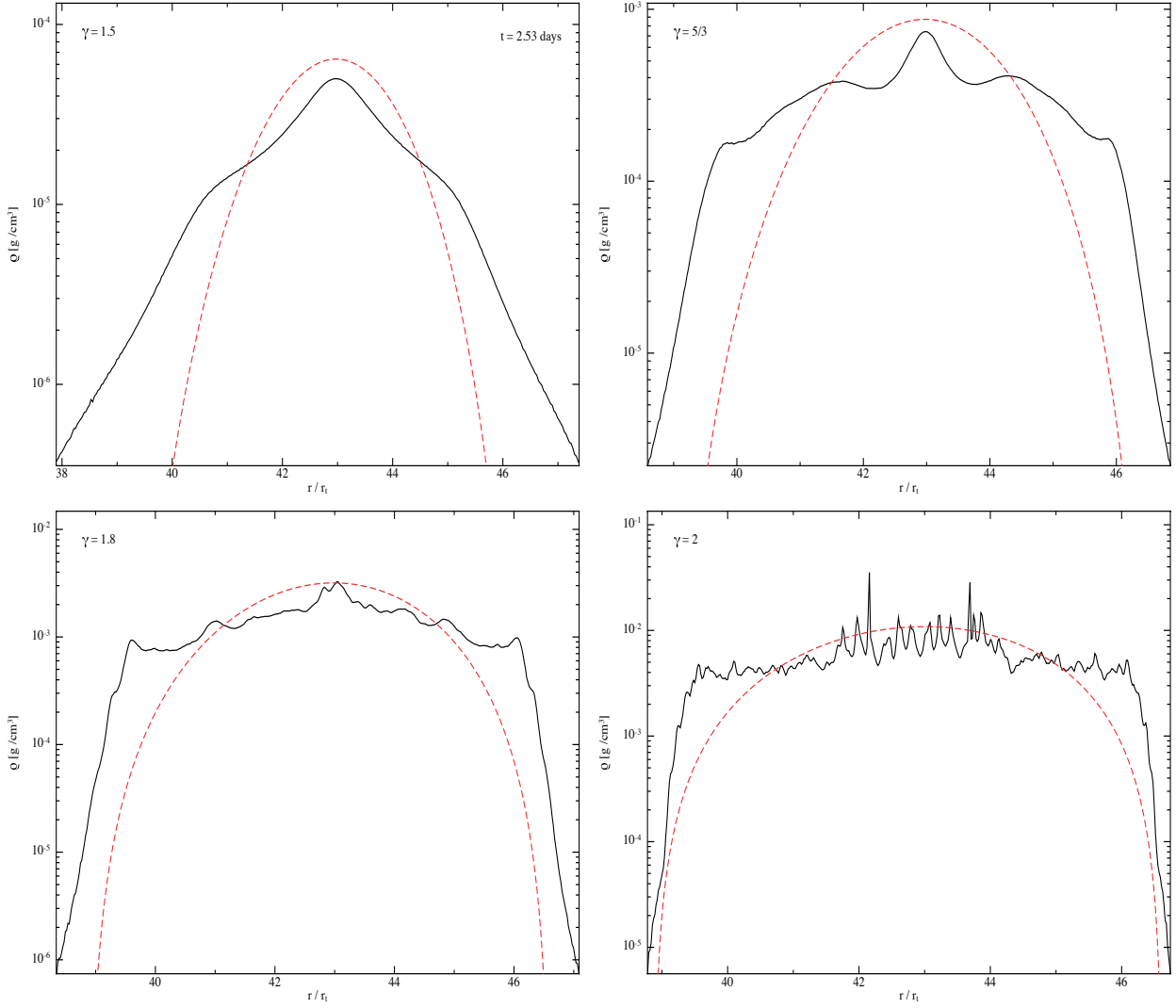


Figure 3.7: The average density (same as Figure 6) as a function of  $r$  for  $\gamma = 1.5$  (top, left panel),  $\gamma = 5/3$  (top, right panel),  $\gamma = 1.8$  (bottom, left panel), and  $\gamma = 2$  (bottom, right panel) at a time of 2.53 days after disruption (see Figure 3.5 for the shape of the streams at this time). The black, solid curves give the numerical solutions, while the red, dashed curves show the analytic predictions. It is apparent that larger adiabatic indices correspond to an enhanced amount of variability in the density along the stream, while a smaller adiabatic index results in more extended wings (this is also apparent from the tidal fans in the edges of the streams in Figure 3.5.)

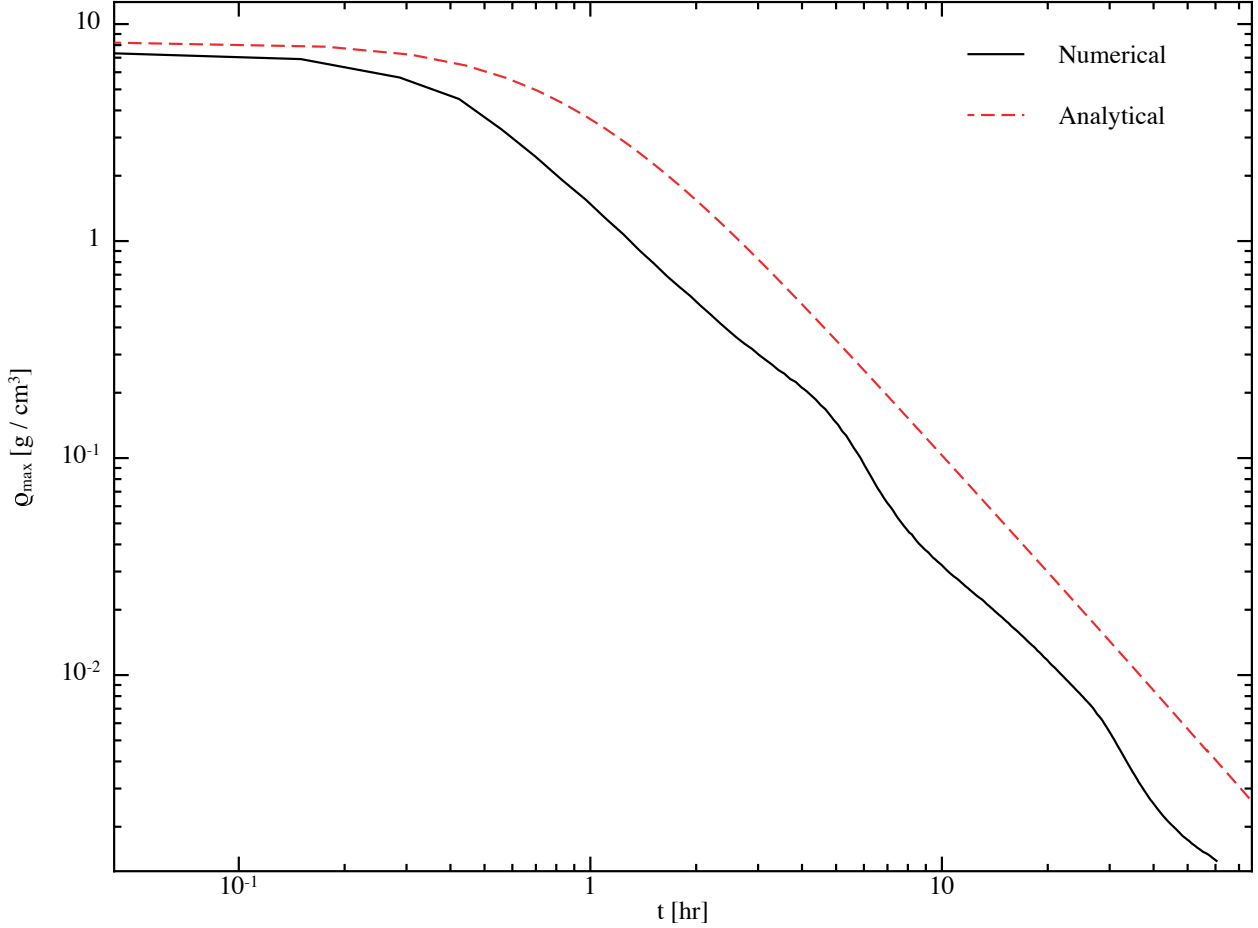


Figure 3.8: The maximum density along the stream as a function of time with  $\gamma = 5/3$  ( $n = 1.5$ ); the numerical solution is given by the black, solid curve, and the analytical solution (equation 3.18) is given by the red, dashed curve. A time of zero here corresponds to the time at which the star reaches the tidal radius. The time at which the numerically-obtained density starts to decrease is slightly earlier than the analytic one, suggesting that the time at which the star is “disrupted” is actually pre-periapsis. The first bump in the numerical solution, which occurs after a couple of hours, indicates where the pancake starts to augment the maximum density. At late times, both solutions follow the approximate power-law decline  $\rho \propto t^{-1.8}$ .

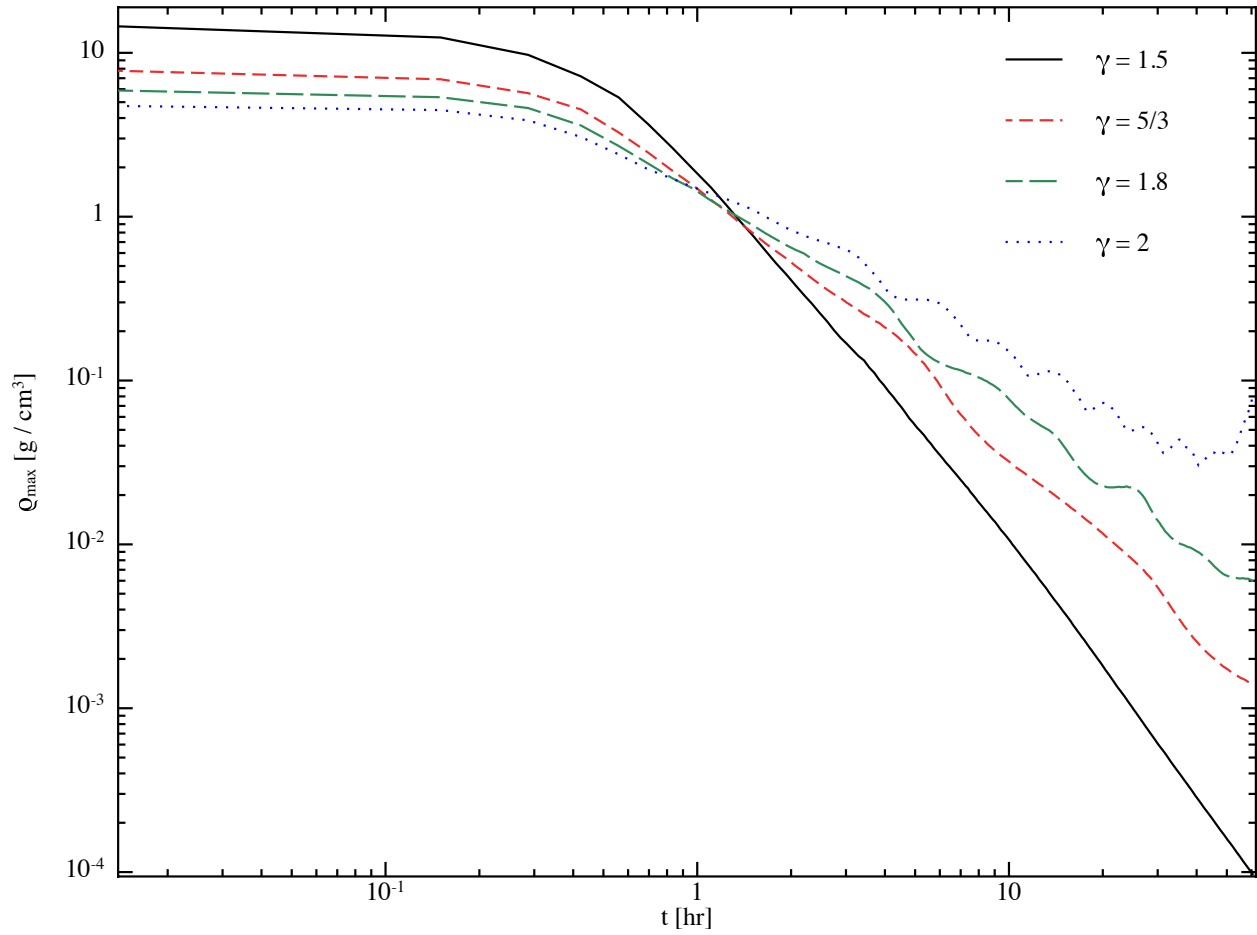


Figure 3.9: The maximum density as a function of time for  $\gamma = 1.5$  (black, solid curve),  $\gamma = 5/3$  (red, dashed curve),  $\gamma = 1.8$  (green, long-dashed curve), and  $\gamma = 2$  (blue, dotted curve). It is apparent that the initial perturbation induced by the pancake is induced sooner for larger  $\gamma$ , and the oscillation timescale of the perturbation is shorter for larger  $\gamma$ .

approximately maintains hydrostatic balance for all times during the disruption in the transverse direction. Note that this result contrasts the findings of Kochanek (1994), who assumed that the stream was in free expansion until three dynamical times post-disruption, which is roughly 1.5 hours for the disruption of a solar-type star by a  $10^6 M_\odot$  hole (however, the assumption of free expansion may hold in the limit of  $\beta \gg 1$ ). This plot also demonstrates that the first perturbation to the density appears at a couple hours after disruption, resulting in a “ripple” that over- and under-estimates the average value. The perturbations induced on the stream therefore behave as compression-rarefaction waves.

Figure 3.9 shows the maximum density along the stream for the four different adiabatic indices. It is evident that the first bump in the density occurs slightly sooner for larger  $\gamma$ , appearing at around an hour for  $\gamma = 2$ , and that the temporal frequency of the perturbations increases as  $\gamma$  increases. The average maximum density also falls off as a power-law for late times, which agrees with the analytic prediction (Figure 3.8), with the power-law index being shallower for larger  $\gamma$ . In particular, if we set  $\rho_{max} \propto t^{-m_\gamma}$ , we find  $m_{1.5} = 2.4$ ,  $m_{5/3} \simeq 1.8$ ,  $m_{1.8} \simeq 1.5$ , and  $m_2 \simeq 1.2$ .

### 3.4 Discussion

We saw in the previous subsection that the impulse approximation – assuming that the star retains its spherical, undisturbed structure until it reaches the tidal radius – does a reasonable job of fitting the numerically-obtained density profile of the tidally-disrupted debris stream when  $\beta = r_t/r_p = 1$  (Figure 3.7). This agreement demonstrates that the stream width is set by hydrostatic balance, while the length is determined by the radial positions of the gas parcels orbiting in the potential of the black hole. However, at times corresponding to a few hours after disruption, the density profile begins to exhibit anomalous, small-scale structure that is not predicted analytically, with important ramifications for the late-time evolution of the stream (Figures 3.7–3.9).

This behavior was also noted by Lodato et al. (2009), who commented on the existence of the shoulders present in the density profile (see their Figure 7; they were interested in the behavior of  $dm/d\epsilon \propto \rho H^2$ , the distribution of mass in energy space, as this yields information about the

fallback rate). Since they renormalized their specific energy distribution to match the peak, they did not notice the sharper structure exhibited by the density in the central portion of the stream. They argued that these shoulders arose from shock compression within the stream.

However, we find it unlikely that shocks alone can account for these anomalous features. For one, shocks occur primarily in the outermost regions of the envelope at the time of disruption. The majority of the material involved in the shocks is therefore confined to the tidal tails of the debris stream (the fans at the edges of the streams in Figure 3.5; see Figure 8 of Lodato et al. 2009), comprising only a small fraction of the total amount of mass contained in the stream. However, the perturbations occur throughout the majority of the stream, affecting a much larger fraction of the material. The time at which the fluctuations begin to appear is also hours after the disruption, well after the shocks that occur at pericenter. Furthermore, we have run additional simulations that include shock heating; in these cases, the density profiles we find are nearly identical to those presented here, indicating that the amount of material that shocks significantly is small.

On the contrary, we find that a more reasonable origin for the anomalous structure present in the numerical solutions is the combination of self-gravity and the “perpendicular pancake” discussed in Section 2.2 – where in-plane compression of the star causes the front and back edges of the star to converge to a one-dimensional line, or caustic (see Figure 3.3). This interpretation is supported by the temporal coincidence of the ripples present in Figure 3.7 and the analytic prediction of when the caustic arises, both occurring on the order of hours after disruption. We also note that the majority of the stream, not just the central maximum, seems to be undergoing an increase in density when the first perturbation occurs. This can be seen from Figure 3.8, which shows that the first increase in the density for the  $\gamma = 5/3$  run starts to appear around a few hours after disruption. However, the top, left panel of Figure 3.6 shows that at a time of roughly six hours after disruption, long after the first perturbation has started to augment the maximum in the density, the entire stream still retains a smooth density distribution that is well-matched by the analytic prediction. Indeed, the sharper peak and shoulders do not seem to appear until around 10 hours after disruption, which is the top, right-hand panel of Figure 3.6. This indicates that the first increase in the maximum

density is occurring over the **entire** stream, not just in the central region where the maximum occurs (for which Figure 3.8 applies), and the density everywhere is being incremented by the same factor.

In further support of the interpretation that the caustic occurs in the simulations and enhances the density perturbations, recall that the existence of the caustic is ultimately related to the initial conditions at the time of disruption: because every gas parcel is moving with the center of mass of the star, the parcels comprising the back edge of the star have not yet reached their periapses, while those comprising the front have already passed through theirs. This configuration then causes the back to accelerate and the front to decelerate, resulting in their eventual merger. In a realistic TDE, the star does not retain perfect spherical symmetry all the way until the tidal radius (Figure 3.4). In particular, the less dense, outer regions of the envelope will be stripped earlier, causing them to violate the condition that they move with the center of mass. The denser, central regions, however, may better retain their unperturbed structure, resulting in a pancake that occurs mainly in the center of the stream.

To test this hypothesis, we ran a simulation in which we took the output of the  $\gamma = 5/3$  PHANTOM run when the star reached pericenter and evolved the particles solely in the gravitational field of the hole, neglecting pressure and self-gravity. Figure 3.10 shows the distribution of particles at a time of 37 minutes (left panel), 50 minutes (middle panel), and 62 minutes (right panel) post-disruption, the red particles being those that composed the back of the star at pericenter, the black particles the front. This Figure shows that, at roughly an hour after disruption, the front and back edges of the stream switch places, with the point of maximum compression occurring in the middle panel. Specifically, the half-width of the center of the stream at 50 minutes is roughly  $H \simeq 0.1r_t$ , which is only five times the value when the star is at pericenter. This Figure confirms that the caustic still exists with realistic initial conditions. However, as predicted, the fans at the edge of the stream do not undergo a similar amount of compression and retain their original colors, which is due to the fact that they were not moving with the center of mass at the time of disruption (i.e., they were already stripped from the star; this is also supported by the fact that the fans extend

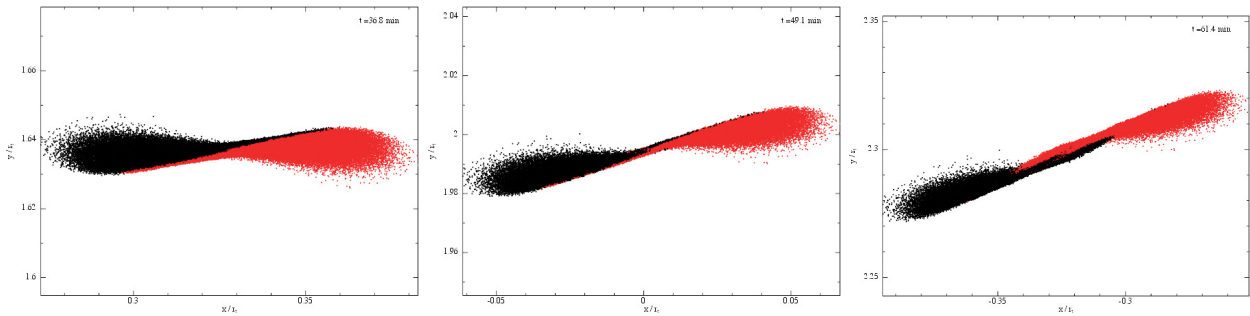


Figure 3.10: The particle distributions from an  $N$ -body simulation, where the initial conditions were taken from the  $\gamma = 5/3$  run at periapsis, at 37 minutes (left panel), 50 minutes (middle panel), and 62 minutes (right panel) post-disruption. The red particles comprised the back of the star at the time of disruption, while the black constituted the front of the star. This Figure demonstrates that a caustic – where the front and back of the stream merge to form an infinitely thin line – still occurs in the presence of realistic initial conditions. However, as mentioned in the text, the outermost layers of the star that are stripped earlier (and therefore violate the frozen-in condition) do not undergo this compression; this is evidenced from the fact that the “fans” present in this figure undergo no distortion in terms of their color. The central panel corresponds to the point at which the width of the stream has reached a minimum, the half-width being  $H \simeq 0.1 r_t$ .

farther in radially than the analytic solutions predict, which is apparent in Figure 3.7).

The preceding arguments illustrate that it is likely the caustic discussed in Section 2.2 that augments the importance of self-gravity and generates the density fluctuations in the stream. Interestingly, Figures 3.8 and 3.9 show that this perpendicular pancake does not simply increase the density, but instead generates a compression-rarefaction wave. This is due to the fact that the increase in the density likewise generates an increase in the pressure, which resists the compression. Eventually, the continued squeezing of the stream results in the material being overpressured in the transverse direction, which causes the stream to “bounce.”

The sharper peak that develops in the center of the stream arises from the self-gravity of the debris. In particular, the compression in the transverse direction augments the central density to the point where material can be drawn in gravitationally in the radial direction, which creates the more massive central peak and the two dips on either side of that peak in Figure 3.6. The two shoulders that develop are regions of the stream that have not been gravitationally drained of material by the central peak and are slightly denser than one would predict analytically due to the pancake. More structure develops at late times, and local maxima are imprinted due to the oscillation of the stream, ultimately due to the self-gravitating nature of the debris (see also Figure 3 of Kochanek (1994), who found oscillations in the stream width and height due to pressure and self-gravity). The points at which the density sharply drops off are the fans present in Figure 3.5, and have thus not been affected by the caustic (note from Figure 3.7 that the rate at which the density falls off with radius in these regions parallels the analytic one, which confirms this interpretation).

From Figure 3.7, it is apparent that larger adiabatic indices result in more drastic fluctuations that are induced by the caustic. The reason for this scaling is likely two-fold, the first being that, for the same physical radius  $R_*$ , polytropes with larger adiabatic indices have flatter density profiles (note that this is not true in the dimensionless space spanned by  $\xi$ ). Therefore, since the density throughout the envelope differs from that of the core only when we are near the surface of the star, polytropes with higher adiabatic indices can better retain their structure until they reach

periapsis. This then results in more of the stream experiencing the effects of the caustic, which correspondingly results in a more drastic increase in the density along the majority of the stream. This is supported by Figure 3.7, which shows that the shoulders extend farther from the center of the stream as  $\gamma$  increases.

The second reason is that the stream is thinner for larger  $\gamma$ , which is evident from Figure 3.5. Since the equilibrium width of the stream increases as  $\gamma$  decreases, the pancake is less effective in compressing the stream and correspondingly increasing the density to the point where self-gravity can amplify the perturbations. Additionally, this scaling with  $H$  causes the average density of the stream to decrease less rapidly with time for larger  $\gamma$  (Figure 3.9). The overdensities within the stream are therefore more dense in an absolute sense, which increases the ability of the self-gravity of the debris to counteract the tidal shear imposed by the black hole.

### 3.4.1 Is the pancake necessary?

Figures 3.6 – 3.9 show that self-gravity can drastically modify the density profile of the disrupted debris stream from a TDE, causing a sharper peak near the center, small-scale fluctuations, and “shoulders,” all of which are not predicted analytically. These effects are long-lived, altering the structure of the debris stream for days to months post-disruption (see also section 5). In addition, we saw in Section 2 that a caustic – where the front and the back of the stream intersect to form a two-dimensional plane – occurs not long after the disruption of the star under the impulse approximation. Figure 3.10 shows that, even in a realistic TDE where the frozen-in assumption does not apply, the orbits of the gas parcels near the center of the star converge to form this post-periapsis pancake. Therefore, the self-gravity of the stream is augmented by the dynamical focusing of the gas parcels in the transverse direction.

Because the numerical method treats the full complexity of the problem, including pressure, self-gravity, and the influence of the SMBH, the simulations presented here have not isolated the effects of self-gravity and the pancaking of the orbits. Is it possible that the latter is actually unimportant, with the majority of the variation in the density of the stream due solely to the

self-gravity of the debris?

To answer this question, recall that the pancake arises from the fact that, under the impulse approximation, the front of the star is decelerating at the time of disruption while the back is accelerating. Equivalently, the requirement that the entire star move with the center of mass means that the gas parcels comprising the front of the star have already passed through their pericenters, while those comprising the back have not yet passed through theirs. Therefore, to avoid the caustic but still maintain a realistic distribution of specific energies (half bound, half unbound), one can simply impose that the initial velocities of the gas parcels satisfy  $\dot{r}_i = 0$ ,  $\dot{\theta}_i = 0$ , and  $r_i^2 \sin^2 \theta_i \dot{\phi}_i^2 = 2GM_h/r_t$ . Thus, if the star had these (albeit contrived) initial conditions, the post-disruption evolution would be unaffected by the caustic.

To examine the isolated effects of self-gravity, we used the output of the PHANTOM runs when the star was at pericenter (Figure 3.4) and modified the instantaneous velocities to reflect the initial conditions that avoid the caustic, i.e., we set  $\dot{r}_i = 0$ ,  $\dot{\theta}_i = 0$ , and  $r_i^2 \sin^2 \theta_i \dot{\phi}_i^2 = 2GM_h/r_t$  for all of the particles. What we generally found was that the anomalous features of the density profile were still present, i.e., shoulders still formed and a more concentrated peak developed. However, the **magnitude** of each of these features was significantly reduced; in particular, the shoulders were much less pronounced, the central density peak was less sharp, and the density fluctuations were less concentrated. The overall magnitude of the density was also down by a factor of a few, and the increase in the density that occurred over the entire stream (see discussion above) was not observed in the modified runs (see Figure 3.11, which illustrates these points). Finally, the morphology of the streams also differed, having larger widths and more extended fans in the cases where the pancake did not occur.

These tests show that, in general, the anomalous features arise from the self gravity of the debris modifying the radial density distribution throughout the stream. However, as was suggested in the previous subsection, the post-periapsis pancake is quite important for magnifying and sustaining the self-gravitating nature of the stream.

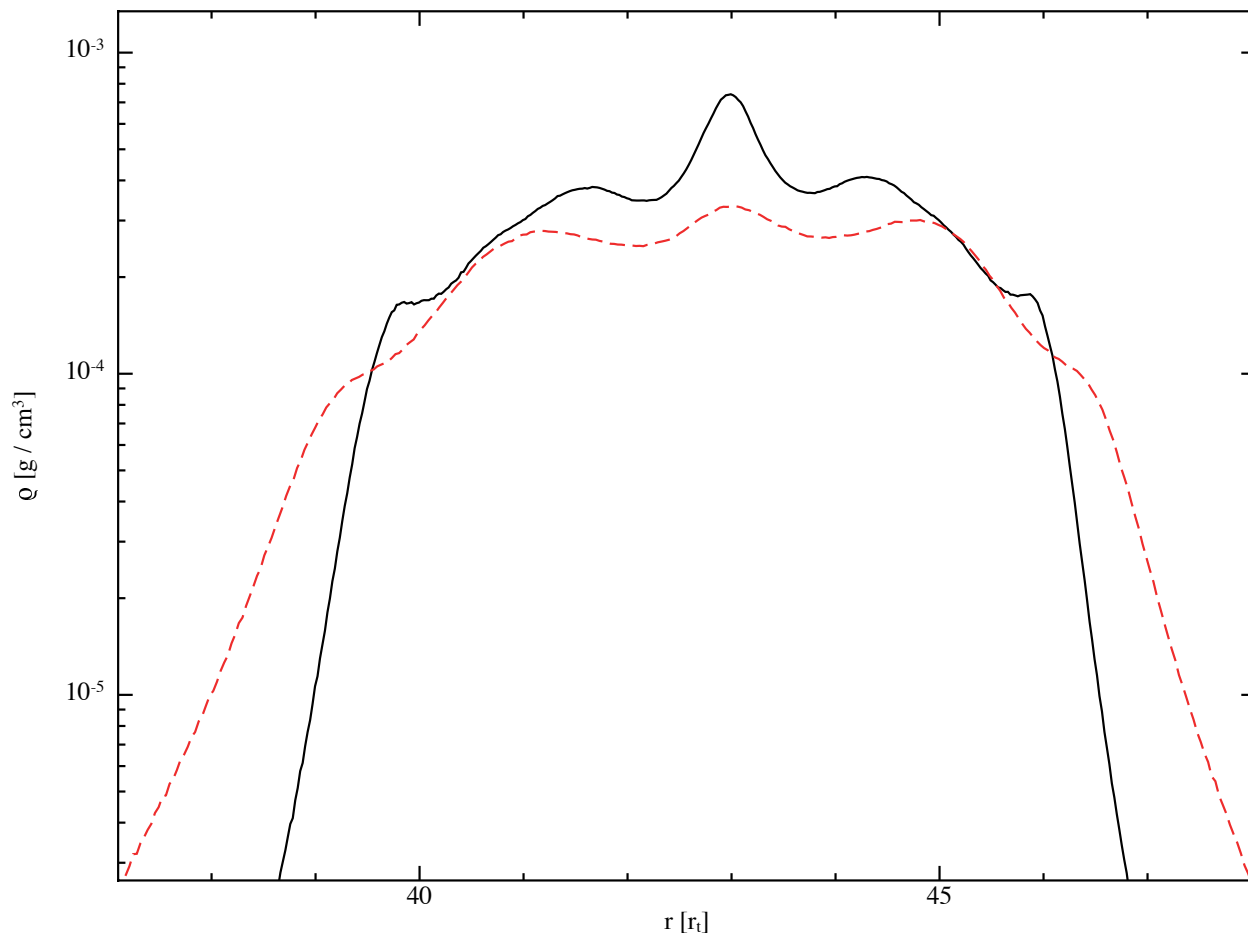


Figure 3.11: The average density as a function of  $r$  for the unaltered,  $\gamma = 5/3$  run (solid, black curve) and the run that avoids the caustic (dashed, red curve), both at a time of 2.53 days (the same time as in Figure 3.7). This Figure shows that the pancake amplifies the anomalous density structures along the stream, effectively enhancing the ability of self-gravity.

## 3.5 Implications

We have demonstrated above that a caustic, or a “perpendicular pancake,” augments the importance of self-gravity in the debris stream from a TDE. In particular, we found that this pancake and self-gravity cause density perturbations that are not predicted analytically (Figure 3.7). In this section we briefly discuss several implications of our findings.

### 3.5.1 Fragmentation

One of the most profound implications is that these perturbations can result in the gravitational fragmentation of the stream. For  $\gamma = 2$ , the overdensities present in the stream at a time of 2.53 days are already self-gravitating and starting to collapse into small-scale, gravitationally-bound clumps (see Figure 3.12). For  $\gamma = 1.8$ , the stream also fragments, but not significantly until a time of a couple weeks after disruption. The  $\gamma = 5/3$  run also collapses at late times, but the time at which fragmentation occurs depends on the resolution of the simulation. As was commented upon in Chapter 2, this suggests that the stream itself is gravitationally unstable, but the perturbations induced by the pancake and self-gravity are not sufficient to drive the fragmentation. This finding also suggests that the limiting adiabatic index at which fragmentation occurs is closer to  $\gamma = 5/3$  than  $\gamma = 2$ , as indicated by previous studies of compact object mergers (Lee & Ramirez-Ruiz 2007, in particular their Figure 23; see also our discussion below regarding the origin of this marginal stability). We have run the  $\gamma = 1.5$  simulation presented here out to nearly 10 years and have not found recollapse, suggesting that the density profile of the stream is gravitationally stable.

In the  $\gamma = 1.8$  run, the first clump forms near the center of the stream around a time of five days after disruption, with smaller-mass clumps forming at later times at distances progressively farther from the central portion of the stream. By about two months after disruption, the clump formation becomes less vigorous, and the clump masses saturate at approximately constant values with an average clump mass of  $\bar{M}_c \simeq 0.55M_J$ , where  $M_J \simeq 9.54 \times 10^{-4}M_\odot$  is the mass of Jupiter. The maximum clump mass, however, is  $M_{c,max} \simeq 1.5M_J$ , showing that the clumps span a large

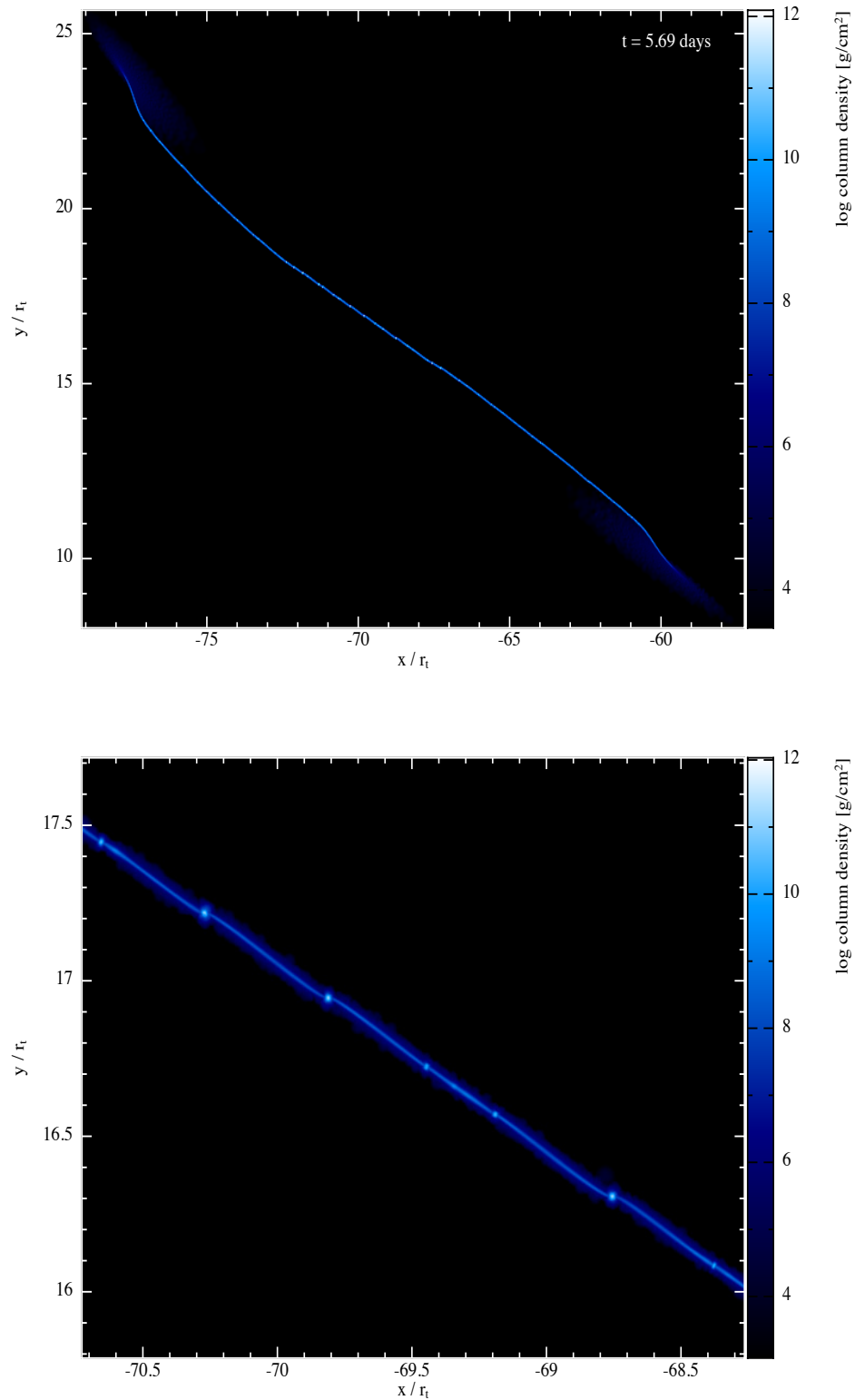


Figure 3.12: The stream from the  $\gamma = 2$  run (top panel) and a closeup view of the stream (bottom panel), showing the clumps that have formed throughout the majority of the stream, both at a time of 5.69 days after disruption.

range in mass.

On the other hand, the first clumps form at a time of around three days after disruption for the  $\gamma = 2$  run, and instead of forming one clump in the center of the stream, between five and ten form around the same time at approximately evenly-spaced intervals along the stream (this agrees with the findings of Lee & Ramirez-Ruiz 2007 and other studies of the tidal tails produced during compact object mergers where very stiff equations of state were used). Fragmentation ceases with an average clump mass of  $\bar{M}_c \simeq 2.6M_J$  around two weeks after disruption, and the maximum clump mass in this case is  $M_{c,max} \simeq 37M_J$ .

Since the  $\gamma = 5/3$  run collapsed at late times but due to the small-scale numerical noise inherent in the simulation, additional, resolved perturbations are required to study true fragmentation in this case. This marginal instability of the stream is likely due to the fact that the maximum density in the stream drops off as  $\rho \propto t^{-1.8}$  (see Figure 3.8), whereas the “density” of the black hole scales as  $\rho \propto 1/r^3 \propto 1/t^2$ , the last proportionality resulting from the fact that the orbits of the gas parcels initially follow  $r \propto t^{2/3}$ . The decline in the density for the  $\gamma = 5/3$  case is thus barely above that of the black hole, meaning that the stream self-gravity only outweighs the tidal shear by a small margin. Additionally, since  $\rho \propto t^{-2.4}$  for  $\gamma = 1.5$ , we do not expect fragmentation to occur in this case, and this is consistent with what is observed from the simulation.

### 3.5.2 Fallback rate features

When one of the of these clumps returns to pericenter, the fallback rate can spike above the average,  $t^{-5/3}$  decline by a significant fraction, as is apparent from Figure 3.13 for times greater than a few years, and from Figure 3.14 for times greater than a few months (the small amount of scatter present for the  $\gamma = 1.5$  fallback curve is due to numerical noise). If the tidally-disrupted debris has already formed an accretion disk, the interception of one of these clumps by the disk can significantly augment the accretion rate onto the hole (though this is only true during the early stages of the fallback, when the viscous time is short compared to the infall time; Cannizzo et al. 1990).

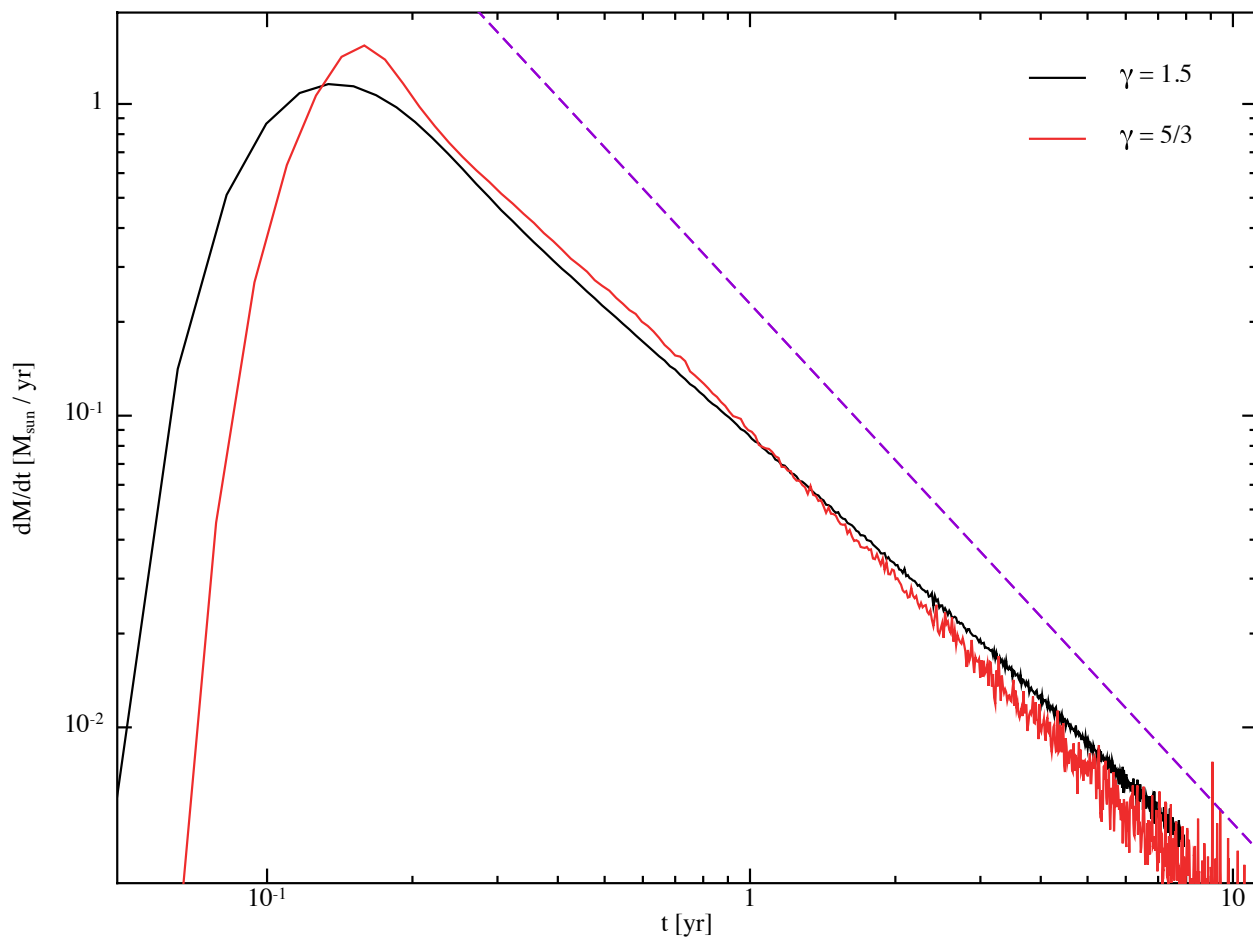


Figure 3.13: The fallback rate computed for the  $\gamma = 1.5$  (black curve) and  $\gamma = 5/3$  (red curve) runs. The purple curve is the canonical  $t^{-5/3}$  fallback rate for reference. It is apparent that the return time of the most bound material is earlier for smaller  $\gamma$ , which is related to the amount of distortion imparted to the star at the time of disruption. At late times, the accretion of clumps that have formed in the  $\gamma = 5/3$  stream causes the fallback rate to deviate significantly from the mean (the small amount of deviation present in the  $\gamma = 1.5$  run is numerical noise).

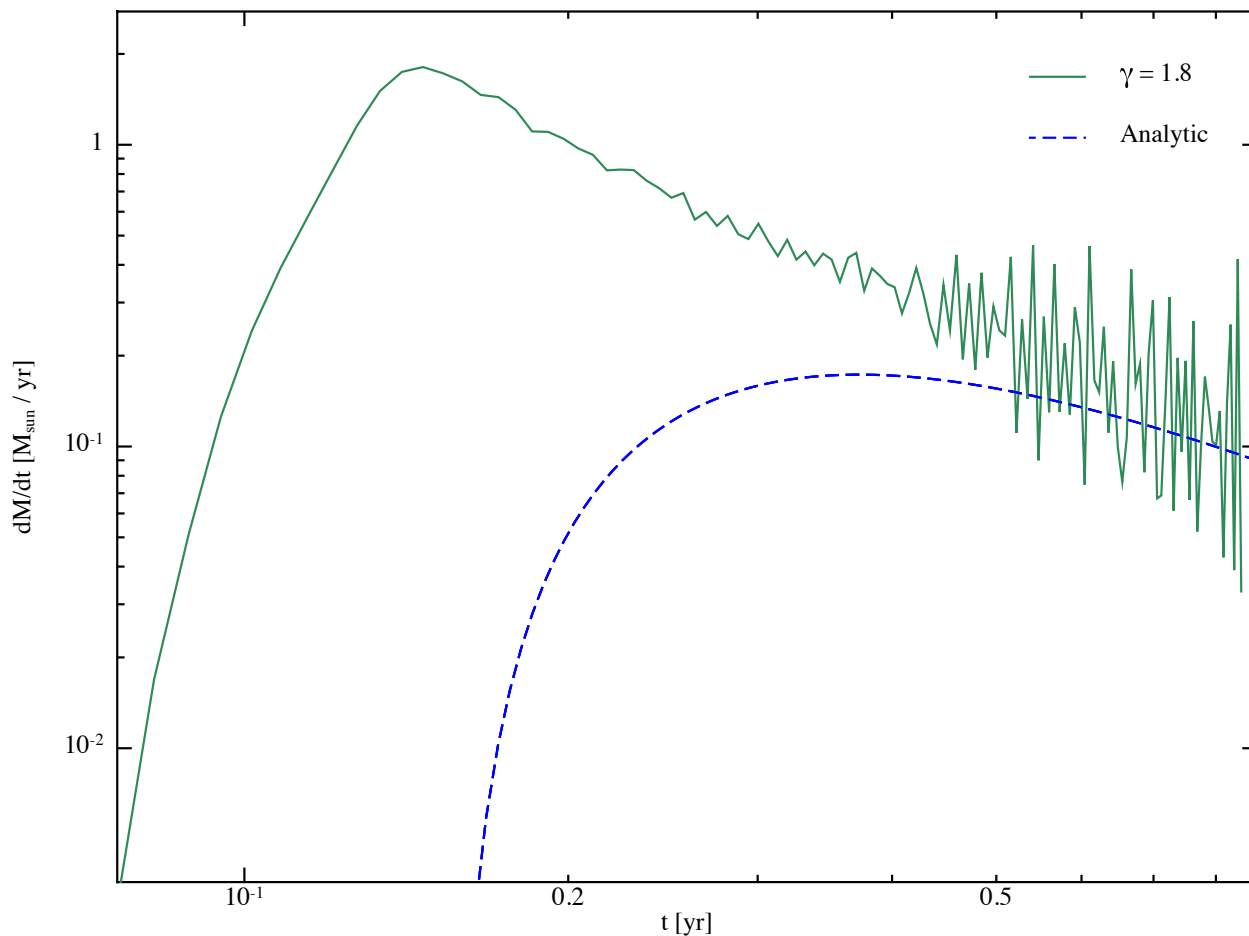


Figure 3.14: The fallback rate for the  $\gamma = 1.8$  run (green, solid curve) and the analytic prediction (blue, dashed curve). We see that the numerical solution is larger than the analytic one by an order of magnitude, and the fallback of bound clumps causes significant deviation from the average,  $t^{-5/3}$  fallback at times greater than about 6 months from disruption.

Figure 3.13 shows that, shortly after reaching their peaks, the fallback rates for both the  $\gamma = 1.5$  and  $\gamma = 5/3$  runs fall below the canonically-assumed  $t^{-5/3}$  power-law. There is then a period during which the rate is slightly shallower than the  $5/3$  rate; for the  $5/3$  run, this latter period lasts from a few months until about a year, after which the rate resumes the  $t^{-5/3}$  decay. For the  $\gamma = 1.5$  run, however, the power-law is less steep than the  $5/3$  law after nearly ten years from the disruption. This variable fallback rate is due to the accretion of various parts of the stream: the rate drops below  $5/3$  when the dip between the first shoulder and the central peak of the stream (Figure 3.7) is accreted. The rate then becomes shallower than the  $5/3$  law when the denser, central regions are accreted. This variation in the fallback rate means that observed TDEs may not follow the  $t^{-5/3}$  law for much later times than previously suspected.

Figure 3.14 demonstrates that the peak fallback rate is significantly higher than the analytic prediction (this is also true for the  $\gamma = 1.5$  and  $\gamma = 5/3$  runs), where the latter was calculated by using the energy-period relation, which gives  $\mu(t) = (t/T)^{-2/3}$ ,  $T = 2\pi M_h / (M_* \sqrt{GM_h}) (R_*/2)^{3/2}$  being the period of the most tightly bound debris, and the frozen-in condition (see Chapter 5 for more details). This increase in the fallback rate arises from the fact that the pancake has increased the density above what would be predicted analytically, as is apparent from Figure 3.7. This means that the accretion rate onto the black hole is much higher than thought previously, making it more likely that the TDE will result in a phase of super-Eddington accretion. Indeed, if we assume an efficiency of  $\epsilon = 0.1$  and  $\dot{M}_{acc} = \dot{M}_{fb}$  where  $\dot{M}_{acc}$  is the accretion rate onto the black hole, then the peak accretion rate for the  $\gamma = 1.8$  run in Figure 3.14 corresponds to an accretion luminosity of  $L_{acc} \simeq 80L_{Edd}$ , compared to the analytic estimate of  $L_{acc} \simeq 8L_{Edd}$ . Since the degree to which the fallback rate is super-Eddington is inversely proportional to the black hole mass, we see that more TDEs could be accompanied by a jetted-outflow phase like that seen for **Swift** J1644+57 (Zauderer et al., 2011).

### 3.5.3 Clump fates

If an accretion disk has not yet formed, the clumps that are bound to the black hole can return to the original pericenter distance. Since their densities will likely be lower than that of the stellar progenitor, the tidal disruption radii of the clumps will be outside the tidal radius of the original star. The returning clumps will therefore be “redisrupted” before reaching their pericenters, leading to complicated interactions between the streams of incoming and outgoing debris that could avoid the “dark year for tidal disruption events” suggested by Guillochon et al. (2015). Also, depending on the magnitudes of general-relativistic apsidal and Lense-Thirring precession, these redisruptions may tend to isotropize the accretion process, leading to a more symmetric inflow. This symmetric inflow may then lead to super-Eddington accretion luminosities, puffing up the accretion disk and potentially leading to the production of jets (Chapter 5).

The clumps that form in the unbound portion of the stream will make their way out of the sphere of influence of the central SMBH and into the galaxy. In particular, if we recall that the escape velocity of the most unbound material is  $v_{esc} \simeq \sqrt{2GM_*/R_*}(M_h/M_*)^{1/6}$ , then we find that the unbound clumps leave the sphere of influence of the black hole on a timescale of

$$t_{esc} \sim 10 \sigma_{100}^{-2} \left( \frac{M_h}{10^6 M_\odot} \right)^{2/3} \left( \frac{M_*}{M_\odot} \right)^{-1/6} \left( \frac{R_*}{R_\odot} \right)^{1/2} \text{ yrs}, \quad (3.19)$$

Although their long-term evolution is uncertain and depends on the specific properties of the gas (e.g., heating and cooling rates due to ionizations and recombinations), these unbound clumps could condense into planetary mass objects and brown dwarfs, producing a new class of hypervelocity objects that eventually leaves the host galaxy. Since the clump formation is most vigorous for adiabatic indices  $\gamma \gtrsim 5/3$ , those adiabatic indices being somewhat unphysical for real stellar progenitors, it may seem as though the production of unbound objects is largely inhibited for realistic TDEs; however, if cooling can significantly decrease the entropy (see below), then the number of clumps could be significantly augmented. Therefore, if there are between  $10^{-4}$  and  $10^{-5}$  disruptions per galaxy per year, the number of hypervelocity, low-mass objects could significantly outweigh the number of hypervelocity stars. We plan to perform a more in depth analysis of the

detailed properties of the clumps in a future paper.

We also recall that the marginally bound material recedes to very large distances before returning to the black hole. Therefore, similar to the unbound material, the clumps that form in this region of the stream may have time to collapse into much denser objects (e.g., planets). These objects may then be able to survive their plummet back into the tidal region of the black hole (though interactions with the surrounding stellar population may alter their pericenter distances to be larger than the original tidal radius), forming a class of low-mass objects that remain bound to the black hole. Since they would still be very weakly bound, their orbital periods would be anywhere from tens to thousands of years. Furthermore, if the clumps in this region do not become overly dense, they may form weakly-bound clouds that are consistent with those observed near the Galactic Center (e.g., the cloud G2; Burkert et al. 2012; Gillessen et al. 2012; Guillochon et al. 2014a).

### 3.5.4 Entropy

In these simulations, the gas maintained approximately constant entropy throughout the entire disruption process. In reality, the gas energy equation will be modified by losses due to radiative cooling and cooling or heating (depending on the optical depth of the stream) due to recombinations, which could significantly alter the equation of state of the gas and affect the nature of the caustic. A more realistic equation of state might therefore be of the form

$$p = S(\mathbf{r}, t)\rho^\gamma, \quad (3.20)$$

where  $S(\mathbf{r}, t)$  is related to the entropy of the gas that is, in general, a function of both space and time. When  $S(\mathbf{r}, t)$  is a constant, it is apparent from this expression that, for the same change in density, a smaller adiabatic index results in a correspondingly smaller decrease in the pressure. This scaling then results in a larger cross-sectional radius of the stream, which ultimately enables the debris to better resist the pancake and fragmentation for smaller adiabatic indices. We see, however, that if the entropy decreases with time, then the pressure could decrease faster than

would be predicted by an isentropic equation of state. Therefore, if cooling is efficient enough to significantly reduce the entropy of the gas, the pancake could induce fragmentation for  $\gamma$  less than  $5/3$ . This result is particularly apparent if we use equation (3.20) in equation (3.16), which shows that the cross-sectional radius scales as

$$H \propto S^{1/2} \rho^{\frac{\gamma-2}{2}}, \quad (3.21)$$

and using this relation in equation (3.10) yields

$$\rho = \rho_{ad}(r, t) \left( \frac{S}{S_0} \right)^{-n}. \quad (3.22)$$

Here  $\rho_{ad}$  is the density one obtains for an adiabatic equation of state, given by equation (3.18),  $S_0$  is the original entropy of the gas at the time of stellar disruption, and we recall that  $n = 1/(\gamma - 1)$ . We see that a decrease in the entropy has a more pronounced effect for smaller  $\gamma$ , meaning that efficient cooling would more easily result in recollapse for softer equations of state. In particular, since  $\rho_{ad} \propto t^{-2.4}$  for  $\gamma = 1.5$  ( $n = 2$ ), we would only need  $S \propto t^{-0.2}$  to bring the power-law to  $\rho \propto t^{-2}$ , which would make the stream marginally unstable to gravitational collapse.

### 3.6 Summary and conclusions

We have shown that a caustic – a surface where the orbits of the gas parcels comprising the stream of tidally-disrupted debris formally attain infinite density – results from the impulse approximation applied to  $\beta = r_t/r_p \simeq 1$  tidal encounters. This pancake is analogous to the one discovered by Carter & Luminet (1982); however, in this case the pancake occurs post-periapsis (on the order of an hour after the star reaches pericenter for the disruption of a solar-type star by a  $10^6 M_\odot$  hole), and the compression occurs in the plane of the orbit of the stream, which causes the orientation of the pancake to be perpendicular to the plane of the orbit (see Figure 3.3).

In a realistic TDE, the pressure of the gas will prevent the existence of a true caustic. To test the effects of pressure in resisting the pancake, we simulated four tidal encounters between a

solar type star ( $R_* = R_\odot$  and  $M_* = M_\odot$ ) and a  $10^6 M_\odot$  hole with the pericenter of the center of mass of the parabolic, stellar orbit at the tidal radius ( $\beta = 1$ ). The simulations differed only in the adiabatic index of the gas, being  $\gamma = 1.5, 5/3, 1.8$  and  $2$ , making our parameter space close to that chosen by Lodato et al. (2009).

A few hours after disruption, the density of the streams of debris produced by the disruption exhibit anomalous behavior, showing compression-rarefaction oscillations not accounted for by the analytic model (see Figures 3.6 – 3.9). We interpret these features as arising from the combination of the perpendicular pancake and self-gravity, not only because of the temporal coincidence of the two phenomena, but also because the majority of the stream seems to be undergoing a systematic increase in the density at the start of the first compression. This can be seen by noting that the first increase in the maximum stream density starts at a time of roughly an hour after disruption, yet the stream seems to retain its stretched-polytropic structure, predicted analytically, after six hours post-disruption (compare Figures 3.8 and 3.6). This suggests that a large portion of the stream is being compressed simultaneously and by the same factor, which is predicted for the pancake; furthermore, this systematic increase in the density was not observed in the test runs that avoided the caustic (see section 4.1). By using the periapsis velocities and positions of the gas parcels generated from the PHANTOM runs as the initial conditions for an N-body simulation, we also showed that the orbits of the central portions of the stream do tend to form a caustic (Figure 3.10). This finding is consistent with the fact that the dense, central portions of the star likely retain their structure better until reaching pericenter, thus creating the conditions necessary to form a post-periapsis pancake. On the other hand, the outer, less-dense regions of the envelope are stripped from the star sooner, violating the impulse criterion that they move with the center of mass until reaching pericenter, and thus avoiding the caustic.

The self-gravity of the stream, supplemented by the caustic, induces fluctuations on top of the otherwise-smooth, analytically-predicted density profile, as evidenced in Figure 3.7. The fact that the analytic predictions match the numerical solutions well means that the stream width is predominantly set by the balance between pressure and self-gravity, and does not undergo any

episode of free expansion immediately after pericenter passage as expected previously (Kochanek, 1994). The effects of the caustic are long-lived, and the density profile of the stream evolves for a considerable amount of time after the initial perturbations are imposed. The variations induced by the caustic and self-gravity drive deviations from the canonically-assumed  $t^{-5/3}$  fallback rate, the power-law being first steeper and then shallower than  $5/3$ , which can be seen from Figure 3.13. The peak in the accretion rate is also higher than would be predicted analytically (Figure 3.14).

Remarkably, the combination of the caustic and self-gravity can cause the stream to fragment into small-scale, gravitationally-bound clumps if the adiabatic index is high enough. Specifically, for  $\gamma = 2$  and  $\gamma = 1.8$ , we find that the stream collapses at a time of a few days and a couple of weeks, respectively. After a relatively short time — about two weeks for  $\gamma = 2$  and two months for  $\gamma = 1.8$  — the clump formation stops and the masses of the clumps saturate. For  $\gamma = 2$  the average clump mass is  $\bar{M}_c \simeq 2.6M_J$ , while that for the  $\gamma = 1.8$  run is  $\bar{M}_c \simeq 0.55M_J$ ,  $M_J \simeq 9.54 \times 10^{-4}M_\odot$  being the mass of Jupiter. In both of these cases, however, the maximum clump mass is an order of magnitude above the average, showing that there is a large range of clump masses. For  $\gamma = 5/3$ , the stream does collapse, but the instability is started by small scale noise and so future simulations with realistic perturbations are required (see also Chapter 2). For  $\gamma = 1.5$ , we find no fragmentation out to a simulated time of ten years post-disruption, suggesting that the stream is gravitationally stable.

The formation of these clumps has a number of interesting repercussions. For one, if an accretion disk has already formed from the tidally-stripped debris, it can intercept one of the infalling clumps and, especially if the clump mass is on the larger side ( $\gtrsim 1M_J$ ) of the distribution, significantly augment the accretion rate onto the black hole if the viscous timescale in disk is short (see Figure 3.14). Such periodic increases would be seen as variability in the lightcurve of the TDE, consistent with that observed for **Swift** J1644+57 (Burrows et al., 2011; Levan et al., 2011; Zauderer et al., 2011), and also for the events **Swift** J2058+05 (Cenko et al., 2012) and **Swift** J1112.2-82 (Brown et al., 2015). If an accretion disk has not yet formed, these clumps can be “redisrupted,” creating complicated interactions between the incoming and outgoing debris streams. This would

then tend to isotropize the accretion process onto the hole and cause increased variability in the lightcurve of the TDE. The clumps that form in the marginally bound material may have time to condense into more compact objects, such as planets and brown dwarfs, that can survive their eventual return to pericenter, allowing them to remain bound to the hole. The clumps formed in the marginally bound segment of the stream may also form less dense clouds, the likes of which are observed near our own Galactic Center (e.g., G2; Gillessen et al. 2012; Burkert et al. 2012). Finally, the unbound clumps may form a new class of low-mass, hypervelocity objects that make their way out of the host galaxy on timescales of millions of years.

Our results are based on the encounter between a solar-type star and a  $10^6 M_\odot$  black hole. In reality, the properties of the star and black hole undergoing a tidal encounter may differ from the fiducial parameters chosen here. However, the existence of the in-plane pancake, and the observational consequences derived therefrom, depends only on the fact that the pericenter distance be comparable to the tidal radius. In particular, if  $\beta \gg 1$ , the star will be disrupted well before reaching periapsis, while if  $\beta \ll 1$  the star will only be partially disrupted, as noted by Guillochon & Ramirez-Ruiz (2013). Interestingly, Guillochon & Ramirez-Ruiz (2013) also found that if  $0.75 \lesssim \beta \lesssim 0.85$  for a  $\gamma = 5/3$  equation of state, the star was initially completely destroyed by a  $10^6 M_\odot$  black hole; however, at a time greater than  $10^4$  seconds post-disruption, the central portion of the stream recollapsed into a single, massive core, with the outer extremities of the stream remaining as tidal tails. We suggest that the perpendicular pancake pointed out here may have contributed to this recollapse, and we plan to further investigate this possibility.

The origin of the pancake can be seen directly from equation (3.4), which shows that the gas parcels comprising the front of the star at the time of disruption are decelerating, while those at the back are accelerating; this results in the eventual merger of the in-plane edges of the stream. The differential acceleration across the star is given by equation (3.13), which shows that the magnitude of the pancake is primarily affected by the properties of the progenitor star. However, the inverse scaling with the black hole mass, although weak, implies that smaller mass black holes lead to a larger differential acceleration and, hence, stronger pancakes.

The pancake alone can augment the self-gravity to the point where the stream gravitationally fragments in the cases where  $\gamma = 1.8$  and 2, and this result is ultimately related to the fact that larger adiabatic indices result in a decreased resistance to the compression. However, a non-adiabatic equation of state could alter these results quite dramatically. In particular, any cooling would decrease the equilibrium width of the stream, enabling the pancake to leave a much more pronounced effect on the debris. The effects of a time-dependent entropy are also increased for smaller  $\gamma$ , as is apparent from equation (3.22), meaning that even streams with very low adiabatic indices could collapse if the gas-energy equation were evolved self-consistently. We plan to investigate alternative equations of state in a future paper.

## Chapter 4

### On the Structure of Tidally-disrupted Stellar Debris Streams

#### 4.1 Introduction

When a star comes within a supermassive black hole's (SMBH) tidal radius  $r_t = R_*(M_h/M_*)^{1/3}$ , where  $R_*$  is the stellar radius and  $M_h$  and  $M_*$  are the black hole and stellar masses, respectively, the tidal shear due to the hole overcomes the self-gravity of the star. The tidal force subsequently tears the star apart, with half of the torn stellar debris bound to the black hole, the other half unbound (Lacy et al., 1982; Rees, 1988).

These tidal disruption events (TDEs) have been studied analytically, numerically, and observationally for nearly forty years. The earliest analytic studies showed that the rate of return of the bound material,  $\dot{M}_{fb}$ , should scale roughly as  $\dot{M}_{fb} \propto t^{-5/3}$  at late times (Phinney, 1989), and early numerical simulations supported this scaling (Evans & Kochanek, 1989). Dozens of putative TDEs have now been discovered (e.g., Komossa & Greiner 1999; Gezari et al. 2008; Burrows et al. 2011; Cenko et al. 2012; Bogdanović et al. 2014; Miller et al. 2015; see Komossa 2015 for a review of the observational status of TDEs), and the rates at which they have been discovered show tentative agreement with early estimates of the rate at which TDEs occur ( $10^{-4} - 10^{-5}$  per galaxy per year; Frank & Rees 1976; Stone & Metzger 2014).

In Chapter 2 we demonstrated numerically that the streams of tidally-stripped debris were gravitationally unstable when the adiabatic index of the gas was set to  $\gamma = 5/3$ , resulting in their fragmentation into bound clumps. These clumps, when accreted at discrete times, caused the late-time fallback rate to fluctuate about the  $t^{-5/3}$  average (the minima being induced by the

accretion of lower-density material in between clumps). In Chapter 3 we then performed a more comprehensive numerical study of TDEs in which the pericenter distance was comparable to the tidal radius, varying the polytropic index of the gas. They found that, for stiffer equations of state ( $\gamma \gtrsim 5/3$ ), collapse was induced sooner and was enhanced by a “post-periapsis pancake” that takes place soon after the disruption.

Here we construct a model of the stream of debris produced from a TDE in an attempt to characterize its general properties. We first demonstrate the existence of a simple, self-similar solution for the radial velocity profile along the stream in Section 2, and we compare it to the results of past simulations and use it to determine the stream position as a function of radial distance and time. In Section 3 we show how the stream width varies with density and radial position and varies between its hydrostatically-equilibrated value and self-similar expansion. Section 4 provides approximate, analytic forms for the density along the stream and we compare these expressions to numerically-computed values. We analyze the rough scaling of the density with time in Section 5, and we also demonstrate that there is a critical adiabatic index at which the stream fragments, equal to  $\gamma_c = 5/3$  for an isentropic equation of state. Section 6 provides a discussion of our findings and considers the results of including other effects in our analytic treatment, and we summarize and conclude in Section 7.

## 4.2 Velocity distribution

### 4.2.1 Self-similar velocity profile

As was noted in Chapter 3, assuming that the tidal disruption takes place impulsively provides a very good approximation for the radial positions of the gas parcels from a TDE when the impact parameter of the star is  $\beta = r_t/r_p = 1$ , where  $r_p$  is the pericenter distance of the star. This impulse approximation states that the star is able to maintain hydrostatic equilibrium until it reaches the tidal radius, at which point it is “destroyed,” meaning that the self-gravity and pressure of the resultant gas become negligible at this location and for any moment in time thereafter. Therefore,

each gas parcel of the tidally-stripped debris moves solely under the influence of the gravitational field of the black hole.

When one applies the impulse approximation to the SMBHs we are considering here, the orbital eccentricities of the stream occupy a very narrow range of values centered around one. Therefore, the velocity along the stream is very nearly radial for times not long after disruption. Furthermore, as was also demonstrated in Chapter 3, the self-gravity of the stream keeps it narrowly confined in the  $\phi$  and  $\theta$  directions. As a first approximation we can thus let  $\mathbf{v}(r, \theta, \phi, t) \simeq v_r(r, t)\hat{r}$ , where  $\mathbf{v}$  is the velocity vector of the material in the stream and  $\hat{r}$  is the unit vector in the radial direction. If we further neglect the influence of pressure gradients and self-gravity in the  $r$ -momentum equation, both of which should be small in comparison to the gravitational field exerted by the hole, then the radial component of the momentum equation is

$$\frac{\partial v_r}{\partial t} + v_r \frac{\partial v_r}{\partial r} = -\frac{GM_h}{r^2}, \quad (4.1)$$

where  $M_h$  is the mass of the SMBH.

As we noted above, the eccentricities of the orbits are very nearly one for the entire stream. Furthermore, the relevant timescale at any given distance from the hole is set by the dynamical time,  $\tau_d = r^{3/2}/\sqrt{2GM_h}$ , at that radius. Therefore, a reasonable assumption for the radial velocity is that it varies self-similarly according to

$$v_r = \sqrt{\frac{2GM_h}{r}} f(\xi), \quad (4.2)$$

where

$$\xi = \frac{\sqrt{2GM_h}t}{r^{3/2}} \quad (4.3)$$

is time normalized to the dynamical time at radius  $r$ . If we insert this ansatz into equation (5.1),

we find the following self-similar equation to be solved for  $f$ :

$$f' = \frac{f^2 - 1}{2 - 3\xi f}, \quad (4.4)$$

where a prime denotes differentiation with respect to  $\xi$ .

In addition to this equation, one must also impose a boundary condition on  $f$  in order to obtain the full solution for the velocity profile. To do so, recall that the specific energies of the stream are narrowly distributed about zero and are

$$\epsilon = \frac{v_r^2}{2} - \frac{GM_h}{r} = \frac{GM_h}{r} (f^2 - 1), \quad (4.5)$$

which shows that  $f$  is narrowly distributed about 1 initially. Investigating equation (4.4), the location at which  $f = 1$  will correspond to  $f' = 0$  if  $\xi \neq 2/3$ ; however, if  $f' = 0$ , then it is easy to see by taking more derivatives of equation (4.4) that every higher derivative of  $f$  is also zero, i.e.,  $f(\xi) = 1$  is the solution if  $f' = 0$  when  $f = 1$ . Since we require the energies of the gas parcels to be distributed about, but not exactly equal to, zero, we see that the point  $f = 1$  must coincide with  $\xi = 2/3$ . Therefore, our boundary condition on  $f$  is  $f(2/3) = 1$ , which we note corresponds to a critical point in equation (4.4)<sup>1</sup>.

In further support of the fact that  $f(2/3) = 1$  is the only boundary condition that can describe the debris stream, we note that equation (4.4) can be integrated exactly to give

$$\frac{C + f\sqrt{f^2 - 1} - \ln\left(f + \sqrt{f^2 - 1}\right)}{(f^2 - 1)^{3/2}} = \xi, \quad (4.6)$$

where  $C$  is a constant of integration. This equation cannot be solved analytically to isolate  $f(\xi)$ ; however, if we set  $f = 1$ , the left-hand side of this equation is singular **unless**  $C = 0$ . The only solution for  $v_r$  that smoothly passes through marginally-bound portion of the stream must therefore have  $C = 0$ . If we adopt this value of  $C$  and use L'Hospital's rule to determine the limit of  $f \rightarrow 1$ , we find, as we expect, that  $\xi \rightarrow 2/3$ .

---

<sup>1</sup> The derivative at this point for the non-trivial solution, it can be shown, is  $f'(2/3) = -5/2$ .

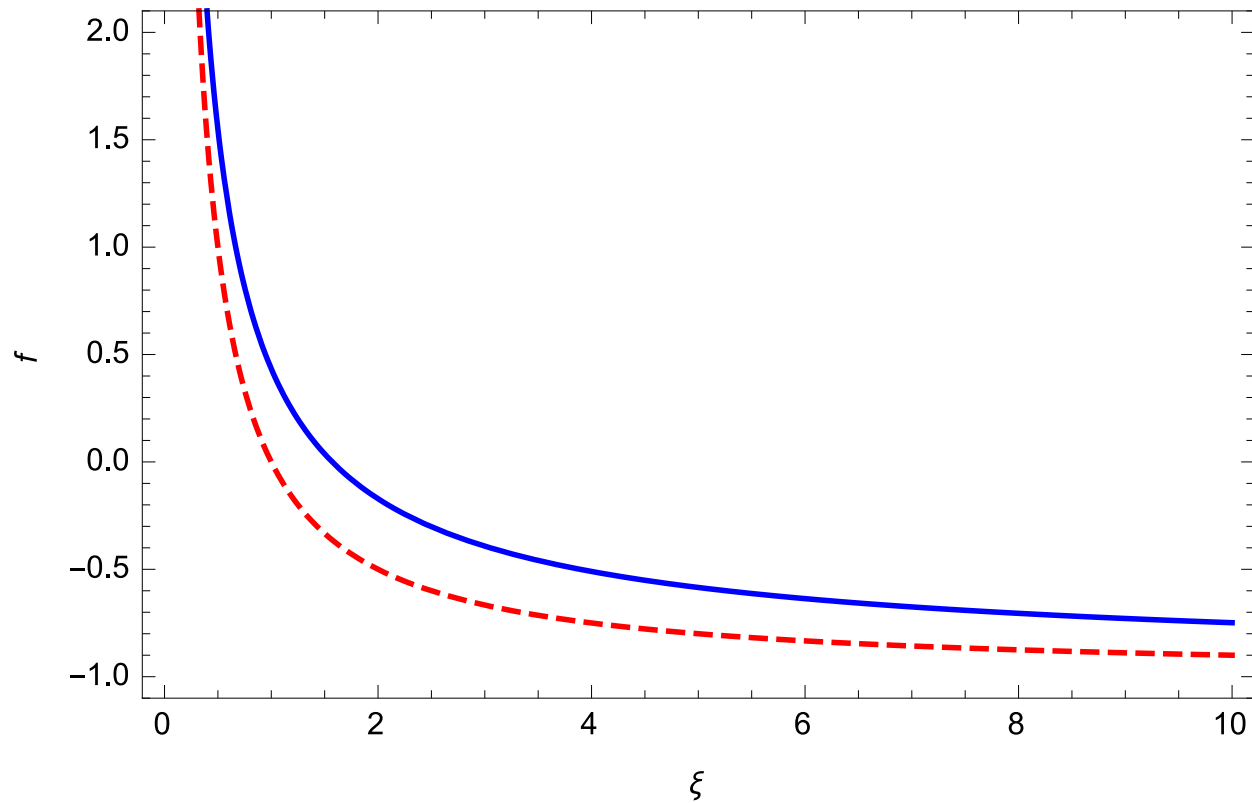


Figure 4.1: The solution to equation (4.4) passing through the critical point  $f(2/3) = 1$  (blue, solid curve). The approximate solution given by  $f = -1 + 1/\xi$ , which matches the asymptotic limits of the true solution, is shown by the red, dashed, curve.

Figure 4.1 shows this critical solution by the blue, solid curve. For contrast, the red, dashed curve shows the approximate solution  $f \simeq -1 + 1/\xi$ , which aids in seeing the asymptotic behavior of the true function.

In order to assess the validity of the self-similar solution in matching the radial velocity profile of tidally-disrupted debris streams, Figure 4.2 compares the self-similar solution for  $v_r$  (Equation 4.2) to the numerical simulation of Chapter 2. In this simulation a solar-type star (one with a solar mass and solar radius) was destroyed by a  $10^6 M_\odot$  SMBH; the pericenter distance of the stellar progenitor was equal to the tidal radius, the gas followed an adiabatic,  $\gamma = 5/3$  equation of state, and pressure and self-gravity were included at all stages of the simulation (see Chapter 2 for more details). The different curves in Figure 4.2 correspond to the stream of debris at different times, with the earliest (farthest left on the plot) being roughly two weeks after disruption, the latest (occupying the largest radial extent) at almost two years (the Figure caption gives the precise times). This Figure shows that the analytic, self-similar solution agrees extraordinarily well with the numerical solution. The inset, which is a closeup of the velocity profiles at a time of 601 days after disruption, quantifies the agreement to better than 1 part in  $10^{-4} - 10^{-5}$ .

Figure 4.3 shows the difference in velocity,  $\Delta v$ , between the numerically-obtained radial velocity profile and the analytic velocity profile, i.e.,  $\Delta v = v_n - v_{ss}$ ,  $v_n$  being the numerical solution,  $v_{ss}$  the analytic solution (equation 4.2), normalized to the speed of light. Each set of points corresponds to the time chosen in Figure 4.2. The small differences illustrated by this plot may be due to the neglect of angular momentum in the self-similar solution (see Section 6.1).

### 4.2.2 Radial positions

With the function  $f$  completely determined, the radial positions of the gas parcels comprising the stream can be found by solving the differential equation

$$\dot{r}_i = \sqrt{\frac{2GM_h}{r_i}} f(\xi_i), \quad (4.7)$$

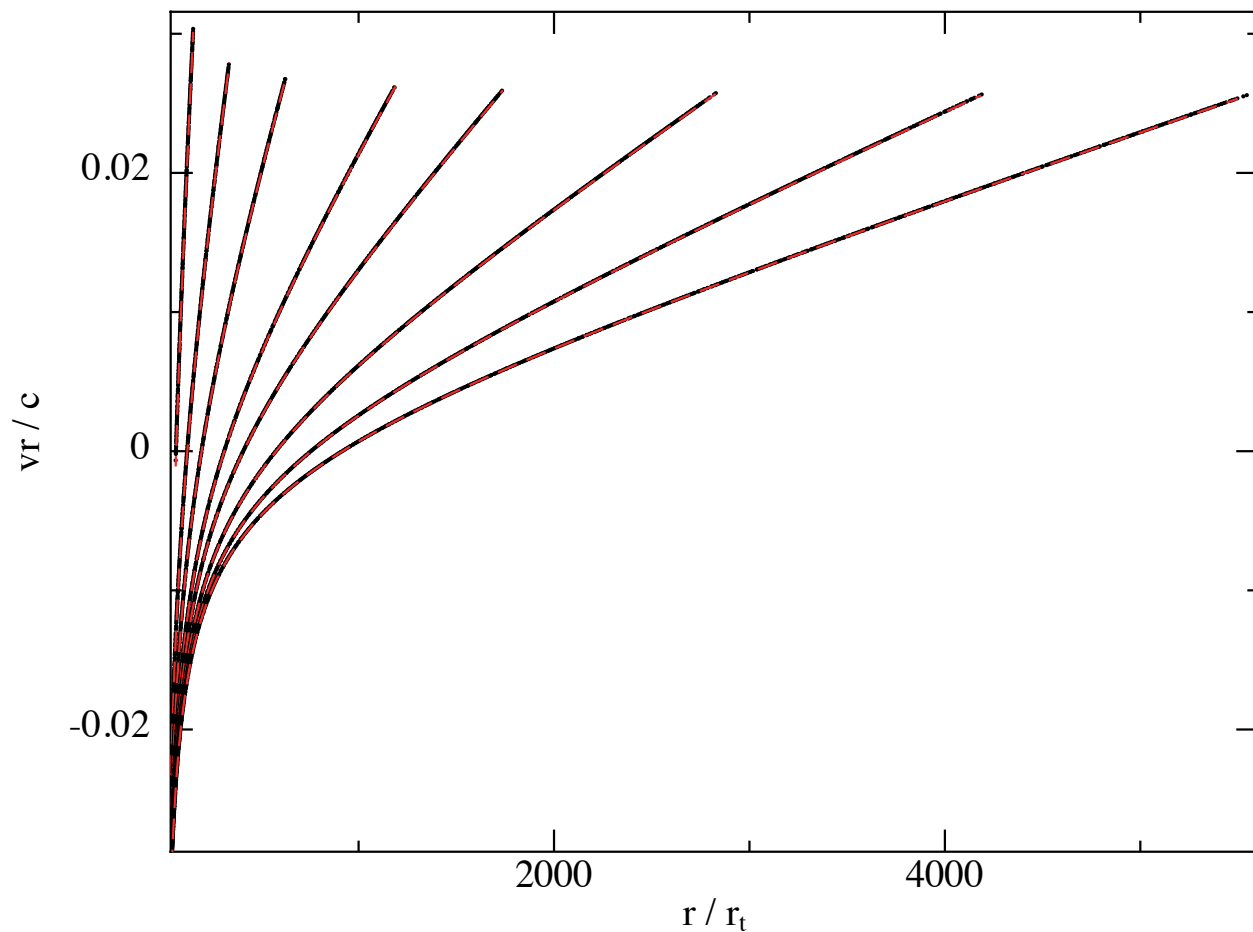


Figure 4.2: A comparison between the self-similar (red, dashed curves) and numerical (black points) radial velocity profiles, both normalized to the speed of light, for the debris stream produced by the disruption of a solar-like star by a  $10^6 M_\odot$  black hole. The numerical solution was taken from the simulation in Chapter 2. The different curves represent the stream at different times, with each curve corresponding to, from left to right, 11, 30, 60, 120, 180, 300, 451, and 601 days since disruption.

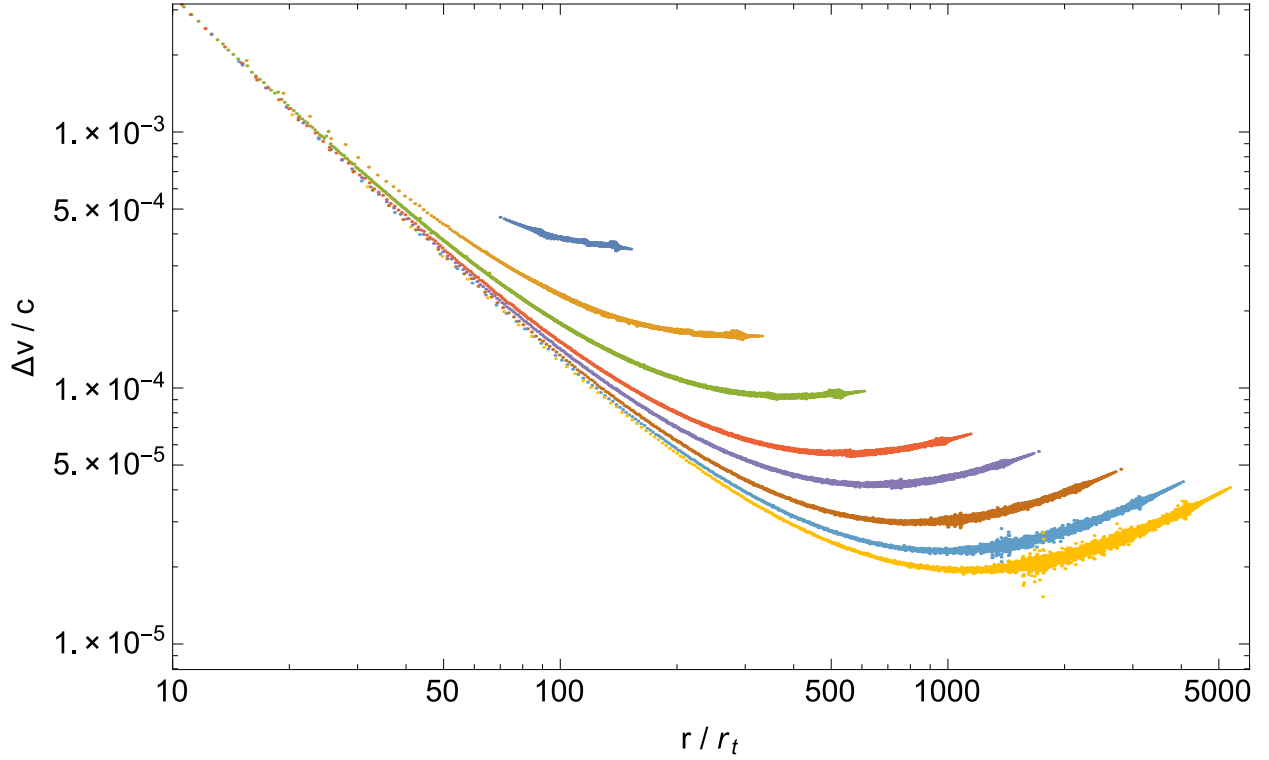


Figure 4.3: A log-log plot of the difference in velocity normalized to the speed of light, i.e.,  $\Delta v/c \equiv (v_n - v_{ss})/c$ , where  $v_n$  is the numerically-obtained radial velocity and  $v_{ss}$  is the analytic solution (equation 4.2), for the same times chosen in Figure 4.2 (i.e., the dark blue set of points is 11 days after disruption, the light yellow set of points is 601 days after disruption, and each set of points in between corresponds to the appropriate curve in Figure 4.2). As discussed in Section 6.1, the small discrepancies shown here can plausibly be attributed to the neglect of angular momentum in the self-similar solution.

where  $r_i(t)$  is the radial position of gas parcel  $i$ ,  $\xi_i = \sqrt{2GM_h t}/r_i^{3/2}$  is the self-similar variable of gas parcel  $i$ , and dots denote differentiation with respect to time.

Because  $f$  is not analytic, this equation cannot be integrated exactly to give  $r_i(t)$ . However, we note that there is an exact solution for the marginally-bound material:

$$r_m = \left( \frac{3}{2} \sqrt{2GM_h t} \right)^{2/3}. \quad (4.8)$$

As a check, differentiating this equation with respect to time gives  $\dot{r}_i = \sqrt{2GM_h/r}$ , which, from equation (4.7), demands  $f(\xi_m) = 1$ . On the other hand,  $\xi_m = \sqrt{2GM_h t}/r_m^{3/2} = 2/3$ , and since our boundary condition is  $f(2/3) = 1$ , we see that equation (4.8) does indeed solve equation (4.7).

To determine the remaining positions of the gas parcels, we will apply an argument similar to the impulse approximation: at some time  $t_m$ , the stream is closely confined to the position of the marginally-bound segment of the stream, with its radial extent equal to the diameter of the disrupted star. We will thus let

$$r_i(t_m) = r_m(t_m) + \delta r_i, \quad (4.9)$$

where  $\delta r_i = \mu_i R_* \ll r_m(t_m)$  and  $|\mu_i| < 1$ . Furthermore, we know that the tidal force of the black hole imparts a spread of energies to the debris of (Lacy et al., 1982; Rees, 1988)

$$\epsilon_i = \frac{GM_h R_*}{r_t^2} \mu_i, \quad (4.10)$$

where  $\mu_i$  is the dimensionless distance of gas parcel  $i$  from the center of mass of the star at the time of disruption. However, from equation (4.5) we have that the energies of the gas parcels at time  $t_m$  are

$$\epsilon_i = \frac{GM_h}{r_i} (f^2 - 1), \quad (4.11)$$

where the entire right-hand side is evaluated at  $t_m$ , and since the stream is narrowly confined to

the position of the marginally-bound parcel, we have

$$f \simeq 1 - \frac{5}{2} \left( \xi - \frac{2}{3} \right). \quad (4.12)$$

This equation is just a Taylor expansion of  $f$  about the point  $\xi = 2/3$ , and we used the fact that  $f'(2/3) = -5/2$  (see footnote above). We therefore have that

$$\epsilon_i = -\frac{5GM_h}{r_i} \left( \xi - \frac{2}{3} \right), \quad (4.13)$$

and using equations (4.9) and (4.10) and keeping only first order terms in  $\delta r_i$ , we find that the positions of the gas parcels satisfy

$$\delta r_i = \frac{1}{5} \frac{r_m^2}{r_t^2} R_* \mu_i. \quad (4.14)$$

Setting  $\delta r_i = \mu_i R_*$ , we see that the time at which the energies are “frozen in” corresponds to  $r_m = \sqrt{5} r_t$  in the self-similar approximation. This shows that, if we adopt our self-similar function for the velocities, we cannot impose the impulse approximation exactly, which would amount to setting the center of the star at  $r_t$  at  $t = 0$  with the radial extent of the stream equal to  $2R_*$ . This occurs because, by specifying the positions of the gas parcels at some time  $t_0$ , we automatically know their velocities via equation (4.7) and, consequently, their energies. Therefore, we do not expect that the energies will automatically correspond to the correct values (equation 4.10) by enforcing  $r_i(t_0) = r_t + \mu_i R_*$ , and indeed we see that we must have  $r_i(t_0) = \sqrt{5} r_t + \mu_i R_*$  to correctly match the energies.

With the initial conditions  $r_i = r_m(t_m) + \mu_i R_*$ ,  $r_m(t_m) = \sqrt{5} r_t$ , and  $t_m$  given by equation (4.8) with  $r_m = \sqrt{5} r_t$ , we can numerically integrate equation (4.7) to solve for the positions of the gas parcels as a function of time. However, we can obtain an approximate expression for the initial evolution of the debris stream by letting

$$r(\mu, t) \simeq r_m(t) + \mu r_1(t) + \mathcal{O}(\mu^2), \quad (4.15)$$

where we have let  $\mu_i \rightarrow \mu$  become a continuous variable and  $r_1$  is a small correction (on the order of  $R_*/r_t$ ) to the marginally-bound orbit  $r_m(t)$  (note that this is just a Taylor expansion of  $r(\mu, t)$  about  $\mu$ , truncated at first order). If we now insert equation (4.15) into equation (4.7), use equation (4.12) for the function  $f$ , and keep only terms to first order in  $\mu r_1$ , performing a bit of algebra reveals that

$$\frac{\dot{r}_1}{r_1} = \frac{4}{3t}. \quad (4.16)$$

This shows that the correction to the positions of the material from the marginally-bound orbit, during the initial evolution of the debris stream, scales as  $r_1 \propto t^{4/3}$ . Using this expression for  $r_1$  in equation (4.15), this also shows that

$$\left. \frac{\partial r}{\partial \mu} \right|_{\mu=0} = r_1(t) \propto t^{4/3}. \quad (4.17)$$

Note that this result is exact, as all of the higher-order  $\mu$  corrections are zero at  $\mu = 0$ . We will use this result in Section 3.2.

Finally, while equation (4.15) is useful for the early evolution of the debris, it breaks down once the orbits of the material start to deviate from  $r_i \propto t^{2/3}$ . We can obtain an approximate expression for the positions of the gas parcels, one that is roughly valid over the whole stream, by recalling that the function  $f$  is reasonably well-approximated by the function

$$f \simeq -1 + \frac{1}{\xi}, \quad (4.18)$$

as depicted in Figure 4.1. If we use this approximate form for  $f$ , then we can show that equation (4.7) can be solved for  $r_i(t)$  to give

$$r_i(t) = \left( 3\sqrt{2GM_h t} + A_i t^{3/2} \right)^{2/3}, \quad (4.19)$$

where  $A_i$  is a constant of integration particular to gas parcel  $i$ . We can determine these constants by, as above, requiring that the length of the stream is narrowly confined, initially, about the

marginally-bound position, i.e.,  $r_i(t_m) = r_m(t_m) + \delta r_i$ , with  $\delta r_i = \mu_i R_*$ . Doing so gives

$$A_i = \frac{9\sqrt{3}}{2} \frac{(2GM_h)^{3/4} R_*}{r_m^{7/4}} \mu_i. \quad (4.20)$$

Unfortunately, the value of  $r_m$  cannot be determined by requiring that the energies match those from the impulse approximation; this is because the marginally-bound orbit from equation (4.19) – where  $r \propto t^{2/3}$  – occurs at  $\xi = 1/3$ , while from equations (4.5) and (4.12) it occurs where  $\xi = 1/2$ . This discrepancy means that the energies do not correlate with the properties of the orbits, and arises ultimately from the fact that the boundary condition  $f(2/3) = 1$  is not satisfied by equation (4.18). Therefore, in this case we will simply let  $r_m = \sqrt{5}r_t$  – the same value found above when the correct form of  $f$  is used – and note that the positions of the gas parcels from equation (4.19) will differ from the true values because of the erroneous energies. We thus find that the approximate positions of the gas parcels are

$$r_i(t) = \left( 3\sqrt{2GM_h t} + \chi\mu_i t^{3/2} \right)^{2/3}, \quad (4.21)$$

where we defined

$$\chi \equiv \frac{9\sqrt{3}}{2} \frac{(2GM_h)^{3/4} R_*}{r_m^{7/4}}. \quad (4.22)$$

### 4.3 Stream width

The previous section exploited the fact that, to a very good approximation, the radial positions of the gas parcels can be found by considering them as non-interacting test particles in the gravitational field of the hole. However, this will not necessarily be the case for the transverse structure of the stream, as self-gravity and pressure can be important at both early and late times (Kochanek 1994, Chapters 2 and 3). If we account for self-gravity and pressure, the transverse

momentum equation becomes

$$\frac{\partial v_s}{\partial t} + v_r \frac{\partial v_s}{\partial r} + v_s \frac{\partial v_s}{\partial s} + \frac{1}{\rho} \frac{\partial p}{\partial s} = g_{sg} + g_{M,\perp}, \quad (4.23)$$

where  $s$  is the cylindrical distance from the stream center,  $v_s$  is the velocity in the  $s$ -direction,  $g_{sg}$  is the force due to self-gravity in the  $s$  direction, and  $g_{M,\perp}$  is the gravitational force arising from the black hole in the  $s$ -direction. Poisson's equation can be written

$$\nabla \cdot \mathbf{g}_{sg} = -4\pi G\rho. \quad (4.24)$$

If we assume that the radial dependence of  $g_{sg}$  is small in comparison with its  $s$ -dependence, which should be a good approximation owing to the degree of symmetry of the stream about its center of mass and breaks down only near its radial extremities, then this equation can be integrated using Gauss' law to give

$$g_{sg} \simeq -2\pi G\rho s. \quad (4.25)$$

The perpendicular component of the gravitational field of the hole can also be written down as

$$g_{M,\perp} \simeq -\frac{GM_h s}{r^3}. \quad (4.26)$$

Substituting these equations into equation (4.23) then gives

$$\frac{\partial v_s}{\partial t} + v_r \frac{\partial v_s}{\partial r} + v_s \frac{\partial v_s}{\partial s} + \frac{1}{\rho} \frac{\partial p}{\partial s} = -2\pi G\rho s - \frac{GM_h s}{r^3}. \quad (4.27)$$

### 4.3.1 Quasi-hydrostatic width

During the early evolution of the debris, the pressure and self-gravity of the material are high enough that the stream remains approximately in gravitational equilibrium in the transverse direction (approximately because the density is evolving with time and the planar motions can

cause the stream to be slightly over-pressured, resulting in oscillations; Chapter 3). In this limit we can balance the pressure and self-gravity terms in equation (4.27), which gives

$$H_{eq}^2 \simeq \frac{p}{2\pi\rho^2G}, \quad (4.28)$$

Here we will assume that the pressure varies as

$$p = S(r, t)\rho^\gamma, \quad (4.29)$$

where  $S(r, t)$  is related to the entropy of the gas. A perfect polytrope is obtained by setting  $S(r, t)$  to a constant; however, the stream of debris will cool radiatively as it evolves, and will do so increasingly as the material becomes optically thin to the radiation released during recombinations. Also, recombinations can heat the gas when it is still optically thick (Kasen & Ramirez-Ruiz, 2010), and shocks can likewise serve to heat the material if the star is on a deeply-plunging orbit. To model these thermodynamic aspects of the problem, we will therefore permit  $S(r, t)$  to be a function of  $r$  and  $t$  that could, in principle, be determined from the gas energy equation if all of the effects controlling the internal energy of the gas were known. The equilibrium width is thus

$$H_{eq}^2 = \frac{S\rho^{\gamma-2}}{2\pi G}, \quad (4.30)$$

which is the same scaling that we found in Chapter 3.

### 4.3.2 Shear dominated

Depending on the adiabatic index of the gas or the amount of heating and cooling, the density will fall off at such a rate that the tidal shear term on the right-hand side of equation (4.27) will overcome the self-gravity (Chapter 3). The pressure gradient will also be insufficient to balance the tidal compression when this happens, meaning that the advective terms on the left-hand side

of equation (4.27) must become non-negligible. In this limit equation (4.27) becomes

$$\frac{\partial v_s}{\partial t} + v_r \frac{\partial v_s}{\partial r} + v_s \frac{\partial v_s}{\partial s} = -\frac{GM_h s}{r^3}. \quad (4.31)$$

We expect that the solution for  $v_s$  will again scale self-similarly, as the dynamical time is the only relevant timescale and only the gravitational field of the hole serves to alter the velocity  $v_s$ . We find that indeed there is a self-similar solution, and it is given by

$$v_s = \frac{s}{r} \sqrt{\frac{2GM_h}{r}} f(\xi), \quad (4.32)$$

where  $f(\xi)$  is the same function that appears in the distribution of the radial velocity. Since  $v_s = ds_i/dt$ , where  $s_i$  is the transverse position of gas parcel  $i$ , and  $\sqrt{2GM_h/r} f(\xi) = dr_i/dt$ , we find that the transverse extent of the stream evolves as

$$H_i(t) = \frac{H_{i,0}}{r_{i,0}} r_i(t), \quad (4.33)$$

where  $H_{i,0}$  is the width of the stream at time  $t_0$ . When the stream is dominated by the tidal shear of the hole, this equation shows that the width of the stream simply scales in proportion to its radial position and the entire evolution proceeds self-similarly.

### 4.3.3 Approximate, full solution

The above two restricted solutions demonstrate that, when the self-gravity of the stream dominates over the tidal shear of the black hole, the width of the stream is set by hydrostatic balance. On the other hand, when the tidal force of the black hole overwhelms self-gravity,  $H \propto r$  and the entire stream evolves self-similarly.

Along the full radial extent of the debris, the extremities will typically be shear-dominated, while the density in the central region is high enough to dominate over the shear of the hole (Kochanek 1994, Chapter 3). We therefore expect the scaling of  $H$  to vary between the self-gravity dominated limit and the shear-dominated limit as we traverse the extent of the stream. In between

those two limits, both the shear terms and the self-gravity terms are important in equation (4.27), and as a result we do not expect a simple solution for the velocity  $v_s$ .

We can, however, obtain an approximate solution that interpolates between the self-gravity and shear-dominated extremes by simply letting  $H$  be piece-wise defined about the point where  $2\pi\rho = M_h/r^3$ . We thus have

$$H^2 = \begin{cases} \frac{S\rho^{\gamma-2}}{2\pi G} & \text{for } 2\pi\rho \geq \frac{M_h}{r^3} \\ \frac{H_0^2}{r_0^2} r^2 & \text{for } 2\pi\rho \leq \frac{M_h}{r^3} \end{cases} . \quad (4.34)$$

To ensure the continuity of the solution,  $H_0$  and  $r_0$  are given by the self-gravitating solution where  $2\pi\rho = M_h/r^3$ . In the next section we will see how  $\rho$  is related to  $H$ .

#### 4.4 Density

In addition to knowing the geometry of the stream, we would also like to be able to infer its density. To do so, we note that the mass contained in some segment of the stream is

$$M = \int_{V(t)} \rho(V, t) dV, \quad (4.35)$$

where  $V(t)$  is the volume of the stream segment that is, in general, time-dependent. The total mass contained in the segment is, however, time-independent, so the differential equation to be solved for  $\rho$  is

$$\frac{d}{dt} \left( \int_{V(t)} \rho(V, t) dV \right) = 0. \quad (4.36)$$

When the limits of integration in this equation are functions of time, using the fundamental theorem of calculus results in the continuity equation. However, if we can transform to a specific set of coordinates in which the volume element is time-**independent**, then the resulting equation can be immediately inverted to solve for  $\rho$ . In particular, if we write the new set of coordinates

collectively as  $T$ , then the equation for  $\rho$  is simply

$$\rho \frac{\partial V}{\partial T} = \frac{\partial M}{\partial T}, \quad (4.37)$$

where  $\partial V/\partial T$  is the Jacobian of the transformation between the physical ( $V$ ) and time-independent ( $T$ ) coordinates. Here  $\partial M/\partial T$  is the differential amount of mass contained in the volume element  $dT$ .

We can achieve the transformation  $V \rightarrow T$  by choosing our physical coordinates as  $(r, s, \varphi)$ , where  $r$  is the radial position of the center of the stream,  $s$  is cylindrical distance measured perpendicular from  $r$ , and  $\varphi$  is the angle swept out by  $s$  as it revolves around  $r$ . In terms of these coordinates, the mass contained in any segment of the stream is

$$M = \int \rho s ds d\phi dr. \quad (4.38)$$

If we further define the  $H$ -averaged density as

$$\pi H^2 \bar{\rho} \equiv \int \rho s ds d\phi, \quad (4.39)$$

then the mass is given by

$$M = \pi \int_{r_0(t)}^{r_1(t)} H^2 \rho dr, \quad (4.40)$$

where we dropped the bar for ease of notation. By now transforming from  $r \rightarrow \mu$ , where  $\mu$  is the dimensionless original position of the stream, we find (see also equation 2 of Chapter 2)

$$\pi H^2 \rho \frac{\partial r}{\partial \mu} = \frac{\partial M}{\partial \mu}. \quad (4.41)$$

In order to make more progress with this equation, we must determine the quantities  $H(\rho, r)$ ,  $\partial r/\partial \mu$  and  $\partial M/\partial \mu$ . As we saw in the previous section,  $H$  depends on  $\rho$  and  $r$  in a non-trivial way, and will behave differently depending on whether the stream is shear dominated or self-gravity dominated. However, we noted that a full, approximate solution can be obtained by assuming that

$H$  switches between its hydrostatic equilibrium value and self-similar expansion at the point where  $2\pi\rho = M_h/r^3$ , which gives equation (4.34) for  $H$ .

The most rigorous way of calculating  $\partial r/\partial\mu$  is to do so numerically, i.e., calculate the positions of the gas parcels comprising the stream,  $r(\mu, t)$ , via equation (4.7) for a large number of  $\mu$  and  $t$ , and at a specific time  $t$  interpolate over all of the  $\mu$  to determine  $\partial r/\partial\mu$ . However, we can also use equation (4.21), which gives an approximate solution for the positions of the gas parcels as functions of  $\mu$  and  $t$ , to obtain an analytic expression. Doing so gives

$$\frac{\partial r}{\partial\mu} = \frac{2}{3}\chi t^{3/2}r^{-1/2}, \quad (4.42)$$

which we note is approximately valid over the entire extent of the stream (this expression, however, gives  $\partial r/\partial\mu|_{\mu=0} \propto t^{7/6}$ , in contrast to the exact value of  $\partial r/\partial\mu|_{\mu=0} \propto t^{4/3}$ ).

Finally, the function  $\partial M/\partial\mu$  can be determined by using the impulse approximation and considering the star at the time of disruption. This assumption then gives (see Lodato et al. (2009), Chapter 3 and Chapter 5 for details)

$$\frac{\partial M}{\partial\mu} = \frac{1}{2}M_*\xi_1 \frac{\int_{|\mu|\xi_1}^{\xi_1} \Theta(\xi)^n \xi d\xi}{\int_0^{\xi_1} \Theta(\xi)^n \xi^2 d\xi}, \quad (4.43)$$

where  $\Theta(\xi)$  is the solution to the Lane-Emden equation and  $\xi$  is the dimensionless radius of the polytrope (Hansen et al., 2004). A slight difficulty arises from the fact that, if the energies of the gas parcels using our self-similar prescription are to match those from the true impulse approximation (the one that accounts for the finite angular momentum of the material), then the “time of disruption” – the point at which the energies are frozen in – corresponds to when the marginally-bound segment of the stream is at a distance of  $r_m = \sqrt{5}r_t$ , not at  $r_t$  (see Section 2.2). This means that using equation (4.43) with the self-similar solution will overestimate the density, as we expect that the stream will have stretched by some factor by the time it reaches the distance  $\sqrt{5}r_t$  and correspondingly decreased the density.

Since the functions  $\Theta(\xi)$  are only analytic for a select few values of  $n$ , equation (4.43) cannot,

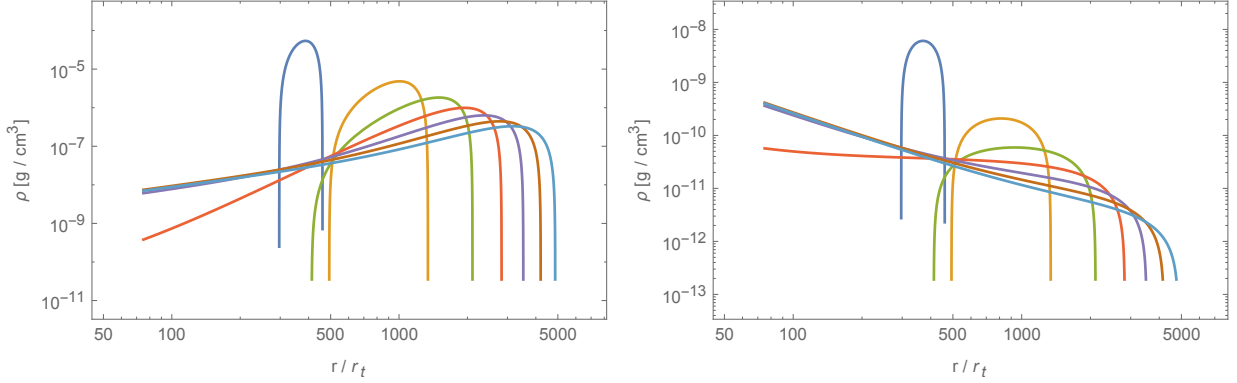


Figure 4.4: The analytic solution for the density when self-gravity dominates the shear of the black hole (equation 4.45), shown in the left panel, and when the shear dominates the self-gravity of the stream (equation 4.46), shown in the right panel, as functions of  $r$  for the disruption of a solar-like star by a  $10^6 M_\odot$  SMBH. We assumed isentropic gas with  $\gamma = 5/3$  and entropy calculated for solar-like parameters ( $S = 2.48 \times 10^{14}$  [cgs]; Hansen et al. 2004). The different colors correspond to different times, with the earliest time being  $2500 \times r_t^{3/2} / \sqrt{2GM_h} \simeq 32$  days after disruption (left-most, dark blue curve), the latest being  $47500 \times r_t^{3/2} / \sqrt{2GM_h} \simeq 620$  days after disruption (right-most, light blue curve), and each curve differing from the previous one by  $7500 \times r_t^{3/2} / \sqrt{2GM_h} \simeq 98$  days.

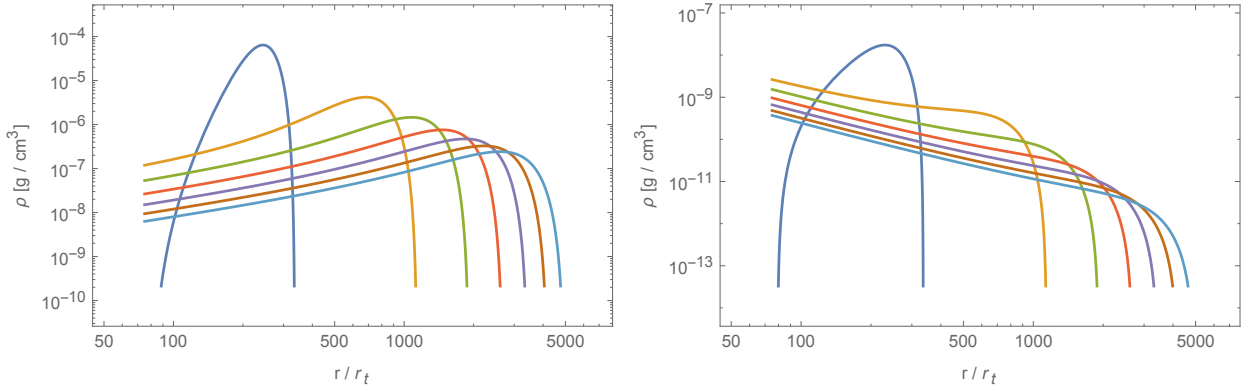


Figure 4.5: The numerical solution for the density when self-gravity dominates the shear of the black hole (the solution to equation 4.41 with  $H$  given by equation (4.30),  $\partial r / \partial \mu$  calculated numerically, and  $\partial M / \partial \mu$  calculated numerically from equation (4.43) with  $n = 1.5$ ), shown in the left panel, and when the shear dominates the self-gravity of the stream (the solution to equation 4.41 with  $H$  given by equation (4.33),  $\partial r / \partial \mu$  calculated numerically, and  $\partial M / \partial \mu$  calculated numerically from equation (4.43) with  $n = 1.5$ ), for the same parameters and times chosen in Figure 5.3.

in general, be simplified further. However, we can obtain an approximate solution by letting  $\Theta(\xi) \simeq 1$ , which is valid in the inner regions of all polytropes. We can therefore write

$$\frac{\partial M}{\partial \mu} \simeq \frac{3}{4} M_* (1 - \mu^2). \quad (4.44)$$

Because  $H$  switches between its equilibrium value and self-similar expansion along the length of the stream, equation (4.41), even with the approximate, analytic expressions for  $\partial r / \partial \mu$  and  $\partial M / \partial \mu$ , cannot be rearranged to write  $\rho$  in closed-form over the entire extent of the stream. However, in the limit that self-gravity or the tidal shear dominates, we can solve the equation exactly. Inserting equations (4.42) and (4.44) into equation (4.41) and inverting the function (4.19) to solve for  $\mu(r, t)$ , we find that these limits correspond to

$$\rho_{sg}^{\gamma-1} = B_{sg} \frac{r^{1/2}}{t^{3/2}} \left( 1 - \frac{r^3}{\chi^2 t^3} \left( 1 - \frac{3\sqrt{2GM_h t}}{r^{3/2}} \right)^2 \right) \quad (4.45)$$

$$\rho_{sh} = B_{sh} \frac{r^{-3/2}}{t^{3/2}} \left( 1 - \frac{r^3}{\chi^2 t^3} \left( 1 - \frac{3\sqrt{2GM_h t}}{r^{3/2}} \right)^2 \right) \quad (4.46)$$

where  $\rho_{sg}$  and  $\rho_{sh}$  refer to the density in the self-gravity and shear-dominated cases, respectively, and for compactness we defined

$$B_{sg} \equiv \frac{9GM_*}{4S\chi} \quad (4.47)$$

and

$$B_{sh} = \frac{45M_*}{8\pi\chi} \left( \frac{M_h}{M_*} \right)^{2/3}. \quad (4.48)$$

For the shear-dominated solution, we let  $H_0 = R_*$  when  $r = \sqrt{5}r_t$ , which is consistent with the impulse approximation under our self-similar prescription as we saw in Section 2.2.

Figure 5.3 shows these two solutions, the left panel the self-gravity dominated case, the right panel being shear dominated, when  $M_h = 10^6 M_\odot$ ,  $R_* = 1R_\odot$ ,  $M_* = 1M_\odot$ ,  $\gamma = 5/3$ , and the gas is isentropic with  $S = 2.48 \times 10^{14}$  [cgs], which is the value appropriate for a sun-like star (Hansen

et al., 2004). The different colors correspond to different times since disruption, with the earliest time being  $2500 \times r_t^{3/2}/\sqrt{2GM_h} \simeq 32$  days after disruption (left-most, dark blue curve), the latest being  $47500 \times r_t^{3/2}/\sqrt{2GM_h} \simeq 620$  days after disruption (right-most, light blue curve), and each curve differing from the previous one by  $7500 \times r_t^{3/2}/\sqrt{2GM_h} \simeq 98$  days. We see that the density structure differs substantially between the two analytic cases, retaining an “inverted” profile when the stream is self-gravitating (the density increases as a function of  $r$ ), but quickly assuming a density profile that decreases monotonically for the shear-dominated case.

Figure 4.5 shows the numerical solution to equation (4.41) when self-gravity dominates (left-hand panel) and when shear dominates (right-hand panel). For these solutions, we calculated  $\partial r/\partial\mu$  directly by numerically integrating equation (4.7) for a large number of  $\mu$  (20000 points) and  $t$ ,  $\partial M/\partial\mu$  was computed numerically from equation (4.43) with  $n = 1.5$  ( $\gamma = 5/3$ ), and the physical parameters were the same as those in Figure 5.3. We see that the positions of the gas parcels disagree between the analytic solutions – equations (4.45) and (4.46) – and the numerical solutions that used the exact, directly computed forms for  $\partial r/\partial\mu$  and  $\partial M/\partial\mu$  (compare for example the locations at which the density of the bound material goes to zero between the left-hand panels of Figures 5.3 and 4.5). In particular, the return time of the most bound material is vastly overestimated because of the incorrect scaling of the energies in the analytic case. However, the overall scaling of the density with  $r$  is upheld.

The solution that adopts a piecewise-continuous form for  $H$  (equation 4.34) is shown in Figure 4.6. The different curves correspond to the solution at the same times as Figures 5.3 and 4.5, and the dashed line shows the curve  $M_h/(2\pi r^3)$ . We see that these solutions possess properties of both the left and right-hand panels of Figure 4.5: when the stream is self-gravity dominated, the density retains an inverted profile and increases as we move outward in specific energy. However, when the bound material nears the black hole and becomes shear-dominated, the tidal compression serves to decrease the stream width and produces an “up-turn” in the density profile as we approach the hole.

Interestingly, the density profile of the simulation in Chapter 2 does not exhibit this up-turn

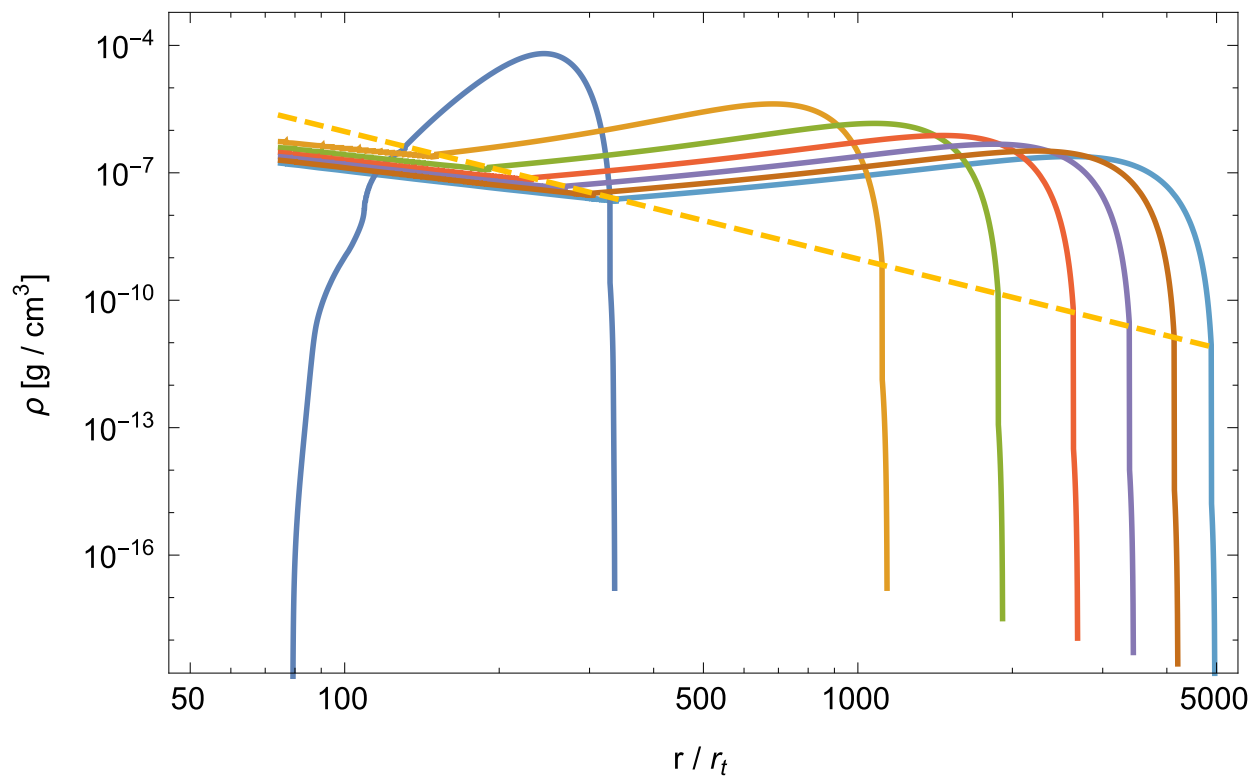


Figure 4.6: The numerical solution for the density that adopts the piecewise behavior for  $H$  (equation 4.34) so that the density is shear dominated in regions where  $\rho < M_h/(2\pi r^3)$  and self-gravity dominated where  $\rho > M_h/(2\pi r^3)$ , for the same parameters and times chosen in Figure 5.3. The yellow, dashed line shows the curve  $M_h/(2\pi r^3)$ .

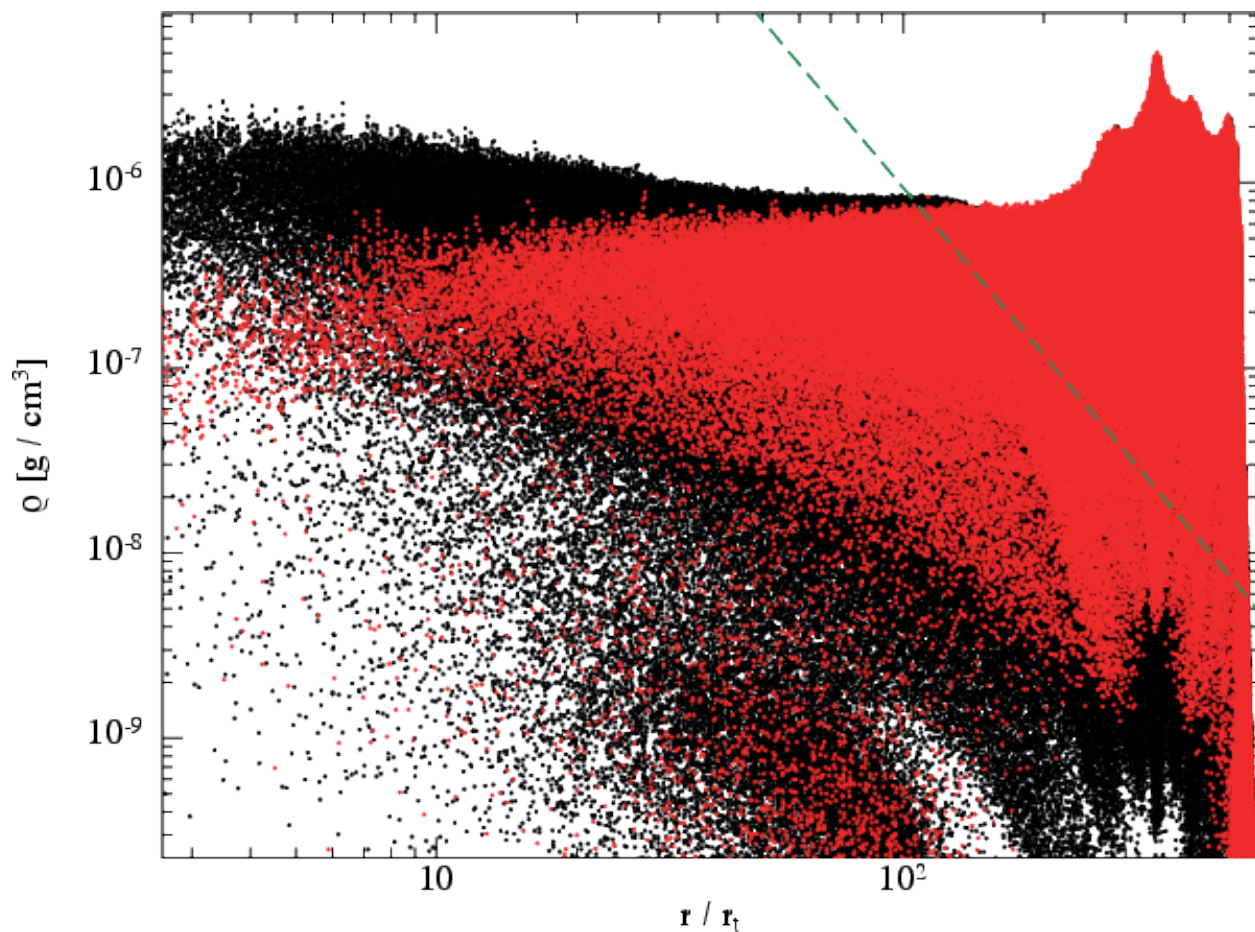


Figure 4.7: A particle plot of the density in the stream  $\rho$  in units of  $\text{g} / \text{cm}^3$  as a function of  $r$  in tidal radii at a time of 57 days post-disruption. The red points are from the simulation used in Chapter 2, the black points are from an identical simulation but with  $10^7$ , as opposed to  $10^6$ , particles, and the green, dashed curve shows the function  $M_h / (2\pi r^3)$  – the approximate dividing line between the shear and self-gravity dominated solutions.

in the density as the material approaches the black hole. This anomalous behavior is demonstrated by the red points in Figure 4.7, which is a particle plot of density versus  $r$  from the simulation in Chapter 2. The black points in this Figure, on the other hand, are from a simulation that is identical to that from Chapter 2 except that, instead of  $10^6$  particles,  $10^7$  SPH particles were used. The green, dashed line shows the curve  $M_h/(2\pi r^3)$ . The fact that the black points show the upturn in the density as we approach the black hole, consistent with what we expect from the analytic arguments presented here, shows that the disagreement between the simulation in Chapter 2 and our predictions arises from the resolution of the simulation. Since the increase in the density arises from the tidal compression exerted by the black hole, which results from the differential gravitational force acting across the diameter of the stream, we see that the width of the incoming debris stream is underresolved when only  $10^6$  particles are used.

## 4.5 Density scalings and fragmentation conditions

The most accurate way of determining how the density of the stellar debris stream produced from a TDE varies with  $r$  and  $t$  is to solve equation (4.41) numerically. However, this direct way doesn't yield an obvious trend for how the density roughly scales with distance and time. Even from equations (4.45) and (4.46), which give approximate expressions for  $\rho$  in the self-gravity and shear-dominated limits, respectively, it is not overly apparent how the density qualitatively behaves as the stream recedes from the black hole. We can, however, discern how certain **parts** of the stream behave by returning to equation (4.41) and focusing only on specific energy, or specific  $\mu$ , ranges.

### 4.5.1 Marginally bound material

Recall that the marginally-bound segment of the stream corresponds to  $\mu = 0$ , follows  $r \propto t^{2/3}$ , and, from Section 2.2, satisfies  $\partial r/\partial \mu \propto t^{4/3}$ . Returning to equation (4.41), we thus find

$$H^2 \rho_m \propto t^{-4/3}, \quad (4.49)$$

where  $\rho_m$  refers to the density at the marginally-bound part of the stream. If we now assume that the stream is self-gravity dominated, then using equation (4.30) for  $H$  shows

$$\rho_m \propto S^{-\frac{1}{\gamma-1}} t^{-\frac{4}{3(\gamma-1)}}. \quad (4.50)$$

If we now assume that the gas is isentropic, then, for adiabatic indices of  $\gamma = 1.5, 5/3, 1.8,$  and  $2,$  we find that  $\rho_m \propto t^{-8/3}, t^{-2}, t^{-5/3},$  and  $t^{-4/3},$  respectively, which is in good agreement with the scalings found in Chapter 3.

Equation (4.50) holds when the self-gravity of the debris dominates over the tidal field of the hole; however, if the density of the debris falls off at a rate steeper than  $t^{-2},$  then even if it starts out as being self-gravitating, the tidal shear of the black hole will eventually dominate the self-gravity of the debris. As we saw above, the critical  $\gamma$  at which self-gravity and the tidal field of the hole balance one another at the marginally-bound portion of the stream, which we will denote  $\gamma_{c,m},$  is given by

$$\gamma_{c,m} = \frac{5}{3}. \quad (4.51)$$

When the tidal shear dominates the self-gravity of the stream, the ability of the debris to collapse locally and fragment is seriously hindered. Therefore, we expect  $\gamma_{c,m}$  to represent the critical adiabatic index at which fragmentation is marginally possible: for  $\gamma > \gamma_{c,m},$  the stream can fragment, while for  $\gamma < \gamma_{c,m},$  the stream is stable to fragmentation. This interpretation is supported by the results of Chapter 3, where we found that the stream fragmented vigorously for  $\gamma = 1.8$  and  $2,$  fragmented at late times and due to numerical noise for  $\gamma = 5/3,$  and did not exhibit any fragmentation for  $\gamma = 1.5$  (see also Section 6 for a further discussion of this point).

When the tidal shear of the black hole dominates the stream self-gravity, then using the fact that  $H^2 \propto r^2$  shows that the isentropic density scales as

$$\rho_m \propto t^{-8/3}. \quad (4.52)$$

This demonstrates that the density of the stream will not necessarily fall off as a single power-law throughout its entire evolution. For example, if the stream starts out self-gravitating and has an adiabatic index of  $\gamma = 1.5$ , then it will initially follow  $\rho_m \propto t^{-2.66}$  before eventually transitioning to the shallower power-law  $\rho_m \propto t^{-2.22}$ .

If we let the entropy scale as  $S \propto t^{-p}$ , which provides some insight into the ability of heating and cooling to affect the evolution of the stream density, then it is simple to show that the critical adiabatic index along the marginally-bound portion of the stream becomes

$$\gamma_{c,m} = \frac{5}{3} - \frac{p}{2}. \quad (4.53)$$

This illustrates that cooling does not need to be very efficient to significantly alter the fragmentation properties of the stream. Alternatively, if shocks play a significant role in heating the gas, then the ability of the stream to fragment will be correspondingly diminished. On the other hand, once the gas temperature drops to about  $10^4\text{K}$ , the gas can start to recombine and heat the debris, stalling its temperature at  $10^4\text{K}$  and resulting in an adiabatic index of order unity. However, once the neutral fraction becomes significant, the optical depth decreases dramatically and recombinations will serve to cool the gas, corresponding to a larger effective  $\gamma$  (Kasen & Ramirez-Ruiz, 2010).

#### 4.5.2 Unbound material

For the material in the unbound portion of the stream, the gas parcels follow  $r \propto t^{2/3}$  initially, but eventually transition to  $r \propto t$ . We therefore have  $\partial r / \partial \mu \propto t$  when the material recedes to large distances from the hole, and we find that equation (4.41) becomes

$$H^2 \rho_u \propto t^{-1}, \quad (4.54)$$

where  $\rho_u$  refers to the density in the unbound portion of the stream. If we now focus on the self-gravity dominated limit, using equation (4.30) shows

$$\rho_u \propto t^{-1/(\gamma-1)}. \quad (4.55)$$

From this expression we see that the density of the unbound material falls off at a **shallower** rate than the marginally-bound debris. Specifically, for  $\gamma = 5/3$  we find  $\rho_u \propto t^{-3/2}$  as compared to  $\rho_{mb} \propto t^{-2}$ . Furthermore, since the density of the black hole falls off as  $M_h \propto t^{-3}$  for the unbound debris as opposed to  $M_h \propto t^{-2}$  for the marginally-bound debris, the critical adiabatic index at which the black hole density equals the stream density is correspondingly smaller. In particular, if we set  $\rho_u \propto t^{-3}$ , we find that the critical adiabatic index in the unbound portion of the stream is  $\gamma_{c,u} = 4/3$ .

When the tidal shear of the hole dominates the self-gravity, using equation (4.33) in equation (4.54) gives

$$\rho_u \propto t^{-3}. \quad (4.56)$$

As was true for the marginally-bound case, this shows that the density of the unbound material will not necessarily fall off as a single power-law throughout its evolution if it passes from being self-gravity to being shear-dominated.

Furthermore, because the energies of the debris are greater than zero by only a small amount, the initial evolution of even the unbound debris will still follow approximately  $r_u \propto t^{2/3}$ , and only at some time  $t_{tr}$  will the orbits transition to  $r_u \propto t$ . If we rewrite equation (4.15) as

$$r(\mu, t) \simeq \left( \frac{3}{2} \sqrt{2GM_h t} \right)^{2/3} + \frac{R_* \mu}{t_m^{4/3}} t^{4/3}, \quad (4.57)$$

where the second term in this equation comes from equation (4.16) with the requirement that

$r_i(t_m) = r_m(t_m) + \mu_i R_*$ , then we see that the time at which this transition occurs is approximately

$$t_{tr} \simeq \frac{5\sqrt{5}}{3} \frac{q}{\mu^{3/2}} \frac{R_*^{3/2}}{\sqrt{2GM_h}}. \quad (4.58)$$

Thus, if the unbound stream is self-gravitating, then at  $t_{tr}$  we expect the density to transition from  $\rho_u \propto t^{-2}$  to  $\rho_u \propto t^{-1.5}$ . Equivalently, if we are following an unbound fluid parcel with a narrow range of specific energies, then we expect the density to transition from  $\rho_u \propto r^{-3}$  to  $\rho_u \propto r^{-1.5}$  at this time. For the disruption of a solar-type star by a  $10^6 M_\odot$  SMBH, this time corresponds to  $t_{tr} \simeq 48$  days post-disruption.

### 4.5.3 Bound material and overall scalings

The above two subsections show that the marginally-bound and unbound material behave quite differently in terms of their asymptotic scalings. As was true for the unbound material, the initial evolution of the bound material will follow approximately  $r_b \propto t^{2/3}$  because the specific energies, while being negative, are very close to zero. Since the bound material inevitably falls back to the origin no matter how close the energy is to zero, though, there is unfortunately no simple way of discerning the asymptotic behavior of this segment of the stream.

One quantity that gives some insight into its behavior, however, is the number  $q \equiv d \ln(\rho r^3) / d \ln t$  as a function of  $\mu$ . When taking this logarithmic derivative, the quantities  $\rho$  and  $r$  are considered functions of  $\mu$  and  $t$  and  $\mu$  is a constant. Therefore,  $q$  gives the power-law index of the ratio of the density along the stream relative to the density associated with the black hole tidal field as a function of time and as we move along with a fluid element.

Figure 4.8 shows a plot of  $q(\mu)$  for  $\gamma = 5/3$  and the disruption of a solar-type star by a  $10^6 M_\odot$  SMBH ( $S$  was set to a constant). The left-hand panel gives the solution when the flow is dominated by self-gravity, while the right-hand panel shows the case when the flow is shear dominated. The different curves give different times since disruption, with the blue curve at  $\simeq 13$  days after disruption, the brown curve at  $\simeq 143$  days after disruption, and each curve differing from the next closest curve by  $\simeq 26$  days. As we mentioned, the quantity  $q$  characterizes the

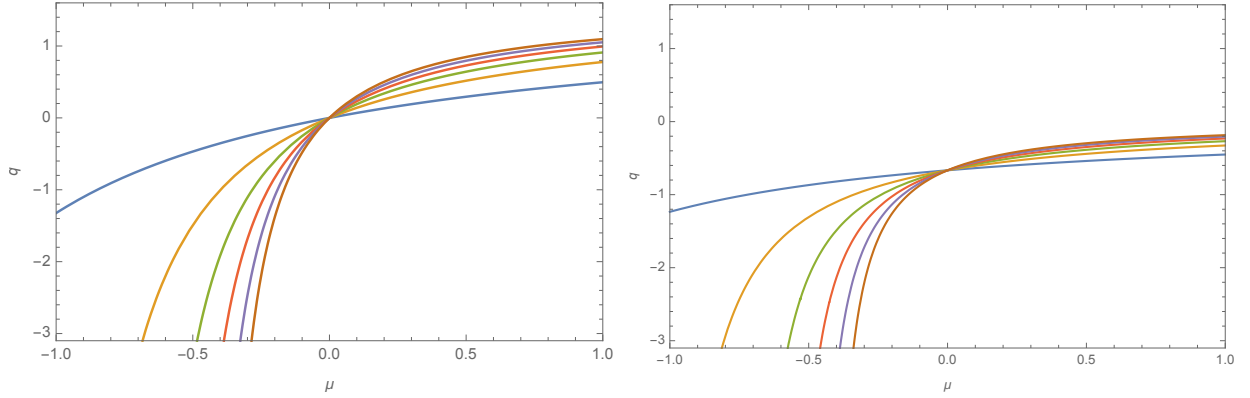


Figure 4.8: The quantity  $q = d\ln(\rho r^3)/d\ln t$  as a function of  $\mu$  when  $\gamma = 5/3$ ,  $M_h = 10^6 M_\odot$ , the progenitor is solar, and the gas is isentropic; the flow is assumed to be self-gravity dominated in the left-hand panel and shear-dominated in the right-hand panel. The different curves show different times, with the blue curve at  $1000 \times r_t^{3/2} \sqrt{2GM_h} \simeq 13$  days after disruption, the brown curve at  $11000 \times r_t^{3/2} \sqrt{2GM_h} \simeq 143$  days after disruption, and each curve differs from the next closest curve by  $2000 \times r_t^{3/2} \sqrt{2GM_h} \simeq 26$  days (e.g., the yellow curve is 26 days after the blue curve, the green curve is 26 days after the yellow curve, etc.). The range of the  $y$ -axis was set to the same values for each plot for ease of comparison. Fluid elements in the stream follow vertical lines from one curve to the next.

instantaneous power law of the product  $\rho r^3$ , i.e., the ratio of the density in the stream to that of the black hole scales instantaneously as  $\rho r^3 \propto t^q$ .

These plots show us what to expect when we consider lines of constant  $\mu$  – when we follow along a single fluid element. When  $\mu > 0$ , the specific energy of the gas parcel is greater than zero, and thus initially follow  $r \propto t^{2/3}$  but eventually transition to  $r \propto t$  for late times. We would thus expect that, at early times, the ratio of the density of the stream to that of the black hole should follow  $\rho r^3 \propto 1$  ( $\rho r^3 \propto t^{-2/3}$ ) for self-gravity dominated (shear dominated) streams, while at late times it should follow  $\rho r^3 \propto t^{1.5}$  ( $\rho r^3 \propto 1$ ) for self-gravity dominated (shear dominated) streams. This behavior is exactly shown in the left and right-hand panels of Figure 4.8, and specifically the rate at which this transition occurs. Likewise, if the material is **exactly** at  $\mu = 0$ , it will always follow  $\rho r^3 \propto 1$  ( $\rho r^3 \propto t^{-2/3}$ ) for self-gravity (shear)-dominated streams, and this is seen in the Figure.

Figure 4.8 also shows how the density of the bound material, fluid elements with  $\mu < 0$ , evolves with respect to the density of the SMBH. As we mentioned, there is no asymptotic behavior for the bound material because it inevitably falls back to the black hole. However, we see that the ratio of the stream density to the black hole density always scales as some power of  $t$  that is less than 1, and in fact this power-law decreases as time increases. We thus expect that all material bound to the black hole, if it follows a  $\gamma = 5/3$  equation of state, will eventually become shear-dominated.

## 4.6 Discussion

In the preceding sections we developed pseudo-analytical expressions for the velocity profile of the debris, the positions of the gas parcels comprising the debris stream, and the density of the debris stream. Here we discuss how the angular momentum of the debris might alter these expressions, make comparisons to the previous work of Kochanek (1994) on tidally-disrupted debris streams, consider the fate of the debris that satisfies the critical adiabatic index condition, and explore how the entropy of the gas should realistically behave.

### 4.6.1 The neglect of angular momentum

The solutions we have given here rely on the fact that the angular momentum of the material is small enough to be ignored when considering the evolution of the debris stream. Since the  $\phi$ -component of the velocity is approximately given by  $r\dot{\phi} \simeq \ell/r$ , where  $\ell \simeq \sqrt{GM_h r_p}$  is the specific angular momentum of the material and  $r_p \simeq r_t$  is the pericenter distance of the star, we find that  $v_\phi/v_r \simeq (r/r_p)^{-1/2}$ . Thus, the neglect of angular momentum only breaks down for small radii, and should be increasingly accurate as the pericenter distance of the progenitor gets smaller. This argument also agrees with Figure 4.3, which shows that the agreement between the self-similar solution and the numerical solution gets better as we proceed to larger distances from the hole (and, as a consequence, the ratio of the angular velocity to the radial velocity gets smaller).

One consequence of accounting for the finite angular momentum of the material is that the position of the center of the stream (in terms of its width) is not purely radial, but instead sweeps out some angle (see also Guillochon et al. 2015). Thus, the extent of the stream is not exactly  $(\partial r/\partial \mu)dr$ , but is instead given by

$$\frac{\partial r}{\partial \mu} d\mu \rightarrow \sqrt{\left(\frac{\partial r}{\partial \mu}\right)^2 + r^2 \left(\frac{\partial \phi}{\partial \mu}\right)^2} d\mu, \quad (4.59)$$

where  $\phi$  is the in-plane angular position of the center of the stream; this is the equation employed in Chapters 2 and 3. Therefore, the overall length of the stream is slightly underestimated by ignoring the angular momentum of the gas.

A more important consequence of the angular momentum of the material is that the orientation of the tidal force of the SMBH will change as the bound material returns to the origin. Specifically, by assuming that the motion of the gas parcels was radial with a transverse extent  $s$ , the tidal field of the hole only served to compress material in the transverse direction (viz. equation 4.26) and increase the density of the stream. However, once the orientation of the cross-sectional width of the stream  $H$  rotates to the point where it is aligned with the radial displacement of the center of the stream, the tidal compression will transition to a tidal shear that results in a decrease

of the density.

Figure 4.9 shows a rough drawing, not to scale, of the cross-section of the returning debris stream that illustrates this point: the left side shows the current assumption about the nature of  $H$  versus the position of the center of the stream, while the right side gives a more accurate picture that accounts for the finite angular momentum of the material. From this schematic we see that, under the current, radial approximation for the position of the center of the stream (in terms of the transverse width), the tidal field of the black hole will only compress the stream and consequently enhance the density near the black hole. In actuality, however, the small amount of angular momentum possessed by the debris causes it to miss the black hole, changing the tidal compression of the hole into a tidal shear that actually decreases the density.

#### 4.6.2 Comparison with Kochanek (1994)

Kochanek (1994) also performed an analysis of the debris streams produced from TDEs, in an attempt to discern the nature of the self-intersection that ensues when the bound material is swung through its general relativistic apsidal precession angle (roughly ten degrees for a solar-like star disrupted by a  $10^6 M_\odot$  SMBH; Rees 1988). Here we make a brief comparison between his findings and ours.

One important result of Kochanek (1994) was that, if the impact parameter  $\beta \equiv r_t/r_p$ , where  $r_p$  is the pericenter distance of the center of mass of the progenitor star, is large enough, then self-gravity will not be important for determining the evolution of the stream. Here we find a similar trend: from Figure 4.8, shear-dominated streams always follow  $\rho r^3 \propto t^{-q}$  with  $q < 0$ . Thus, if the impact parameter is high enough such that the density everywhere satisfies  $2\pi\rho < M_h/r^3$ , then the stream density will never be able to surmount the tidal shear of the SMBH (although the unbound material does asymptotically follow  $\rho \propto r^{-3}$ ).

Kochanek (1994) also found that the width of the stream varies as  $H \propto r^{1/4}$  for a  $\gamma = 5/3$  equation of state. This result ultimately comes from the fact that the mass per unit length  $\Lambda \equiv \partial M/\partial r$  is assumed to be  $\Lambda \propto r^{-1}$  (see also Guillochon et al. 2014b for the expression when

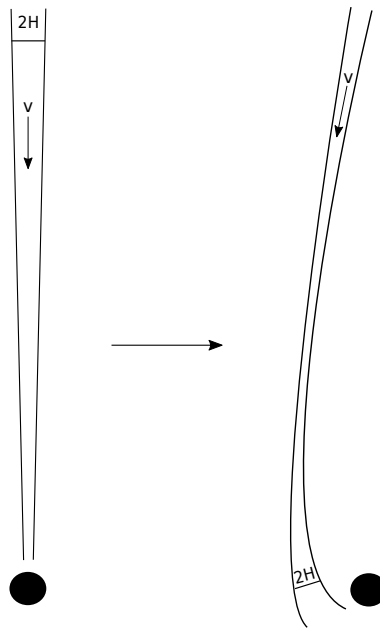


Figure 4.9: A schematic of the debris stream, not drawn to scale, returning to the black hole under the approximations set out in our analysis (left drawing) and a more realistic distribution that accounts for the finite angular momentum of the hole (right drawing). This shows that, as the material gets very close to the hole, the tidal compression becomes a tidal shear that serves to decrease the density.

general  $\gamma$  are used alongside this prescription). However, we found from our analysis that the early evolution of the stream – when all of the gas parcels are following approximately  $r \propto t^{2/3}$  orbits – is characterized by

$$\Lambda = \frac{\partial M}{\partial r} = \left( \frac{\partial r}{\partial \mu} \right)^{-1} \frac{\partial M}{\partial \mu} \propto t^{-4/3} \propto r^{-2}, \quad (4.60)$$

where the last relation follows from the fact that  $r \propto t^{2/3}$ . Since  $H^2 \rho \propto dM/dr$ , and  $\rho \propto t^{-2} \propto r^{-3}$  during this phase, we thus find

$$H \propto r^{1/2}, \quad (4.61)$$

which disagrees with the scaling  $H \propto r^{1/4}$  found by Kochanek (1994). For general  $\gamma$ , using equations (4.30) and (4.50) gives

$$H \propto r^{\frac{2-\gamma}{\gamma-1}}. \quad (4.62)$$

Figure 4.10 shows  $H/R_\odot$  at the marginally-bound portion of the stream as a function of  $r/r_t$ , with the solid, black curve from the simulation described in Chapter 2 but using  $10^7$  particles, and the red, dashed curve from the analytic prediction  $H/R_\odot \propto (r/r_t)^{1/2}$  (the proportionality constant was set to 0.33, which provides a good by-eye fit). The width was calculated from the simulation by first determining the number of particles that had specific energies within a small range centered around zero; for this plot, the absolute value of the maximum energy was  $10^{-6}c^2$  (as compared to the energy of the most energetic particles of  $\sim 2 \times 10^{-4}c^2$ ; see equation 4.10), which amounted to roughly  $10^5$  particles and a total mass of  $\delta m \simeq .01M_\odot$  contained within the zero-energy bin. The maximum and minimum radii,  $r_{max}$  and  $r_{min}$ , respectively, within that bin were computed, giving a radial extent  $\delta r = r_{max} - r_{min}$  of the marginally-bound portion of the stream. We then calculated the quantity  $dM/dr \simeq \delta M/\delta r$ , determined the average density, and used equation (4.41) to calculate the width. This Figure shows that the analytic prediction of  $H \propto r^{1/2}$  fits the data well. The disagreement between the prediction and the numerical results at early times is likely because

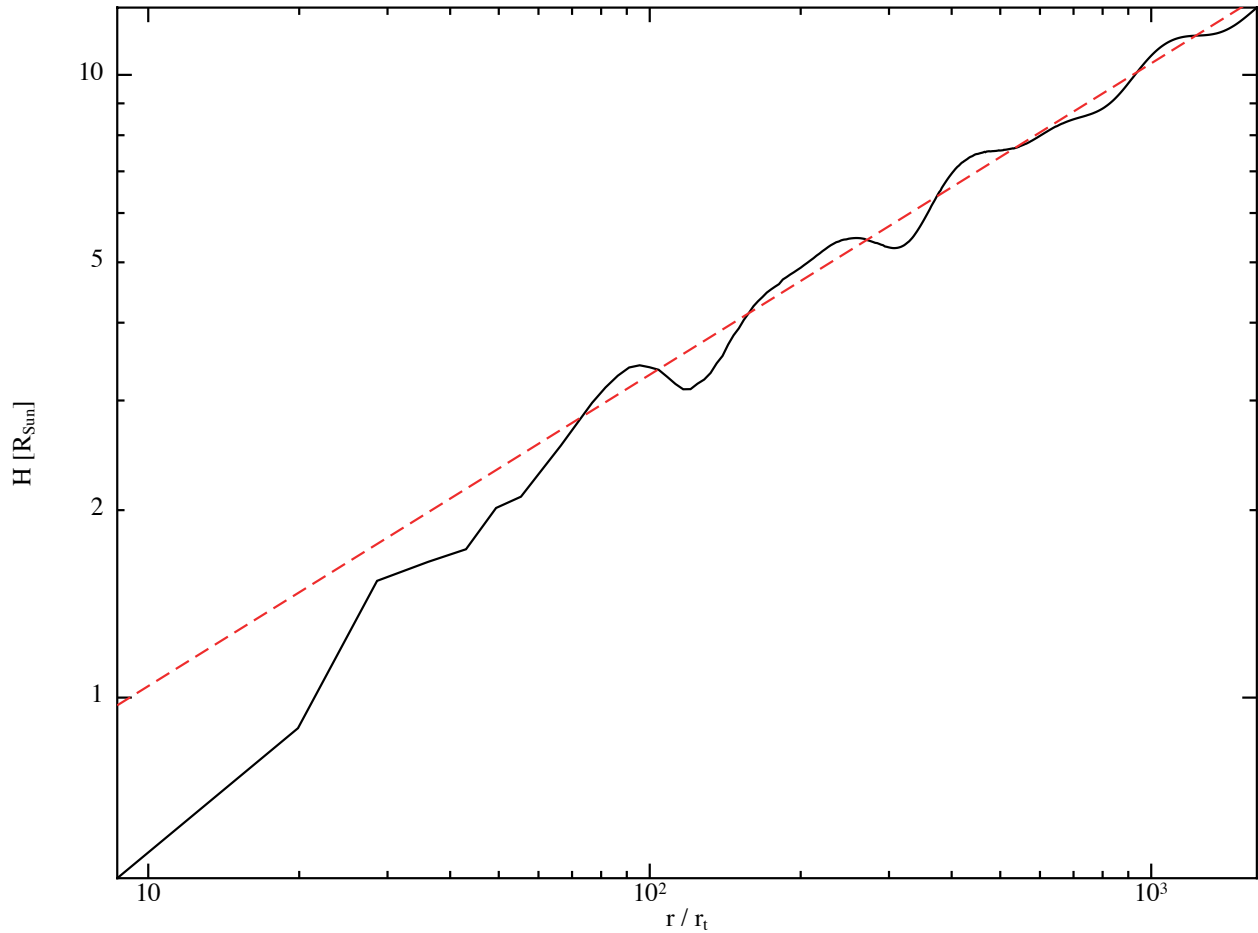


Figure 4.10: A log-log plot of the stream width,  $H$ , in units of solar radii at the marginally-bound location along the stream as a function of Lagrangian distance (i.e., moving with the marginally-bound portion of the stream) from the SMBH. The black, solid curve shows the solution from the same simulation performed in Chapter 2 (i.e., a solar-like star destroyed by a  $10^6 M_\odot$  SMBH) but with  $10^7$  particles, while the red, dashed curve shows the analytic prediction  $H/R_\odot \propto (r/r_t)^{1/2}$  (the constant of proportionality was set to 0.33).

self-gravity is still acting to modify the specific energies in the radial direction. This interpretation is supported by the fact that the number of particles in the marginally-bound energy bin goes from  $\sim 8.2 \times 10^4$  to  $\sim 1.08 \times 10^5$  during that initial transient phase, after which point it remains almost exactly constant.

Once the orbits of the unbound material transition to  $r \propto t$ , which occurs around 50 days for the disruption of a solar-like star by a  $10^6 M_\odot$  SMBH, we recover the  $\partial M/\partial r \propto r^{-1}$  scaling assumed by Kochanek (1994). Using the fact that  $\rho \propto t^{-3/2} \propto r^{-3/2}$  during this phase, the relation  $H^2 \rho \propto \partial M/\partial r$  yields  $H \propto r^{1/4}$ , which is in agreement with Kochanek (1994).

Kochanek (1994) also discussed how ionizations and recombinations, viscosity, and an ambient medium affect the evolution of the debris stream. We will return to these points in Section 6.4, where we reconsider the entropy of the gas.

### 4.6.3 To fragment or not to fragment?

When the density of the black hole  $\rho_h \sim M_h/r^3$  falls off at a rate that is steeper than the density of the debris stream, we expect that the self-gravity of the stream in the radial direction will eventually overcome the shear of the black hole. Equivalently, if  $\rho \gtrsim \rho_h$ , the dynamical timescale  $\tau_d \sim r^{3/2}/\sqrt{GM_h}$ , which is the time over which material is sheared in the radial direction, will be longer than the free-fall timescale  $\tau_{ff} \simeq 1/\sqrt{4\pi G\rho}$ . Thus, in this case the material is able to aggregate faster than the rate at which it is being torn apart, and we expect the stream to be gravitationally unstable. Conversely, when  $\rho$  falls off more steeply than  $r^{-3}$ , the ordering of the timescales reverses, and overdensities are sheared apart faster than they can collapse. We thus expect the stream to be gravitationally stable when  $\rho$  falls off faster than  $r^{-3}$ .

These arguments are supported by Chapter 2, where we investigated, from a numerical perspective, how the evolution of the debris stream from a TDE depends on the adiabatic index of the gas. We found that, when  $\gamma = 1.8$  and 2, the stream fragmented early on in its evolution; from our analysis  $\rho_m \propto t^{-5/3}$  and  $t^{-4/3}$  when  $\gamma = 1.8$  and 2, and thus we expect the stream to fragment in these cases. On the other hand, in Chapter 3 we found that the stream never fragmented –

even after ten years post-disruption – when the adiabatic index of the gas was 1.5. From equations (4.50) and (4.52), the density should fall off as  $\rho \propto t^{-8/3}$  for  $\gamma = 1.5$ , which is significantly steeper than  $t^{-2}$  and we therefore expect, consistent with the numerical findings, that the stream is stable to fragmentation in this case.

In Chapters 2 and 3 we also ran simulations in which the adiabatic index of the gas was set to  $\gamma = 5/3$ . In this case, we found that the stream still fragmented, but the time at which fragmentation occurred depended on the resolution of the simulation. In particular, if the number of particles was increased, the stream fragmented later and vice versa. This finding then **suggests** that the stream is gravitationally unstable, but that the noise inherent in the numerical method is seeding the instability.

Is this finding and interpretation consistent with our analysis here? As we saw above,  $\gamma = 5/3$  marks the critical adiabatic index (for an isentropic equation of state) where  $\rho \propto t^{-2}$  during the early evolution of the debris. In this case, then, the freefall and collapse timescales are proportional to one another, and it is unclear whether or not the stream **should** fragment.

To answer this question, we note that a precisely analogous situation is encountered when one considers Jeans collapse in the early Universe: as primordial overdensities form and try to collapse, they are continuously stretched apart by the fact that the background density scales as  $\rho \propto t^{-2}$  (see, e.g., Coles & Lucchin 1995, p. 202). In this case, then, the freefall and dynamical timescales are comparable, and the fate of the overdensities becomes unclear. However, one can show that there are still growing, unstable modes, but instead of evolving as exponentials they only scale as power-laws in time. To understand the origin of this result, we can argue somewhat heuristically that the relation

$$\delta\dot{\rho}_+ \simeq \frac{\delta\rho_+}{\tau_{ff}}, \quad (4.63)$$

where  $\delta\rho_+$  is the growing mode of the instability and  $\tau_{ff}$  is the free-fall timescale, holds more generally than just when  $\tau_{ff}$  is time-independent (and, as a consequence, the instability grows

exponentially). Thus, if we write  $\tau_{ff} \simeq t/\sqrt{G\rho_0 t_0^2}$ , where  $t_0$  is a characteristic timescale and  $\rho_0$  is a characteristic density, then it follows immediately that  $\delta\rho_+ \propto t\sqrt{G\rho_0 t_0^2}$  – the overdensities grow as power-laws.

For a star being disrupted by a SMBH, the characteristic timescale is the dynamical time at the tidal radius, so  $t_0 \simeq r_t^{3/2}/\sqrt{GM_h}$ , while the characteristic density  $\rho_0$  is the original stellar density. We thus expect that when  $\gamma = 5/3$ , the growing modes should scale roughly as

$$\delta\rho_+ \propto t^{\sqrt{\alpha}}, \quad (4.64)$$

where  $\alpha = \rho_* r_t^3/M_h$  is the ratio of the stellar density,  $\rho_*$ , to the density of the SMBH at the time of disruption,  $M_h/r_t^3$ .

These arguments illustrate that when the density of the stream falls off as  $\sim 1/r^3$  – which occurs for the early evolution of the marginally-bound material when  $\beta \sim 1$  and  $\gamma = 5/3$ , and also occurs for the shear-dominated portion of the unbound stream for any  $\gamma$  – there are growing unstable modes. A more rigorous approach would be to perform a perturbation analysis on the fluid equations, and when this is done for Jeans collapse in the early Universe, the results of the heuristic argument are upheld (Coles & Lucchin, 1995). Since the problem is identical here in terms of the scalings of the variables, it follows that the heuristic argument is also valid, and for completeness we have checked that equation (4.64) is recovered if one performs a perturbation analysis. (Technically, the result is that  $\rho \propto t^{N\sqrt{\alpha}}$ , where  $N$  is a number of order unity.)

We thus find that the results of Chapters 2 and 3 are consistent with our analytical arguments: when  $\gamma = 5/3$ , the stream is unstable to fragmentation. However, because the dynamical timescale and collapse timescale are proportional in this case, the overdensities grow as power-laws instead of exponentials. This considerably weaker growth rate means that resolving the instability is much more difficult, and the noise in the density that is induced by the numerical method becomes the dominant contributor to the fluctuations that seed the instability. However, in the presence of a sufficiently dense ambient medium, the shear between the stream and that medium would provide

a physical origin for the perturbations (Bonnerot et al., 2015).

Before moving on, we note that the simulations of Chapters 2 and 3 found that bound portions of the stream, specifically those very close to the marginally-bound orbit, also exhibited fragmentation. Based on Figure 4.8, we would not expect this, as  $\rho r^3 \propto t^q$  with  $q$  less than zero for the bound material. However, our treatment here of the radial velocity ignored the effects of self-gravity in the radial direction; it can be seen from Figure 4.7, though, that the denser material towards the marginally bound segment of the stream generates a gravitational force on the bound material that serves to counteract the gravitational pull of the SMBH. This additional force will serve to reduce the amount of shear present within the flow, correspondingly lengthening the dynamical time and conceivably allowing some parts of the bound material to collapse.

#### 4.6.4 A more realistic entropy prescription

Most of the examples we considered here assumed that the constant-entropy nature of the polytrope was preserved throughout the evolution of the debris. However, our equation (4.30) permits a radially and temporally dependent entropy, which, through equation (4.41), would serve to alter the nature of the stream. In particular, if the entropy decreases due to cooling, the density is correspondingly increased, making it easier for the stream to overcome the  $\gamma = 5/3$  marginally-unstable condition (equation 4.53); likewise, if the internal energy of the gas increases, the width of the stream grows and results in the gravitational stability of the stream.

When the stream initially starts to expand, any cooling is initially controlled by the fact that the surface radiates approximately as a blackbody:

$$dL = \sigma T_{eff}(r, t)^4 dA, \quad (4.65)$$

where  $\sigma = 5.67 \times 10^{-5}$  [cgs],  $dA$  is the area of the emitting surface, and  $T_{eff}$  is the effective temperature that is, in general, dependent on time and position along the stream. The assumption

of a blackbody is justified by the fact that the optical depth across the width of the stream is

$$\tau \simeq \rho\kappa H \simeq \kappa\rho_*R_* \left(\frac{r}{r_t}\right)^{-5/2} \simeq \kappa\rho_*R_* \left(\frac{t}{t_0}\right)^{-5/3}, \quad (4.66)$$

where  $\kappa$  is the Rosseland mean opacity and  $\kappa\rho_*R_* \gtrsim 2 \times 10^{10}$  for solar-like progenitors ( $R_* = R_\odot$  and  $\rho_* \simeq 1 \text{ g / cm}^3$ ). The stream is therefore very optically thick when the stream is still highly ionized, which justifies the assumption of local thermodynamic equilibrium (but see below for when recombinations start to change the opacity). The area of the stream is simply  $dA \simeq 2\pi H dr$ ,  $dr$  being the infinitesimal distance along the stream. Since the total amount of internal energy contained in the stream is comparable to the amount contained in the original star,  $E_{int} \simeq GM_*^2/R_* \simeq 10^{48}$  ergs for a solar-like progenitor, any radiation escaping from the photosphere should decrease the internal energy on roughly the Kelvin-Helmholtz timescale – thousands to millions of years if the disrupted star is roughly solar. Thus, the early evolution of the debris stream should be very nearly adiabatic.

However, recombinations will start to occur as the temperature of the debris reaches roughly  $10^4$  K. As recognized by Kochanek (1994) and Kasen & Ramirez-Ruiz (2010), this could have important consequences for the evolution of the debris stream, heating the material when it is optically thick and cooling it as it becomes optically thin. If the stream follows a  $\gamma = 5/3$  adiabatic equation of state and is self-gravity dominated, then we can show, by returning to equation (4.41), using equations (4.30), (4.57) and (4.43), and the ideal gas law, that temperature evolves as

$$T \simeq 2.35 \frac{GM_*m}{k_B R_*} \left(\frac{t}{t_m}\right)^{-4/3}, \quad (4.67)$$

where the factor of 2.35 resulted from evaluating equation (4.43) numerically for  $n=1.5$  ( $\gamma = 5/3$ ) at  $\mu = 0$ ,  $m \simeq 1.67 \times 10^{-24}$  g is the mean molecular mass in the stream,  $k_B = 1.38 \times 10^{-16}$  [cgs] is Boltzmann's constant, and  $t_m = (\sqrt{5}r_t)^{3/2}/\sqrt{2GM_h} \simeq 1.05$  h for a solar-like progenitor and a

$10^6 M_\odot$  SMBH. Solving this equation for  $t_{rec}$ , the time at which  $T = 10^4$ , gives

$$t_{rec} \simeq 27 \text{ days} \quad (4.68)$$

after disruption. This number could be slightly sooner or later depending on the mean molecular weight (we adopted  $m = m_h = 1.67 \times 10^{-24}$  g) and the initial temperature of the star.

Equation (4.68) should really be interpreted as an average value over the entire extent of the stream. In particular, since the density, and hence the temperature, is maximized near the marginally-bound portion of the stream (see Figure 5.3), recombinations will start to occur at a later time than they will toward the radial extremities of the stream where the temperature is correspondingly lower. Likewise, the stream is not an infinitely thin line, but has a finite width  $H$ ; near  $H$  the gas temperature is lower, generating an earlier recombination time.

Initially – when the gas is still largely ionized – the optical depth is quite high, as evidenced from equation (4.66), meaning that recombinations will heat the gas and keep it at a roughly constant temperature of  $10^4$  K. Once recombinations start to occur, however, the decrease in the ionized fraction will correspondingly lower the opacity of the gas and allow more of the stream to cool, generating a “cooling front” that moves inward from  $H$  (Kasen & Ramirez-Ruiz, 2010). Thus, while recombinations will initially heat the gas and serve to increase the specific entropy  $S$ , at later times the optical thinness of the stream means that continued recombinations will actually serve to decrease the specific entropy.

The local shear within the stream could also serve to heat the gas. If we prescribe the coefficient of dynamic viscosity by  $\eta$ , then viscous heating will modify the gas energy equation via (Chapter 6)

$$\frac{p}{\gamma - 1} \left( \frac{\partial}{\partial t} \ln S + v_r \frac{\partial}{\partial r} \ln S \right) \simeq \eta \left( \frac{\partial v_r}{\partial r} \right)^2, \quad (4.69)$$

where  $p$  is the gas pressure and  $S = p/\rho^\gamma$  is the entropy as we defined it for a polytrope. We see that the right-hand side of this equation falls off approximately as  $\propto 1/r^3$  (assuming that the

temporal and spatial dependence of  $\eta$  is not too large), and consequently the viscous heating of the gas should not play a large role in the overall evolution of the debris stream.

Finally, the background radiation field present in the circumnuclear medium will also alter the thermodynamical evolution of the stream. If the stream is optically thin, then the entire stream would be maintained at the temperature of the radiation field  $T_b$  (in the most extreme case,  $T_b$  would be the temperature of the cosmic microwave background). When the stream is still optically thick, on the other hand, the radiation will be reprocessed by a thin, outer sheath (Kochanek, 1994).

When the recombinations or radiation from background sources start to heat the gas, it will become over-pressured with respect to self-gravity. In this case, if we return to equation (4.27), we see that the cross-sectional width of the stream varies as

$$H \simeq c_s t, \quad (4.70)$$

where

$$c_s \simeq \sqrt{\frac{p}{\rho}} \quad (4.71)$$

is the adiabatic sound speed. If we now use this expression for  $H$  in equation (4.41) and again assume that the evolution proceeds adiabatically ( $p = S\rho^\gamma$ , where this  $S$  is a constant that is larger than the value before heating started), then we find

$$\rho^\gamma t^2 \propto \left(\frac{\partial r}{\partial \mu}\right)^{-1} \frac{\partial M}{\partial \mu}. \quad (4.72)$$

While the stream is still in the marginally-bound phase,  $\partial r/\partial \mu \propto t^{-4/3}$ , and we thus find

$$\rho \propto t^{-\frac{10}{3\gamma}}. \quad (4.73)$$

In this case, we see that  $\gamma = 5/3$  still marks the critical  $\gamma$  at which  $\rho \propto t^{-2} \propto r^{-3}$ .

## 4.7 Summary and conclusions

In this paper we have presented a semi-analytic analysis of the debris streams produced from TDEs, showing that there is a simple, self-similar prescription for the radial velocity of the debris. Specifically, we found that if one assumes that the radial velocity varies as  $v_r = \sqrt{2GM_h/r}f(\xi)$ , where  $f$  is a function of the self-similar variable  $\xi = \sqrt{2GM_h}t/r^{3/2}$ , then the function  $f$  is given by the solution to the equation

$$f' = \frac{f^2 - 1}{2 - 3f\xi} \quad (4.74)$$

with the boundary condition  $f(2/3) = 1$ . Figure 4.2 compares this velocity profile to the numerical solution of Chapter 2, and shows that the two agree very well (see also Figure 4.3).

We also computed the cross-sectional radius of the stream,  $H$ , as a function of time and density. We found that, when the density and pressure are high enough, the stream width varies in a quasi-hydrostatic manner as  $H^2 \propto \rho^{\gamma-2}$ . However, if the shear of the black hole dominates self-gravity and pressure, then the entire stream evolves self-similarly with  $H \propto r$ .

The self-similar velocity profile and the solution for the cross-sectional radius of the stream allowed us, in conjunction with equation (4.41), to solve for the density of the debris stream,  $\rho$ , as a function of space and time. Our approximate, analytical expressions (equations 4.45 and 4.46) were shown to agree well with the more exact, numerical solutions that used the full forms for the quantities  $\partial r/\partial \mu$  and  $\partial M/\partial \mu$  (see Figures 5.3 and 4.5). An inverted density profile – where the density increases as a function of  $r$  – is actualized when the material is self-gravitating, while the density decreases monotonically when the shear of the black hole dominates the stream self-gravity.

We analyzed the general scaling of  $\rho$  with time and distance from the black hole, and showed that, during the initial stage of evolution when the orbits of the gas parcels comprising the debris stream follow  $r \propto t^{2/3}$ , the portions of the stream that are self-gravitating satisfy  $\rho \propto t^{-4/(3(\gamma-1))}$ . This scaling demonstrates that  $\gamma = 5/3$  marks the critical adiabatic index above which self-gravity always dominates the tidal shear of the black hole, below which the self-gravity of the stream

becomes negligible. On the other hand, the unbound portion of the stream eventually follows  $r \propto t$ , which shows  $\rho \propto t^{-1/(\gamma-1)}$  and the critical adiabatic index is  $\gamma = 4/3$ . Finally, when the stream falls below the self-gravitating limit (when  $2\pi\rho < M_h/r^3$ ), the entire stream behaves self-similarly and  $\rho \propto r^{-2}(\partial r/\partial\mu)^{-1}$ . During this self-similar regime, the density falls off as  $r^{-4}$  when  $r \propto t^{2/3}$  (marginally-bound material, early evolution of the entire stream) and  $r^{-3}$  when  $r \propto t$  (unbound material, late evolution).

Finally, we showed that the finite angular momentum of the debris, which was ignored in our self-similar models, should have a small but noticeable effect as material falls back to the black hole. Comparisons between our results and those of Kochanek (1994) were made, demonstrating that we agreed on many aspects of the evolution of the debris stream but disagreed on some; in particular, our finding that the width of the stream scales as  $H \propto r^{1/2}$  for a  $\gamma = 5/3$ , self-gravitating stream contrasts the scaling  $H \propto r^{1/4}$  found by Kochanek (1994). We showed that when  $\gamma = 5/3$ , the stream of debris produced from a TDE should be gravitationally unstable; however, because the density of the stream scales as  $\rho \propto r^{-3}$  for early times, which is identical to that of the black hole, the perturbations grow only as power-laws in time (specifically,  $\delta\rho_+ \propto t^{\sqrt{\alpha}}$ , where  $\alpha \simeq \rho_* r_t^3/M_h$  is the ratio of the density of the stellar progenitor to the density of the black hole at the time of disruption). We also considered how the entropy of the debris stream might evolve more realistically, given that the gas will start to recombine after a certain time and that the ambient medium may serve to heat the gas.

Our investigations assumed that the density of the circumnuclear medium does not affect the propagation of the debris stream produced from a TDE. Because the original stellar density is so much higher than the densities near the centers of most galaxies, this assumption is justified, with the bulk dynamics of the material largely unaffected (Kochanek, 1994). However, the Kelvin-Helmholtz instability could be important for modifying the density profile of some portions of the returning debris stream (Bonnerot et al., 2015), and could also provide a physical length scale over which density perturbations occur that cause the stream to fragment. Also, once the stream propagates out to very large distances from the SMBH, the stream density will become comparable

to that of the ambient medium, and drag effects will start to alter its motion (Guillochon et al., 2015).

In order to make comparisons with past simulations, we only computed the explicit velocity profile (the one that depends on both  $r$  and  $t$ ) and compared it to the numerical solution for the case when a solar-like star is destroyed by a  $10^6 M_\odot$  SMBH and the pericenter distance of the progenitor star was equal to the tidal radius. However, we expect that this self-similar solution is accurate over a very wide range of parameters (SMBH mass, stellar mass, impact parameter  $\beta$ , etc.) because it depends only on the local velocity and the local dynamical time, and this concern only for local quantities should be true for most TDEs (i.e., we expect that the specifics of the initial conditions of the encounter are rapidly forgotten as the stream recedes from the black hole). Even for encounters in which the star is only partially destroyed or recollapses to form a bound core (Guillochon & Ramirez-Ruiz, 2013), this self-similar velocity profile should hold for the disrupted debris and only break down once we get very near to the surviving core.

The analysis performed here was done with the specific application of stars disrupted by supermassive black holes in mind. However, we note that many of the results we obtained can be applied to other tidally-interacting systems. In particular, the self-similar velocity profile and the physical properties of the debris stream (the width and density distributions) described here are also applicable to compact object mergers (e.g., Lee & Ramirez-Ruiz 2007), the disruptions of planets by stars (e.g., Faber et al. 2005), and conceivably the tidal tails generated from galactic interactions (e.g., Knierman et al. 2012).

## Chapter 5

### Hyperaccretion During Tidal Disruption Events: Weakly Bound Debris Disks and Jets

#### 5.1 Introduction

Tidal disruption events (TDEs), encounters between a star and a massive ( $\gtrsim 10^5 M_\odot$ ) black hole in which the star passes within the tidal radius of the hole  $r_t = R_*(M_h/M_*)^{1/3}$ , where  $R_*$  is the stellar radius,  $M_*$  is its mass, and  $M_h$  is the mass of the SMBH, have interested the astronomical community for decades. Initial studies of TDEs focused on their potential for generating the luminosities observed in active galactic nuclei (Frank & Rees, 1976; Frank, 1978). While this pursuit fell by the wayside (but see Milosavljević et al. 2006), TDEs continue to be useful for determining the presence of black holes within galactic centers (Lacy et al., 1982; Rees, 1988). Many investigations, both computational and analytical, have been undertaken over the last forty years to elucidate the dynamics of the interaction between a star and a black hole and the luminosities associated with the resultant TDE (Carter & Luminet, 1983; Evans & Kochanek, 1989; Loeb & Ulmer, 1997; Kim et al., 1999; Tchekhovskoy et al., 2014; Guillochon & Ramirez-Ruiz, 2013).

The earliest studies of the physics of the disruption noted that, due to the difference in the gravitational potential across the star, nearly half of the progenitor mass is ejected from the system on hyperbolic orbits (Lacy et al., 1982; Carter & Luminet, 1982; Hills, 1988). The other half remains bound to the black hole, with the orbits initially Keplerian (meaning that pressure forces have not yet altered particle trajectories). After a few revolutions of the innermost material, which occurs shortly after the disruption, hydrodynamical effects begin to modify the flow. These

interactions result in the heating of the debris.

One heating agent arises from the pressure distribution of the tidally-disrupted star, which causes some of the orbits to possess a substantial inclination angle to the orbital plane of the center of mass of the star. When the material on these orbits intersects the mid-plane of the disk, occurring roughly at periapsis, shock heating will simultaneously increase the internal energy of the gas and damp the inclination angle of the orbit. Because the innermost orbit has specific energy  $\mathcal{E} \approx GM_h R_*/r_t^2 = GM_h/2R_i$ , we see that  $R_i \approx (R_*/2)(M_h/M_*)^{2/3}$  is its semi-major axis. For a solar-mass star and a million-solar-mass hole, the advance of periapsis at this orbit can amount to degrees. Because the innermost debris has the highest velocity within the disk, after one revolution it will impact the slower-moving, outer material, generating a shock. The shock heating further increases the thermal energy of the material and circularizes the orbits. Finally, material continues to fall back at a rate that can greatly exceed the Eddington limit for some time (Evans & Kochanek, 1989; Strubbe & Quataert, 2011). This accretion stage pumps a significant amount of energy into the flow.

Many authors have modeled the disks of bound material produced by TDEs (e.g., Cannizzo et al. 1990; Cannizzo 1992) using the standard  $\alpha$  parametrization of the viscosity and considering the disk to be radiatively efficient and geometrically thin (Shakura & Sunyaev, 1973). However, the processes outlined in the previous paragraph add a large amount of thermal energy to the debris, which consequently “puffs up” the disk in the vertical direction. The super-Eddington accretion also means that radiative diffusion is not effective in cooling the disk. We therefore believe that the thin disk model is incapable of describing the bulk properties of the flow during the super-Eddington phase.

Loeb & Ulmer (1997) invoked the low specific angular momentum of the debris to enable them to describe the gas as roughly spherical; they then assumed that the black hole accretes at a rate to match its Eddington luminosity. To make this model self-consistent, they assumed that the spherical envelope, with an isentropic equation of state and a steep density profile  $\rho \sim r^{-3}$ , surrounded a rotating inner accretion flow, which would have to have a much flatter (and possible

even inverted) density profile to obtain the required accretion rate. The boundary between these regions was assumed to lie at roughly the tidal disruption radius, where the mean specific angular momentum of the debris is approximately Keplerian. While this model requires substantial angular momentum transport within the inner accretion flow, it offers no explanation as to why angular momentum should not be transferred to the outer envelope. If this happened, the boundary between the two zones would move to smaller radii, requiring the density profile of the inner flow to become even flatter (or more inverted), while the effect of rotation on the outer envelope would remain small. It is difficult to see how such a configuration could continue to regulate its accretion rate to remain at the Eddington limit. On the contrary, it seems likely that the energy generation rate would become supercritical, with the envelope absorbing the excess energy until it became unbound.

In an alternate approach, Strubbe & Quataert (2009) forced the material to conform to a “slim disk,” (Abramowicz et al., 1988) and supposed that an outflow carried away unbound debris. However, a slim disk also necessitates that the rate at which matter reaches the black hole is only mildly super-Eddington, and therefore a fair amount of mass must be contained at large radii – in this case, far outside the tidal radius. The assumption of nearly-Keplerian orbits, built into the slim disk model, then implies that the total angular momentum required to support the flow is larger than the angular momentum available.

The past twenty years have seen the emergence of direct observational evidence to support the existence of TDEs and their associated accretion disks (Piro et al., 1988). **ROSAT** discovered the first potential candidates for TDEs in the X-ray (Bade et al., 1996; Komossa & Greiner, 1999). Despite the fairly small set of statistics, astronomers used the **ROSAT** data to tentatively validate the rate of  $10^{-5}$  events per galaxy per year (Donley et al., 2002). **Chandra**, **GALEX**, and **XMM-Newton** surveys have followed up on the events discovered by **ROSAT**, demonstrating that the luminosity-decay relation scales roughly as  $t^{-5/3}$ , as expected from early theoretical studies of TDEs (Phinney 1989, but see Lodato et al. (2009) and Guillochon & Ramirez-Ruiz (2013) for arguments against this scaling; also see section 4); they also found a few new potential candidates (Komossa

et al., 2004; Halpern et al., 2004; Gezari et al., 2008). Most recently, a flurry of analyses has followed the discovery of the  $\gamma$ -ray, X-ray, and radio transient **Swift** J164449.3+573451 (hereafter J1644+57), which is popularly believed to be the result of a TDE (Burrows et al., 2011; Bloom et al., 2011; Cannizzo et al., 2011). These studies, in particular the X-ray and radio observations, not only demonstrated the existence of a roughly  $t^{-5/3}$  power-law decline of the undoubtedly super-Eddington luminosity, but also confirmed the novel association of a relativistic jet with the TDE (Zauderer et al., 2011; Tchekhovskoy et al., 2014).

The combination of super-Eddington luminosity and a powerful jet suggests that accretion onto the black hole is not self-regulated, in contrast to previous models. Here we adopt a different approach to modeling the super-Eddington accretion phase of the geometrically thick disks produced by TDEs. We assume that the structure of the flow is regulated by its ratio of angular momentum to mass, which is quite sub-Keplerian between the vicinity of the black hole and the photospheric radius. Such a flow loses the ability to regulate its accretion luminosity, and absorbs energy liberated near the black hole until it becomes very weakly bound. Instead of blowing itself apart, however, we conjecture that these marginally bound envelopes can persist, with the excess accretion energy emerging as a jet through the narrow rotational funnel. We propose that such a model is consistent with the existence of a jet in **Swift** J1644+57; it also may be relevant (with gas self-gravity included) to the formation of gamma-ray burst jets in collapsars and to the rapid growth of black holes inside quasi-stars.

In section 2 we illustrate the model that describes the fallback disks in super-Eddington TDEs and promote reasons as to why this model is appropriate. In section 3 we use the results of section 2 to analyze a disk whose parameters (mass, angular momentum, etc.) are those of a typical TDE and we show that the internal structure of the disk depends only on those bulk parameters. In section 4 we consider the inner regions of the disk, where general relativity is important, discuss the properties of the jet, delineate the temporal evolution of the disk properties, and compare our model directly to the case of **Swift** J1644+57. We conclude and review the results in section 5.

## 5.2 Zero-Bernoulli accretion model

The disk of stellar material created by a super-Eddington TDE should be thick in the sense that its scale height is some substantial fraction of its radial extent. Narayan & Yi (1994) were among the first to discover self-similar solutions for the vertically-averaged density, pressure, and angular momentum in which the velocity distribution was proportional to Keplerian. One interesting consequence of their models was that the Bernoulli parameter, given by  $B = \Omega^2 r^2 / 2 - GM_h / r + H$ , where  $\Omega$  is the angular velocity and  $H$  is the enthalpy, was shown to be greater than zero. Because the Bernoulli function is a measure of the specific energy of the gas, this result implies that any parcel of gas given an initial kick away from the SMBH would have energy at infinity.

The latter point motivated Blandford & Begelman (1999) to describe a flow consisting of an advection dominated accretion flow (with  $\dot{M}$  a function of radius) and a pressure-driven wind, calling these states “adiabatic inflow-outflow solutions” (ADIOS). The inflowing gas maintains a negative Bernoulli parameter by transferring mass, angular momentum, and energy to the wind. The model, however, requires some unspecified mechanism – presumably some dissipative process – to drive the outflow. Moreover, the inflow zone shares the characteristic of slim disks that the specific angular momentum must be very close to Keplerian – more than 87 percent of the Keplerian value for the case of  $\gamma = 4/3$ . To avoid a highly super-Eddington accretion luminosity, this angular momentum distribution must extend to radii far beyond the tidal disruption radius. The gas returning to the vicinity of the black hole following a TDE, however, has too little angular momentum to permit this.

Thus, the gas distribution during the super-Eddington phase of a TDE is likely to resemble the quasi-spherical envelope of the Loeb & Ulmer (1997) model, but without the ability to regulate its accretion luminosity to a value close to the Eddington limit. The shock heating of different parts of the disk and the energy input of the accreting black hole both raise the internal energy of the material, with turbulence, convection and internal shocks distributing that energy fairly evenly throughout the disk. Eventually there will come a point in time where the Bernoulli parameter

approaches zero, leaving a marginally-bound, highly-inflated envelope.

Any further augmentation of the energy would start to unbind material. The question is whether this unbound material is launched from a wide range of radii or from close to the black hole, where the energy is injected. In the case of an ADIOS, the large angular momentum contained in the flow allows the system to maintain a disklike geometry, with a large “free” surface along which a wind can develop. But in the present case, for which  $B$  approaches zero, the disk closes up to a vanishingly narrow funnel, leaving the outer, quasi-spherical surface as the only plausible location for the development of a wide-angle wind.

However, the injection of energy from the accreting black hole occurs deep in the interior of the envelope, where timescales are much shorter than those throughout the bulk of the flow. The accretion energy, pumped into the gas at a rate that is highly supercritical, is thus unlikely to be able to be efficiently advected to the outer regions where a wind could regulate the super-Eddington luminosity. The only viable exhaust route left for the excess energy is then along the poles, where the surface of the inflated envelope closes. We thus propose that, at this point in the evolution of the fallback disk, where the accretion luminosity augments the binding energy of the envelope to the point where a wind would develop if there were a free surface, a jet carries away the excess energy.

In the situations we are considering, the mass of the black hole dominates the total mass of the system. We can therefore approximate the gravitational potential by  $\phi = -GM_h/r$ , where  $M_h$  is the mass of the SMBH and  $r$  is the radial distance from the hole (we are neglecting any contribution from post-Newtonian gravity; see section 4.1 for a discussion of relativistic effects). In spherical coordinates with this potential and the Bernoulli parameter equal to zero, the momentum equations and the Bernoulli equation are, respectively,

$$\frac{1}{\rho} \frac{\partial p}{\partial r} = -\frac{GM_h}{r^2} + \frac{\ell^2 \csc^2 \theta}{r^3}, \quad (5.1)$$

$$\frac{1}{\rho} \frac{\partial p}{\partial \theta} = \frac{\ell^2 \cot \theta \csc^2 \theta}{r^2}, \quad (5.2)$$

$$-\frac{GM_h}{r} + \frac{\ell^2 \csc^2 \theta}{2r^2} + \frac{\gamma}{\gamma - 1} \frac{p}{\rho} = 0, \quad (5.3)$$

where  $\ell$  is the specific angular momentum of the gas. In the final line we used a specific form for the enthalpy and assumed that the azimuthal velocity is much greater than the poloidal or radial velocity. Here  $\gamma$  is the adiabatic index of the gas, generally between 4/3 and 5/3 depending on the relative contributions from radiation pressure and gas pressure. For most of what follows we will assume that  $\gamma \approx 4/3$ , as radiation pressure dominates the support of TDE debris against gravity during the super-Eddington phase. This fluid description is appropriate to a ZERo-BERnoulli Accretion (ZEBRA) flow.

### 5.2.1 Gyrentropic flow

In Blandford & Begelman (2004), the authors described ADIOS disks as marginally stable to the Høiland criteria. This assumption, verified numerically (Stone et al. 1999), demanded that the surfaces of constant Bernoulli parameter, angular momentum, and entropy all coincide; these surfaces are termed **gyrentropes**. While the Høiland criteria determine a disks's stability to convection in the absence of magnetic fields, even a vanishingly small poloidal field can completely destabilize a differentially rotating disk that is stable to those criteria (Balbus & Hawley, 1991, 1992; Stone & Norman, 1994). We will now show, however, that the zero-Bernoulli assumption ensures the gyrentropicity of the flow, even in the presence of the magnetorotational instability (MRI).

One can show that  $\nabla B = H \nabla \ln S + \Omega \nabla \ell$ , where  $H$  is the enthalpy,  $S$  is the entropy, and  $\Omega$  is the angular velocity of the gas (Blandford & Begelman, 2004). Thus, since  $B \approx 0$ ,  $\nabla S \propto -\nabla \ell$ . This relationship implies that surfaces of constant  $S$  are also those of constant  $\ell$ , which must then be surfaces of constant  $B$ . This type of disk is therefore also gyrentropic, the constancy of  $B$  being the

only assumption which led to that conclusion. Thus, while MRI may invalidate the assumption of gyrentropicity on the grounds of the Høiland criteria, a constant-Bernoulli disk retains gyrentropic flow (assuming that the magnetic energy density is not large enough to substantially alter the dynamical equilibrium).

### 5.2.2 Self-similar solutions

From an analysis of equations (5.1), (5.2), and (5.3), one can show that the general solution of  $\ell(r, \theta)$  could have any functional form that depends on  $r$  and  $\theta$  only through the combination  $r \sin^2 \theta$  (see Appendix A, notably equation (A.10)). When the envelope subtends a large range in radii, however, we expect the solution to have a roughly self-similar structure between the inner and outer boundaries of the disk. Blandford & Begelman (2004) derive the gyrentropic solutions for arbitrary Bernoulli parameter  $B(\theta)/r$ ; the ZEBRA solutions are the special case with  $B = 0$ . We will simply quote their findings here, and adapt our notation to one which is consistent with theirs. For the density, pressure, and specific angular momentum (squared), respectively, we find

$$\rho(r, \theta) = \rho_0 \left( \frac{r}{r_0} \right)^{-q} (\sin^2 \theta)^\alpha, \quad (5.4)$$

$$p(r, \theta) = \beta \frac{GM_h \rho_0}{r} \left( \frac{r}{r_0} \right)^{-q} (\sin^2 \theta)^\alpha, \quad (5.5)$$

$$\ell^2(r, \theta) = aGM_h r \sin^2 \theta, \quad (5.6)$$

where

$$q \equiv 3/2 - n, \quad (5.7)$$

$$\alpha = \frac{1 - q(\gamma - 1)}{\gamma - 1}, \quad (5.8)$$

$$\beta = \frac{\gamma - 1}{1 + \gamma - q(\gamma - 1)}, \quad (5.9)$$

$$a = 2 \frac{1 - q(\gamma - 1)}{1 + \gamma - q(\gamma - 1)}, \quad (5.10)$$

$r_0$  is some characteristic inner radius and  $\rho_0$  is the density at that radius (and at the disk midplane). The parameter  $n$  is defined by Blandford and Begelman so that the accretion rate is proportional to  $r^n$ ; mass-conserving accretion has  $n = 0$ .

One interesting aspect of these solutions is that  $n$ , and therefore  $q$ , which describes how steeply the density and pressure fall off as functions of  $r$ , is not specified a priori, which introduces another degree of freedom into the models. In general, however, we require that the exponent of  $\sin^2 \theta$  remain positive, ensuring that the density and pressure do not go to infinity at the poles. We also expect that the energy produced in the disk should be a decreasing function of radius. From the energy equation, we know that the luminosity is given by  $L \sim \dot{M} v_r^2$ , and assuming that the power is produced by gas in regions with velocity appropriate to that for free-fall, we find that  $L \propto r^{n-1}$ . These two restrictions then impose that  $3/2 - 1/(\gamma - 1) < n < 1$ , which translates to  $1/2 < q < 1/(\gamma - 1)$ . We see that, since the exponent of  $\sin^2 \theta$  is always greater than or equal to zero in our self-similar expressions, the density goes to zero only exactly at the poles. These solutions thus represent quasi-spherical envelopes. The angular momentum distribution is modified from that of Keplerian by the factor  $a$ , which is always less than unity for permissible values of  $n$ .

Blandford & Begelman (2004) noted the additional degree of freedom contained in their solutions. They then went on to describe the physical scenarios appropriate to different values of  $n$ . In particular, different  $n$  give rise to larger or lesser amounts of outflow, accretion rates, energy generation rates, etc. For our present considerations, however, a wind is unnecessary. The question of the value of  $n$  therefore merits some careful consideration. In the next section we will see how the properties of the disrupted star and the black hole in a TDE determine this as-yet-undetermined parameter in our analysis. Interestingly, the ZEBRA models admit a wider range of  $n$ -values than

the range ( $0 < n < 1$ ) consistent with ADIOS models.

### 5.3 ZEBRA models of TDE debris disks

The structure and evolution of a ZEBRA model for a TDE are governed by the total mass and angular momentum of the envelope, which change as matter falls back and is accreted or expelled in a jet. The total angular momentum and mass of the fallback disk are, respectively,  $\mathcal{L} = \int \ell \rho dV$  and  $\mathcal{M} = \int \rho dV$ , where  $dV$  is an infinitesimal volume element and the integral is taken over the whole fluid. Using the formalism and notation of the previous section, these can be written

$$\mathcal{L} = \frac{4\pi\rho_0\sqrt{aGM_h}}{r_0^{-q}} \int_0^{\pi/2} \int_{r_0}^{\mathcal{R}} r^{-q+5/2}(\sin^2\theta)^{\alpha+1} dr d\theta, \quad (5.11)$$

$$\mathcal{M} = \frac{4\pi\rho_0}{r_0^{-q}} \int_0^{\pi/2} \int_{r_0}^{\mathcal{R}} r^{-q+2}(\sin^2\theta)^{\alpha+1/2} dr d\theta, \quad (5.12)$$

where  $r_0$  is simultaneously the radius at which we specify the density and the inner radius of the disk, and  $\mathcal{R}$  denotes the outer radius. Due to the influence of the black hole, we expect  $r_0$  to be on the order of the Schwarzschild radius (or, more precisely, the location of the innermost stable circular orbit (Bardeen et al., 1972)), and so we will write  $r_0 = \chi 2GM_h/c^2$ , with  $\chi$  a pure number of order a few. To determine the outer radius, we compare the ability of the disk to transport energy via advection to its ability to transport energy via radiative diffusion.

Although the photosphere of the envelope may be radiating at close to the Eddington limit, the amount of energy generated in the interior of the disk will generally be much greater than that able to be carried via diffusion; specifically, the luminosity carried into the polar regions exceeds the Eddington limit by a factor of order  $\ln(\mathcal{R}/r_0)$  (Jaroszynski et al., 1980; Paczyński & Wiita, 1980; Sikora, 1981). The dominant mode of energy transport will therefore be turbulent advection. The advective flux can be written  $F_a = ypv$ , where  $p$  is the pressure,  $v$  is the local sound speed, and  $y$  is a number less than or of order one that describes the efficiency of advection (since we are really concerned with the flux of enthalpy, which is  $4p$  for a radiation-dominated gas,  $y$  could conceivably

be greater than 1). Since  $p \sim \rho v^2$  and the advective luminosity is  $L_a \sim 4\pi r^2 F_a$ , we have that  $L_a \sim 4\pi y r^2 \rho v^3$ . When the saturated advective luminosity becomes roughly equal to the Eddington limit, radiative diffusion will become the dominant mode of energy transport, allowing the disk to cool and become thin. Symbolically we have  $4\pi y_{max} r^2 \rho v^3 \sim 4\pi G c M_h / \kappa$ , where  $\kappa$  is the relevant opacity. In this case we will use the opacity for electron scattering, given by  $\kappa \approx 0.34 \text{ cm}^2/\text{g}$  for cosmological abundances. This definition is equivalent to that which defines the trapping radius – the point in the flow at which the diffusion timescale equals the advective timescale (Begelman, 1978). Fluid interior to this radius entrains photons, rendering them incapable of escaping.

In addition to having a magnitude, the advective flux has a directionality. Writing  $\mathbf{F}_a = F_a \hat{n}$ , the advective luminosity is obtained by integrating the dot-product of this vector over an area. Because we are concerned with the energy escaping from the hole, the relevant area is the two-sphere, and hence the only component of the flux relevant to the luminosity is that in the  $\hat{r}$ -direction. The quantity  $\hat{n} \cdot \hat{r}$  will, in general, depend on  $\theta$ , and in fact we expect it to be less than one as much of the flux is transported into the polar regions. Because we are unaware of the specifics of the directional dependence of the flux, we will simply incorporate those uncertainties into our efficiency factor  $y$ , letting  $\int y p v \hat{n} \cdot \hat{r} dS \equiv \bar{y} \int p v dS$ , where  $S$  is the two-sphere and  $\bar{y}$  is an effective efficiency. Performing the integrations, we find that the outer radius is given by

$$\mathcal{R}^{-q+1/2} = \frac{2c}{\kappa\sqrt{\pi}} \frac{\Gamma(\alpha + 3/2)}{\Gamma(\alpha + 1)} \frac{r_0^{-q}}{\rho_0 y \beta \sqrt{a G M_h}}. \quad (5.13)$$

The  $\Gamma$ -functions resulted from our integration of the angular dependence of  $p$  over the two-sphere, and for simplicity we replaced  $\bar{y}$  with  $y$ . Numerically we find that  $1 < (2/\sqrt{\pi})(\Gamma(\alpha+3/2)/\Gamma(\alpha+1)) < 2$  over permissible values of  $\alpha$ , so that its inclusion in our expression does not significantly alter our results. We will include the  $\Gamma$ -functions here, however, because they will simplify (visually) some of the relationships we will describe in later sections. To offer some insight into the meaning of the

previous expression, note that it may be written

$$\mathcal{R} \simeq \left(\frac{v_0}{c/\tau_0}\right)^{\frac{1}{q-1/2}} r_0, \quad (5.14)$$

where  $\tau_0$  is the optical depth and  $v_0$  is the local Keplerian velocity, both evaluated at  $r_0$ . From this form of the equation, it is evident that photons must be trapped at  $r_0$ , namely the inequality  $v_0 > c/\tau_0$  must hold, to ensure that our assumption about the radiative inefficiency of the flow be upheld.

Recall that  $1/2 < q < 1/(\gamma - 1)$ , a restriction that resulted from requiring the density to be finite at all angles and the energy generation rate to increase inwards. The adiabatic index of the gas will generally be between  $4/3$ , and  $5/3$ , meaning that  $1/(\gamma - 1) < 3$ , and consequently  $1/2 < q < 3$ . Returning to equations (5.11) and (5.12), we see that this range of  $q$  will always leave the lower bound on the radial integration, namely  $r_0$ , relatively unimportant (unless  $q$  is exactly 3, a case that we will have to consider separately) if  $\mathcal{R} \gg r_0$ , an assumption that we can check. With these considerations, we find for the total angular momentum and mass

$$\mathcal{L} = \frac{2\pi^{3/2}\rho_0\sqrt{aGM}\Gamma(\alpha+3/2)}{r_0^{-q}\Gamma(\alpha+2)} \frac{\mathcal{R}^{-q+7/2}}{-q+7/2}, \quad (5.15)$$

$$\mathcal{M} = \frac{2\pi^{3/2}\rho_0}{r_0^{-q}} \frac{\Gamma(\alpha+1)}{\Gamma(\alpha+3/2)} \frac{\mathcal{R}^{-q+3}}{-q+3}. \quad (5.16)$$

Solving for the radius of the disk in terms of the mass of the disk and the mass of the black hole, we find

$$\mathcal{R} = \left(\frac{y\kappa\beta\sqrt{a}(3-q)}{4\pi c}\mathcal{M}\sqrt{GM_h}\right)^{2/5} \quad (5.17)$$

$$\simeq 9 \times 10^{14} \left(\frac{\mathcal{M}}{M_\odot}\right)^{2/5} \left(\frac{M_h}{10^6 M_\odot}\right)^{1/5} \text{ cm}. \quad (5.18)$$

This relation yields  $\mathcal{R} \approx 10^3 r_s$ ,  $r_s$  being the Schwarzschild radius of the black hole, for  $M_h = 10^6 M_\odot$  and  $\mathcal{M} = 1M_\odot$ . Because we expect that  $r_0 \approx \text{few} \times r_s$ , we see that neglecting the lower bound in

the integrations of  $\mathcal{M}$  and  $\mathcal{L}$  was justified.

Our goal is to use the total mass and angular momentum, calculable from initial conditions, to determine  $q$ . This value will then inform us of how a larger progenitor star, a larger black hole, or more angular momentum will influence how steeply the density or pressure falls off with distance from the hole. By performing a bit of algebra, we can rearrange equations (5.13), (5.15), and (5.16) to yield

$$f(\mathcal{M}, \mathcal{L}, M_h) \equiv \left( \frac{y\kappa}{4\pi c} \right)^{1/6} \frac{\mathcal{M}\sqrt{GM_h}}{\mathcal{L}^{5/6}} = \frac{\Gamma(\alpha + 1)^{5/6}\Gamma(\alpha + 2)^{5/6}}{\beta^{1/6}a^{1/2}\Gamma(\alpha + 3/2)^{5/3}} \frac{(7/2 - q)^{5/6}}{3 - q}. \quad (5.19)$$

The left-hand side of this expression, denoted  $f(\mathcal{M}, \mathcal{L}, M_h)$ , depends only on the total mass of the disk, the total angular momentum of the disk, and the black hole mass (in addition to a few physical constants; note that its dependence on  $y$ , the parameter we introduced to describe the efficiency of convection, is to the 1/6th power, and therefore only affects our answers very weakly). The right-hand side, on the other hand, is only a function of  $q$ , which we could in principle invert to isolate  $q$  itself. The gross properties of the progenitor star and the black hole therefore determine the density, pressure, and angular momentum profiles of the fallback disks associated with super-Eddington TDEs.

In order to calculate  $q$  for a given TDE, we need to parametrize the total mass and angular momentum in terms of those values appropriate to a certain event, both of which will depend on the progenitor star. In order to be tidally disrupted, the star must pass within the tidal radius  $r_t \approx R_*(M_h/M_*)^{1/3}$  of the black hole, where  $R_*$  is the stellar radius and  $M_*$  is its mass (the precise point of disruption clearly depends on the details of the stellar composition, rotation, and other complications, but numerical results indicate that the true location does not vary from that given by more than a factor of  $\sim 1.5$  for realistic interiors; Ivanov & Novikov 2001). Due to the tidal force on the star and the tidal potential, nearly half of the stellar debris is ejected from the black hole on hyperbolic orbits (Lacy et al., 1982). The other half remains bound to the SMBH. The initial mass of the disk should therefore be on the order of  $\mathcal{M} \approx M_*/2$ , though the actual amount

should be slightly less than this when we account for material that has already been accreted and the still-raining-down debris outside  $\mathcal{R}$  (see section 4). At the tidal radius, conservation of energy dictates that the star has a velocity of  $v_* = \sqrt{2GM_h/r_t}$ , and hence the disk material has a total angular momentum of  $\mathcal{L} \approx M_* \sqrt{GM_h R_*/2} (M_h/M_*)^{1/6}$  (again, this is a slight overestimate). By parametrizing the mass and angular momentum as such, equation (5.19) becomes

$$5y^{1/6} \frac{M_{*\odot}^{11/36}}{M_6^{1/18} R_{*\odot}^{5/12}} = \frac{\Gamma(\alpha+1)^{5/6} \Gamma(\alpha+2)^{5/6} (7/2-q)^{5/6}}{\beta^{1/6} a^{1/2} \Gamma(\alpha+3/2)^{5/3} (3-q)}. \quad (5.20)$$

Here  $M_{*\odot}$  is the progenitor's mass in units of solar masses,  $R_{*\odot}$  is its radius in units of solar radii, and  $M_6$  is the black hole mass in units of  $10^6 M_\odot$ . Interestingly, the left-hand side is virtually independent of the black hole mass, meaning that the density and pressure distributions of TDE fallback disks are almost exclusively determined by the progenitor star.

Figure 5.1 illustrates the value of  $q$  obtained as we vary the function  $f(\mathcal{M}, \mathcal{L}, M_h)$ . As we increase  $f(\mathcal{M}, \mathcal{L}, M_h)$ , the value of  $q$  approaches  $q \rightarrow 1/(\gamma - 1)$ . By analyzing equation (7.15), we can show that  $\alpha = 0$  for this value of  $q$ ; recalling that  $\rho \propto (\sin^2 \theta)^\alpha$ , we see that the flow is spherically symmetric. This result makes sense when we realize that, in order for  $f(\mathcal{M}, \mathcal{L}, M_h)$  to approach large values, the angular momentum must be very small.

The value of  $q$  rapidly decreases as we decrease  $f$ . Recalling our lower limit on  $q$ , namely that  $q > 1/2$ , we see that there is a lower limit on the value of the left-hand side of (5.19) which is, after further investigation of Figure 5.1, nearly independent of the adiabatic index. Numerically we find

$$y^{1/6} \frac{\mathcal{M} \sqrt{GM}}{\mathcal{L}^{5/6}} \gtrsim \begin{cases} 179 & \text{for } \gamma = 5/3 \\ 163 & \text{for } \gamma = 4/3 \end{cases}, \quad (5.21)$$

where we have used the opacity for Thomson scattering and the units are cgs. If one violates these lower bounds, our model ceases to describe the disk adequately. We can show that, if the inequality is not satisfied, then  $\mathcal{R} < R_c$ , where  $R_c = \mathcal{L}^2/(GM_h \mathcal{M}^2)$  is the circularization radius, which is

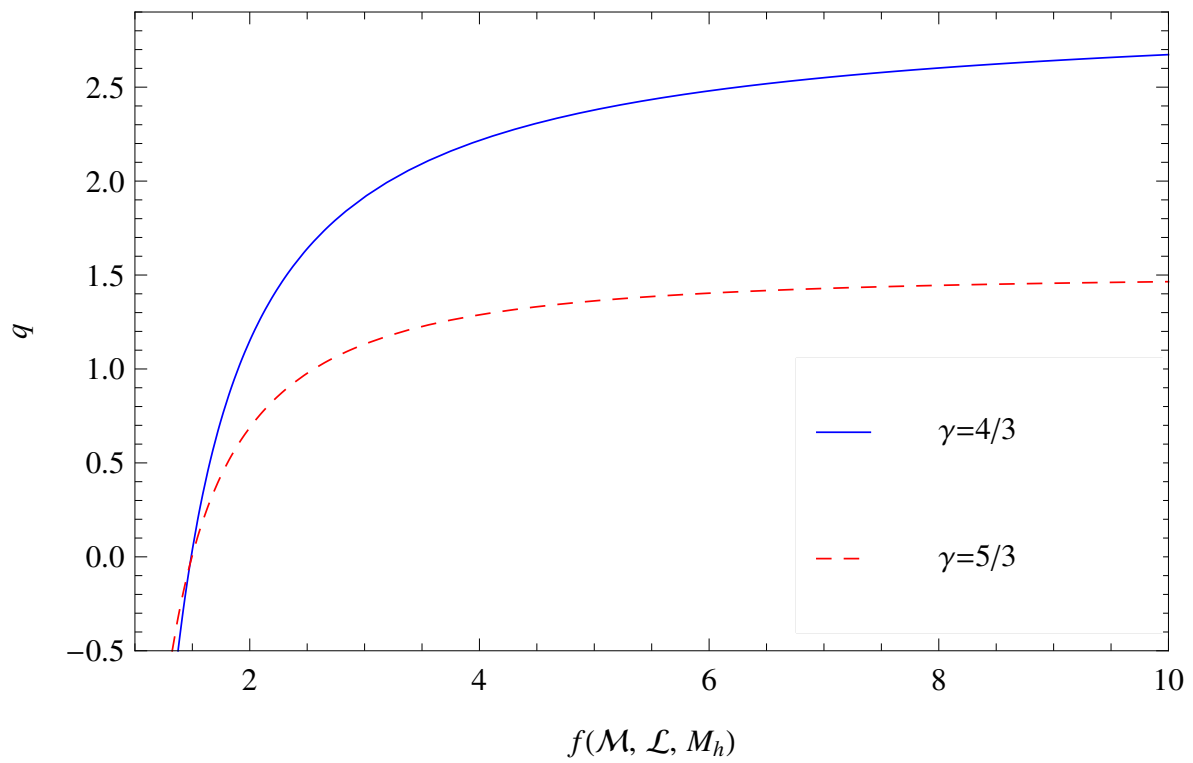


Figure 5.1: The value of  $q$  obtained for  $\gamma = 4/3$  (blue, solid) and  $\gamma = 5/3$  (red, dashed) as we vary the left-hand side of equation (5.19).

obtained by balancing gravity and the centrifugal force. When  $f(\mathcal{M}, \mathcal{L}, M_h)$ , defined in equation (5.19), falls below this critical value, pressure forces play a negligible role in the dynamics of the system, and the disk becomes thin. It is therefore no surprise that our model breaks down in this limit.

The total mass and angular momentum of the disk thus determine the large scale properties of the envelope, which in turn determine the density and pressure profiles. Extrapolating these profiles to the region of the disk near the black hole, we can estimate conditions in the vicinity of the innermost stable circular orbit, which then quantify the accretion rate and rate of energy generation. Because any further absorption of energy would lead to a positive Bernoulli parameter and unbind the envelope (see Appendix B for notions concerning non-zero Bernoulli parameter), we conjecture that the accretion energy must escape through the funnel in the form of a fast jet.

We would like to be able to say something about the properties of this jet. Also, the accretion of the black hole and the continual fallback of material outside the envelope (at a rate roughly proportional to  $t^{-5/3}$  for later times) are changing the mass and angular momentum of the system; the values of  $q$  resulting from this section should therefore be interpreted as initial, or bulk, parameters. By modeling the mass and angular momentum of the disk in a time-dependent manner, we will be able to gain some insight into possible observational diagnostics one could use to infer the presence of a ZEBRA flow.

## 5.4 Jet properties and temporal evolution

### 5.4.1 Inner regions of the accretion disk

In the above analysis we assumed that ignoring the inner regions of the accretion disk, where general relativistic effects become important, was permissible. In those regions, however, we know that the angular momentum must exceed its Keplerian value, i.e., that with  $\phi = -GM_h/r$ , to account for the stronger gravitational acceleration. This excess of angular momentum at smaller radii and its interplay with the pressure gradient could, in principle, significantly alter the flow at

larger radii and change our results.

Models that investigated the inner regions of thick disks around black holes, termed “Polish doughnuts”, were developed in the late 1970’s and early 80’s, and research along these lines continues to the present day (Abramowicz et al., 1978; Kozłowski et al., 1978; Paczyński & Wiita, 1980; Jaroszynski et al., 1980; Paczynski & Abramowicz, 1982; Komissarov, 2006; Qian et al., 2009; Abramowicz & Fragile, 2013; Pugliese et al., 2013). In these models, authors assume ad hoc forms for both the specific entropy and angular momentum, and from these functional forms one may infer the pressure and density from the relativistic energy and momentum conservation equations. The portion of the ZEBRA envelope closest to the black hole should in many respects resemble a Polish doughnut, with the extra constraint that the flow has zero Bernoulli function. Instead of pursuing the lines followed by many authors in examining the consequences of the relativistic conservation equations, we will follow a slightly different route which incorporates our model.

To analyze the specifics of the flow near the black hole and its impact on the outer regions of the envelope, we will restrict our attention to the case where the space-time metric is that of Schwarzschild. With this assumption, we then replace the standard point-mass potential with the “pseudo-Newtonian” potential of Paczyński & Wiita (1980), so  $\phi \rightarrow -GM_h/(r - r_s)$ , where  $r_s = 2GM_h/c^2$  is the Schwarzschild radius. While this potential tends to produce inaccurate numbers for some quantities (Tejeda & Rosswog, 2013), its prediction of the innermost stable circular orbit and the marginally bound orbit suffice for our treatment.

By manipulating the momentum and Bernoulli equations with this potential, we can show that the most general form of the angular momentum must satisfy  $\ell^2(r, \theta) = \ell^2(\phi r^2 \sin^2 \theta)$ , i.e., the angular momentum is only a function of the combination  $\phi r^2 \sin^2 \theta$  (note that this result is consistent with equation (A.10) in which a specific basis set for the functions is used). In the self-similar limit, we showed that  $\ell^2 = a\phi r^2 \sin^2 \theta$ . However, in addition to approaching the self-similar value in the  $r \rightarrow \infty$  limit, the angular momentum must also match that of the pseudo-Newtonian distribution (that with the Paczyński-Wiita potential but without a pressure gradient) at some inner radius where the pressure gradient goes to zero. Because the self-similar solution will not

necessarily satisfy the second condition, we must search for non-self-similar distributions. The specific form we will adopt is  $\ell^2 = A + D GM_h r^2 / (r - r_s)$ , where  $A$  and  $D$  are constants and we are restricting our attention to the equatorial plane. In general the angular momentum distribution could be more complicated. However, it must monotonically increase with radius throughout – a decrease in the specific angular momentum with radius is highly unstable to convection (Goldreich & Schubert, 1967; Seguin, 1975), unless it is accompanied by a strong increase in entropy, which is unlikely. It must also approach the self-similar solution in the asymptotic limit. The previous form is the simplest that satisfies both of these criteria.

Requiring that the angular momentum approach its self-similar value for large  $r$  yields  $D = a$ , where  $a$  is given by equation (5.10). With our specific form for the angular momentum, we can manipulate the momentum equations to find exact expressions for both the density and the pressure. Setting the pressure gradient equal to zero at some radius  $r_m$  where  $\ell^2(r_m) = \ell_{PN}^2(r_m)$ , where  $\ell_{PN}^2 = 2GM_h r / (r - r_s)^2$  is the pseudo-Newtonian angular momentum, yields  $A = 8GM_h r_s (1 - a/2)$  and  $r_m = 2r_s$ , which is the marginally bound orbit. Our solution for the self-consistent angular momentum is thus

$$\ell^2 = GM_h \left( 4r_s(2 - a) + \frac{ar^2}{r - r_s} \right). \quad (5.22)$$

Figure 5.2 illustrates three different angular momentum distributions for a given set of parameters: that given in equation (5.22), the self-similar solution, and the pseudo-Newtonian distribution. As we can see, the self-consistent model flattens out in the inner region to exceed both the pseudo-Newtonian distribution and the self-similar angular momentum.

It may seem like this excess of specific angular momentum could alter significantly our estimates of  $q$ ,  $\mathcal{R}$ , and other properties of the envelope. However, the two conserved quantities in a tidal disruption event are the **total** angular momentum and **total** mass, and it is not clear how much these differ from those in the self-similar limit. Therefore, to answer whether or not this modified potential truly affects our results, we must also determine how the density varies in

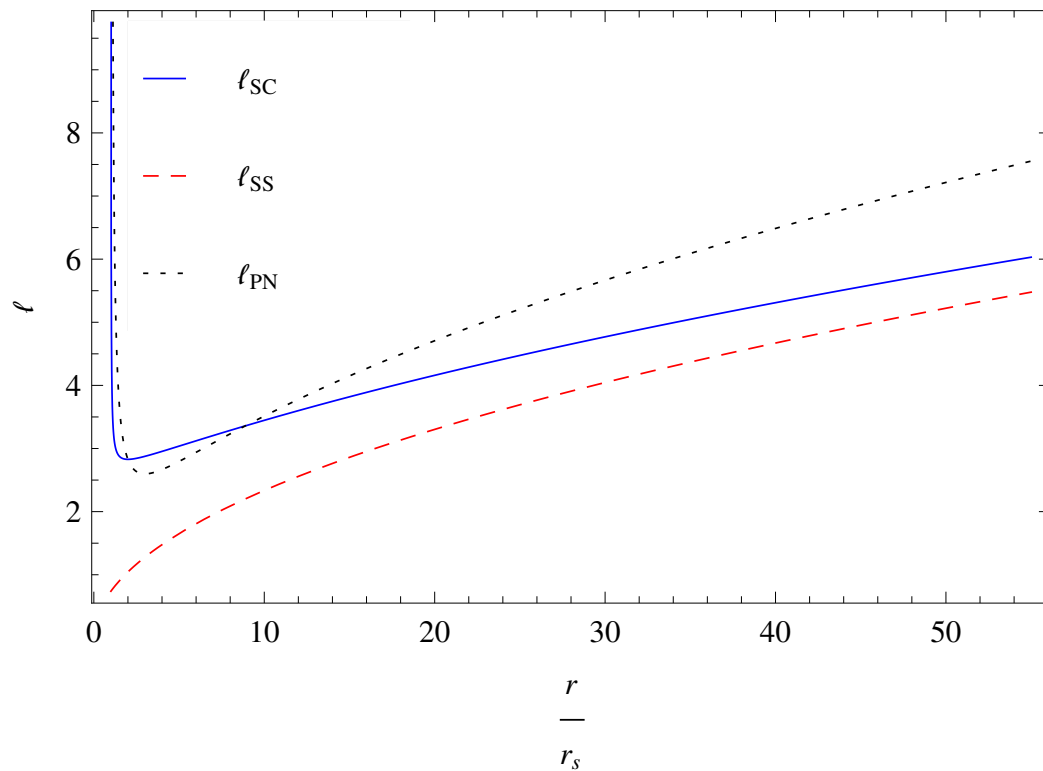


Figure 5.2: The self-consistent model (equation (5.22)) for the angular momentum (blue, solid), the self-similar model (red, dashed), and the psuedo-Newtonian distribution (black, dotted). Here we've set  $q = 1.5$ ,  $\gamma = 4/3$ , the abscissa is in units of Schwarzschild radii, and the angular momentum is normalized by  $\sqrt{GM_h r_s}$ .

the self-consistent limit. After evaluating the density, we can form the integrals  $\int^r 4\pi r^2 \rho dr$  and  $\int^r 4\pi r^2 \ell \rho dr$  to obtain the enclosed mass and angular momentum as functions of  $r$ , respectively (the lower bound will not significantly affect the result in either case). By comparing these functions to their analogs in the self-similar limit, we can assess how significantly the pseudo-Newtonian potential affects our conclusions.

Figure 5.3 displays the density for both the self-consistent (using equation (5.22) for the angular momentum) and self-similar solutions. At small radii strong gravity reduces the density from that in the self-similar limit, while at large radii they are indistinguishable. Figure 5.4 illustrates the total mass contained within  $r$  for the self-similar and non-self-similar models, while Figure 5.5 shows the total angular momentum contained within  $r$  for both models. The self-consistent model predicts an increased amount of mass and angular momentum at larger radii, which is due to a slight increase in its density, relative to the self-similar solution, at intermediate radii. This means that the use of the Pascyński-Wiita potential makes a more compact ZEBRA (in other words, we would enclose the same amount of mass and angular momentum, fixed by the TDE, at a smaller radius). However, we do not believe that this alteration will change our results much, as the physics is largely dictated by the ratio of the total angular momentum to mass, which is conserved from the TDE. Thus, while relativity can alter significantly the behavior of the density, pressure, and angular momentum at small radii, its effects on the bulk properties of the ZEBRA are minimal. We therefore expect that its inclusion in our models will not significantly change the results.

If the Bernoulli parameter were very small (compared to  $GM_h/r$ ) all the way to the black hole, the gas would release little energy in the form of a jet. However, we expect that this is not realistic, and that fluctuations in the inner part of the flow will lead to the root-mean-squared value of the binding energy being some significant fraction of that for the innermost stable circular orbit (ISCO) ( $= 6GM_h/c^2$  for a Schwarzschild black hole). To quantify this statement, recall that, for a

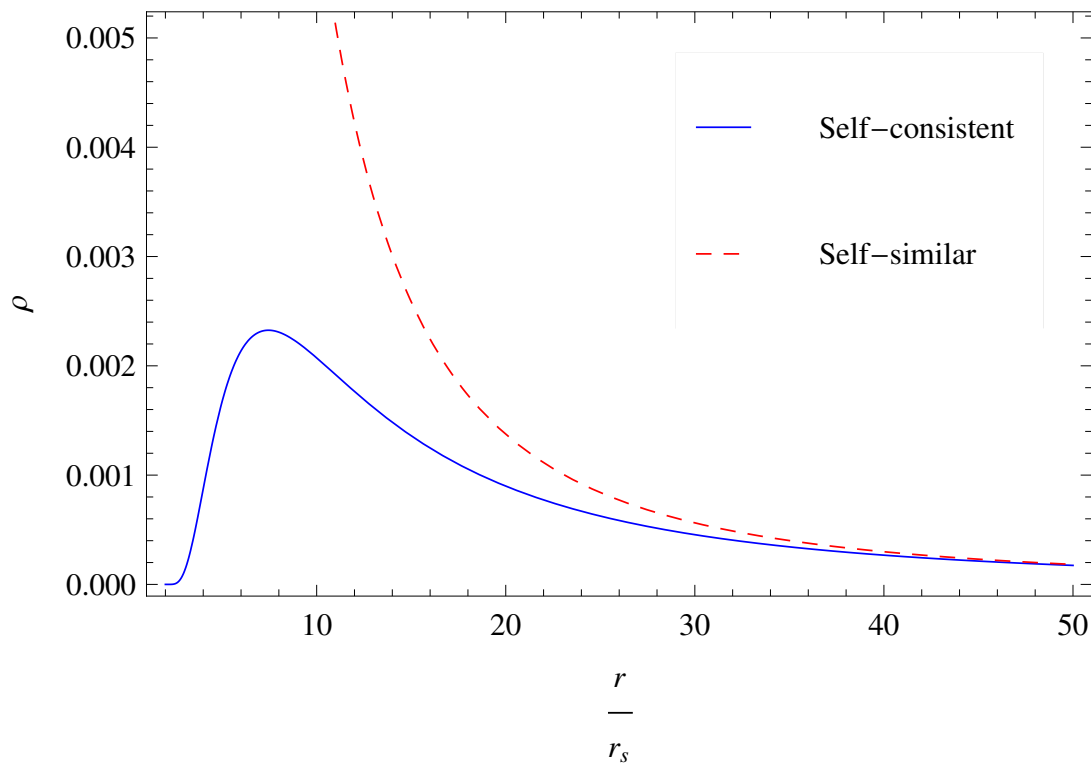


Figure 5.3: Solutions for the density in the non-self-similar (blue, solid) and self-similar (red, dashed) limits. Here  $q = 1.5$ ,  $\gamma = 4/3$ , the x-axis is in units of Schwarzschild radii, and the density is measured in units such that  $\rho_0 (r_s/r_0)^{-q} = 1$ , i.e., the red, dashed curve is simply  $(r/r_s)^{-2.2}$ .

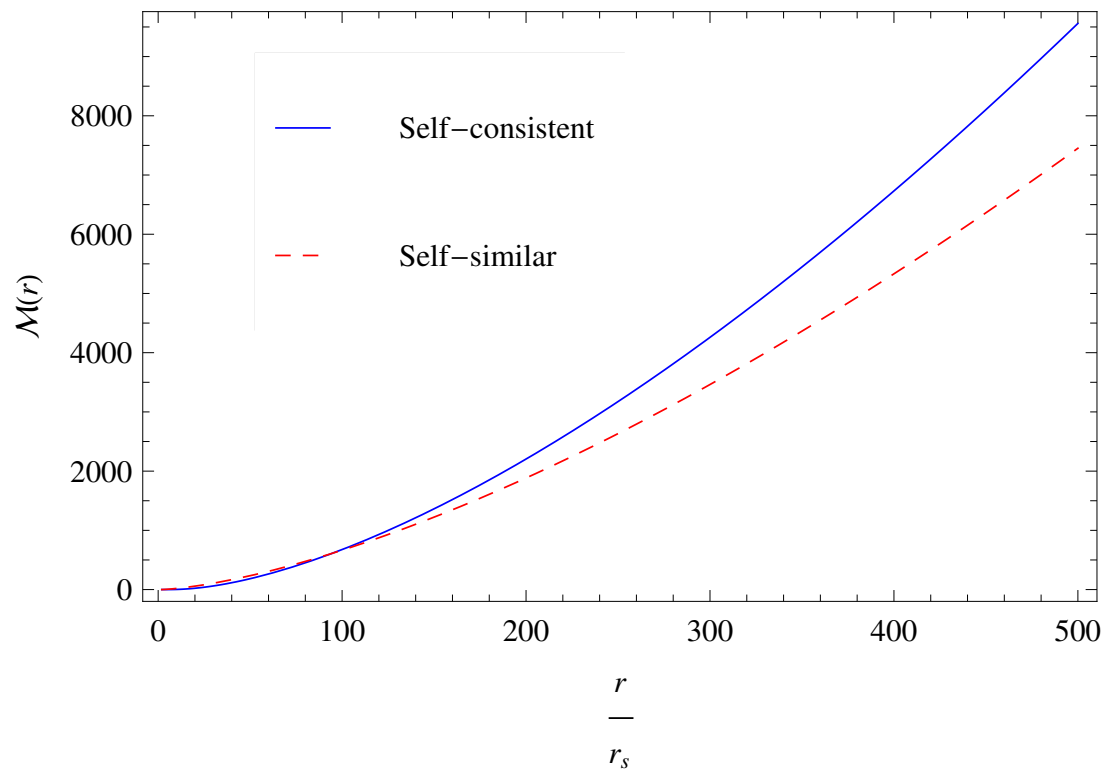


Figure 5.4: The mass contained within  $r$  for the angular momentum given in equation (5.22) (blue, solid) and that for the self-similar model (red, dashed). The parameters are the same as those in Figure 5.3, with the same normalization for the density.

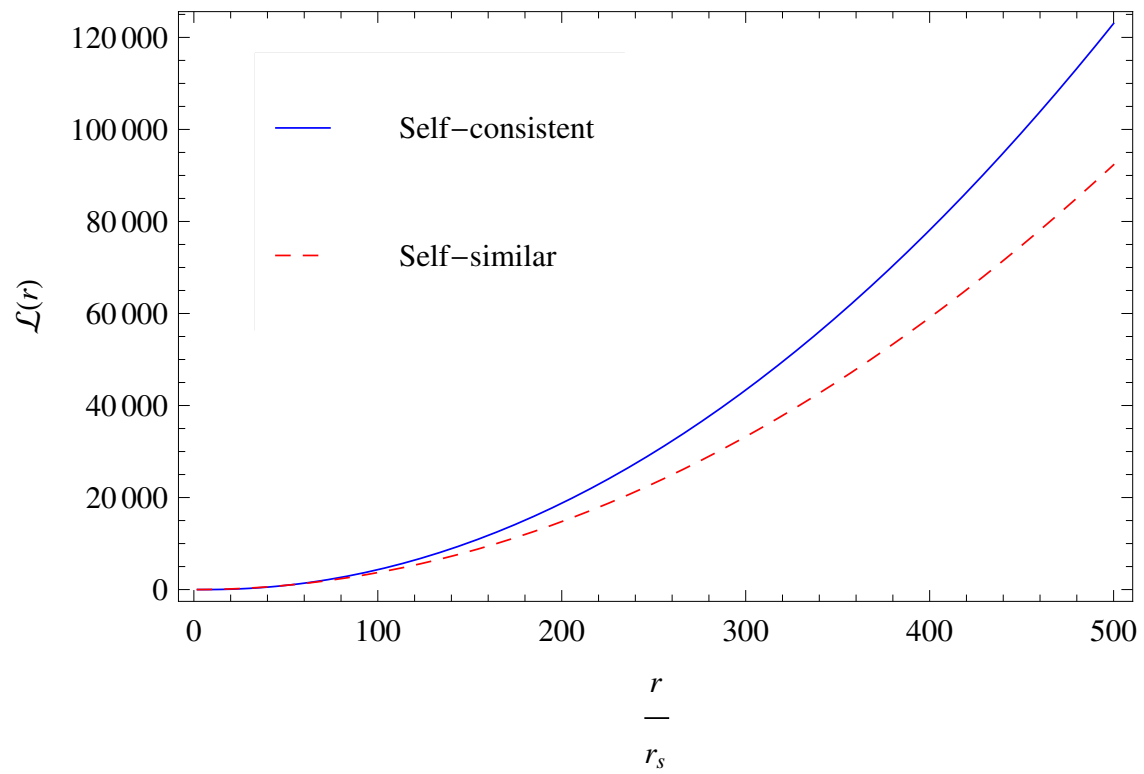


Figure 5.5: The angular momentum contained within  $r$  for the self-consistent model (blue, solid) and the self-similar solution (red, dashed). The parameters and normalization are the same as those in Figure 5.3.

non-steady flow, an additional term must be added to the Bernoulli function:

$$B \rightarrow \overline{B} + \int \frac{\partial \mathbf{v}}{\partial t} \cdot d\mathbf{r}, \quad (5.23)$$

where the integral is taken over the flow line of the fluid element. In terms of scalings, this term is on the order

$$\int \frac{\partial \mathbf{v}}{\partial t} \cdot d\mathbf{r} \sim \frac{\Delta v r}{\tau_d}. \quad (5.24)$$

Here  $\Delta v$  is the change in the velocity over the dynamical timescale,  $\tau_d$ , and  $r$  is the radius at which we are considering the (predominantly circular) flow line. Using  $\tau_d \sim r/v$  and  $\Delta v \sim v$ , we find  $\Delta v r/\tau_d \sim v^2$  (there is also a term, of order  $\sim v^2$ , that arises from the inclusion of the  $\mathbf{v} \cdot \nabla \mathbf{v}$  term in the momentum equation; however, because it is of the same order as the time derivative, it suffices to consider only this term). At the ISCO and regions interior to that radius, this fluctuation term can reach substantial fractions of  $c^2$ . Because the change in velocity can be either positive or negative, the average will cancel out over the whole flow. The root-mean-squared of the additional term will not cancel, however, and will lead to fluctuations that lead to both positive and negative Bernoulli parameter. The fluctuations to the negative side give rise to bound flows, which then release that energy in the form of a very energetic jet.

As in the case of ADIOS models (Blandford & Begelman, 2004), the mechanism responsible for this energy dissipation is not specified — its existence and nature will have to be verified later. Once this energy is injected, however, its escape will most likely be in the form of a jet due to the rotational funnel. Inside the radius at which the material becomes bound, our previous model breaks down. Because this region constitutes a minute fraction of the disk, we do not expect that its presence will have much of an impact on our results.

### 5.4.2 Accretion rate and jet power

We derived the density, pressure, and angular momentum distributions for ZEBRA envelopes under the assumption that the poloidal and radial velocities were significantly less than that in the azimuthal direction. While this proposition is upheld in the bulk of the flow, it must break down in regions near the SMBH, specifically in those regions where relativity prevents the existence of stable circular orbits. It follows that the radial velocity in this region should be appropriate to that of gravitational free-fall, or  $v_r \sim \sqrt{GM_h/r}$ .

To make contact with the self-similar region of the flow, we will take  $r_0$  to be the radius at which gravitational infall becomes substantial, and we have  $v_{r_0} = \delta \sqrt{GM_h/r_0}$ , where  $\delta$  is a number less than one. With this assumption, the mass accretion rate onto the black hole should be on the order of that in the spherically symmetric regime, or  $\dot{M}_{acc} = 4\pi r_0^2 \rho v_{r_0}$ . Plugging in our expressions for relevant quantities, we find

$$\dot{M}_{acc} = 4\pi\delta\rho_0\sqrt{GM_h}r_0^{3/2}. \quad (5.25)$$

We can solve for  $\rho_0$  in terms of the inner radius, the total mass of the disk and the mass of the black hole. Doing so and putting the expression into the equation for  $\dot{M}_{acc}$  yields

$$\dot{M}_{acc} = \delta \chi^{3/2-q} \mathcal{M} \sqrt{GM_h} \left( \frac{2GM_h}{c^2} \right)^{3/2-q} \times \left( \frac{y\sigma_T}{4\pi cm_p} \mathcal{M} \sqrt{GM_h} \right)^{-\frac{2}{5}(3-q)} h(q), \quad (5.26)$$

where

$$h(q) \equiv \frac{2}{\sqrt{\pi}} \frac{\Gamma(\alpha + 3/2)(3-q)}{\Gamma(\alpha + 1)} \left( (3-q)\beta\sqrt{a} \right)^{-\frac{2}{5}(3-q)}, \quad (5.27)$$

which is a function only of  $q$  and  $\gamma$ . We have also parametrized the inner radius in terms of the Schwarzschild radius, viz.  $r_0 = \chi 2GM_h/c^2$ .

The jet luminosity is given by  $L_j = \epsilon \dot{M}_{acc} c^2$ , where  $\epsilon$  is the accretion efficiency of the black hole. To arrive at this result it was necessary to introduce a number of factors that relate to our

uncertainty of the details of the flow, namely  $\epsilon$ , the radiative efficiency,  $\chi$ , the inner edge of the disk,  $\delta$ , the fraction of free-fall of the velocity, and  $y$ , the advective efficiency. However, we expect that  $\epsilon$ ,  $\delta$ , and  $y$  are somewhere in the range of 0.01 – 1.0, and we know that  $\chi$  should be on the order of a few (strictly, this value and the radiative efficiency depend on the spin of the hole and its orientation relative to the disk). Therefore, although we have a number of unknowns, their range in parameter space is rather small. Explicitly we find for the jet power

$$L_j = \mu \mathcal{M} c^2 \sqrt{GM_h} \left( \frac{2GM_h}{c^2} \right)^{3/2-q} \times \left( \frac{\sigma_T}{4\pi c m_p} \mathcal{M} \sqrt{GM_h} \right)^{-\frac{2}{5}(3-q)} h(q), \quad (5.28)$$

where we set  $\mu \equiv \epsilon \delta \chi^{3/2-q} y^{-2(3-q)/5}$  for compactness. For a solar progenitor, a million-solar-mass black hole,  $y = 0.5$ ,  $\delta = 0.05$ , and  $\epsilon = 0.1$ , we find  $L_j \approx 5 \times 10^{47}$  erg s<sup>-1</sup>  $\approx 4 \times 10^3 L_{Edd}$  for the jet luminosity, where  $L_{Edd} = 4\pi G c M_h m_p / \sigma_T$  is the Eddington luminosity of the black hole assuming ionized hydrogen (here we have solved equation (5.20) to determine the value of  $q$ , which, for these numbers, is  $q \approx 2.4$ ).

### 5.4.3 Time-dependent analysis

In order to be tidally disrupted, the stellar progenitor must pass within a pericenter distance of  $r_p = x r_t$ , where  $r_t = R_*(M_h/M_*)^{1/3}$  is the tidal radius and  $x$  is a number that is less than or about one. Here we will restrict our attention to the case where  $x = 1$ . Our motivation for doing so is that other authors have shown, using hydrodynamical simulations, that the complexities of the encounter for smaller and larger  $x$  render an analytical treatment insufficient for describing the physics of the TDE (Guillochon & Ramirez-Ruiz, 2013). Because running a numerical simulation to determine the exact feeding rate to the ZEBRA is outside the scope of this paper, we will only consider those disruptions which occur exactly at the tidal disruption radius and maintain that the analytical approach is accurate enough for our purposes.

After the star is disrupted, the most tightly bound material is placed on an orbit with semi-major axis  $R_i = (R_*/2)(M_h/M_*)^{2/3}$  (see section 1 for a derivation). Because the point of disruption occurs at the tidal disruption radius, the eccentricity of this orbit is very large. Other less-bound

gas parcels (those with larger semi-major axes) are thus on nearly-parabolic orbits as they recede from the hole. The initial configuration of the tidally-stripped material that is going to fall back is therefore a thin, highly-elliptical disk, confined roughly to the plane occupied by the disrupted star.

When the innermost gas undergoes one complete orbit, shock heating and other effects (see Introduction) begin to circularize the orbits and alter the structure of the debris disk. After a certain amount of time has passed, on the order of a few orbits of the innermost material, the heating causes the disk to puff up into a spheroid of radius  $\mathcal{R}_0$  – this is the ZEBRA. In the previous sections we assumed, for simplicity, that the entire mass that is bound to the black hole (nearly half the stellar progenitor) comprised the ZEBRA. However, because tidally-stripped material is continually falling back onto the accretion region, it is not clear that this assumption is valid.

To determine how much mass is contained in the initial ZEBRA and the rate at which material is falling back onto the accretion region, we will pursue a line of analysis similar to that in Lodato et al. (2009), and consider the star at the time of disruption. At this point in time, the center of mass is at the tidal radius, and, assuming the star is on a parabolic orbit, the binding energy of the center of mass is zero. Denote the position of a gas parcel contained in the star by  $r_g = r_t - \eta R_*$ ;  $\eta = 1$  is the edge of the star closest to the hole,  $\eta = -1$  is that farthest from the hole, and we are restricting our attention to the plane of the orbit. The specific gravitational energy of a gas parcel is then given by

$$\epsilon_p = \frac{GM_h}{r_t} - \frac{GM_h}{r_t - \eta R_*} \quad (5.29)$$

$$\simeq -\frac{GM_h R_*}{r_t^2} \eta, \quad (5.30)$$

where in the final line we approximated the tidal radius as being much greater than the stellar radius, valid for the supermassive black holes we are considering. After disruption, the gas parcels fly apart, cooling adiabatically and occupying roughly Keplerian orbits. The energy-period relation

for Keplerian orbits yields the semi-major axes of these orbits:

$$R_p = \frac{R_*}{2\eta} \left( \frac{M_h}{M_*} \right)^{2/3} = \left( \frac{\sqrt{GM_h}}{2\pi} \right)^{2/3} t^{2/3}, \quad (5.31)$$

where  $t$  is the fallback time. Note that, by inserting  $\eta = 1$ , this expression reproduces the correct orbit for the most tightly bound debris.

The rate at which material returns to pericenter is found by using the chain rule, specifically  $dM/dt = (dM/d\eta)(d\eta/dt)$ . From equation (5.31), we can readily determine  $d\eta/dt$ . To calculate  $dM/d\eta$ , we will assume that the stellar progenitor is well-approximated by a polytropic equation of state; a number of authors have shown that the equation of state of the star has important consequences for the rate of return of material, and so it is not adequate simply to consider a constant-density profile (Lodato et al., 2009; MacLeod et al., 2012; Bogdanović et al., 2014; Guillochon & Ramirez-Ruiz, 2013). In this case,  $\rho(R) = \lambda \theta^{1/(\gamma_*-1)}$ , where  $\lambda$  is the density at the center of the star,  $\gamma_*$  is the polytropic index of the gas that comprises the star, and  $\theta(R)$  is the solution to the Lane-Emden equation.  $R$  is spherical distance measured from the center of the stellar object. We will parametrize the location of a gas parcel within the star in terms of the variables  $R$ ,  $r$  and  $z$ , where  $r$  is the distance from the center of the star in the plane of the orbit and  $z$  is the distance perpendicular from the plane of the orbit (see Figure 5.6 for clarification). Using the fact that  $dM = \rho dV$ , where  $dV = 2\pi z dz dr$  is the volume element, and making simple geometric substitutions, we can show that

$$\frac{dM}{d\eta} = 2\pi \int_{\eta R_*}^{R_*} \rho R dR \quad (5.32)$$

$$= \frac{M_* \xi_1}{2} \frac{\int_{\eta \xi_1}^{\xi_1} \theta^{\frac{1}{\gamma_*-1}} \xi d\xi}{\int_0^{\xi_1} \theta^{\frac{1}{\gamma_*-1}} \xi^2 d\xi}, \quad (5.33)$$

where  $\xi$  is the dimensionless radius defined through the Lane-Emden equation and  $\xi_1$  is the first root of  $\theta(\xi)$  (see, e.g., Hansen et al. 2004). Putting everything together, we obtain for the mass

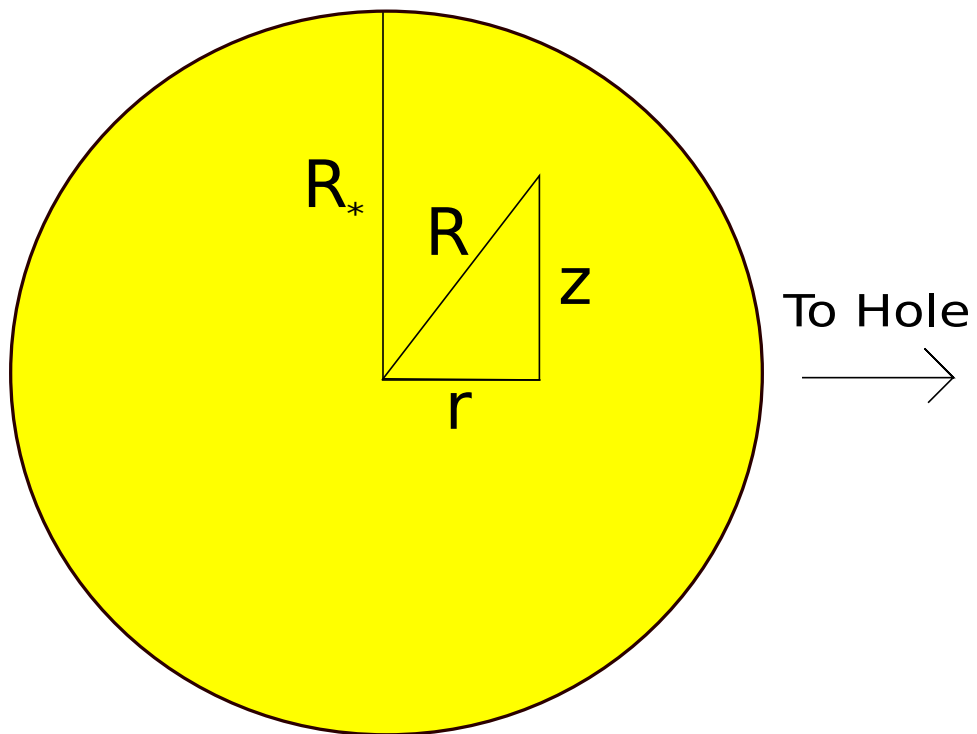


Figure 5.6: A schematic of the star at the time of disruption to illustrate the geometry. Note that  $r = \eta R_*$ .

rate of return

$$\frac{dM}{dt} = \frac{M_* R_* \xi_1}{6} \left( \frac{2\pi M_h}{M_* \sqrt{GM_h}} \right)^{2/3} t^{-5/3} \times \frac{\int_{\eta \xi_1}^{\xi_1} \theta^{\frac{1}{\gamma_*-1}} \xi d\xi}{\int_0^{\xi_1} \theta^{\frac{1}{\gamma_*-1}} \xi^2 d\xi} = \dot{M}_{fb}. \quad (5.34)$$

This expression gives the rate at which material is drained from the tidally-disrupted debris cloud and added to the ZEBRA. Note that equation (5.34) only holds for  $\eta < 1$ , or for times  $t > t_r$ , where

$$t_r = \left( \frac{R_*}{2} \right)^{3/2} \frac{2\pi M_h}{M_* \sqrt{GM_h}} \quad (5.35)$$

is the time taken for the innermost material to undergo one complete orbit. Noting that the original mass contained in the bound tidally-disrupted material is roughly  $M_*/2$ , we can write an expression for the remaining mass that is still raining down onto the ZEBRA after a time  $t$ :

$$M_{fb}(t) = \frac{M_*}{2} - \int_{t_r}^t \frac{dM}{dt'} dt', \quad (5.36)$$

where  $dM/dt'$  is given by expression (5.34) with  $t \rightarrow t'$ .

The jet and black hole are also extracting angular momentum from the disk. However, it is necessary for the disk material to transport a large amount of its angular momentum outwards, via viscous or magnetic processes (neither of which we have attempted to include in this model) in order to be accreted by the black hole. The angular momentum of the disk material is thus nearly unaffected by the presence of the hole. However, as we noted previously, natal stellar material is still falling back onto the envelope. As we have assumed that hydrodynamic effects have only influenced the particles in the region of the ZEBRA envelope, this material still approximately retains its specific angular momentum from the time of disruption, adding this angular momentum to the disk as it falls back. Using equation (5.36), we find for the total angular momentum as a function of time

$$\mathcal{L} = \sqrt{2GM_h R_*} \left( \frac{M_h}{M_*} \right)^{1/6} \left( \frac{M_*}{2} - M_{fb}(t) \right) \quad (5.37)$$

After the ZEBRA has inflated to a radius  $\mathcal{R}_0$ , the envelope will not only lose mass to the black hole at the rate described by equation (5.26), but it will also gain mass at the expense of the tidally-stripped debris that is still falling back. We can solve for  $\mathcal{M}$  in terms of other quantities by rearranging equation (5.19), and our differential equation for  $q$  is then  $\dot{\mathcal{M}} = dM/dt - \dot{M}_{acc}$ , where  $dM/dt$  is given by equation (5.34) and  $\dot{M}_{acc}$  by equation (5.26). To solve this differential equation, we need an initial value for  $q$ . This initial condition can be determined by assuming that the ZEBRA takes some time to inflate, at which point it has some mass and angular momentum, which in turn yield an initial  $q$ . However, the time to inflate depends sensitively on the heating rates and other physical processes, for which we do not have a reliable model. We also expect that any knowledge of the initial conditions should be lost after a certain amount of time, and that they should only reflect a transient initial behavior. We will therefore leave the initial value of  $q$ , which we will denote  $q_0$ , as an unspecified parameter, and only when systems with different  $q_0$  converge on a single solution will we consider our models accurate. After numerically integrating the differential equation for  $q(t)$ , we can go on to compute  $\mathcal{M}(t)$ ,  $\mathcal{L}(t)$  and  $L_j(t)$ .

Figure 5.7 demonstrates how  $q(t)$  changes as we alter  $q_0$  for a solar progenitor, a  $10^5 M_\odot$  black hole, and a number of other input values. As expected, the initial conditions strongly influence the behavior of  $q(t)$  for early times, but, after about 0.1 years, which is about  $2.5 t_r$  for this configuration, the different values become indistinguishable. We can thus say with confidence that after this time our models represent the fully-inflated ZEBRA. This timescale, namely a few revolutions of the innermost material, is also consistent with our expectations concerning the amount of time needed for the shock heating to add enough energy to the system. Figure 5.8 shows  $q(t)$  for various black hole masses and a set of fiducial parameters. The initial conditions cause  $q(t)$  to decrease rapidly. However, the knowledge of such initial conditions is quickly lost, and the system settles into a state in which  $q(t)$  decreases less rapidly. Figure 5.9 shows the mass contained in the envelope as a function of time. Because the fallback rate exceeds the accretion rate, the mass initially increases rapidly. For later times, the accretion rate and the fallback rate both drop significantly enough to leave a roughly constant mass. Figure 5.10 plots the jet luminosity; as we can see, the luminosity

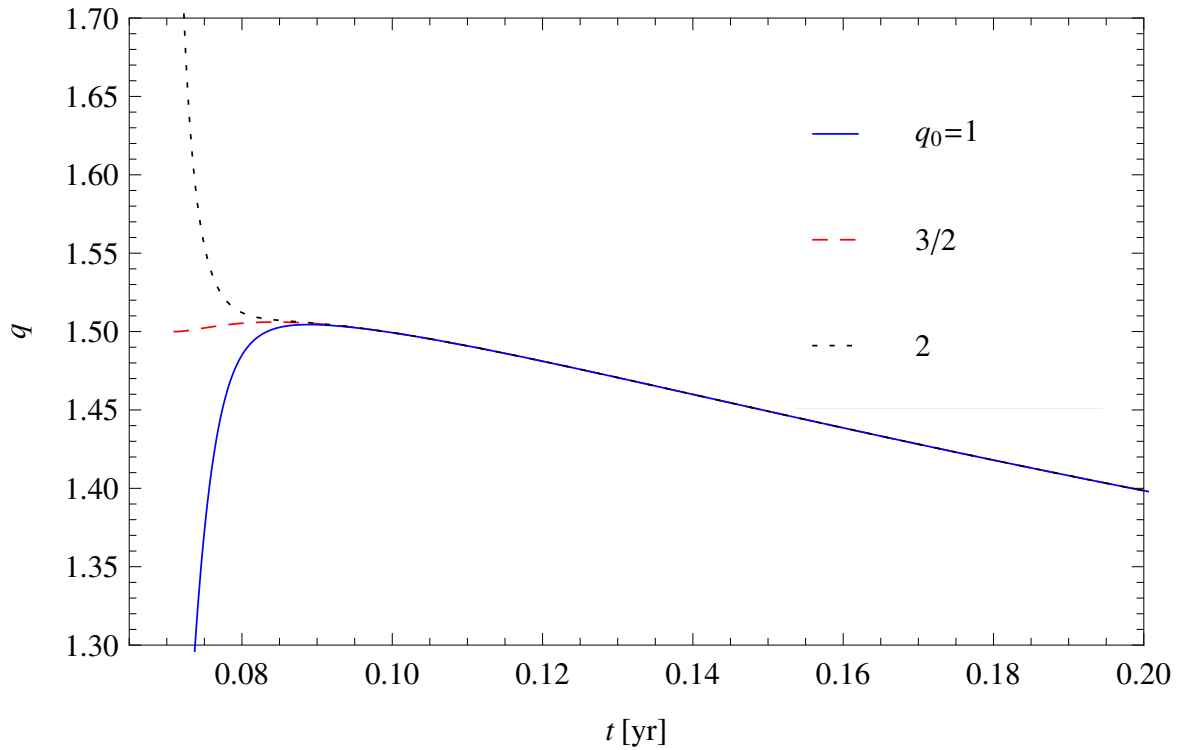


Figure 5.7: The solution for  $q(t)$  with a solar progenitor ( $M_* = 1 M_\odot$ ,  $R_* = 1 R_\odot$ ,  $\gamma_* = 5/3$ ), a radiation pressure-dominated gas ( $\gamma = 4/3$ ),  $M_h = 10^5 M_\odot$ ,  $y = 1$ ,  $\delta = 0.05$ ,  $\chi = 5$ , and three different  $q_0$ , indicated by the legend. As one can see, the initial conditions quickly become irrelevant to the long-term behavior of the solutions.

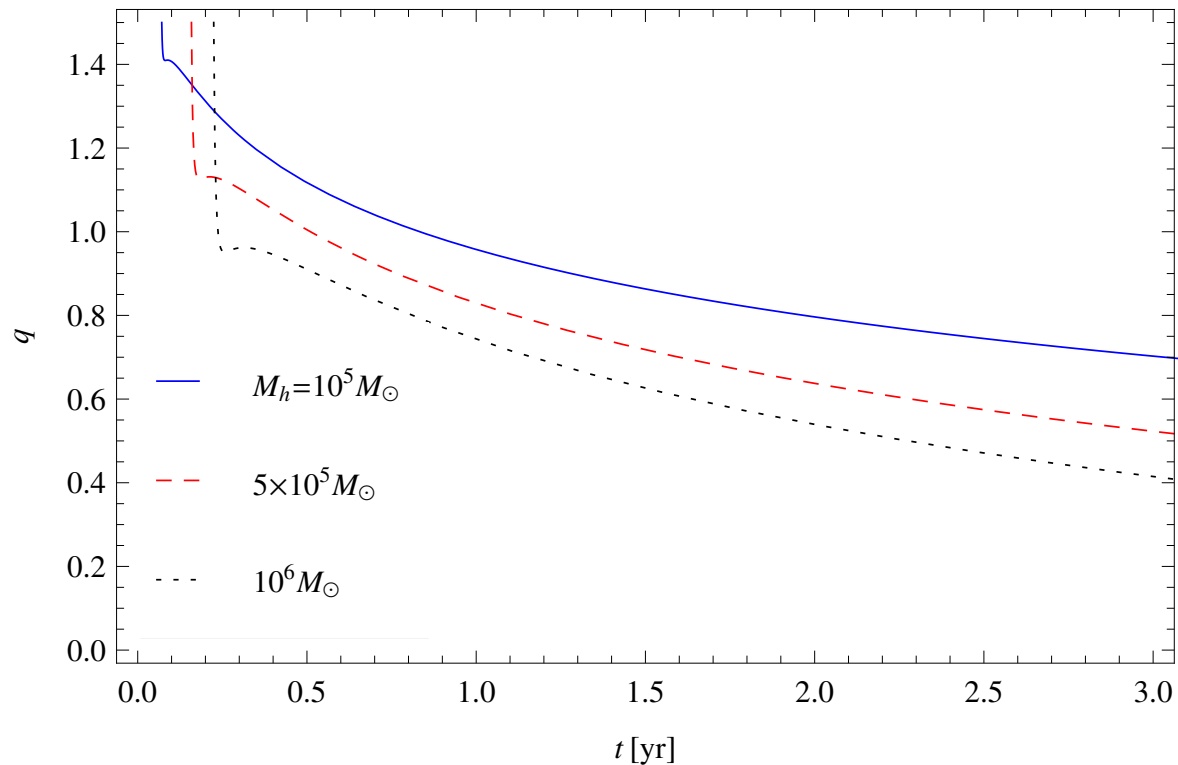


Figure 5.8:  $q(t)$  for a radiation-dominated gas ( $\gamma = 4/3$ ) and a variety of black hole masses. Here  $y = 0.5$ ,  $\delta = 0.05$ ,  $\chi = 5$ ,  $q_0 = 3/2$ ,  $\gamma_* = 5/3$ ,  $M_* = 1M_\odot$ , and  $R_* = 1R_\odot$ . The legend displays the black hole mass in units of solar masses. We see that initially  $q$  falls off very rapidly, which is a consequence of initial conditions. However, the initial conditions stop having a major effect early in the evolution of the system, and  $q$  then decreases less rapidly.

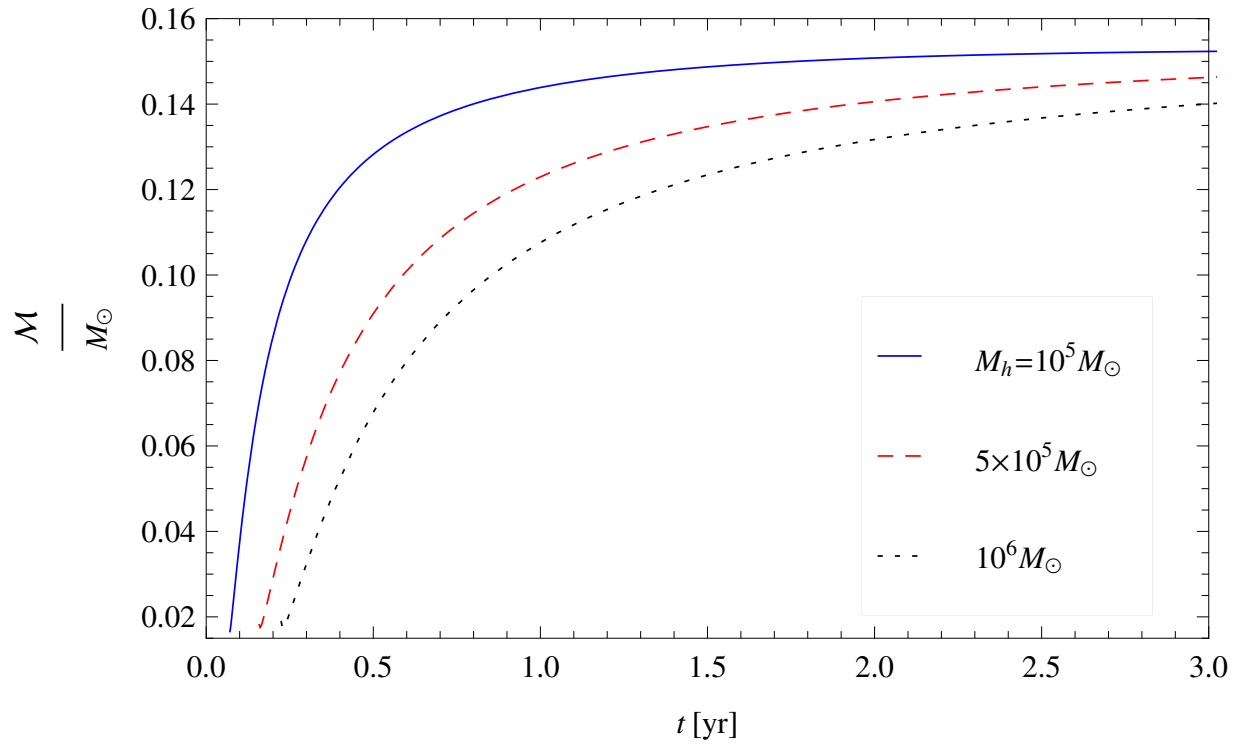


Figure 5.9: The mass contained in the ZEBRA as a function of time for the same parameters as those in Figure 5.8. The mass quickly increases initially, owing to the fact that the fallback rate exceeds the accretion rate. However, as both rates decrease for later times, the mass levels off to a nearly constant value.

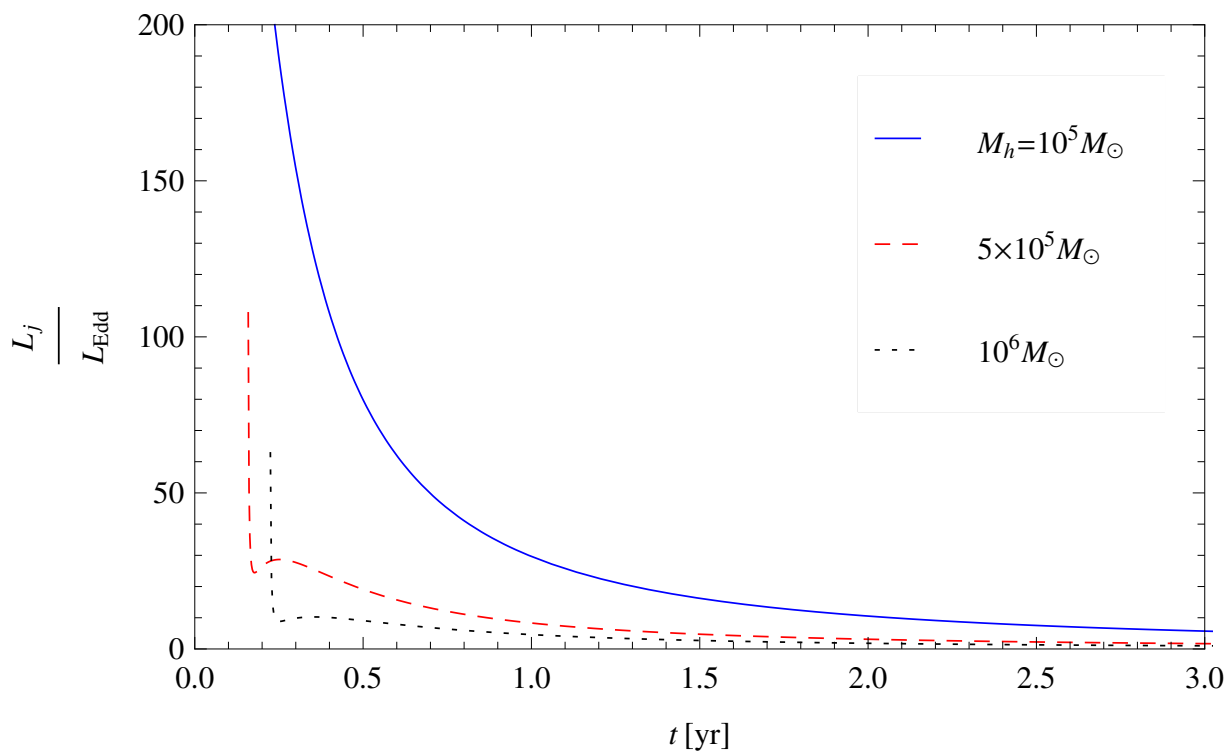


Figure 5.10: The jet luminosity, normalized to the Eddington luminosity of the black hole, for the same parameters as those in Figure 5.8 with an efficiency  $\epsilon = 0.1$ . Initially the luminosity is very super-Eddington, decaying to only mildly super-Eddington at later times.

predicted by our model is super-Eddington for a significant amount of time, though the amount of time for which that statement is true decreases as the black hole mass increases. The fact that the jet power is supercritical is a good consistency check on our model. The time at which the accretion rate becomes sub-Eddington is roughly the same time at which  $q = 0.5$ , where our model begins to break down.

One of the popularly-cited hallmarks of a tidal disruption event is that the accretion luminosity is proportional to  $t^{-5/3}$ . However, this result only holds for a constant-density star. Our models account for the mass distribution in the original progenitor, placing more mass on orbits with larger semi-major axes, and they are also consistent with the initial rise in the fallback rate. Our accretion rate also takes into account fluid interactions, meaning that our black hole accretion rate, and consequently the jet luminosity, does not necessarily mimic exactly the mass fallback rate.

In Figure 5.11 we plot the accretion rate onto the black hole for two different  $q_0$  (we chose two different  $q_0$  to demonstrate when the solutions converge), given by equation (5.26), and the fallback rate onto the accretion region, which is the solution to equation (5.34), for the same set of fiducial parameters as those in Figure 5.8 and the black hole has a mass  $M_h = 10^5 M_\odot$ . It is apparent from the figure that the accretion rate onto the black hole follows the fallback rate rather tightly, but there exist notable differences. The first difference is that the accretion rate is less than the fallback rate for the times shown; this finding is consistent with Figure 5.9, as the mass is increasing for all times shown. The second is that there exists a temporal lag between the qualitative features shared by the two rates; the most salient example of this characteristic is the difference in the time taken to reach the maximum, which is evident in the figure. Specifically, the fallback rate reaches its maximum at  $t \approx 0.094$  years, while the black hole accretion rate peaks at  $t \approx 0.11$  years. The third difference is that the accretion rate of the black hole follows a less-steep power law than the fallback rate for later times. By fitting the fallback rate as  $\dot{M}_{fb} \propto t^{-m_{fb}}$  between 1 and 2 years, we find that the power law is  $m_{fb} \approx 1.63$ ; by inspecting equation (5.34), we expect that the fallback power law should asymptotically approach  $m_{fb} = 5/3$ . By fitting the accretion rate for the same amount of time and by the power-law form  $\dot{M}_{acc} \propto t^{-m_{acc}}$ , we find that  $m_{acc} \approx 1.49$ . As one can

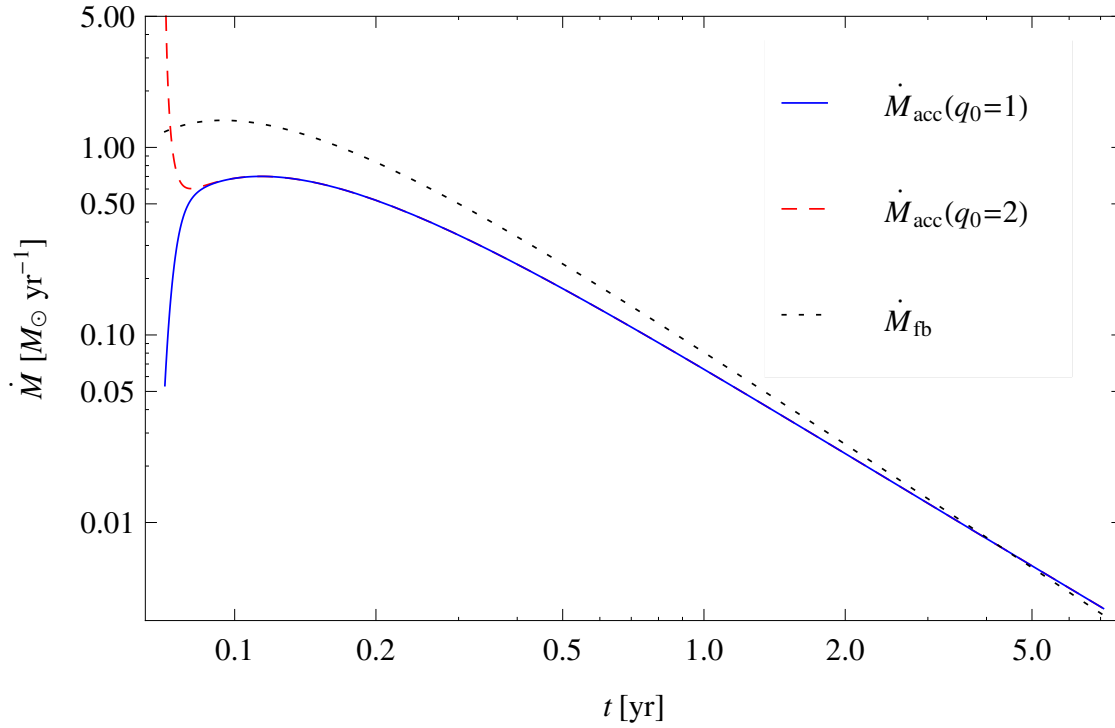


Figure 5.11: The black hole accretion rate, given by equation (5.26), in solar masses per year for  $q_0 = 1$  (blue, solid curve) and for  $q_0 = 2$  (red, dashed curve) to illustrate where the solutions have converged; the parameters are the same as those in Figure 5.8 and the black hole has a mass  $M_h = 10^5 M_\odot$ . We have also plotted the fallback rate, shown by the black, dotted curve, to illustrate how the two accretion processes compare. It is apparent from this figure that they match each other closely, and that after about 4 years, the black hole accretion rate exceeds the fallback rate.

see in the figure, at a time of about 4 years the black hole accretion rate exceeds the fallback rate, corresponding to a decrease in the mass contained in the ZEBRA. This result makes sense, as we expect accretion to occur even if there is no fallback of material onto the envelope.

Another property of the envelope that we can calculate is its effective temperature. As we have argued in section 3, the surface should occur roughly at the trapping radius, and so the temperature is given by

$$T = \left( \frac{GcM_h m_p}{\sigma_T \sigma_{SB} \mathcal{R}^2} \right)^{1/4} \quad (5.38)$$

$$\simeq 6.5 \times 10^4 \left( \frac{M_h}{10^6 M_\odot} \right)^{1/4} \left( \frac{\mathcal{R}}{10^{14} \text{cm}} \right)^{-1/2} \text{K}, \quad (5.39)$$

where  $\sigma_{SB} = 5.67 \times 10^{-5}$  cgs is the Stefan-Boltzmann constant. ZEBRA envelopes produced by TDEs thus tend to peak in the far-UV or soft X-ray band. We can also solve for the effective temperature as a function of time, as shown in Figure 5.12.

Because  $\mathcal{R}$  is proportional to  $\mathcal{M}^{2/5}$  (see equation (5.17)), the temperature decreases initially as mass is gained from the fallback of tidally-stripped material. However, for later times when the black hole accretion rate and the fallback rate both decrease substantially, the temperature remains nearly constant.

Owing to the fact that the photons are trapped interior to  $\mathcal{R}$ , we expect there to be a high degree of coupling between the particles comprising the ZEBRA envelope and the photons produced at the photosphere. The spectrum should therefore be very well-matched by a blackbody distribution. Depending on the temperature of the envelope and the composition of the disrupted star, however, there may also be present a number of absorption and emission features. With these temperatures, electron scattering may also produce a color-corrected spectrum.

#### 5.4.3.1 Power-law fallback rate

As one can see in Figure 5.11, the black hole accretion rate closely matches the fallback rate

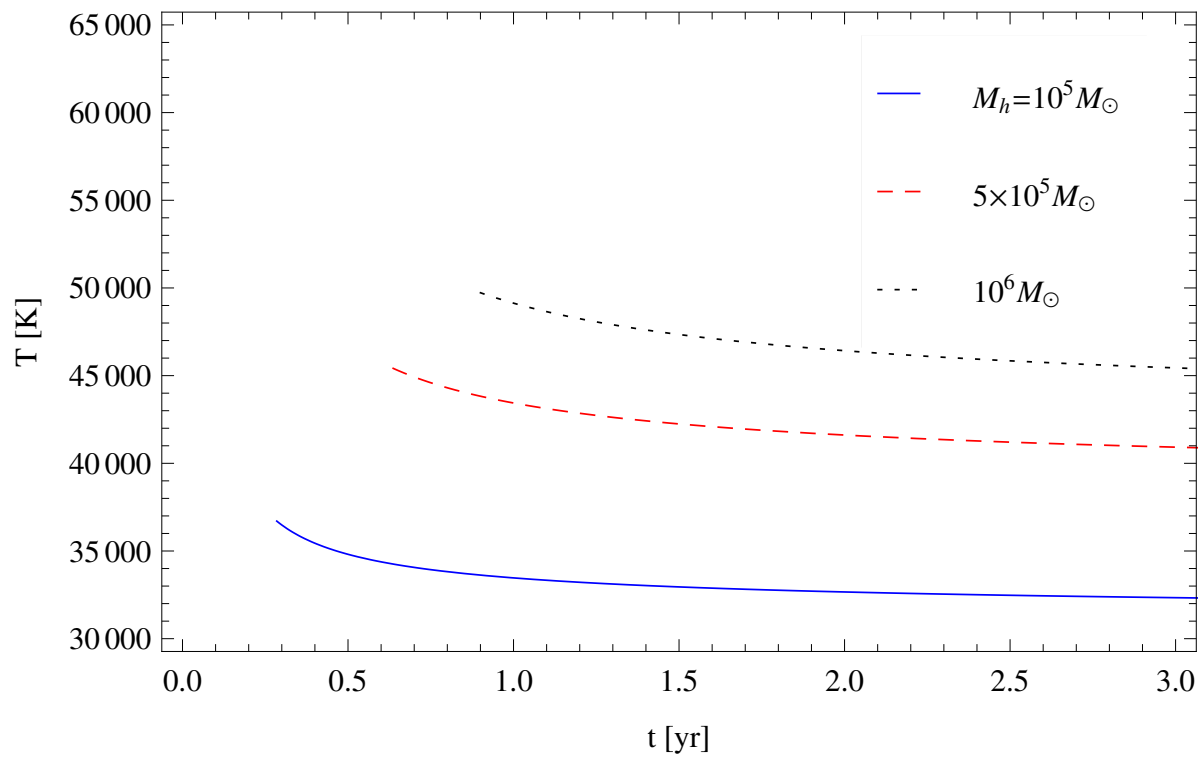


Figure 5.12: The effective temperature as a function of time for different black hole masses. The fiducial parameters are the same as those in Figure 5.8.

of the tidally-disrupted material. An interesting question is whether this close equality is always true, or if it just happens to be the case for the specific analytic model that we chose. To analyze the effects of altering the fallback rate, we will let  $\dot{M}_{fb}$  scale as a power-law, specifically

$$\dot{M}_{fb} = M_0(m - 1) t^{-m}, \quad (5.40)$$

where the proportionality constant has been chosen to be consistent with the fact that at  $t_r$ , the orbital period of the innermost material,  $\dot{M}_{fb} = M_0$ , where  $M_0$  is the mass of the material that has yet to be accreted (note, however, that we are not considering the equation accurate until much later than  $t_r$ , as the fallback rate must first peak and then decline to the power-law decay). From the initial work of Phinney (1989), it was thought that  $m$  should always be on the order of  $5/3$ . Our Figure (5.11) also indicates that this scaling holds for later times. More recently, however, it has been shown that this power-law decay may not be followed, even for times much later than that at which the peak fallback occurs. In particular, Guillochon & Ramirez-Ruiz (2013) demonstrated that variations in the impact parameter, which we defined as  $x$ , can lead to partial disruptions that, owing to the continued gravitational influence of the surviving stellar core, cause  $m$  to deviate significantly from  $5/3$ . We will therefore leave this quantity as a variable and inquire as to the effects of its variation on the black hole accretion rate.

One might expect that  $M_0 = M_*/2$ , as the TDE leaves roughly half of the progenitor bound to the black hole. However, partial disruptions, which result from grazing encounters with the black hole, leave an intact stellar remnant. In these instances, the total mass bound to the hole is always less than  $M_*/2$ . We will therefore leave  $M_0$  as a free variable, typically on the order of a fraction of  $M_*/2$ .

As we argued previously, the material that comprises the ZEBRA must lose its angular momentum before being accreted by the black hole. By following the same line of reasoning, we

can show that the angular momentum contained in the envelope is given by

$$\mathcal{L} = M_0 \sqrt{2GM_h R_*} \left( \frac{M_h}{M_*} \right)^{1/6} \left( 1 - \left( \frac{t}{t_r} \right)^{1-m} \right). \quad (5.41)$$

With this expression, we can go through the same analysis as in the previous subsection and numerically solve for  $q(t)$  and all other time-dependent quantities. However, instead of reproducing all of the plots in the previous subsection for different values of  $m$ , we will concentrate on how the accretion rate onto the black hole compares to the fallback rate, which will inform us of the way in which the jet luminosity relates to the fallback rate.

Guillochon & Ramirez-Ruiz (2013) demonstrated that  $m$  varies between roughly 1.5 and 2.2, depending on the value of the impact parameter (see their Figure 7). They also showed that steeper fallback rates follow from shallower impact parameters, as a result of the gravitational influence of the surviving stellar remnant. Consequently, the values of  $m$  and  $M_0$  are not completely independent. We can show, however, that there exists a nearly-linear scaling between  $M_0$  and the magnitude of the black hole accretion rate. Since the fallback rate is also linear in  $M_0$ , we will simply consider  $M_0$  a constant and note that the true value of the accretion rate for a given  $m$  may be higher or lower.

Figure 5.13 illustrates, on a log-log scale, the accretion rate and the fallback rate for  $M_0 = 0.1 \times M_\odot/2$ ,  $M_h = 10^5 M_\odot$ ,  $m = 2$ , and the parameters adopted in Figure 5.8. We see that the accretion rate also follows a power-law decline, but one that is shallower than that for the fallback. Defining  $\dot{M}_{acc} \propto t^{-m_{acc}}$ , we find, in this case, that  $m_{acc} \approx 1.70$ .

For other power-law fallback rates, a qualitatively similar behavior is exhibited by the accretion rate. In particular, the rate at which mass is accreted by the hole falls off as a power-law, but one that is less steep than the rate at which material impacts the ZEBRA. To illustrate how the value of  $m$  affects  $m_{acc}$ , Figure 5.14 shows the value of  $m_{acc}$  given the value of  $m$ . To determine  $m_{acc}$ , we have performed a best-fit over the timescale of  $t = 0.2 - 1.5$  years, during which time all of the accretion rates follow power-law decays. As one can see, the relationship between the

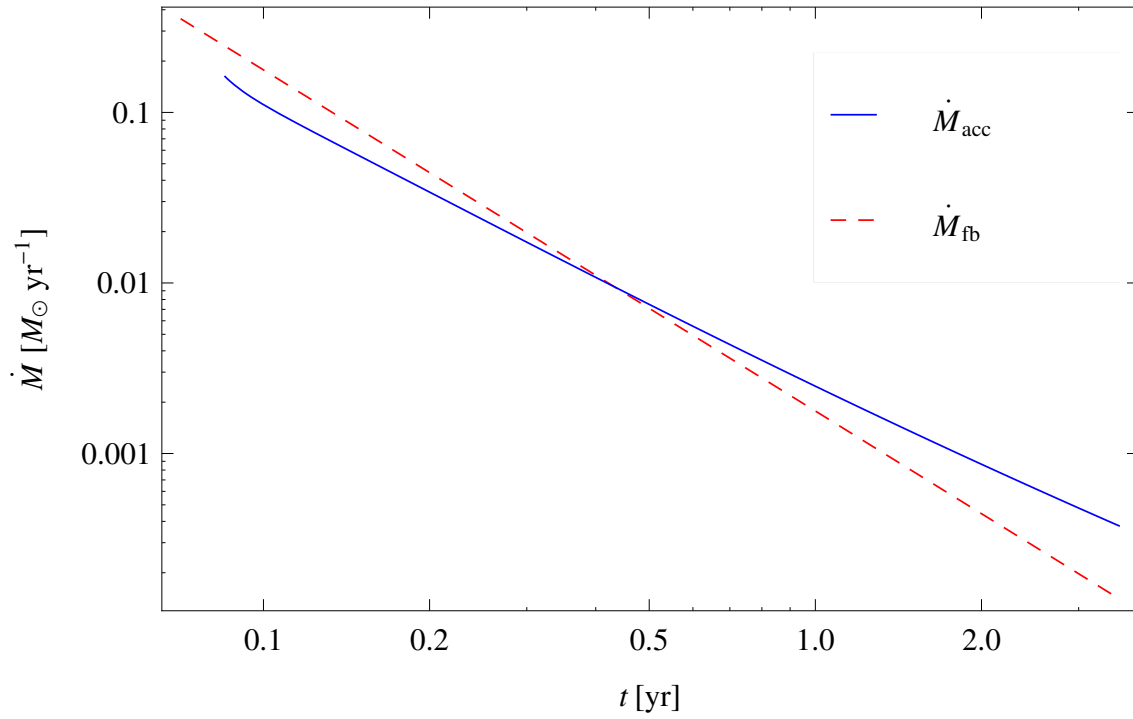


Figure 5.13: The black hole accretion rate (blue, solid curve) and the fallback rate (red, dashed curve) for  $M_0 = 0.1 \times M_{\odot}/2$ ,  $M_h = 10^5 M_{\odot}$ ,  $m = 2$ , and otherwise the same parameters as in Figure 5.8, plotted on a log-log scale. The accretion rate follows a shallower power-law than the fallback rate, causing the former to exceed the latter for times greater than about 0.5 years.

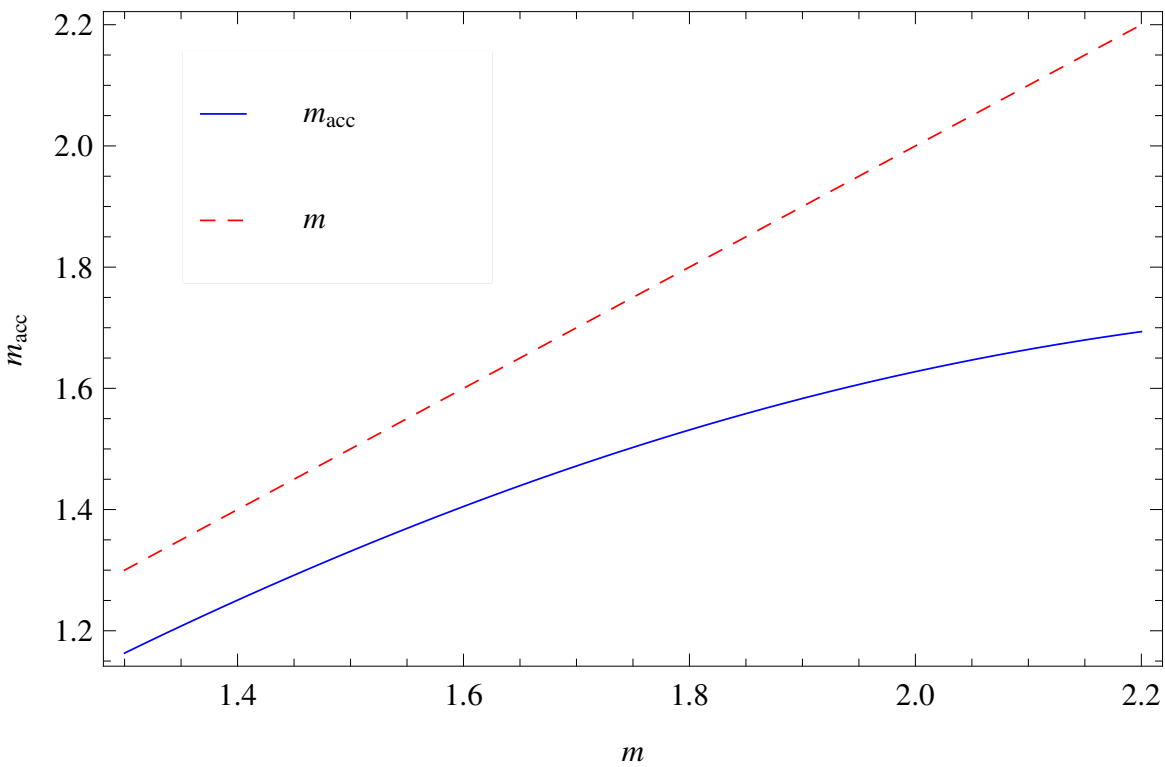


Figure 5.14: The power-law of the accretion rate, which we defined as  $m_{acc}$ , as a function of the power-law index of the fallback rate is shown by the blue, solid curve. The value of  $m_{acc}$  is determined by performing a best-fit to the black hole accretion rate between  $t = 0.2$  and 1.5 years, during which time the accretion rate, for all values of  $m$ , is well-described by a power-law. We have also plotted  $m$  for comparative purposes (red, dashed curve). We see that  $m_{acc}$  is always less than  $m$ . For small values of  $m$ , the relationship between  $m_{acc}$  and  $m$  is roughly an offset, linear one. As  $m$  becomes larger, however,  $m_{acc}$  displays a more nonlinear behavior, and the difference between the two power-law indices becomes larger.

two power-laws is approximately linear for low values of  $m$ , becoming increasingly nonlinear as  $m$  increases. Thus, while the difference between the two is approximately  $\Delta m \equiv m - m_{acc} \approx 0.15$  for  $m = 1.4$ , the disparity becomes  $\Delta m \approx 0.50$  for  $m = 2.2$ .

#### 5.4.4 **Swift J1644+57**

The object **Swift J1644+57** was found as both a source of X-rays and  $\gamma$ -rays by the **Swift** satellite, and thought initially to be a gamma-ray burst (GRB) (Markwardt et al., 2011). However, the variability and longevity of the source soon proved that such an association was unlikely, and the proximity of the event to the nucleus of a host galaxy at redshift  $z = 0.354$  led to the belief that the event was triggered by a TDE (Levan et al., 2011). By modeling the spatially and temporally coincident radio emission by the interaction of fast-moving ejecta with the circumnuclear environment, it was demonstrated that a mildly relativistic jet was likely generated during the TDE (Zauderer et al., 2011; Metzger et al., 2012). Here we investigate the consistency of our ZEBRA models with the observations of **Swift J1644+57**.

The peak, isotropic X-ray luminosity of **Swift J1644+57** reached  $4 \times 10^{48} \text{ erg s}^{-1}$ , with an average value appropriate to  $\sim \text{few} \times 10^{47} \text{ erg s}^{-1}$  (Burrows et al., 2011). When corrected for beaming effects, we recover a true luminosity of  $L_X \sim 10^{45} - 10^{46} \text{ erg s}^{-1}$  for a jet opening angle of  $5^\circ$  (Bloom et al., 2011). The mechanism responsible for the generation of the X-rays is still unclear, though its origin is consistent with inverse Compton scattering of photons near the launching point of the jet (Markoff et al., 2005; Bloom et al., 2011). It is difficult to constrain directly the mass of the black hole that resides in the host galaxy, but empirical galaxy luminosity relations imply  $10^5 M_\odot \lesssim M_h \lesssim 10^6 M_\odot$  (Saxton et al. (2012) and references therein). The energy generation rate is therefore highly super-Eddington (even if we increase the upper limit of the black hole mass to  $10^7 M_\odot$ ).

The prompt evolution of the X-ray emission was highly chaotic. However, after about 10 days from the initial trigger, the flux followed a decline that was well-approximated by a power-law (see Figure 1 in Tchekhovskoy et al. 2014). Therefore, if our model is to adequately describe the

evolution of **Swift** J1644+57, the first constraint it must satisfy is that the X-ray flux follow a power-law decline for later times. The exact value of the power-law index is uncertain owing to the large degree of intrinsic scatter in the X-ray data, but it is consistent with the range predicted in Guillochon & Ramirez-Ruiz (2013) (also see Tchekhovskoy et al. 2014).

The second constraint on our model comes from the fact that the X-ray flux of **Swift** J1644+57 dropped precipitously after about 500 days, most likely indicating the shut-off of the jet (Zauderer et al., 2013). Because our model requires the accretion rate to be super-Eddington during the jetted phase, our jet luminosity should be roughly the Eddington limit of the hole at  $t \approx 500$  days. However, because the initial behavior of the X-ray flux was highly chaotic, it is unclear at what point from the time of disruption the **Swift** satellite began observing the source, and the timeline of 500 days is therefore ambiguous.

For the analytical models described in the previous subsection, the luminosity of the jet depends not only on the black hole mass, but also on a number of other parameters which describe the details of the flow, e.g.,  $y$ ,  $\delta$ , etc. However, the results are largely insensitive to those parameters, and hence we will adopt the values that produced Figures 5.8 – 5.10. Moreover, if the impact parameter differs significantly from  $x = 1$ , making the power-law model the most valid description of the fallback process, the values of  $m$  and  $M_0$  must also be incorporated into the model.

The flux we observe is altered by the Lorentz factor and opening angle of the jet, both of which are uncertain and could change with time. However, if we assume that both of these quantities are constant, the flux we observe and the accretion luminosity of the hole are linearly related. Thus, while the magnitude of the observed flux cannot be determined exactly with our model (without performing a more in-depth analysis of the jet), its qualitative appearance can be reproduced. The value of  $M_0$ , which is a relevant quantity if the TDE occurs outside the tidal radius, also affects the magnitude of the jet luminosity. The time of disruption is also unknown, as the initial chaotic behavior of the event is not predicted by any model, making the time at which the observed flux reached a maximum incalculable. However, since there is a steady decline after a timescale on the order of days with no recurring rise, it is probable that the maximum fallback

rate occurred somewhere near in time to the triggering event.

With all of these considerations, we will restrict our attention to times greater than roughly 15 days after the trigger, where the observed flux approximately follows a power law. Given this restriction and our uncertainty in the exact value of the intrinsic flux, the first constraint on our model is that the power-law index of the jet luminosity should be between 1.5 and 2.2. The second constraint is that the accretion luminosity produced by the hole should be near the Eddington limit of the hole after about 500 days from the time of the triggering. The luminosity of the jet must also change by about an order of magnitude during this length of time, evident in Figure 1 of Tchekhovskoy et al. (2014).

If we adopt the model discussed in the beginning of section 4.3, which places the periapsis of the disrupted star exactly at the tidal radius, and we choose the set of fiducial parameters that produced Figure 5.8, the only free parameter left is the mass of the black hole. Because the power-law index for later times is around 1.5, there will exist a qualitatively good fit between the model and the data. Our models predict that smaller black holes produce a greater change in the jet luminosity over the duration of the super-Eddington event, and an order-of-magnitude change in the luminosity requires a black hole of mass  $M_h \simeq 10^5 M_\odot$ . For black holes with masses in this range, the accretion luminosity of the hole is on the order of its Eddington limit around 500 days after the maximum fallback. This prescription is thus broadly consistent with **Swift** J1644+57.

If the tidal disruption occurs at a distance such that the star is only partially destroyed, the power-law rate of return is the most appropriate method by which we can analyze the fallback onto the ZEBRA. Since the power-law associated with the accretion luminosity is always between about 1.5 and 1.7, there will exist qualitative good agreement between the observations of **Swift** J1644+57 and the ZEBRA prediction. For these models, the change in flux being an order of magnitude again requires that  $M_h \simeq 10^5 M_\odot$ , consistent with the description that places the periapsis of the star at the tidal disruption radius. For these fallback rates, the accretion luminosity is near the Eddington limit of the hole after 500 days from the maximum, though the precise number depends on  $M_0$ .

## 5.5 Discussion and conclusions

We have outlined a novel approach to describing the super-Eddington accretion disks generated during tidal disruption events. Following Loeb & Ulmer (1997), we used the low specific angular momentum of the tidally-disrupted material to place the material in a nearly-spherically symmetric configuration around the hole. However, instead of forcing a strictly spherical envelope to enclose a thick disk, which we believe to be unstable due to the absorption of energy and transfer of angular momentum, we self-consistently account for the distribution of angular momentum throughout the material.

In our models, the accretion energy released by the black hole and shock heating pump a significant amount of energy into the debris, puffing up the disk. We encounter a point where the Bernoulli parameter approaches zero, leaving a quasi-spherical envelope that is marginally bound. Further energy input would unbind the material, most likely resulting in a wind (see Appendix B). Instead of creating a wind, we posit that the accretion energy of the black hole is instead redirected to the poles, resulting in the formation of a jet that serves as the exhaust route for the excess energy. The resulting configuration is a zero-Bernoulli accretion (ZEBRA) flow, threaded by a bipolar jet. This type of object is specifically relevant to the recently observed X-ray transient **Swift** J1644+57.

The creation of the jet is a natural consequence of the fact that ZEBRA envelopes are closed up all the way to the poles, leaving no disk surface from which one could launch a wind and remove the super-Eddington accretion luminosity. Because the liberated gravitational energy would have to propagate through the entire system to be released at the photosphere, which is not possible owing to the supercritical nature of its generation rate, it is forced to exit along the poles. Another consequence of the super-Eddington luminosity is the inability of the flow to cool efficiently, forcing it to maintain its zero-Bernoulli nature. The supercritical accretion luminosity thus forms the cornerstone of the consistency of our model.

Following the analysis of Blandford & Begelman (2004), we demonstrated the existence of

self-similar solutions to the momentum and Bernoulli equations with  $B = 0$ , which form a particular subset of the gyrentropic flows discussed by those authors. The gyrentropic nature of our flows is a result only of our assumption of the globally-zero Bernoulli parameter, independent of any stability considerations, such as the presence or absence of MRI. The ZEBRA flows were shown to close up only exactly at the poles, indicating the quasi-spherical nature of the envelopes.

We showed that there exists an unspecified parameter, denoted by  $q$  (linearly related to the parameter  $n$  of Blandford & Begelman 2004), which characterizes the radial gradients of the density and pressure and the sub-Keplerian nature of the flow. For TDEs, the total mass and angular momentum of the progenitor star, coupled to our specification of the trapping radius as the edge of the envelope, determine the value of  $q$ . For low specific angular momentum, the gradients of the density and pressure increase, approaching the isentropic value of a non-rotating star as the angular momentum goes to zero.

ZEBRA envelopes have a radial extent of hundreds to thousands of Schwarzschild radii, validating our neglect of general relativistic effects over the bulk of the flow. However, the excess of angular momentum at small radii to account for the relativistic gravitational field could play a significant role in our determination of the gross properties of the configuration. By using the pseudo-Newtonian potential of Paczyński & Wiita (1980), we demonstrated that, while the specific angular momentum, pressure, and density can deviate significantly from their Newtonian values in regions close to the hole, the total mass and angular momentum of the envelope are largely unaffected.

These models apply to the super-Eddington phase of accretion, namely when the flow is unable to cool via radiative losses. We were able to predict the accretion and jet luminosities associated with ZEBRA flows, and found that, indeed, the rates are highly supercritical, providing a self-consistency check on our assumptions. Another aspect of our flows that is asserted a priori is that the Bernoulli parameter is precisely zero, which we know must break down close to the hole. The implications of a non-zero, but constant,  $B$  are addressed in Appendix B. The results derived in the previous sections are shown to be insensitive to this assumption provided that  $|B| < GM_h/r$ .

Because of the very high accretion rates, an appreciable amount of mass is lost on a dynamically relevant timescale. This consideration allowed us to determine the time-dependent nature of the properties of the accretion flow and the jet. By using an analytic model closely following that of Lodato et al. (2009) to describe the fallback rate of tidally-stripped material, it was shown that the jet luminosity roughly follows the rate at which material returns to pericenter, but with a few notable differences. In addition to using the model for which the pericenter distance of the disrupted star equals the tidal radius, we investigated the consequences of letting the fallback onto the ZEBRA scale as a power-law. This model serves as a proxy for the late evolution of TDEs for which the pericenter of the stellar progenitor lies outside the tidal radius. In these cases, the accretion rate onto the hole also follows a power-law decline, but with a power-law index that is less steep than that of the fallback rate. We also demonstrated that ZEBRA envelopes produced by TDEs should have approximately-constant effective temperatures of  $T \simeq 5 \times 10^4$  K, placing the peak of their bolometric luminosities in the far UV to soft X-ray.

We compared our models with the observed properties of the transient X-ray source **Swift** J1644+57. Because of the uncertainties in the opening angle of the jet, its Lorentz factor, and the time at which the X-ray flux reached its peak magnitude, we were unable to place many direct constraints on our model. However, we found broad consistency with our models and the observations if the black hole has a mass on the order of  $10^5 M_{\odot}$ , assuming a disrupted star of solar type and a constant jet Lorentz factor and opening angle.

The existence of a ZEBRA is contingent on the availability of an exhaust route for the excess energy produced in the accretion process. In this account we have presupposed the existence of a jet as this conduit, and we demonstrated its consistency with the source **Swift** J1644+57. We have foregone, however, any explicit analysis concerning its generation or its interaction with the ZEBRA flow. We also neglected any changes in the Lorentz factor or the beaming angle of the jet, both of which would have observable effects on the X-ray luminosity. These aspects of the problem will be addressed in a future paper.

In addition to tidal disruption events, ZEBRA flows may manifest themselves in other as-

trophysical systems. One such application is to failed supernovae, or collapsars (Woosley, 1993; MacFadyen & Woosley, 1999). In this model, a highly evolved, rotating star undergoes a type II supernova. The core collapses directly to a black hole, the remaining stellar material creating an accretion disk and producing a jet. The internal shocks within the jet provide one mechanism capable of producing the gamma rays we observe in long gamma-ray bursts (GRB). Outflows farther from the poles are thought to unbind the envelope and produce the supernova signature observed in many long GRBs (Woosley & Bloom, 2006). However, there have been a few cases in which we observe a GRB devoid of any supernova afterglow (Fynbo et al., 2006), even though the location of the GRB should have provided no impediment (e.g., dust extinction or light contamination) to our observation of the afterglow. It is possible that, in these instances, the outflows away from the poles were not sufficient to unbind the envelope, leaving it intact above the black hole. This environment is precisely that in which a ZEBRA flow would arise, as a wind is unable to be created due to the presence of the overlying stellar material. As more energy is pumped into the material, the entire mass of the progenitor may come to an approximate equilibrium described by our  $B = 0$  prescription. Another application would be in the deep interior of a quasi-star, a giant proto-galactic gas cloud supported by black hole accretion (Begelman et al., 2006b, 2008). Because the black hole accretes at the Eddington limit of the total quasi-star, whose mass far exceeds that of the hole, the accretion rate is highly supercritical. The overlying gas prevents the generation of a wind or any other exhaust mechanism, making a ZEBRA flow the most appropriate description of the fluid.

In both of the previous examples, the accretion rates and other physical processes create a natural environment for ZEBRAs. However, they both differ from tidal disruption events in the gravitational role played by the black hole: in TDEs, the black hole dominates the mass of the system, and so the gravitational potential is given by that of a point mass. In a failed supernova, the black hole generated by the collapse is on the order of the mass of the overlying material. Thus, as we move away from the hole into the ZEBRA envelope, there will come a point where the enclosed mass roughly equals that of the hole. The point-mass prescription then becomes invalid. For a quasi-star, the black hole constitutes only a small fraction of the total mass, and hence the

self-gravitating nature of the flow must be considered in order to adequately describe the properties of the ZEBRA.

The fluid and Bernoulli equations with an arbitrary gravitational potential may be written down in a straightforward manner, Poisson's equation being the extra constraint that closes the system. An analysis of these relations, in which we self-consistently include both the angular momentum of the gas and its self-gravitating nature, will be deferred to a later paper.

## Chapter 6

# The General Relativistic Equations of Radiation Hydrodynamics in the Viscous Limit

### 6.1 Introduction

Radiation contributes substantially to the dynamics of many astrophysical systems. The most natural way to analyze the mechanics of such systems is through the formalism of radiation hydrodynamics, wherein one treats the radiation as a fluid that interacts with matter. With the covariant derivative denoted  $\nabla_\mu$ , the equations of radiation hydrodynamics can be generalized to include both gravitational fields and relativistic motions by writing them in the manifestly covariant form

$$\nabla_\mu(T^{\mu\nu} + R^{\mu\nu}) = 0, \quad (6.1)$$

where Greek indices range from 0 to 3, repeated upper and lower indices imply summation,

$$T^{\mu\nu} = w'U^\mu U^\nu + p'g^{\mu\nu} \quad (6.2)$$

is the energy-momentum tensor of the massive constituents of the fluid ( $w'$  is the enthalpy in the fluid rest-frame,  $U^\mu$  is the four-velocity,  $p'$  is the pressure in the fluid rest-frame, and  $g^{\mu\nu}$  is the inverse of the metric associated with the background geometry) and

$$R^{\mu\nu} = \int k^\mu k^\nu f \frac{d^3k}{k^0} \quad (6.3)$$

is the energy-momentum tensor of the radiation (see, e.g., Mihalas & Mihalas 1984 for a more thorough discussion of the origin of this tensor). In equation (6.3),  $k^\mu$  is the four-momentum of a photon,  $f$  is the distribution function of the radiation that describes the density of quanta in both momentum and position space, and  $d^3k/k^0$  is the Lorentz-invariant phase-space volume. Because  $f$  is a scalar, such a “moment” formalism, i.e., proceeding by taking integrals over the distribution function, is a natural way to analyze the dynamics of the radiation in a covariant fashion. Note, however, that equation (6.3) is only valid in a locally-flat frame – one in which  $g_{\mu\nu} = \eta_{\mu\nu}$ ,  $\eta_{\mu\nu}$  being the Minkowski metric – as otherwise one must include factors that depend on the metric (see, e.g., Debbasch & van Leeuwen 2009a). To ensure that the radiation energy-momentum tensor (and derivatives thereof) transforms correctly at all points in the spacetime under consideration, one can explicitly insert the metric-dependent factors that enter into the phase-space volume element. Another, equally valid manner by which one can obtain the general-relativistic form of  $R^{\mu\nu}$ , however, is by evaluating the integrals in equation (6.3) and writing the results in a manifestly-covariant form, guaranteeing their frame independence. Because we will be working directly with the distribution function, the latter route is the simpler one to follow and is the one that we will pursue in our ensuing analyses (see sections 3 and 4).

For many astrophysical applications of the equations of radiation hydrodynamics, the medium under consideration is optically thick, meaning that the radiative flux observed at any location within the fluid is very nearly zero. This means, equivalently, that a photon is scattered a large number of times as it propagates through the medium, and that the radiation field as seen by a moving fluid element within the medium is approximately isotropic. It has been known for some time, however, that the finite mean free path of a photon leads to the presence of viscous-like terms in the radiation energy-momentum tensor (Thomas, 1930). The viscous nature of some fluids, especially in applications for which photons dominate the pressure of a system, can therefore be attributed in part to their interactions with radiation.

Eckart (1940) analyzed the origin of generic, viscous effects in relativistic fluids, whether due to radiation or to other phenomena (see also Landau & Lifshitz 1959). He exploited the fact that

the four-velocity of the fluid,  $U^\mu$ , and the projection tensor,  $\Pi^{\mu\nu} = U^\mu U^\nu + g^{\mu\nu}$ , are time-like and space-like tensors, respectively, that can be used to decompose any arbitrary tensor. Eckart realized that each of the terms in his decomposition had a physical interpretation, related to the dynamic viscosity or heat conduction of the fluid, which allowed him to postulate a form for the viscous stress tensor of a relativistic fluid that reduced correctly to its non-relativistic counterpart.

Thomas (1930) (and others after him, e.g., Lindquist 1966; Castor 1972; Buchler 1979; Munier 1986; Chen & Spiegel 2000) used the special relativistic Boltzmann equation, which describes changes to the distribution function due to particle-particle collisions, to derive the correction to the radiation energy-momentum tensor for the special case of Thomson scattering. Eckart's approach, on the other hand, was more phenomenological in nature, employing thermodynamic arguments and an understanding of the Newtonian limit of the viscous stress tensor to derive its relativistic generalization. Weinberg (1971), with the intent of using the results to analyze entropy production in the early universe, compared the two approaches and showed that one of Eckart's assumptions, namely that the viscous stress tensor be trace free, led to the incorrect conclusion that the bulk viscosity of the fluid vanish (see also Misner & Sharp (1965), where a similar approach is used to evaluate radiative effects during core-collapse supernovae). In his analysis, the part of the relativistic stress tensor expressing viscosity and heat conduction, a slightly generalized version of Eckart's, was of the form

$$\begin{aligned} \Delta T^{\mu\nu} = & -\eta \Pi^{\mu\sigma} \Pi^{\nu\rho} \left( \nabla_\sigma U_\rho + \nabla_\rho U_\sigma - \frac{2}{3} g_{\sigma\rho} \nabla_\alpha U^\alpha \right) - \zeta \Pi^{\mu\nu} \nabla_\alpha U^\alpha \\ & - \chi \left( \Pi^{\nu\sigma} U^\mu + \Pi^{\mu\sigma} U^\nu \right) \left( T U^\rho \nabla_\rho U_\sigma + \nabla_\sigma T \right), \end{aligned} \quad (6.4)$$

where  $\eta$ ,  $\zeta$ , and  $\chi$  are the coefficients of dynamic viscosity, bulk viscosity, and heat conduction, respectively, and  $T$  is the temperature of the gas. In the special-relativistic limit,  $\nabla_\mu = \partial_\mu$  is just the partial derivative, but is the covariant derivative if curvilinear coordinates are being used (or if the fluid is in a gravitational field). His comparison between the two theories enabled him to calculate  $\eta$ ,  $\zeta$ , and  $\chi$  for a radiating fluid, confirming the notion that small-scale anisotropies in the

radiation field, i.e., on the order of the mean free path of a photon, generate viscous-like effects.

Although they yield similar results, the fluid/thermodynamic approach of Eckart (1940), and correspondingly that of Weinberg (1971), is fundamentally different from the kinetic theory approach of Thomas (1930). The first difference arises from the fact that the former is a single-fluid analysis, meaning that  $\Delta T^{\mu\nu}$ , as given by equation (6.4), is the viscous correction to “the fluid.” The second disparity comes about because Eckart defines thermodynamic quantities in terms of the energy-momentum tensor of the fluid; for example, Eckart (1940) and Weinberg (1971) both **define** the comoving energy density as  $e' = U_\mu U_\nu T^{\mu\nu}$ , meaning that there is no correction to the observed energy. It is for this reason that there is no term proportional to  $U^\mu U^\nu$  in equation (6.4); however, the Eckart decomposition for an arbitrary tensor, one that has no restriction imposed upon it concerning the comoving energy density, will have such a term.

On the other hand, the kinetic theory approach considers the radiation and the matter to be two separate, interacting fluids – the same viewpoint that underlies all of radiation hydrodynamics – meaning that the viscous terms are understood as corrections to the radiation energy-momentum tensor, rather than that of the matter. Also, the kinetic theory description uses the Boltzmann equation to determine the distribution function, the viscous stress tensor then being written in terms of integrals over that function, viz., equation (6.3). There is thus no need to define bulk physical parameters, such as the temperature  $T$  or the comoving energy density  $e'$ , in terms of the stress tensor. Indeed, one could verify the validity of Eckart’s assumption that  $\Delta e' = U_\mu U_\nu \Delta T^{\mu\nu} = 0$  if one knew the distribution function.

Our goal here is to analyze the Boltzmann equation and thereby evaluate the stress tensor for a relativistic, radiating fluid in the limit that the finite mean free path of the radiation provides the source of the viscosity. In section 2 we present the general relativistic Boltzmann equation, the formalism of general relativity being necessary because of the fact that scattering is handled most easily in the comoving (accelerating) frame of the fluid. In section 3 we restrict our attention to the case where the scattering is dominated by Thomson scattering and we solve the resultant equation for the distribution function to first order in the mean free path. Section 4 presents the equations

of radiation hydrodynamics in the viscous limit and we demonstrate that the stress tensor departs from equation (6.4) in a few important ways, the first being that our equation has an additional correction to the comoving energy density, and the second being that our result is independent of thermodynamic considerations, such as the assignment of a temperature, and is therefore applicable to non-equilibrium radiation fields. Our coefficient of bulk viscosity also differs from that derived by Weinberg (1971). We perform a Fourier analysis of the perturbed equations in section 5 and show that they are indeed stable to perturbations of the fluid on scales larger than the mean free path of the radiation. A discussion of future applications, some comments on current radiation magnetohydrodynamic codes and conclusions are presented in section 6.

## 6.2 Relativistic Boltzmann equation

The distribution function for the radiation must satisfy a transfer equation – some statement of the conservation of photon number. As mentioned in the introduction, a natural choice for this equation is the Boltzmann equation, which describes the changes to the distribution function owing to emission, absorption, and scattering processes. However, because photons are massless, we must use a relativistic version of the Boltzmann equation; an obvious generalization to the relativistic regime is

$$\begin{aligned} \frac{\partial f}{\partial t} + v^i \frac{\partial f}{\partial x^i} + \dot{v}^i \frac{\partial f}{\partial v^i} &= \delta f|_{coll} \\ \rightarrow k^\mu \frac{\partial f}{\partial x^\mu} + \dot{k}^\mu \frac{\partial f}{\partial k^\mu} &= \delta f|_{coll}, \end{aligned} \tag{6.5}$$

where Latin indices adopt the range 1 – 3, Greek indices range from 0 – 3, repeated upper and lower indices imply summation, and  $k^\mu$  is the four-momentum of a photon. The right-hand sides represent changes to the distribution function through interactions with the surrounding medium. Equation (6.5) is the relativistic Boltzmann equation often encountered in the literature (e.g., Mihalas & Mihalas 1984). There are, however, two important subtleties associated with equation (6.5) that

are often not mentioned explicitly.

The first issue is that the sum over  $\dot{k}^\mu$  on the left-hand side of (6.5) must incorporate the constraint that the four-momentum of the photon lie on the null cone, viz.,  $k_\mu k^\mu = 0$  (this problem vanishes in flat space because photons travel in straight lines, and hence  $\dot{k}^\mu = 0$ ), which raises the question of whether or not the sum should occur over all four components of the momentum or just three. Furthermore, if we take the latter route, which three should we choose? Comparing equation (6.5) to the non-relativistic expression suggests taking the three spatial components; relativistic covariance, however, demands that the time component should not be treated differently from the spatial momenta.

The second subtlety stems from the fact that, in general relativity, there are two different momenta from which we can choose to describe the system: the covariant,  $k_\mu$ , and the contravariant,  $k^\mu$ , components, related by  $k_\mu = g_{\mu\nu} k^\nu$  where  $g_{\mu\nu}$  is the metric. The distribution function treats the spatial variables,  $x^\mu$ , as independent of the momentum. Therefore, should we consider  $x^\mu$  and  $k^\mu$  as independent coordinates, or  $x^\mu$  and  $k_\mu$ ? It is apparent that, depending on which one we choose, the results will differ as the metric  $g_{\mu\nu}$  is a function of the spatial coordinates.

In our ensuing treatment of equation (6.5), we will be analyzing interactions in the fluid frame – the one comoving with a given fluid parcel. Such a frame will, in general, be accelerating, meaning that  $\dot{k}^\mu \neq 0$  and there will be an acceleration-induced metric  $g_{\mu\nu}$ , forcing us to confront each of the previously-raised questions. Recently, Debbasch & van Leeuwen (2009a,b) addressed these issues directly by returning to the most general definition of the distribution function, a sum of Dirac delta functions in position and momentum space. They demonstrated (Debbasch & van Leeuwen, 2009a) that one may consider either the covariant, spatial components  $k_i$  or the contravariant components  $k^i$  as the momentum independent from  $x^\mu$ . However, as we mentioned previously, the Boltzmann equations that result from these choices are not identical, meaning that one must also define two different distribution functions, one dependent on the covariant components and the other on the contravariant components, to proceed unambiguously. Even though the routes were shown to be equivalent, one must be careful to use the components appropriate to a given Boltzmann equation.

In Debbasch & van Leeuwen (2009b), the authors showed that equation (6.5) is correct if 1) the sum involving  $\dot{k}^i$  in the second term is performed over the three spatial components, 2) the distribution function  $f$  is considered to be a function of the contravariant, spatial components  $k^i$ , and 3) any appearance of  $k_0$  (or  $k^0$ ) is replaced by  $k_0(k^i)$ . The dependence of  $k_0$  on the spatial momenta can be determined by solving the equation  $k_\mu k^\mu = 0$  for  $k_0$ . As we stated, the frame of interest is the comoving frame of the fluid, and we will denote the components of any tensor in this frame with a prime on the index; e.g.,  $k^{i'}$  is the  $i$ th component of the momentum in the comoving frame. With this convention, the relativistic Boltzmann equation becomes

$$k^{\mu'} \frac{\partial f}{\partial x^{\mu'}} - \Gamma_{\mu'\nu'}^{i'} k^{\mu'} k^{\nu'} \frac{\partial f}{\partial k^{i'}} = \delta f|_{coll}, \quad (6.6)$$

where we have used the geodesic equation,

$$\dot{k}^{i'} + \Gamma_{\mu'\nu'}^{i'} k^{\mu'} k^{\nu'} = 0, \quad (6.7)$$

to replace  $\dot{k}^{i'}$ , and

$$\Gamma_{\mu'\nu'}^{i'} = \frac{1}{2} g^{i'\alpha'} \left( \partial_{\mu'} g_{\nu'\alpha'} + \partial_{\nu'} g_{\mu'\alpha'} - \partial_{\alpha'} g_{\mu'\nu'} \right) \quad (6.8)$$

are the Christoffel symbols associated with the metric  $g_{\mu'\nu'}$  which, for our purposes, is induced by the acceleration associated with the comoving frame.

Equation (6.6) was provided by Lindquist (1966) and Castor (1972). Since they were considering spherically symmetric flows, they opted to change the form of equation (6.6) by using an orthonormal tetrad adapted to spherical coordinates. For our purposes, however, we will not be in the position to take advantage of any specific coordinate symmetries, so equation (6.6) will suffice.

Finally, it should also be mentioned that the right-hand side is evaluated at a specific location – the point in space and time where the collision occurs. The left-hand side, therefore, must also be evaluated at that spacetime point.

### 6.3 Diffusion approach to the transport equation

Here we will first make the approximation that the temperature of the gas is high enough such that all species, considered to comprise a single, massive fluid, are ionized, meaning that the right-hand side of equation (6.6) incorporates effects due only to scattering. In this case, the collisional term can be written (Hsieh & Spiegel, 1976)

$$\delta f|_{coll} = n' \int R(k^{\mu'}, k_i^{\mu'}) f(x^{\mu'}, k_i^{\mu'}) \frac{d^3 k_i^{\mu'}}{k_i^{0'}} - n' \int R(k_f^{\mu'}, k^{\mu'}) f(x^{\mu'}, k^{\mu'}) \frac{d^3 k_f^{\mu'}}{k_f^{0'}}, \quad (6.9)$$

where  $R$  is the redistribution function (not to be confused with the stress-energy tensor) and  $n'$  is the rest-frame number density of scatterers. The first term represents scatterings into the state  $k^{\mu'}$  from any initial momentum state  $k_i^{\mu'}$ , while the second embodies scatterings out of state  $k^{\mu'}$  into any other state  $k_f^{\mu'}$ . As long as photon wavelengths are long compared to the Compton wavelength and the gas is non-relativistic in the rest frame of the fluid, two suppositions we will make here, the redistribution function (in the comoving frame of the fluid) is that appropriate to Thomson scattering:

$$R(k^{\mu'}, k_i^{\mu'}) = \frac{3\sigma_T}{16\pi} \left( 1 + (\hat{k}^{x'} \hat{k}_i^{x'} + \hat{k}^{y'} \hat{k}_i^{y'} + \hat{k}^{z'} \hat{k}_i^{z'})^2 \right) \delta(k^{0'} - k_i^{0'}), \quad (6.10)$$

where  $\sigma_T$  is the Thomson cross section (or, more generally, the cross section relevant to the scatterer). The equation for  $R(k_f^{\mu'}, k^{\mu'})$  is identical to that for  $R(k^{\mu'}, k_i^{\mu'})$  but with  $k_i^{\mu'} \rightarrow k_f^{\mu'}$ . Inserting equation (6.10) into equation (6.9) and the result of that substitution into equation (6.6) gives our final form for the transfer equation.

It should be noted that the integrals in equation (6.9) are performed under the restriction that the photon four-momenta lie on the null cone. Since collisions occur instantaneously at fixed locations in space, we can approximate the metric to be locally that of flat space, i.e.,  $g_{\mu'\nu'} = \eta_{\mu'\nu'}$ , and we can use the null cone condition ( $k_{\mu'} k^{\mu'} = 0$ ) to write  $k^{0'} = |\mathbf{k}'| = \sqrt{(k^{x'})^2 + (k^{y'})^2 + (k^{z'})^2}$ . Every appearance of  $k^{0'}$  in equation (6.9) can thus be replaced by  $|\mathbf{k}'|$ .

Our goal here is to discern how the radiation field responds to gradients in the flow velocity.

In the next section, we will use the equations of radiation hydrodynamics to deduce how the flow couples to changes in the radiation field, thereby completing the picture. To achieve this goal we will adopt a diffusion approximation, asserting that the distribution function may be written as  $f \simeq f_0 + f_1$ , where  $f_1$  is a small correction to  $f_0$ . The “smallness” of  $f_1$  is encoded in the mean free path  $\sim (n'\sigma_T)^{-1}$  and the gradients of the flow velocity,  $v$ , across the mean free path, meaning that  $f_1 \sim f_0 dv/d\tau$ , where  $\tau \sim n'\sigma_T x$  is the optical depth.

Because the right-hand side of equation (6.6) is proportional to the optical depth (per unit length), the consistency of our diffusion approach demands that  $\delta f_0|_{coll} = 0$ . It can be verified that the right-hand side vanishes for any function  $f_0$  that depends only on the magnitude of the momentum, meaning that  $f_0$  is isotropic in the comoving frame. This result is consistent with the expectation that, in an optically-thick medium, the flux of radiation observed in a frame comoving with a fluid parcel is very nearly zero. Since the collision operator acts at a point in spacetime, however, the zeroth-order distribution function can also contain any other secular variation in space and time, meaning that its most general form is  $f_0(k^{\mu'}, x^{\mu'}) = f_0(|\mathbf{k}'|, x^{\mu'})$ . The first-order transfer equation, to be solved for  $f_1$ , is then

$$k^{\mu'} \frac{\partial f_0}{\partial x^{\mu'}} - \Gamma_{\mu'\nu'}^{i'} k^{\mu'} k^{\nu'} \frac{\partial f_0}{\partial k^{i'}} = \delta f_1|_{coll}. \quad (6.11)$$

To make more progress on this relation, we must determine the metric associated with the comoving frame. To do so, we will first assume a planar configuration of the fluid, with neither velocity nor variation in the  $x$  direction. We will then use the fact that the coordinate transformation to move into the comoving frame of a given fluid parcel is a local Lorentz transformation, the inverse of which is given by

$$t = \int_0^{t'} \Gamma dt'' + \int_0^{z'} \Gamma v_z dz'' + \int_0^{y'} \Gamma v_y dy'', \quad (6.12)$$

$$z = \int_0^{t'} \Gamma v_z dt'' + \int_0^{z'} \left(1 + \frac{v_z^2}{v^2} (\Gamma - 1)\right) dz'' + \int_0^{y'} \frac{v_z v_y}{v^2} (\Gamma - 1) dy'', \quad (6.13)$$

$$y = \int_0^{t'} \Gamma v_y dt'' + \int_0^{z'} \frac{v_z v_y}{v^2} (\Gamma - 1) dz'' + \int_0^{y'} \left( 1 + \frac{v_y^2}{v^2} (\Gamma - 1) \right) dy'', \quad (6.14)$$

$$x = x', \quad (6.15)$$

where  $v^2 = v_z^2 + v_y^2$ ,  $\Gamma = (1 - v^2)^{-1/2}$  is the Lorentz factor (not the Christoffel symbol), and we have, without loss of generality, chosen the origin of the primed coordinate system to coincide with that of the lab frame. The integrals are necessary here because the velocities are all dependent on the coordinates  $t'$ ,  $z'$ , and  $y'$ , but because we will ultimately be evaluating our expressions at the origin, one would obtain the same answer by letting  $\int_0^{t'} \Gamma dt'' = \Gamma t'$ , etc. Double-primed coordinates are simply dummy variables where for each integrand we let  $t' \rightarrow t''$ , etc. The line element, which in flat space is given by

$$ds^2 = -dt^2 + dz^2 + dy^2 + dx^2, \quad (6.16)$$

is invariant with respect to our choice of coordinates; the metric can therefore be determined by differentiating equations (6.12) – (6.15), inserting the results into equation (6.16) and grouping terms (see Castor 1972 for a similar, but non-relativistic, approach).

Calculating the Christoffel symbols, using the chain rule to determine  $\partial f / \partial k^{i'}$  and  $\partial f / \partial x^{\mu'}$ , inserting the expressions into equation (6.6) and evaluating the result at the origin (as this is the location of the fluid parcel – where the scattering occurs and where spacetime is locally Minkowskian), we find

$$k^{\mu'} \frac{\partial f_0}{\partial x^{\mu'}} - \Gamma_{\mu'\sigma'}^{i'} k^{\mu'} k^{\sigma'} \frac{\partial f_0}{\partial k^{i'}} =$$

$$k^{\mu'} \frac{\partial f_0}{\partial x^{\mu'}} \Big|_{|\mathbf{k}'|} - \frac{\Gamma^2}{v^2} \frac{\partial f_0}{\partial |\mathbf{k}'|} \left( A_1 (k^{z'})^2 + A_2 (k^{y'})^2 + A_3 |\mathbf{k}'| k^{z'} + A_4 |\mathbf{k}'| k^{y'} + A_5 k^{y'} k^{z'} \right), \quad (6.17)$$

where, by using the definitions of the Christoffel symbols and using  $U^{\mu'} = \delta^{\mu'}_{0'}$ , it can be shown that

$$\frac{\Gamma^2}{v^2} A_1 = \nabla_{z'} U_{z'}, \quad (6.18)$$

$$\frac{\Gamma^2}{v^2} A_2 = \nabla_{y'} U_{y'}, \quad (6.19)$$

$$\frac{\Gamma^2}{v^2} A_3 = \nabla_{0'} U_{z'}, \quad (6.20)$$

$$\frac{\Gamma^2}{v^2} A_4 = \nabla_{0'} U_{y'}, \quad (6.21)$$

$$\frac{\Gamma^2}{v^2} A_5 = \nabla_{y'} U_{z'} + \nabla_{z'} U_{y'}. \quad (6.22)$$

We broke up the derivative  $\partial/\partial x^{\mu'}$  into two separate components:  $\partial f_0/\partial|\mathbf{k}'|$ , taken such that all appearances of  $x^{\mu'}$  not contained in the definition of  $|\mathbf{k}'| = \sqrt{g_{i'j'} k^{i'} k^{j'}}$ , through the metric, are kept constant, and  $\partial f_0/\partial x^{\mu'}|_{|\mathbf{k}'|}$ , taken such that all spatial coordinates that appear through  $|\mathbf{k}'|$  are held fixed. Note that we must use the relativistically-correct version of the magnitude of the photon momentum, i.e., one involving the metric, because we are taking derivatives of the distribution function before evaluating the result at the location of the fluid parcel. Thus, even though spacetime is flat exactly at the point of interest, deviations exist at neighboring locations – the derivative requiring that we evaluate the distribution function at those locations. Though we did not explicitly denote it, the derivatives in equations (6.18) – (6.22) are to be evaluated at the origin.

The right-hand side of equation (6.6) involves an integral over  $f_1$  (recall that  $R(k^{\mu'}, k_i^{\mu'})$  is given by equation (6.10)), and the most direct means of evaluating  $f_1$  would be to expand both the left-hand side of the transfer equation and the function  $f_1$  in terms of spherical harmonics. Instead

of pursuing this route, however, we will make the educated guess

$$f_1 = B_1(k^{z'})^2 + B_2(k^{y'})^2 + B_3k^{z'} + B_4k^{y'} + B_5k^{z'}k^{y'}, \quad (6.23)$$

where the  $B$ 's are functions of  $x^{\mu'}$  and  $|\mathbf{k}'|$  (since the  $k$ 's are just linear combinations of spherical harmonics, this method yields the same result as proceeding in the more rigorous fashion of expanding the functions in terms of spherical harmonics). Inserting this ansatz into  $\delta f_1|_{coll}$ , performing the integrals and comparing powers of  $k$  on both sides, we find

$$B_1 = \frac{10}{9} \frac{1}{n'\sigma_T} \frac{1}{|\mathbf{k}'|} \frac{\partial f_0}{\partial |\mathbf{k}'|} \nabla_{z'} U_{z'}, \quad (6.24)$$

$$B_2 = \frac{10}{9} \frac{1}{n'\sigma_T} \frac{1}{|\mathbf{k}'|} \frac{\partial f_0}{\partial |\mathbf{k}'|} \nabla_{y'} U_{y'}, \quad (6.25)$$

$$B_3 = \frac{1}{n'\sigma_T} \left( \frac{\partial f_0}{\partial |\mathbf{k}'|} \nabla_{0'} U_{z'} - \frac{1}{|\mathbf{k}'|} \frac{\partial f_0}{\partial z'} \Big|_{|\mathbf{k}'|} \right), \quad (6.26)$$

$$B_4 = \frac{1}{n'\sigma_T} \left( \frac{\partial f_0}{\partial |\mathbf{k}'|} \nabla_{0'} U_{y'} - \frac{1}{|\mathbf{k}'|} \frac{\partial f_0}{\partial y'} \Big|_{|\mathbf{k}'|} \right), \quad (6.27)$$

$$B_5 = \frac{10}{9} \frac{1}{n'\sigma_T} \frac{1}{|\mathbf{k}'|} \frac{\partial f_0}{\partial |\mathbf{k}'|} \left( \nabla_{y'} U_{z'} + \nabla_{z'} U_{y'} \right). \quad (6.28)$$

In addition, however, we find that there are isotropic terms, i.e., only dependent on  $|\mathbf{k}'|$ , that arise from the integrations over  $(k^{z'})^2$  and  $(k^{y'})^2$ ; it is also apparent that  $k^{0'} \partial f_0 / \partial t'$ , the first term in the sum in equation (6.17), represents an isotropic contribution to the left-hand side. Since the collision integral is zero for any isotropic term, however, these additional terms cannot be accounted for with our correction to the distribution function. (Equivalently, there are terms proportional to the  $Y_0^0$  spherical harmonic, a constant, that cannot be balanced by adding more terms to the distribution function.) We are therefore forced to equate these extraneous collision terms and

the time derivative, yielding an extra constraint that the zeroth-order distribution function must satisfy:

$$\frac{1}{3} \nabla_{i'} U_{i'} \Big|_{|\mathbf{k}'|} \frac{\partial f_0}{\partial |\mathbf{k}'|} = \frac{\partial f_0}{\partial t'} \Big|_{|\mathbf{k}'|}. \quad (6.29)$$

What does this condition mean physically? As an illustrative example, let us take the case where the zeroth-order distribution function is given by that for blackbody radiation:

$$f_0 = \frac{C}{e^{\frac{|\mathbf{k}'|}{T}} - 1}, \quad (6.30)$$

where  $C$  is a constant, the value of which is unimportant, and we have taken Boltzmann's constant to be one. With this form for  $f_0$ , equation (6.29) becomes

$$\frac{\partial T}{\partial t'} = -\frac{1}{3} T \nabla_{i'} U_{i'}. \quad (6.31)$$

This, however, is just the gas energy equation for an isentropic, relativistic gas in the frame comoving with the fluid. Equation (6.29), therefore, is equivalent to the statement that the zeroth-order distribution function be isentropic.

The first-order correction to the distribution function, using equations (6.24) – (6.28), is thus

$$\begin{aligned} \rho' \kappa f_1 = & \frac{10}{9} \frac{1}{|\mathbf{k}'|} \frac{\partial f_0}{\partial |\mathbf{k}'|} \left( (k^{z'})^2 \nabla_{z'} U_{z'} + (k^{y'})^2 \nabla_{y'} U_{y'} + k^{y'} k^{z'} (\nabla_{y'} U_{z'} + \nabla_{z'} U_{y'}) \right) \\ & + \frac{\partial f_0}{\partial |\mathbf{k}'|} \left( k^{z'} \nabla_{0'} U_{z'} + k^{y'} \nabla_{0'} U_{y'} \right) - \frac{1}{|\mathbf{k}'|} \left( k^{z'} \frac{\partial f_0}{\partial z'} \Big|_{|\mathbf{k}'|} + k^{y'} \frac{\partial f_0}{\partial y'} \Big|_{|\mathbf{k}'|} \right) \end{aligned} \quad (6.32)$$

where  $\kappa = n' \sigma_T / \rho'$  is the opacity. Since we used a relativistic approach to derive this expression, we should be able to write it in a covariant fashion. This is indeed the case, the covariant form being

$$\rho' \kappa f_1 = \frac{10}{9} \frac{1}{|\mathbf{k}'|} \frac{\partial f_0}{\partial |\mathbf{k}'|} \Pi_{\sigma'}^{\mu'} \Pi_{\alpha'}^{\nu'} k^{\sigma'} k^{\alpha'} \nabla_{\mu'} U_{\nu'} + \frac{\partial f_0}{\partial |\mathbf{k}'|} \Pi_{\sigma'}^{\nu'} k^{\sigma'} U^{\mu'} \nabla_{\mu'} U_{\nu'} - \frac{1}{|\mathbf{k}'|} \Pi_{\nu'}^{\mu'} k^{\nu'} \nabla_{\mu', |\mathbf{k}'|} f_0, \quad (6.33)$$

where  $\Pi^{\mu'\nu'} = U^{\mu'}U^{\nu'} + g^{\mu'\nu'}$  is the projection tensor introduced by Eckart (1940) (see section 1). We introduced the quantity  $\nabla_{\mu',|\mathbf{k}'|}$  to signify the derivative with respect to coordinate  $x^{\mu'}$  holding  $|\mathbf{k}'|$  constant. This is an important distinction if we want to calculate derivatives of  $f_1$  as we must use the relativistically-correct definition  $|\mathbf{k}'| = \sqrt{g_{i'j'}k^{i'}k^{j'}}$  and  $g_{i'j'}$  depends on  $x^{\mu'}$ .

The preceding analysis only considered a single fluid element. However, the location of our origin, tantamount to the position of the fluid element under consideration, is arbitrary, meaning that equation (6.33) is applicable to the entire fluid. Also, even though we only considered planar flows, we can easily generalize the approach to include three-dimensional motion and variations, and (6.33) still holds. Greek indices therefore range from 0 to 3 in equation (6.33).

In the next section we will use equation (6.33) and integrals thereof to write the equations of radiation hydrodynamics, equation (6.1), in terms of the four-velocity of the fluid, the mass density, and the radiation energy density, to which we will add the continuity equation for the scatterers to close the system. How do we reconcile these with equation (6.29), which seems to be an additional constraint? Recall that equation (6.29) was derived by equating the “extra,” isotropic terms arising from both the collision integral and the derivatives of  $f_0$ . If we were to attempt to derive the **second** order correction to the distribution function,  $f_2$ , we would doubtless encounter more isotropic terms arising from the derivatives of  $f_1$  and collision integrals of  $f_2$ , this time to first order in the optical depth, which we would have to add to equation (6.29). Equation (6.29) therefore only captures effects to zeroth order in the mean free path. Although it constrains the spatial and temporal derivatives of  $f_0$  appearing in equation (6.33), it has no effect on the form of this equation. However, the gas energy equation (see equation 6.50) should reduce to equation (6.29) in the limit that  $\rho'\kappa \rightarrow \infty$ .

#### 6.4 Relativistic, diffusive equations of radiation hydrodynamics

The equations of radiation hydrodynamics, valid in any frame, are given by equation (6.1). Because we now have the distribution function to the requisite order in the optical depth, we can simplify those equations by writing the radiation energy-momentum tensor as  $R^{\mu\nu} = R_0^{\mu\nu} + R_1^{\mu\nu}$ ,

where each  $R^{\mu\nu}$  is given by equation (6.3) with the appropriate distribution function. We will derive each of these tensors in the comoving frame but write them in a manifestly covariant form, the results then being applicable in any coordinate system.

The comoving, isotropic energy-momentum tensor is given by

$$R_0^{\mu'\nu'} = \int k^{\mu'} k^{\nu'} f_0 \frac{d^3 k'}{k^{0'}},$$

which we can show is equivalent to

$$R_0^{\mu'\nu'} = e' U^{\mu'} U^{\nu'} + \frac{1}{3} e' \Pi^{\mu'\nu'}, \quad (6.34)$$

where

$$e' = 4\pi \int_0^\infty f_0 |\mathbf{k}'|^3 d|\mathbf{k}'| \quad (6.35)$$

is the isotropic radiation energy density. Since the projection tensor is orthogonal to the four-velocity, a time-like vector that selects the energy component of a tensor, it is reasonable to associate  $e'/3$  with the pressure, or momentum density, exhibited by the fluid. With this association, equation (6.34), not surprisingly, demonstrates that radiation acts like a gas with a relativistic equation of state, i.e., one with an adiabatic index of 4/3.

The correction to the energy-momentum tensor,

$$R_1^{\mu'\nu'} = \int k^{\mu'} k^{\nu'} f_1 \frac{d^3 k'}{k^{0'}}, \quad (6.36)$$

will have a number of terms, as evidenced by equation (6.33). Integrating by parts and performing some simple manipulations, we can show that  $R_1^{\mu'\nu'}$  is given by

$$\begin{aligned} \rho' \kappa R_1^{\mu'\nu'} = & -\frac{10}{9} \frac{4}{3} e' U^{\mu'} U^{\nu'} \nabla_{\alpha'} U^{\alpha'} - \frac{10}{9} \frac{4}{15} e' \Pi^{\mu'\sigma'} \Pi^{\nu'\rho'} \left( \nabla_{\sigma'} U_{\rho'} + \nabla_{\rho'} U_{\sigma'} - \frac{2}{3} g_{\sigma'\rho'} \nabla_{\alpha'} U^{\alpha'} \right) \\ & - \frac{10}{9} \frac{4}{9} e' \Pi^{\mu'\nu'} \nabla_{\alpha'} U^{\alpha'} - \frac{1}{3} \left( U^{\mu'} \Pi^{\nu'\sigma'} + U^{\nu'} \Pi^{\mu'\sigma'} \right) \left( 4e' U^{\rho'} \nabla_{\rho'} U_{\sigma'} + \nabla_{\sigma'} e' \right). \end{aligned} \quad (6.37)$$

Written in this manner, it is evident that  $R_1^{\mu\nu}$  transforms like a tensor. It should also be noted that each term in the tensor contains a derivative of a quantity, either the fluid velocity or the energy of the radiation field, with respect to the optical depth, which is what we expected.

Equation (6.37) differs from equation (6.4), the viscous stress tensor proposed by Weinberg (1971), in two notable ways. The first is that we have not postulated the existence of a temperature; instead we just used the fact that the zeroth-order distribution function is isotropic in the comoving frame to leave the comoving energy density, given by equation (6.35), as an unknown. The temperature has in fact been a difficult quantity to define in past treatments (see Weinberg's discussion of the reconciliation between the results of Thomas (1930) and Eckart's general form for a relativistic viscous stress tensor; see also Lima & Waga 1990), and it is reassuring to find that the physics is perfectly well-described without invoking such a quantity.

The second difference is contained in the presence of the first term of our stress tensor, proportional to  $U^\mu U^\nu$ , which shows that there is a correction to the comoving radiation energy density – **defined** to be zero by Eckart (1940) and Weinberg (1971) – given by

$$\Delta e' = -\frac{10}{9} \frac{4}{3} \frac{e'}{\rho' \kappa} \nabla_{\alpha'} U^{\alpha'}. \quad (6.38)$$

This expression can be understood as follows: imagine that we take a spherical volume of fluid and contract it by some amount, i.e., such that  $\nabla_{\alpha'} U^{\alpha'}$  is negative. Because of the nature of the Thomson cross section, any radiation intersected by the contracting fluid will be scattered preferentially in the direction of motion. Therefore, the radiation energy in this volume will be increased owing to the in-scattering of photons, which is reflected in equation (6.38). Furthermore, if we recall that the term in the stress tensor proportional to  $\Pi^{\mu'\nu'}$  can be interpreted as the pressure exerted by the radiation on a fluid element, we see that

$$\Delta p' = -\frac{10}{9} \frac{4}{9} \frac{e'}{\rho' \kappa} \nabla_{\mu'} U^{\mu'} = \frac{1}{3} \Delta e'. \quad (6.39)$$

This demonstrates that the change in pressure is 1/3 the change in energy, which is what we expect

– the relativistic nature of the photon gas is preserved independent of the manner in which we expand the distribution function. It can also be shown that the trace of  $R_1^{\mu\nu}$  is zero, which is another familiar property of a relativistic gas.

Comparing the other terms in equation (6.37) to the form of an arbitrary viscous stress tensor given by (6.4), we find

$$\eta = \frac{8}{27} \frac{e'}{\rho'\kappa} \quad (6.40)$$

for the coefficient of dynamic viscosity, which agrees with the findings of Loeb & Laor (1992). Thomas (1930) used an incorrect form for the Thomson cross section, so Weinberg (1971) did not have the factor of 10/9. The proportionality to  $e'$  is sensible, as the viscous effect is mediated by radiation; therefore, a higher radiation energy density permits a higher transfer of energy and momentum to neighboring fluid elements. The viscous effect is also proportional to the mean free path of the radiation, which is also a reasonable result: smaller mean free paths mean that the observed velocity difference across a mean free path is smaller for a given shear, implying less transfer of momentum per scattering. The coefficient of bulk viscosity is found to be

$$\zeta = \frac{1}{3}\eta, \quad (6.41)$$

and is not zero, as predicted by Eckart (1940) and Weinberg (1971) for a radiation-dominated fluid. Because we did not introduce a temperature, we cannot define a coefficient of heat conduction in a manner analogous to that of Weinberg (1971). However, for the case where the zeroth-order distribution function is that of blackbody radiation, it can be verified that  $\chi = 4aT^3/3$ , which agrees with his findings.

We can also calculate the correction to the flux of photons, where the flux four-vector is given by

$$F^\mu = \int k^\mu f \frac{d^3k}{k^0}. \quad (6.42)$$

As expected, the zeroth-order flux only has a non-vanishing number density in the comoving frame, given by

$$F_0^{0'} \equiv N' = 4\pi \int f_0 |\mathbf{k}'|^2 d|\mathbf{k}'|, \quad (6.43)$$

which can be written covariantly as

$$F_0^{\mu'} = N' U^{\mu'}. \quad (6.44)$$

As for the energy-momentum tensor, we can use equation (6.33) and integrate by parts to write the correction to the flux vector in terms of  $N'$ . We find

$$\rho' \kappa F_1^{\mu'} = -\frac{10}{9} N' U^{\mu'} \nabla_{\alpha'} U^{\alpha'} - \frac{1}{3} \Pi^{\mu' \sigma'} \left( 3 N' U^{\alpha'} \nabla_{\alpha'} U_{\sigma'} + \nabla_{\sigma'} N' \right). \quad (6.45)$$

We see that this expression yields

$$\Delta N' = -U_{\mu'} F_1^{\mu'} = -\frac{10}{9} \frac{N'}{\rho' \kappa} \nabla_{\alpha'} U^{\alpha'} \quad (6.46)$$

as the correction to the comoving number density of photons, a result in contrast to the analysis of Eckart (1940), who **defined**  $\Delta N'$  to be zero. However, equation (6.46) has a similar interpretation to equation (6.38): by noting that a contracting gas preferentially scatters photons in the direction of motion of the scatterers, one would expect an increased amount of radiation within that contracting volume. We also find

$$\frac{\Delta e'}{e'} = \frac{4}{3} \frac{\Delta N'}{N'}, \quad (6.47)$$

reaffirming the notion that radiation behaves as a relativistic gas and demonstrating that it is these extra photons,  $\Delta N'$ , that add to the energy of the contracting fluid.

For the case of a cold gas, where  $T^{\mu\nu} = \rho' U^\mu U^\nu$ , we will, for completeness, write down the

full set of equations:

$$\nabla_\mu \left( \rho' U^\mu \right) = 0, \quad (6.48)$$

$$\begin{aligned} \nabla_\mu \left[ \left\{ \rho' + \frac{4}{3} e' \left( 1 - \frac{10}{9} \frac{1}{\rho' \kappa} \nabla_\alpha U^\alpha \right) \right\} U^\mu U^\nu \right] - \frac{8}{27} \nabla_\mu \left[ \frac{e'}{\rho' \kappa} \Pi^{\mu\sigma} \Pi^{\nu\beta} \left( \nabla_\sigma U_\beta + \nabla_\beta U_\sigma + g_{\beta\sigma} \nabla_\alpha U^\alpha \right) \right] \\ + \frac{1}{3} g^{\mu\nu} \partial_\mu e' - \frac{1}{3} \nabla_\mu \left[ \frac{e'}{\rho' \kappa} \left( \Pi^{\mu\sigma} U^\nu + \Pi^{\nu\sigma} U^\mu \right) \left( 4U^\beta \nabla_\beta U_\sigma + \partial_\sigma \ln e' \right) \right] = 0. \end{aligned} \quad (6.49)$$

The first of these is just the continuity equation. We will also derive the gas energy equation, obtained by contracting equation (6.49) with the four velocity, which gives

$$\begin{aligned} \nabla_\mu (e' U^\mu) + \frac{1}{3} e' \nabla_\mu U^\mu = \frac{4}{3} \frac{10}{9} \nabla_\mu \left[ \frac{e'}{\rho' \kappa} U^\mu \nabla_\alpha U^\alpha \right] + \frac{8}{27} \frac{e'}{\rho' \kappa} \left( \nabla_\sigma U_\beta + \nabla_\beta U_\sigma + g_{\sigma\beta} \nabla_\alpha U^\alpha \right) \Pi^{\mu\sigma} \nabla_\mu U^\beta \\ + \frac{1}{3} \Pi^{\mu\sigma} \nabla_\mu \left[ \frac{e'}{\rho' \kappa} \left( 4U^\beta \nabla_\beta U_\sigma + \partial_\sigma \ln e' \right) \right] + \frac{1}{3} \frac{e'}{\rho' \kappa} \left( 4U^\beta \nabla_\beta U_\sigma + \partial_\sigma \ln e' \right) \left( 2U^\mu \nabla_\mu U^\sigma + U^\sigma \nabla_\mu U^\mu \right). \end{aligned} \quad (6.50)$$

The left-hand side is just the change in energy for an adiabatic,  $\gamma = 4/3$  gas, where  $\gamma$  is the adiabatic index. Note that if  $e' \sim T^4$  and we let  $\rho' \kappa \rightarrow \infty$ , the left-hand side equals equation (6.29). The right-hand side therefore represents the energy added to the radiation during interactions with the scatterers (see section 6 for a discussion concerning the entropy generated by this heat addition).

## 6.5 Perturbation analysis

Hiscock & Lindblom (1985) showed that the general viscous tensor proposed by Eckart (1940) is unstable to small perturbations in a fluid. An interesting question is whether or not these instabilities appear in our set of equations.

To answer this question, consider an equilibrium solution  $(\rho', e', U^\mu)$  where all of the variables are constants in space and time, the fluid is motionless and the space is flat. On top of this equilibrium solution we will impose perturbations on our variables  $(\delta\rho', \delta e', \delta U^\mu)$  small enough

such that their products are negligible. With this configuration, the zeroth-order fluid equations are trivially satisfied. The first-order perturbations to the energy-momentum tensors are

$$\delta T^{\mu\nu} = U^\mu U^\nu \delta \rho' + \rho' (U^\nu \delta U^\mu + U^\mu \delta U^\nu), \quad (6.51)$$

$$\delta R_0^{\mu\nu} = \frac{4}{3} U^\mu U^\nu \delta e' + \frac{4}{3} e' (U^\nu \delta U^\mu + U^\mu \delta U^\nu) + \frac{1}{3} g^{\mu\nu} \delta e', \quad (6.52)$$

$$\begin{aligned} \delta R_1^{\mu\nu} = & -\frac{10}{9} \frac{4}{3} \frac{e'}{\rho' \kappa} U^\mu U^\nu \nabla_\alpha \delta U^\alpha - \frac{8}{27} \frac{e'}{\rho' \kappa} \Pi^{\mu\sigma} \Pi^{\nu\rho} \left( \nabla_\sigma \delta U_\rho + \nabla_\rho \delta U_\sigma - \frac{2}{3} g_{\sigma\rho} \nabla_\alpha \delta U^\alpha \right) \\ & - \frac{10}{9} \frac{4}{9} \frac{e'}{\rho' \kappa} \Pi^{\mu\nu} \nabla_\alpha \delta U^\alpha - \frac{1}{3} \left( U^\mu \Pi^{\nu\sigma} + U^\nu \Pi^{\mu\sigma} \right) \left( 4 \frac{e'}{\rho' \kappa} U^\rho \nabla_\rho \delta U_\sigma + \frac{1}{\rho' \kappa} \nabla_\sigma \delta e' \right). \end{aligned} \quad (6.53)$$

We assumed here that the perturbations are small enough such that gravitational corrections can be ignored, i.e.,  $\delta g_{\mu\nu} = 0$ . The first-order conservation equations that must be satisfied are now

$$\nabla_\mu (\delta T^{\mu\nu} + \delta R_0^{\mu\nu}) = -\nabla_\mu \delta R_1^{\mu\nu}. \quad (6.54)$$

These four equations must also be coupled to the mass continuity equation, the first-order correction to which is

$$\nabla_\mu (U^\mu \delta \rho' + \rho' \delta U^\mu) = 0. \quad (6.55)$$

The normalization of the four-velocity,  $U_\mu U^\mu = -1$ , demonstrates that  $\delta U^0 = 0$ .

For the present analysis we will restrict our attention to planar flows, such that  $\delta U^x \equiv 0$  and any perturbations in the  $x$  direction are exactly zero. In this case, only the  $\nu = 0, y$ , and  $z$  components of equation (6.54) are non-trivial. Carrying out the derivatives, we find that they become, respectively,

$$\frac{\partial}{\partial t} \delta e' + \frac{4}{3} e' \nabla_i \delta U^i = \frac{4}{3} \left( 1 + \frac{10}{9} \right) \frac{e'}{\rho' \kappa} \frac{\partial}{\partial t} \nabla_i \delta U^i + \frac{1}{3} \frac{1}{\rho' \kappa} \nabla_i \nabla^i \delta e', \quad (6.56)$$

$$(\rho' + \frac{4}{3}e') \frac{\partial}{\partial t} \delta U^z + \frac{1}{3} \frac{\partial}{\partial z} \delta e' = \frac{8}{27} \frac{e'}{\rho' \kappa} \left( \nabla_i \nabla^i \delta U^z + 2 \nabla_i \nabla_z \delta U^i \right) + \frac{4}{3} \frac{e'}{\rho' \kappa} \frac{\partial^2}{\partial t^2} \delta U^z + \frac{1}{3} \frac{1}{\rho' \kappa} \frac{\partial}{\partial t} \frac{\partial}{\partial z} \delta e', \quad (6.57)$$

$$(\rho' + \frac{4}{3}e') \frac{\partial}{\partial t} \delta U^y + \frac{1}{3} \frac{\partial}{\partial y} \delta e' = \frac{8}{27} \frac{e'}{\rho' \kappa} \left( \nabla_i \nabla^i \delta U^y + 2 \nabla_i \nabla_y \delta U^i \right) + \frac{4}{3} \frac{e'}{\rho' \kappa} \frac{\partial^2}{\partial t^2} \delta U^y + \frac{1}{3} \frac{1}{\rho' \kappa} \frac{\partial}{\partial t} \frac{\partial}{\partial y} \delta e'. \quad (6.58)$$

We will now impose the restriction that each of our perturbations varies periodically as

$$\delta \xi = \xi_0 e^{ik_\mu x^\mu}, \quad (6.59)$$

where  $k_\mu = (-\omega, k_i)$  and  $x^\mu = (t, x^i)$  (this approach is equivalent to taking the Fourier transform of the equations). Before substituting these expressions into equations (6.56) – (6.58), however, first recall that  $\delta R_1^{\mu\nu} < \delta R_0^{\mu\nu}$ , as required by our ordering scheme adopted when solving the Boltzmann equation perturbatively. Investigating the correction to the comoving energy density, this inequality implies

$$\frac{e'}{\rho' \kappa} \nabla_i \delta U^i \lesssim \delta e',$$

or, in terms of the wavenumber,

$$\left| \frac{k_i \delta U^i}{\rho' \kappa} \right| \lesssim \frac{\delta e'}{e'},$$

where we introduced the absolute value signs because of the presence of the imaginary unit. Since  $\delta e' \sim e'$ ,  $\delta U^i \sim 1$  and  $k_i \sim 1/\lambda$ , where  $\lambda$  is the wavelength of the perturbation, this inequality becomes  $\lambda \rho' \kappa \gtrsim 1$ . We see, therefore, that the optical depth across one wavelength must be greater than one in order for this perturbation analysis to hold. Equivalently, the wavelength of the perturbation, or the scale over which the perturbation acts, must be larger than the mean free path of a photon. If we induce changes on spatial scales smaller than the mean free path, we will violate the assumption that the mean free path is a good “smallness” parameter for describing interactions between the fluid and the radiation.

Investigating the other terms in  $\delta R_1^{\mu\nu}$ , we find that the inequality

$$\frac{e'}{\rho'\kappa} U^\rho \nabla_\rho \delta U^\mu \lesssim U^\mu \delta e'$$

must also be upheld, which can be rearranged to give

$$\frac{\omega}{\rho'\kappa} \lesssim 1. \quad (6.60)$$

Recalling that  $1/\omega$  is proportional to the period of oscillation of the perturbation, this inequality means that the oscillation time scale must be longer than the light-crossing time over the mean free path.

With the previous inequalities in mind, we will now insert our Fourier modes into equations (6.56) – (6.58). The resulting three algebraic relations can be written as

$$M_\nu^\mu \delta \xi^\nu = 0, \quad (6.61)$$

where

$$\delta \xi^\nu = \begin{pmatrix} \delta e' \\ \delta U^z \\ \delta U^y \end{pmatrix} \quad (6.62)$$

and

$$M_\nu^\mu = \begin{pmatrix} -i\omega + \frac{1}{3} \frac{1}{\rho'\kappa} k^2 & \frac{4}{3} \left( i e' - \frac{19}{9} \frac{e'}{\rho'\kappa} \omega \right) k^z & \frac{4}{3} \left( i e' - \frac{19}{9} \frac{e'}{\rho'\kappa} \omega \right) k^y \\ \frac{1}{3} \left( i - \frac{\omega}{\rho'\kappa} \right) k^z & -i\omega(\rho' + \frac{4}{3} e') + \frac{8}{27} \frac{e'}{\rho'\kappa} \left( \tilde{k}^2 + 2(k^z)^2 \right) & \frac{16}{27} \frac{e'}{\rho'\kappa} k^z k^y \\ \frac{1}{3} \left( i - \frac{\omega}{\rho'\kappa} \right) k^y & \frac{16}{27} \frac{e'}{\rho'\kappa} k^z k^y & -i\omega(\rho' + \frac{4}{3} e') + \frac{8}{27} \frac{e'}{\rho'\kappa} \left( \tilde{k}^2 + 2(k^y)^2 \right) \end{pmatrix}, \quad (6.63)$$

where  $k^2 \equiv (k^y)^2 + (k^z)^2$  and  $\tilde{k}^2 \equiv k^2 + 9\omega^2/2$ .

If the perturbations  $\delta \xi^\nu$  are to be non-trivial, we demand  $\det(M_\nu^\mu) = 0$ , which results in a dispersion relation that gives  $w(k^i)$ . Before setting the entire determinant equal to zero, recall

that physically-meaningful frequencies and wavenumbers (from the standpoint that they can be described as viscous corrections to the energy momentum tensor) satisfy  $w/(\rho'\kappa) \sim k^i/(\rho'\kappa) \lesssim 1$ . Therefore, a first approximation to the dispersion relation can be obtained by setting all appearances of  $1/(\rho'\kappa)$  to zero in the matrix given by (6.63). Doing so and taking the determinant, we find

$$\det(M_{\nu}^{\mu}) = i\omega \left( \rho' + \frac{4}{3}e' \right) \left( \omega^2 \left( \rho' + \frac{4}{3}e' \right) - \frac{4}{9}e'k^2 \right) = 0,$$

the solutions to which are clearly

$$\omega = 0, \quad \omega = \pm \frac{2}{3} \sqrt{\frac{e'}{\rho' + \frac{4}{3}e'}} k. \quad (6.64)$$

The first of these represents a perturbation with a constant offset from the surrounding medium. The second two are the sound waves that propagate through the optically-thick plasma; if  $e' \ll \rho'$ , we recover the familiar result for the sound speed of a radiation-dominated gas  $c_s = \sqrt{4p'/3\rho'}$ , where  $p' = 3e'$  is the radiation pressure, while for  $e' \gg \rho'$ , we find  $c_s = c/\sqrt{3}$ , which is the correct ultrarelativistic speed of propagation.

We can show that the full determinant can be written

$$\begin{aligned} \det(M_{\nu}^{\mu}) = & \left\{ \frac{8}{27} \frac{e'}{\rho'\kappa} \tilde{k}^2 - i\omega \left( \rho' + \frac{4}{3}e' \right) \right\} \\ & \times \left\{ \left( \frac{1}{3} \frac{k^2}{\rho'\kappa} - i\omega \right) \left( \frac{8}{27} \frac{e'}{\rho'\kappa} \left( \tilde{k}^2 + 2k^2 \right) - i\omega \left( \rho' + \frac{4}{3}e' \right) \right) - \frac{4}{9}e' \left( i - \frac{19}{9} \frac{\omega}{\rho'\kappa} \right) \left( i - \frac{\omega}{\rho'\kappa} \right) k^2 \right\}, \end{aligned} \quad (6.65)$$

meaning that the dispersion relation is given by the solutions to

$$\frac{8}{27} \frac{e'}{\rho'\kappa} \left( k^2 + \frac{9}{2}\omega^2 \right) - i\omega \left( \rho' + \frac{4}{3}e' \right) = 0, \quad (6.66)$$

$$\left( \frac{1}{3} \frac{k^2}{\rho'\kappa} - i\omega \right) \left( \frac{8}{9} \frac{e'}{\rho'\kappa} \left( k^2 + \frac{3}{2}\omega^2 \right) - i\omega \left( \rho' + \frac{4}{3}e' \right) \right) - \frac{4}{9}e' \left( i - \frac{19}{9} \frac{\omega}{\rho'\kappa} \right) \left( i - \frac{\omega}{\rho'\kappa} \right) k^2 = 0, \quad (6.67)$$

where in each of these we used the definition of  $\tilde{k}^2$ .

To solve these, recall that the perturbation frequencies permissible in our analysis are approximately given by equation (6.64) with small corrections of order  $1/(\rho'\kappa)$ . If we set  $\rho'\kappa = 0$  in the preceding two polynomials, we see that the first reduces to  $\omega = 0$ , while the second gives the sound waves. In (6.66), we will therefore let  $\omega = \omega_1/(\rho'\kappa)$  and keep only first order terms in  $1/(\rho'\kappa)$ . Doing so, we find

$$\omega_1 \simeq -i \frac{8}{27} \frac{e'}{\rho' + \frac{4}{3}e'} k^2. \quad (6.68)$$

Since the perturbations scale as  $\delta\xi^\nu \sim e^{-i\omega t}$ ,  $\omega_1$  is a decaying solution. The e-folding timescale of constant-offset perturbations is thus

$$\tau_d \simeq \frac{27}{8} \frac{\rho' c^2 + \frac{4}{3}e' \rho' \kappa}{e' c k^2}, \quad (6.69)$$

where we explicitly reintroduced the speed of light  $c$ , which shows that smaller-scale fluctuations decay more rapidly.

To solve equation (6.67), we will let  $\omega = \omega_\pm + \omega_1/(\rho'\kappa)$ , where  $\omega_\pm$  is given by

$$\omega_\pm = \pm \frac{2}{3} \sqrt{\frac{e'}{\rho' + \frac{4}{3}e'}} k, \quad (6.70)$$

the zeroth-order (in the mean free path) solution to the dispersion relation. Using this approximation and keeping only highest-order terms, we find

$$\omega_1 = -\frac{i}{6} \frac{(\rho')^2 + \frac{32}{27}\rho'e' + \frac{32}{27}(e')^2}{(\rho' + \frac{4}{3}e')^2} k^2. \quad (6.71)$$

The decay timescale for traveling waves is therefore on the same order as that for the constant-offset perturbations.

When we solved these dispersion relations, we used the fact that  $\omega/(\rho'\kappa)$  must be small for our analysis to hold. If we had not taken this perturbative approach, however, we would have

obtained conflicting results. For example, the exact solution to equation (6.66) is

$$\omega = i \frac{\rho' + \frac{4}{3}e'}{\frac{8}{3}\rho'\kappa} \left( 1 \pm \sqrt{1 + \frac{128}{81} \left( \frac{e'k}{\rho'\kappa} \right)^2} \right). \quad (6.72)$$

If we take the root with the negative sign, the result reduces to equation (6.68) in the limit that we keep only first-order corrections in  $k/(\rho'\kappa)$ ; but, if we take the positive sign, we find that the solution is a **growing** mode, showing that the fluid perturbations are unstable. However, since these growing modes always have  $\omega/(\rho'\kappa) > 1$ , our treatment of the equations of radiation hydrodynamics, which only considers fluid perturbations on timescales greater than the light-crossing time over one optical depth, is invalid.

One can understand the physical origin of these growing modes by imagining that we oscillate a fluid parcel in such a way that its period is one-half of the light-crossing time over the mean free path that separates it from its neighboring fluid element. In this case, by the time the information from the neighboring fluid parcel returns back to the originally-perturbed parcel, the relative velocity between the two fluid elements will be in the same direction as the initial perturbation. The viscous force will then serve to increase the amplitude of the oscillation of the fluid element and, taken over many optical depth light-crossing times, this effect will only be amplified, resulting in a runaway process.

It is for this reason that the analysis of Hiscock & Lindblom (1985) resulted in the prediction of growing modes. If we take the positive root of equation (6.72) and use numbers for water at room temperature, we find  $\tau = 1/\omega \simeq 10^{-35}$  s is the e-folding time of the perturbations. As pointed out by Hiscock & Lindblom (1985), viscous heating would cause water to boil on an absurdly short timescale. This result is incorrect, however, because of the inability of the fluid to communicate over such timescales; these high frequencies blatantly violate the assumption that the mean free path of the radiation is sufficiently small to describe local fluid deformations.

For a general coefficient of dynamic viscosity  $\eta$ , this requirement can be translated to a statement similar to, “frequencies must satisfy the inequality  $\omega\eta/e' \lesssim 1$ , where  $e'$  is the locally-observed

energy density of the fluid, in order for viscous effects to describe physically the perturbations that take place in the medium.” It is also not surprising that in the limit of  $c \rightarrow \infty$ , this result disappears as the light-crossing time is zero, meaning that the Newtonian limit of these equations will never suffer from such growing instabilities. We can see this explicitly by reinserting the factors of  $c$  into equation (6.66), which reads

$$\frac{8}{27} \frac{e'}{\rho' \kappa} \left( k^2 + \frac{9}{2} \frac{\omega^2}{c^2} \right) - \frac{i\omega}{c} \left( \rho' c^2 + \frac{4}{3} e' \right) = 0.$$

Ignoring the factor of  $\omega^2/c^2$  and solving reveals only decaying solutions.

## 6.6 Discussion and Conclusions

We have shown, in agreement with intuition and past efforts, that radiation behaves like a viscosity in the optically-thick limit. Our analysis is based on the general relativistic Boltzmann equation, general relativistic corrections being necessary because the scattering, for which we used the differential Thomson cross section, is handled most easily in the local, accelerating frame of the fluid. The correction to the photon distribution function, given explicitly by equation (6.33), was used to calculate the correction to the energy-momentum tensor of the radiation (equation (6.37)), and many of the terms agreed with the predictions of Eckart (1940) and Weinberg (1971).

There are, however, a few differences between our form for the correction to the radiation energy-momentum tensor and the general viscous stress tensor proposed by Weinberg (1971), the first being that ours does not depend on thermodynamic considerations such as the assignment of a temperature to the zeroth-order distribution function. The temperature-independence of our equations means that the isotropic radiation distribution need not correspond to that of blackbody radiation. Indeed, because our approach treats the radiation and the scatterers as two interacting media, it is not clear what a single temperature would mean. The second difference is that our viscous tensor contains a correction to the comoving energy density of the radiation, which is not predicted by previous approaches to deriving the viscous tensor for a relativistic fluid. We

demonstrated that this term appears naturally from the manner in which radiation is scattered in a contracting (or expanding) fluid element. This correction is consistent with, and in fact expected from, the notion that the radiation is a relativistic (adiabatic index of  $4/3$ ) gas. Furthermore, our model predicts a correction to the number density of photons (equations (6.45) and (6.46)), the presence of which corresponds exactly with the increase in the energy density of the fluid.

We performed a perturbation analysis on our equations, took the Fourier transform of the perturbed equations and calculated the dispersion relation (equations (6.66) and (6.67)). Because our treatment is concerned with the limit in which the stress tensor is a small perturbation proportional to the mean free path of the radiation, the wavenumbers ( $k^i$ ) and frequencies ( $\omega$ ) of the Fourier modes must satisfy  $k^i/(\rho'\kappa) \sim \omega/(\rho'\kappa) \lesssim 1$ . These inequalities mean, sensibly, that fluid motions cannot alter the radiation field over scales smaller than the mean free path and at rates faster than the light-crossing time over the mean free path. With these inequalities in mind, we showed that the viscous terms cause the perturbations to decay exponentially, a familiar result. Interestingly, if one solves the dispersion relations without regard to the inequality  $\omega/(\rho'\kappa) \lesssim 1$ , one recovers growing mode solutions. This result sheds light on the results of Hiscock & Lindblom (1985), who demonstrated that the Eckart (1940) relativistic viscous stress tensor is unstable to small perturbations. Our approach shows that such instabilities only arise when one violates the assumption that the viscous nature of the fluid is a “good” approximation, i.e., when the light crossing time over the viscous length scale, defined in any problem by  $\eta/(c e')$ ,  $\eta$  being the coefficient of dynamic viscosity and  $e'$  the locally-observed energy density of the fluid, is short enough to describe local fluid deformations. The unstable nature of the modes also vanishes in the non-relativistic limit as the light-crossing time over any distance is formally zero.

Weinberg (1971) calculated the bulk viscosity of a relativistic radiating fluid to be zero. Our analysis, on the contrary, determined the coefficient to be  $\zeta = \eta/3$ , which can be quite large for radiation-dominated plasmas. It might therefore be expected that our model would predict a different rate of entropy production in the universe. However, if we use his expression for the entropy production rate (see the expression above equation (2.20) in Weinberg 1971) and confine

our analysis to the case in which zeroth-order distribution function can be described by that of a blackbody, we find that our bulk viscosity and the correction to the comoving energy density exactly cancel. We therefore find that Weinberg’s results concerning the entropy generation in the early universe by small anisotropies in the radiation field are upheld.

The previously-developed equations are applicable to a range of physical scenarios, the cosmological evolution of the early universe being one such application (see, in addition to Weinberg 1971, Caderni & Fabbri 1977; Harrison 1977; Tauber 1978; Johri & Sudharsan 1988; Hu & Dodelson 2002; Khatri et al. 2012). Another application would be in analyzing the physics of the boundary layers established between radiation-dominated jets and their environments (Arav & Begelman, 1992), as viscous dissipation due to radiation could be important – especially in the case where the motion of the outflow is relativistic (Walker, 1990). Such an analysis could shed light on the peculiar event **Swift** J1644+57, thought to be the first-observed, jetted, super-Eddington tidal disruption event (TDE) (Burrows et al., 2011; Bloom et al., 2011; Cannizzo et al., 2011; Zauderer et al., 2011). If the transient jet carried away the accretion luminosity generated during the gravitational infall of tidally-stripped debris (Chapter 5), the interaction between the jet and the overlying envelope may be well-described by the equations radiation hydrodynamics in the viscous limit. Comparing the theoretical results with observations could yield insight into the terminal Lorentz factor of the outflow, the properties of the tidally-disrupted star, and the mass of the black hole residing in the center of the host galaxy.

Applying these equations to the outflows predicted by the collapsar model of gamma-ray bursts (GRBs) (Woosley, 1993; MacFadyen & Woosley, 1999), wherein the core of a massive, dying star collapses directly to a black hole from which a jet is launched, may also prove fruitful. If the mechanism that accelerates the outflow is ultimately derived from the prompt accretion of material onto the newly-formed black hole, i.e., if the fireball model correctly describes the dynamics (Rees & Meszaros, 1992), radiation would contribute significantly to the energetics of the jet. Even if the energy is provided by the spin of the black hole (Blandford & Znajek, 1977) or the accretion disk (Blandford & Payne, 1982), radiation could still play a large part in determining the dynamics

of the outflow. An accurate representation of the interaction of the jet with the overlying stellar envelope and the circumstellar environment may therefore be obtained by employing the viscous equations of radiation hydrodynamics. A comparison of the theoretical expectation gleaned from such an analysis with the promptly-emitted gamma rays and the X-ray afterglow could yield new information concerning the progenitors of GRBs and their surrounding environments.

Owing to their apparent complexity, the equations of radiation hydrodynamics, when applied to supercritically accreting compact objects and their surroundings, are often solved numerically (Eggum et al., 1988; Okuda, 2002; Okuda et al., 2005; Ohsuga et al., 2005; Ohsuga, 2007). Simulations of such systems have also been extended to include magnetic fields (radiation magnetohydrodynamic; RMHD), the presence of which is potentially important not only for the dynamics of the gas but also for MRI-induced accretion and jet collimation (Turner et al., 2003; Ohsuga et al., 2009; Sądowski et al., 2014; McKinney et al., 2014). In these simulations, strong gravity is incorporated either through the pseudo-Newtonian potential of Paczyński & Wiita (1980), or by using the covariant set of equations and the Kerr geometry. In all of these numerical schemes, the moment formalism is adopted (see the introduction) when solving for the properties of the radiation and incorporating the coupling of the radiation to the gas. In addition, a “closure” relation is adopted that allows one to truncate the number of moments needed to close the system of equations at a finite level. Given our preceding analysis, an interesting question is whether or not these closure relations accurately capture relativistic radiation viscosity.

Flux-limited diffusion (Levermore & Pomraning, 1981), wherein the flux is proportional to the gradient of the energy density, is one such closure scheme used by, e.g., Ohsuga et al. (2005) and Ohsuga et al. (2009). This approximation allows one to interpolate between optically-thick and thin regimes, useful for an optically-thick disk that launches an optically-thin jet – the result observed in many of these simulations. An issue with this type of closure, especially when considering the present paper, is that the viscosity must be included separately and is not a direct result of the equations of radiation hydrodynamics. Ohsuga et al. (2005), for example, used a modified-alpha prescription for the coefficient of viscosity, setting the coefficient of dynamic viscosity to  $\eta \sim p/\Omega_K$ ,

where  $p$  is the total (gas plus radiation) pressure and  $\Omega_K$  is the Keplerian velocity. This form for the viscosity clearly does not reduce to equation (6.40) in the radiation-dominated, viscous limit. The modified-alpha prescription also does not incorporate relativistic effects, those due to strong gravity or high velocities, both of which could be important in the vicinity of the black hole and in regions of high shear between the jet and the inflated disk. It is therefore unlikely that the flux-limited diffusion closure scheme accurately reproduces the effects of radiation viscosity in the high-optical depth limit.

The M1 closure scheme (Levermore, 1984) assumes that there exists some reference frame, the radiation rest frame (not necessarily the same as fluid rest frame), in which the radiation flux vanishes and the pressure is one third of the energy density (the Eddington approximation), and can also interpolate between optically-thick and -thin regimes. This scheme has been extended to incorporate general relativistic effects (Sądowski et al., 2013), and has been employed by Sądowski et al. (2014) and McKinney et al. (2014) to study the role of radiation on hyperaccreting black hole-disk systems. Because the frame in which the Eddington approximation applies is not the fluid frame, there are small corrections to the energy-momentum tensor of the radiation in the fluid rest-frame when the optical depth is large, which is what one expects. If one keeps the lowest-order corrections to the fluid-frame pressure tensor (see equation (34) of Sądowski et al. (2013)), the result is  $P^{i'j'} \simeq \delta^{i'j'} e'/3 + \mathcal{O}(F^2)$ , where  $F$  is the fluid-frame energy flux, which demonstrates that, indeed, the fluid-frame radiation pressure reduces to the Eddington approximation when the optical depth is large. In the viscous limit, the rest-frame energy flux is proportional to gradients of the energy density and the velocity over the mean free path of the radiation (see the  $(0, i)$  components of our equation (6.37) or note that the diffusion limit is  $\mathbf{F} \sim \nabla e'$ ). The M1 scheme therefore indicates that the first-order deviation of the pressure, or the momentum flux, from the Eddington closure is proportional to the square of the derivative of fluid quantities over the optical depth. This result, however, is in direct contrast with the  $(i, j)$  components of our equation (6.37) that demonstrate, consistent with the manner in which viscosity usually operates, that the lowest-order correction to the momentum flux in the viscous limit is proportional to the gradient of fluid quantities over the

optical depth, i.e., it is of the same order as the energy flux. The M1 closure therefore does not accurately reproduce the viscous transport of momentum in the high-optical depth limit. Due to the covariant manner in which the M1 scheme is incorporated and the self-consistent inclusion of the radiation terms (i.e., no ad-hoc form for the viscosity), higher-order effects of the anisotropic radiation field are likely well-reproduced in the interaction between the relativistic jetted outflows and the inflated torus observed in the simulations of Sądowski et al. (2014) and McKinney et al. (2014).

Finally, Jiang et al. (2014) recently performed a non-relativistic, 3D, RMHD simulation of the gas around a  $\sim 6M_{\odot}$  black hole. Contrary to the previously-mentioned authors, they did not assume a closure relation to compute the moments of the radiation energy-momentum tensor and instead determined the pressure of the radiation directly, offering an unbiased depiction of the manner in which radiation transfers energy and momentum between neighboring gas parcels. The non-relativistic nature of the simulation, however, may underestimate the viscous effects in the transition between the mildly-relativistic outflow observed in their simulation and the disk material.

Having written down the equations of radiation hydrodynamics in the viscous limit, the authors plan to pursue the applications of those equations to relativistic, radiative shear layers in a companion paper. In the process, we plan to quantitatively assess how the differences between our radiation-viscous fluid equations and those of Weinberg (1971) affect the physical evolution of astronomical systems.

## Chapter 7

### Viscous boundary layers of radiation-dominated, relativistic jets. I. The two-stream model

#### 7.1 Introduction

Astrophysical jets almost certainly exist as aggregates of massive particles, magnetic fields, and radiation. In certain scenarios, however, the contribution of radiation to the energetics of the outflow far outweighs those of the particles and magnetic fields, meaning that one can essentially neglect the presence of the latter two entities.

One such scenario occurs in the collapsar model of long gamma-ray bursts (GRBs; Woosley 1993; MacFadyen & Woosley 1999). In this model, the core of a massive, evolved star collapses directly (or with a short-lived neutron star phase) to a black hole during the infall stage of a type-II supernova. The energy released by the material accreting onto the black hole, and ultimately observed as the gamma-ray emission, is collimated into bipolar jets – the jet formation confirmed by energetics arguments (Waxman et al., 1998; Fruchter et al., 1999; Frail et al., 2001) and the observations of breaks in the X-ray afterglow light curves (Panaitescu, 2007; Dado et al., 2008; Racusin et al., 2009) – and is often sufficient to unbind the stellar envelope, resulting in a supernova (Galama et al. 1998; Bersier et al. 2004; Kamble et al. 2009; Levan et al. 2014, but see Fynbo et al. 2006). If one assumes that the mass of the remnant black hole is on the order of a few solar masses, its accretion luminosity exceeds the Eddington limit by roughly ten orders of magnitude, meaning that radiation pressure, even if the flux is nearly isotropic, is likely an important mechanism for driving and sustaining the outflow (the fireball model; Rees & Meszaros 1992). Even if the jet is

launched by magnetohydrodynamical mechanisms (Blandford & Znajek, 1977; Blandford & Payne, 1982), radiation could still play a prominent role in determining the dynamics of the jet. Arguments concerning the time necessary for the jet to break through the stellar envelope also seem to disfavor Poynting-dominated jets (Brown et al. 2015; but see Mundell et al. 2013).

Jets produced during tidal disruption events (TDEs; Giannios & Metzger 2011) – when a star is destroyed by the tidal force of a supermassive black hole – could provide another class of radiation-dominated outflow. After the star is tidally disrupted, roughly half of the shredded debris remains bound to the black hole and returns to the tidal disruption radius. If the black hole has a mass less than roughly  $10^7 M_{\odot}$ , that rate of return can exceed the Eddington limit of the black hole by orders of magnitude for a significant amount of time (on the order of days to months; Evans & Kochanek 1989; Strubbe & Quataert 2009). Provided that this material can rapidly accrete onto the black hole, which is likely the case due to the tidal dissipation of kinetic energy (Kochanek, 1994; Guillochon et al., 2014b) and relativistic precession effects (Rees, 1988; Evans & Kochanek, 1989), the energy released during the accretion process will also be supercritical. It was during this supercritical phase that the event **Swift** J1644+57 was seen to have an associated jetted outflow (Burrows et al., 2011; Bloom et al., 2011; Cannizzo et al., 2011; Zauderer et al., 2011) (the source **Swift** J2058+05 may provide another example of a jetted, super-Eddington TDE; Cenko et al. 2012). Although the jet launching mechanism for this event is uncertain, the magnetic field of the tidally-disrupted star, assuming its flux is approximately conserved, is almost certainly insufficient to power the outflow. Therefore, unless one invokes the existence of a fossil magnetic field (Tchekhovskoy et al., 2014; Kelley et al., 2014), the radiation pressure associated with the accretion luminosity likely plays some role in powering the jet. At any rate, the radiation released during the supercritical accretion process affects the dynamics of the collimated outflow and contributes substantially to its overall energy and momentum.

Collapsar jets inject a significant amount of energy into the overlying stellar envelope as they punch their way into the circumstellar medium, creating a pressurized “cocoon” of shocked material with which the jet interacts (Morsony et al., 2007; Lazzati et al., 2007; López-Cámara

et al., 2013), and the progenitors themselves – usually taken to be highly-evolved, Wolf-Rayet stars (Matzner, 2003; Woosley & Bloom, 2006) – are likely sustained primarily by radiation pressure. The initial stages of collapsar jet propagation are therefore characterized by the transfer of energy and momentum between two radiation-dominated fluids. Because of the high accretion rates and low specific angular momentum, the fallback disks generated during the super-Eddington phase of TDEs are likely optically and geometrically thick and radiation pressure-supported (Rees 1988; Loeb & Ulmer 1997, Chapter 5). In the zero-Bernoulli accretion (ZEBRA) model of Chapter 5, for example, the accreting material is inflated into a quasi-spherical envelope that surrounds the black hole. The dynamics of the jets of supercritical TDEs are therefore also modulated by the presence of a radiation pressure-supported, external medium.

Previous authors used the supersonic propagation of the outflow to model the interaction of the collapsar jet with the overlying envelope as an oblique shock-boundary layer structure (Bromberg & Levinson, 2007; Kohler et al., 2012; Kohler & Begelman, 2012, 2015). In these models, the outflow is assumed to consist of a perfect, single fluid with a relativistic equation of state, and some have included the presence of magnetic fields (e.g., Kohler & Begelman 2012). A more realistic picture, however, is obtained by considering the jet as a composite of the massive scatterers present in the outflow and the radiation that accompanies it. Indeed, this approach constitutes the underlying framework of radiation hydrodynamics. Furthermore, non-ideal, i.e., viscous, effects will tend to “smear” the discontinuities otherwise present in the system, resulting in a more gradual transition of the fluid quantities between the jet and the environment.

In the limit that the mean free path of a photon is small, radiation acts like an effective viscosity, with a coefficient of dynamic viscosity that depends both on the radiation pressure and the density of scatterers (see section 2 of this paper), and transfers momentum and energy between neighboring fluid elements (Weinberg, 1971; Loeb & Laor, 1992). In the radiation-dominated interaction between collapsar jets and TDE jets and their respective ambient media, the effects of radiation viscosity should be quite large. Arav & Begelman (1992) considered the effects of radiation viscosity on the evolution of boundary layers in the two-stream approximation (see section 3 of this

paper); their treatment, however, was of a non-relativistic nature, meaning that their results have limited applicability to GRB and TDE jets.

In this paper, the first of two, we consider the effects of radiation viscosity on the propagation of relativistic jets in radiation-rich environments. In section 2 we present the equations of radiation hydrodynamics in the viscous limit. Section 3 applies those equations to the two-stream problem, wherein the jet and ambient medium are considered to be two separate, interacting fluids, and we compare our results to the non-relativistic treatment of Arav & Begelman (1992). In section 4 we discuss the results of the analysis and comment upon the application of our models to the jets produced by supercritical TDEs such as **Swift** J1644+57, GRBs, and other astrophysical systems. In a second paper (Coughlin & Begelman, 2015) we present an alternate model, the free-streaming jet solution, and compare it to the two-stream solution presented here.

## 7.2 Governing equations

As mentioned in the introduction, radiative forces behave like an effective viscosity in the presence of shear, when the change in fluid quantities across the mean free path of a photon is small. The precise means by which this viscous coupling manifests itself can be determined by analyzing the Boltzmann equation.

In Chapter 6 we used the general relativistic Boltzmann equation for Thomson scattering to discern the effects of radiation viscosity in the presence of both relativistic velocities and gravitational fields (i.e., in accelerating reference frames). Instead of reproducing their work here, we will simply quote the equations of radiation hydrodynamics for a cold gas (gas pressure much less than both the gas rest mass density and the radiation pressure) that result from their analysis (see their equation 49):

$$\begin{aligned} \nabla_\mu \left[ \left\{ \rho' + \frac{4}{3} e' \left( 1 - \frac{10}{9} \frac{1}{\rho' \kappa} \nabla_\alpha U^\alpha \right) \right\} U^\mu U^\nu \right] + \frac{1}{3} g^{\mu\nu} \partial_\mu e' - \frac{8}{27} \nabla_\mu \left[ \frac{e'}{\rho' \kappa} \Pi^{\mu\sigma} \Pi^{\nu\beta} \left( \nabla_\sigma U_\beta + \nabla_\beta U_\sigma + g_{\beta\sigma} \nabla_\alpha U^\alpha \right) \right] \\ - \frac{1}{3} \nabla_\mu \left[ \frac{e'}{\rho' \kappa} \left( \Pi^{\mu\sigma} U^\nu + \Pi^{\nu\sigma} U^\mu \right) \left( 4U^\beta \nabla_\beta U_\sigma + \partial_\sigma \ln e' \right) \right] = 0. \quad (7.1) \end{aligned}$$

Here the speed of light has been set to one, Greek indices range from 0 – 3,  $\rho'$  is the fluid rest-frame density of scatterers,  $e'$  is the fluid rest-frame radiation energy density,  $\kappa$  is the scattering opacity (in units of  $\text{cm}^2 \text{g}^{-1}$ ),  $g_{\mu\nu}$  is the metric of the spacetime,  $\nabla_\mu$  is the covariant derivative,  $U^\mu$  is the four-velocity of the flow, and  $\Pi^{\mu\nu} = U^\mu U^\nu + g^{\mu\nu}$  is the projection tensor. The Einstein summation convention has been adopted here, meaning that repeated upper and lower indices imply summation. This equation shows that the coefficient of dynamic viscosity,  $\eta$ , for an optically-thick, radiation-dominated gas is

$$\eta = \frac{8}{27} \frac{e'}{\rho' \kappa}, \quad (7.2)$$

which agrees with previous findings (Blandford et al., 1985; Loeb & Laor, 1992); note that this specific coefficient is only for the case when the gas and radiation interact through Thomson scattering. The gas energy equation, which will also be useful for us, can be obtained by contracting equation (7.1) with  $U_\nu$ , which we can show becomes (see equation 50 of Chapter 6)

$$\begin{aligned} \nabla_\mu(e'U^\mu) + \frac{1}{3}e'\nabla_\mu U^\mu &= \frac{4}{3}\frac{10}{9}\nabla_\mu \left[ \frac{e'}{\rho'\kappa} U^\mu \nabla_\alpha U^\alpha \right] + \frac{8}{27} \frac{e'}{\rho'\kappa} \left( \nabla_\sigma U_\beta + \nabla_\beta U_\sigma + g_{\sigma\beta} \nabla_\alpha U^\alpha \right) \Pi^{\mu\sigma} \nabla_\mu U^\beta \\ + \frac{1}{3} \Pi^{\mu\sigma} \nabla_\mu \left[ \frac{e'}{\rho'\kappa} \left( 4U^\beta \nabla_\beta U_\sigma + \partial_\sigma \ln e' \right) \right] &+ \frac{1}{3} \frac{e'}{\rho'\kappa} \left( 4U^\beta \nabla_\beta U_\sigma + \partial_\sigma \ln e' \right) \left( 2U^\mu \nabla_\mu U^\sigma + U^\sigma \nabla_\mu U^\mu \right). \end{aligned} \quad (7.3)$$

To close the system, we require that the normalization of the four-velocity be upheld and that particle flux be conserved:

$$U_\mu U^\mu = -1, \quad (7.4)$$

$$\nabla_\mu \left[ \rho' U^\mu \right] = 0. \quad (7.5)$$

Equations (7.1) and (7.3) – (7.5) constitute six linearly independent equations for the six unknowns  $U^\mu$ ,  $e'$ , and  $\rho'$ .

In addition to the energy density of the radiation,  $e'$ , one can also calculate the number density of photons by requiring that the number flux,  $F^\mu$ , be conserved. One can show (see Chapter 6) that the equation  $\nabla_\mu F^\mu = 0$  becomes, in the viscous limit,

$$\nabla_\mu \left[ N' U^\mu \right] = \nabla_\mu \left[ \frac{1}{\rho' \kappa} \left( \frac{10}{9} N' U^\mu \nabla_\sigma U^\sigma + N' U^\alpha \nabla_\alpha U^\mu + \frac{1}{3} \Pi^{\mu\sigma} \nabla_\sigma N' \right) \right], \quad (7.6)$$

where  $N'$  is the rest-frame number density of photons. Once we solve the equations of radiation hydrodynamics for the four-velocity of the fluid and the mass density of scatterers, we can solve equation (7.6) for the number flux of photons.

The goal of the next two sections is to apply equations (7.1) and (7.3) – (7.6) to the boundary layers established between fast-moving jets and their environments. For a more thorough discussion of the nature of the equations of radiation hydrodynamics in the viscous limit, we refer the reader to Chapter 6.

### 7.3 Two-stream boundary layer

Arav & Begelman (1992) considered the Blasius (1908) boundary layer problem, wherein one analyzes the dynamics of viscous flow over a semi-infinite, rigid plate, with the viscous effects attributed to radiation. They showed, however, that the requirement that both velocity components vanish on the lower plate, the no-slip condition, results in a divergent boundary layer thickness. The authors then examined the more physical scenario of two interacting fluids, one moving at some asymptotic velocity and the other asymptotically stationary, known as the two-stream approximation. In this case the no-slip condition no longer applies, and they were able to show that the boundary layer thickness remains finite.

The treatment of Arav & Begelman (1992) was non-relativistic, meaning that their results have limited utility when one considers the boundary layers established between GRBs and super-Eddington TDEs and their ambient media. The enthalpy of the radiation, which is not ignorable in radiation-dominated flows, was also not included in their momentum equation. Here we extend

their analysis to the relativistic regime and we include the radiation enthalpy.

### 7.3.1 Basic setup

We assume that the flow is plane-parallel with no variation in the  $x$ -direction. The covariant derivatives in equations (7.1) and (7.3) – (7.5) can therefore be replaced by ordinary partial derivatives. Even though this simplification significantly reduces their complexity, the most compact representation of the equations is still given by (7.1) and (7.3) – (7.5) with  $\nabla_\mu \rightarrow \partial/\partial x^\mu$ , so we do not write them again here.

The majority of the motion is along the  $z$ -axis, meaning  $v_z \gg v_y$  and  $v_x \equiv 0$ . At some initial point  $y = z = 0$ , the “jet,” whose constant, asymptotic ( $y \rightarrow \infty$ ) velocity is denoted  $v_j$ , encounters the ambient medium, the asymptotic ( $y \rightarrow -\infty$ ) velocity of which is zero. The asymptotic densities of the jet and the ambient medium, denoted  $\rho'_j$  and  $\rho'_a$ , respectively, are both taken to be constant. The line  $y = 0$  represents the surface that divides the jet and ambient material, and consistent with any boundary layer analysis, we also assume that the gradient along  $y$  is much greater than that along  $z$ , so  $\partial/\partial z \ll \partial/\partial y$ .

### 7.3.2 Boundary layer equations

The complexity of equations (7.1) and (7.3) – (7.5) can be reduced by introducing the boundary layer thickness  $\delta y$  such that  $\delta \sim \delta y/\delta z$  is a small parameter when  $\delta z$  is chosen to be a typical length scale in  $z$ . By keeping terms only to lowest order in  $\delta$ , we will recover a set of reduced boundary layer equations.

To determine how  $\delta$  depends on asymptotic fluid quantities (it is the reciprocal of the square root of the Reynolds number in the classical Blasius boundary layer), we compare the lowest-order terms in  $\delta$  in the gas energy equation to the inviscid terms. By equating these terms we are requiring that the viscous heating of the radiation contribute a non-negligible increase in the entropy of the fluid, but because the inviscid terms are proportional to the divergence of the four-velocity (see equation 8.11), this equality can only be true when the gas is compressible, i.e., when the flow

velocity is supersonic. When the flow becomes very subsonic, the energy equation can be ignored as the fluid is essentially incompressible. Making the substitutions  $\partial/\partial y \sim 1/\delta y$ ,  $\partial/\partial z \sim 1/z$ ,  $v \sim v_j$  and  $\rho' \sim \rho'_0$  in equation (8.3), where  $\rho'_0 = \rho'_j$  if we are in the jet ( $y > 0$ ) or  $\rho'_a$  if we are in the ambient medium ( $y < 0$ ), we find that the boundary layer thickness scales as

$$\delta^2 \sim \frac{1}{\rho'_0 \kappa z \Gamma_j v_j}, \quad (7.7)$$

where  $\Gamma_j = (1 - v_j^2)^{-1/2}$  is the Lorentz factor of the jet. The boundary layer thickness therefore scales roughly as  $1/\sqrt{\tau}$ , where  $\tau \sim \rho'_0 \kappa z$  is the fluid-frame optical depth along  $z$ .

We can now use our expression for  $\delta$  (8.7) to keep only lowest-order terms in equations (7.1) and (7.3) – (7.5). The resulting  $\nu = y$ ,  $\nu = z$ , gas-energy and continuity boundary layer equations are, respectively,

$$\frac{\partial e'}{\partial y} = 0, \quad (7.8)$$

$$\frac{\partial}{\partial x^\mu} \left[ \left( \rho' + \frac{4}{3} e' \right) U^\mu \Gamma v_z \right] + \frac{1}{3} \frac{de'}{dz} - \frac{8}{27} \frac{\partial}{\partial y} \left[ \frac{e'}{\rho' \kappa} \frac{\partial}{\partial y} [\Gamma v_z] \right] = 0, \quad (7.9)$$

$$\frac{\partial}{\partial x^\mu} \left[ e' U^\mu \right] + \frac{1}{3} e' \frac{\partial U^\mu}{\partial x^\mu} = \frac{8}{27} \frac{e'}{\rho' \kappa} \frac{\partial U_\mu}{\partial y} \frac{\partial U^\mu}{\partial y}, \quad (7.10)$$

$$\frac{\partial}{\partial z} \left[ \rho' \Gamma v_z \right] + \frac{\partial}{\partial y} \left[ \rho' \Gamma v_y \right] = 0. \quad (7.11)$$

The first of these demonstrates, as in the non-relativistic limit, that the pressure is constant across the boundary layer. For the remainder of this section we will assume that  $e'(z) = e'_0$ , i.e., that the radiation energy density is independent of  $z$ .

### 7.3.3 Self-similar approximation

The solution to the continuity equation (7.11) can be obtained by introducing the stream function  $\psi$  through the definitions

$$\rho' \kappa \Gamma v_z = \frac{\partial \psi}{\partial y}, \quad (7.12)$$

$$\rho' \kappa \Gamma v_y = -\frac{\partial \psi}{\partial z}, \quad (7.13)$$

which manifestly solves the continuity equation; we introduced a factor of  $\kappa$ , the opacity, to ensure that  $\psi$  is dimensionless. These relations also demonstrate that  $v_y \sim \delta v_z$ , which is what we expect: the velocity in the direction perpendicular to the majority of the motion is reduced by a factor of  $\delta$ . Note, however, that the definition of the stream function now involves the density, which is not constant in this analysis.

As is done in the standard Blasius treatment, we assume that the stream function varies self-similarly as

$$\psi = \sqrt{\frac{8}{27} \rho'_0 \kappa \Gamma_j v_j} z^{1/2} f(\alpha), \quad (7.14)$$

where

$$\alpha = y/\delta y = \frac{y}{\sqrt{z}} \sqrt{\frac{27}{8} \rho'_0 \kappa \Gamma_j v_j} \quad (7.15)$$

is our self-similar variable (we used equation (8.7) for the boundary layer thickness) and  $f$  is a function to be determined from equations (8.12) and (8.11). We will also assume that the density varies self-similarly as

$$\rho' = \rho'_0 g(\alpha), \quad (7.16)$$

where  $g$  is a second function.

One can use these definitions in equations (8.12) and (8.11) to derive a set of coupled, nonlinear, ordinary differential equations for  $f$  and  $g$ . It is mathematically convenient, however, to define a new self-similar variable  $\xi$  by

$$\xi = \int_0^\alpha g(\tilde{\alpha}) d\tilde{\alpha}, \quad (7.17)$$

where  $\tilde{\alpha}$  is a dummy variable of integration, and write the functions  $f$  and  $g$  in terms of this variable. This approach is similar to the one taken by Arav & Begelman (1992).

With this parametrization, the velocities are

$$\Gamma v_z = \Gamma_j v_j f_\xi, \quad (7.18)$$

$$\rho' \Gamma v_y = \frac{1}{2\sqrt{z}} \sqrt{\frac{8}{27} \frac{\rho'_0 \Gamma_j v_j}{\kappa}} \left( \alpha f_\xi g - f \right), \quad (7.19)$$

where a function with a subscript  $\xi$  denotes the derivative of that function with respect to  $\xi$ , i.e.,  $f_\xi = df/d\xi$ ,  $f_{\xi\xi} = d^2f/d\xi^2$ , etc. Substituting these relations and the self-similar scaling for  $\rho'$ , equation (7.16), into equations (8.12) and (8.11), we find the following self-similar equations for  $f$  and  $g$ :

$$-\frac{1}{2} \left( g + \frac{4}{3} \mu \right) f f_{\xi\xi} + \mu \Gamma_j^2 v_j^2 \frac{g f_\xi (f_{\xi\xi})^2}{1 + v_j^2 \Gamma_j^2 (f_\xi)^2} = \mu g f_{\xi\xi\xi}, \quad (7.20)$$

$$g_\xi f = \frac{3}{2} \Gamma_j^2 v_j^2 \frac{g^2 (f_{\xi\xi})^2}{1 + \Gamma_j^2 v_j^2 (f_\xi)^2}, \quad (7.21)$$

where we have defined  $\mu$  as the ratio  $e'_0/\rho'_0$ . The term  $-2\mu f f_{\xi\xi}/3$  and the last term on the left-hand side of equation (7.20) were absent in the treatment of Arav & Begelman (1992) because they did not include the enthalpy of the radiation. In the non-relativistic,  $\mu \ll 1$  limit, equation (7.20) reduces to the standard Blasius equation (by rescaling the self-similar variable) and  $g$  and  $f$  decouple from one another, as was found by Arav & Begelman (1992).

Before proceeding further, recall that the two-stream problem separates the jet and ambient material into two distinct media, the dividing line for our problem chosen to be  $y = 0$ , and that the asymptotic densities attained in these two media are  $\rho'_j$  and  $\rho'_a$  for the jet and ambient material, respectively. Therefore, in equations (7.14), (7.15) and (7.16), the parameter  $\rho'_0$  refers to either  $\rho'_j$  or  $\rho'_a$  depending on the sign of  $\alpha$  and, hence,  $\xi$ . The functions  $f$  and  $g$  are thus piecewise defined about  $y = 0$ , as are the self-similar variables  $\alpha$  and  $\xi$ , with solutions for  $\xi > 0$  corresponding to jet quantities and those for  $\xi < 0$  corresponding to the ambient medium. Equations (7.20) and (7.21) should therefore be interpreted as a total of four equations for four functions:  $f$  defined in the jet,  $f$  defined in the ambient medium,  $g$  defined in the jet, and  $g$  defined in the ambient medium. Note that  $\mu$  can also differ between the two media, depending on the asymptotic density (but  $e'_0$  must be continuous across  $y = 0$  because of equation (8.10)).

Keeping in mind this subtlety of equations (7.20) and (7.21), we must additionally determine the boundary conditions satisfied by  $f$  and  $g$ . The first two conditions satisfied by  $f$  can be determined by recalling that  $v \rightarrow v_j$  as  $y \rightarrow \infty$  and  $v \rightarrow 0$  as  $y \rightarrow -\infty$ . Investigating equation (7.18) and noting that  $\xi$  scales with  $y$ , these requirements translate to

$$f_\xi(\infty) = 1, \quad f_\xi(-\infty) = 0. \quad (7.22)$$

We also require that the density approach its asymptotic values in the limits of  $y \rightarrow \pm\infty$ . From equation (7.16), this gives

$$g(\pm\infty) = 1. \quad (7.23)$$

Now, note that if the jet and ambient materials are to retain their respective identities, then the flow along the surface of contact at  $y = 0$  must remain parallel to that surface. In other words, there must not be any mass flow across the boundary, i.e., this surface is a contact discontinuity,

which means that  $v_y(0) = 0$ . From equation (7.19), this shows that  $f$  must satisfy

$$f(0) = 0. \quad (7.24)$$

The other two boundary conditions can be determined by requiring that the normal and transverse components of the energy-momentum tensor, the divergence of which we took to obtain equation (7.1), be continuous across the point of contact  $y = 0$ . We can show that these restrictions demand that  $f_\xi$  and  $f_{\xi\xi}$  be continuous across  $y = 0$ , which closes the system.

We can also calculate the comoving-frame number density of photons  $N'$  by solving equation (7.6). Keeping only terms to lowest order in the boundary layer thickness, the equation of conservation of photon number becomes

$$\nabla_\mu F^\mu = \nabla_\mu \left( N' U^\mu \right) - \frac{1}{3} \frac{\partial}{\partial y} \left( \frac{1}{\rho' \kappa} \frac{\partial N'}{\partial y} \right) = 0. \quad (7.25)$$

As we did for the number density of scatterers, we will assume that the photon number density varies self-similarly across the boundary layer as

$$N' = N'_0 h(\xi), \quad (7.26)$$

where  $N'_0$  is the asymptotic number density of the jet or the ambient medium. With this form for the number density, we find that the equation for  $h$  becomes

$$\frac{3}{2} \Gamma_j^2 v_j^2 \frac{g (f_{\xi\xi})^2}{1 + \Gamma_j^2 v_j^2 (f_\xi)^2} h - f h_\xi = \frac{9}{4} g h_{\xi\xi}. \quad (7.27)$$

As for the functions  $f$  and  $g$ ,  $h$  is really piecewise defined across the boundary  $y = 0$ , and so equation (7.27) is really two equations – one for the photon number density in the jet, and another for that in the ambient medium. The requirement that the number density of photons asymptotically approach its jet and ambient values gives

$$h(\pm\infty) = 1. \quad (7.28)$$

The  $y$ -component of the flux must also be continuous across the boundary, which, when written out, shows that the derivative of  $h$  must be continuous across  $\xi = 0$ , which yields the final two boundary conditions.

Finally, the solutions to equations (7.20), (7.21), and (7.27) will be in terms of the parameter  $\xi$ , which is itself a function of  $g$  (equation (8.40)). We would like the solutions to be in terms of the parameter  $\alpha$ , which is directly related to the physical coordinates  $y$  and  $z$  (equation (7.15)). The transformation can be achieved by differentiating equation (8.40), rearranging, and integrating to yield

$$\int_0^\xi \frac{d\tilde{\xi}}{g(\tilde{\xi})} = \alpha, \quad (7.29)$$

where  $\tilde{\xi}$  is an integration variable and we set the integration constant to zero because we demand  $\xi(\alpha = 0) = 0$ . After solving equations (7.20) and (7.21) for  $g(\xi)$ , we can numerically integrate and solve equation (7.29) for  $\xi$  in terms of  $\alpha$ .

### 7.3.4 Solutions

Equations (7.20), (7.21) and (7.27), together with the boundary conditions on  $f$ ,  $g$ , and  $h$ , govern the behavior of the velocity, number density of scatterers, and number density of photons throughout the two-stream boundary layer. Here we present and analyze the solutions to those equations as we vary the asymptotic jet Lorentz factor  $\Gamma_j$  and the quantity  $\mu = e'_0/\rho'_0$ .

One caveat with the definition of  $\alpha$  is that it depends on  $\Gamma_j$  via equation (7.15). Therefore, if we plot solutions with different  $\Gamma_j$ , we must be careful to incorporate this dependence so that the range of physical space we consider for each solution is the same. Because of this fact, in the following figures we will plot our solutions as functions of the variable

$$\tilde{\alpha} = \frac{\alpha}{\sqrt{\Gamma_j v_j}} = \frac{y}{\sqrt{z}} \sqrt{\frac{27}{8} \rho'_0 \kappa}. \quad (7.30)$$

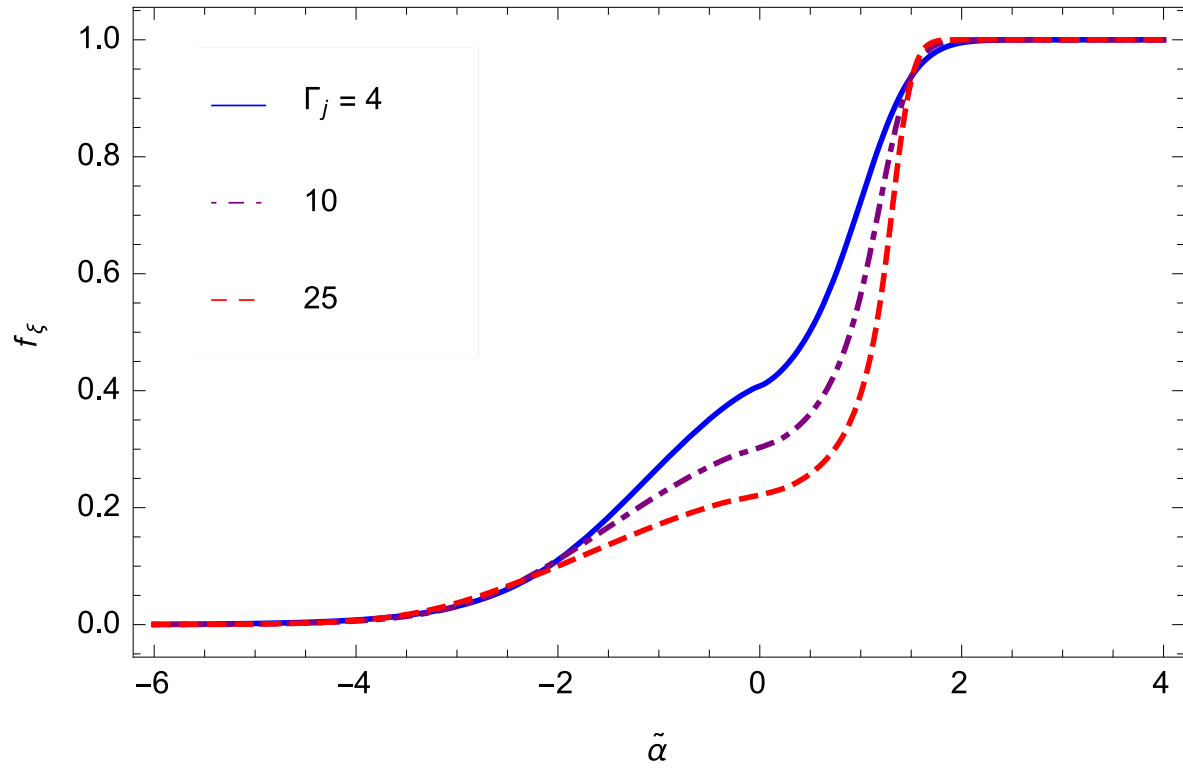


Figure 7.1: The function  $f_\xi$ , which is the normalized  $z$ -component of the four velocity, in terms of the parameter  $\tilde{\alpha} \propto y/\sqrt{z}$ , for  $\mu = 1$  and a number of jet Lorentz factors, as indicated by the legend. As we can see, the thickness of the velocity boundary layer, in terms of  $\tilde{\alpha}$ , is nearly independent of  $\Gamma_j$ .

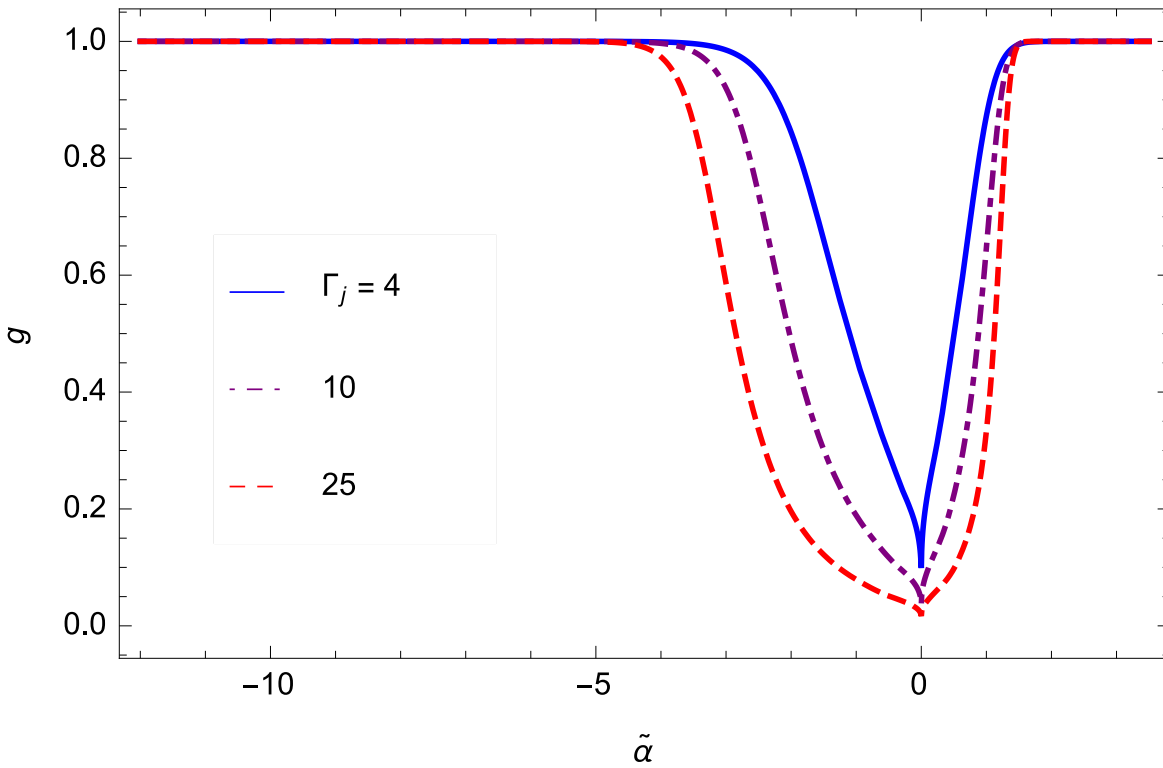


Figure 7.2: The variation of the normalized density, given by  $g$ , as a function of  $\tilde{\alpha}$  for the same parameters as those chosen for Figure 7.1. The density remains below its asymptotic value over a slightly larger range of  $\tilde{\alpha}$  for higher  $\Gamma_j$ , and the decrease in density within the boundary layer is consistent with the findings of Arav & Begelman (1992). The density formally equals zero at  $\tilde{\alpha} = 0$ ; however, because  $g$  approaches zero at a very slow rate (recall  $g(\xi) \propto -1/\ln \xi$ ), it appears from the Figure, which only samples a finite number of points around  $\tilde{\alpha} = 0$ , that the density remains positive and larger for smaller  $\Gamma_j$ .

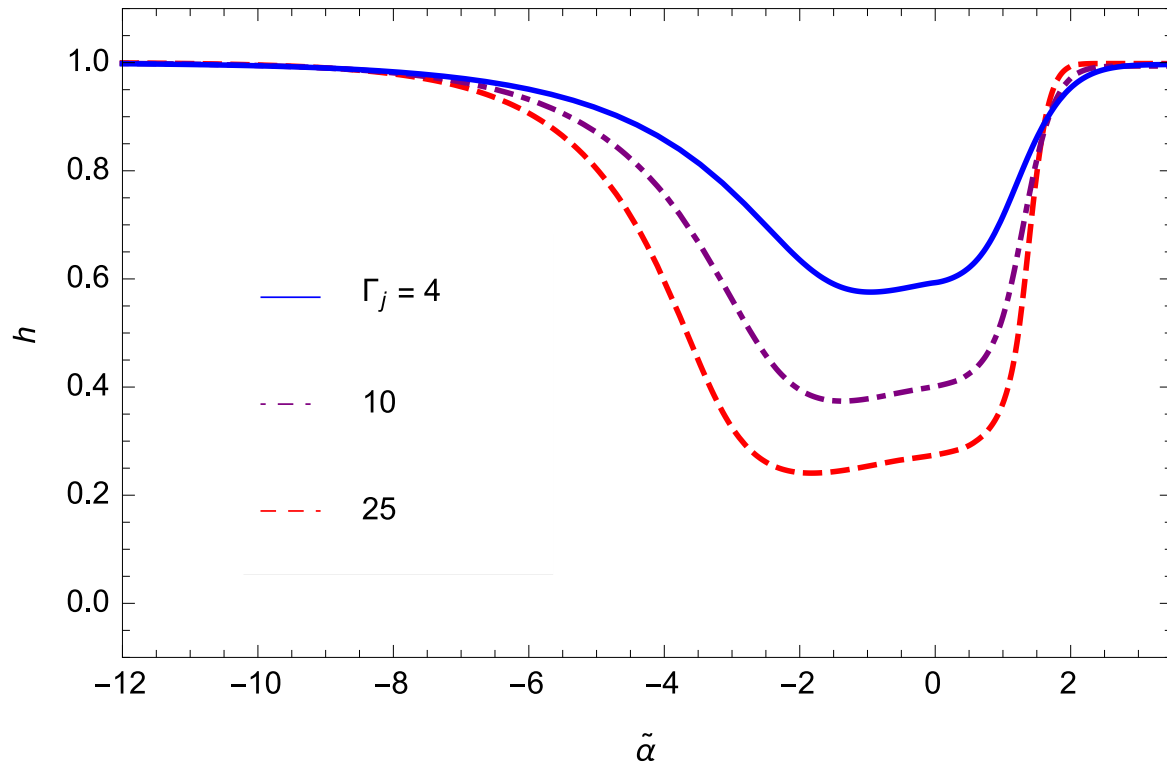


Figure 7.3: The solution to equation (7.27),  $h$ , which is the normalized number density of photons, for the same set of parameters as those chosen in Figure 7.1. The number density of photons is seen to roughly track the number density of scatterers. Because the energy density of the radiation remains constant across the layer, the energy per photon increases in the boundary layer.

Figure 7.1 shows the solution for the normalized  $z$ -component of the four-velocity ( $f_\xi$ ) as a function of the self-similar variable  $\tilde{\alpha} \propto y/\sqrt{z}$  for a number of jet Lorentz factors and  $\mu = 1$ . We see that the width of the boundary layer is nearly unchanged as we vary the Lorentz factor of the asymptotic jet. The value of  $f_\xi$  at the contact discontinuity is lower for larger  $\Gamma_j$ , resulting in a greater shear ( $\sim f_{\xi\xi}$ ) as one proceeds into the jet. The flattening of the velocity around  $\tilde{\alpha} = 0$  arises from the behavior of the density around this region and the function  $\xi(\alpha)$  determined therefrom.

Figure 7.2 illustrates the manner in which the density varies over the boundary layer for the same parameters as those chosen for Figure 7.1. Consistent with the findings of Arav & Begelman (1992), we find that the transition from the jet to the ambient medium carves out a region of low density material. This behavior can be understood by noting that the shear in the flow causes viscous heating of the fluid, which results in an increase in the specific entropy  $s'$ . Since the specific entropy scales as  $s' \propto e'/(\rho')^{4/3}$  for a radiation-dominated gas, an increase in the entropy at constant pressure corresponds to a decrease in the density of scatterers. As was found by Arav & Begelman (1992), the density equals zero at the origin, which can be gleaned from the asymptotic behavior of equation (7.21): for  $\xi \ll 1$ , we can let  $f_\xi \sim f_{\xi\xi} \sim \xi$ , and solving the resultant approximate differential equation shows that  $g \propto -1/\ln(\xi)$ .

In Figure 7.3 we plot the solution to equation (7.27), the normalized, rest-frame number density of photons, for the same set of Lorentz factors and  $\mu = 1$ . By comparing this with Figure 7.2, we see that the photon number density roughly tracks that of the scatterers. However, the photon number density remains below its asymptotic value significantly farther into the ambient medium than does the particle density. Because the energy density of the radiation is constant across the boundary layer, the decrease in photon density corresponds to a higher average energy per photon increases within the boundary layer – a clear manifestation of viscous heating, as noted by Arav & Begelman (1992).

Figures 7.4, 7.5, and 7.6 show the  $z$ -component of the four-velocity, the number density of scatterers, and the photon number density, respectively, for  $\Gamma_j = 25$  and  $\mu = 0.1, 1, \text{ and } 10$ . The overall qualitative behavior of the solutions is similar to that depicted in Figures 7.1 – 7.3. More

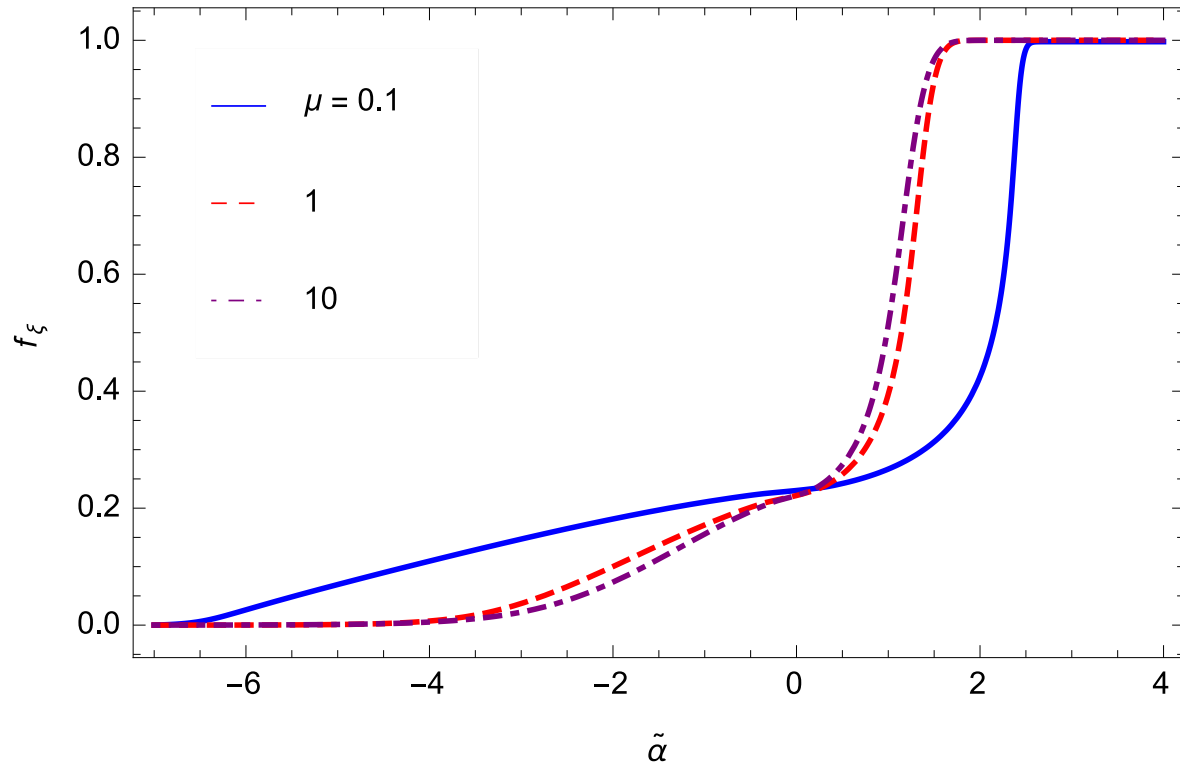


Figure 7.4: The solution for the normalized  $z$ -component of the four-velocity ( $f_\xi$ ) for  $\Gamma_j = 25$  and three different values of  $\mu$ , as indicated by the legend. The velocity profile does not differ much as  $\mu$  increases beyond 1, but for smaller values of  $\mu$  the boundary layer widens noticeably.

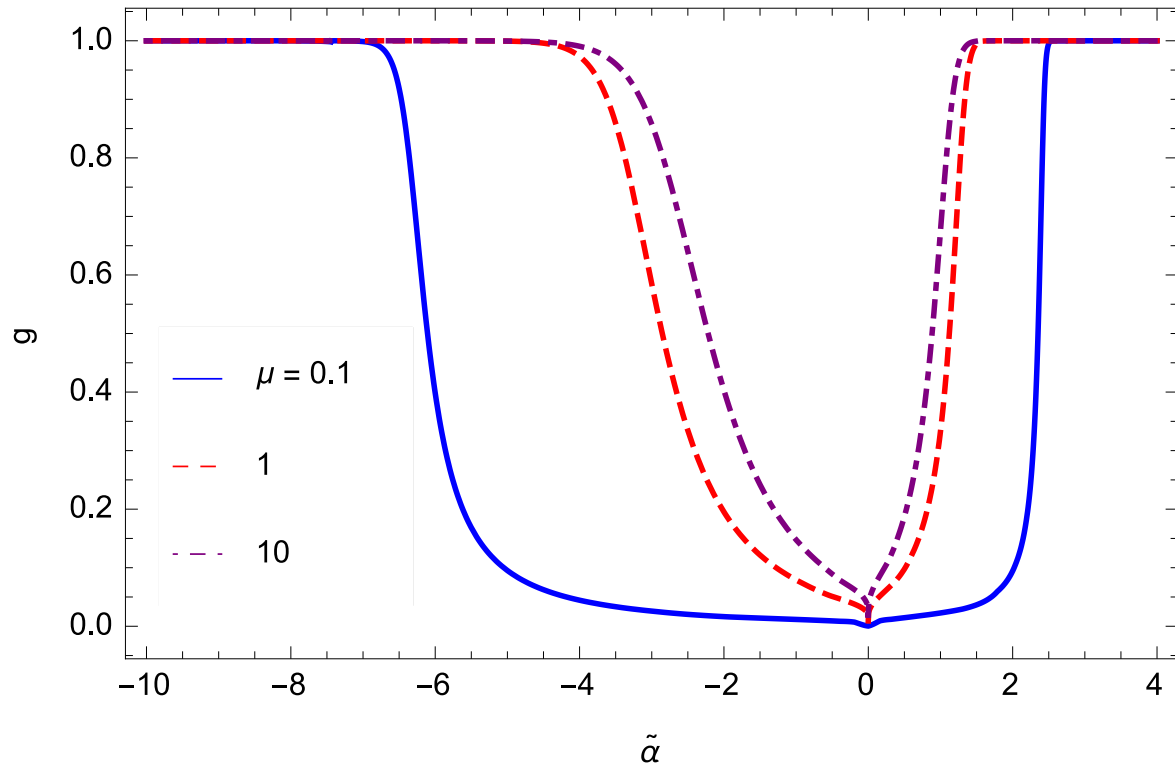


Figure 7.5: The function  $g$ , which is the rest-frame number density of scatterers, for the same parameters as in Figure 7.4. For smaller values of  $\mu$ , the density is significantly reduced from its asymptotic value over a larger range in  $\alpha$ .

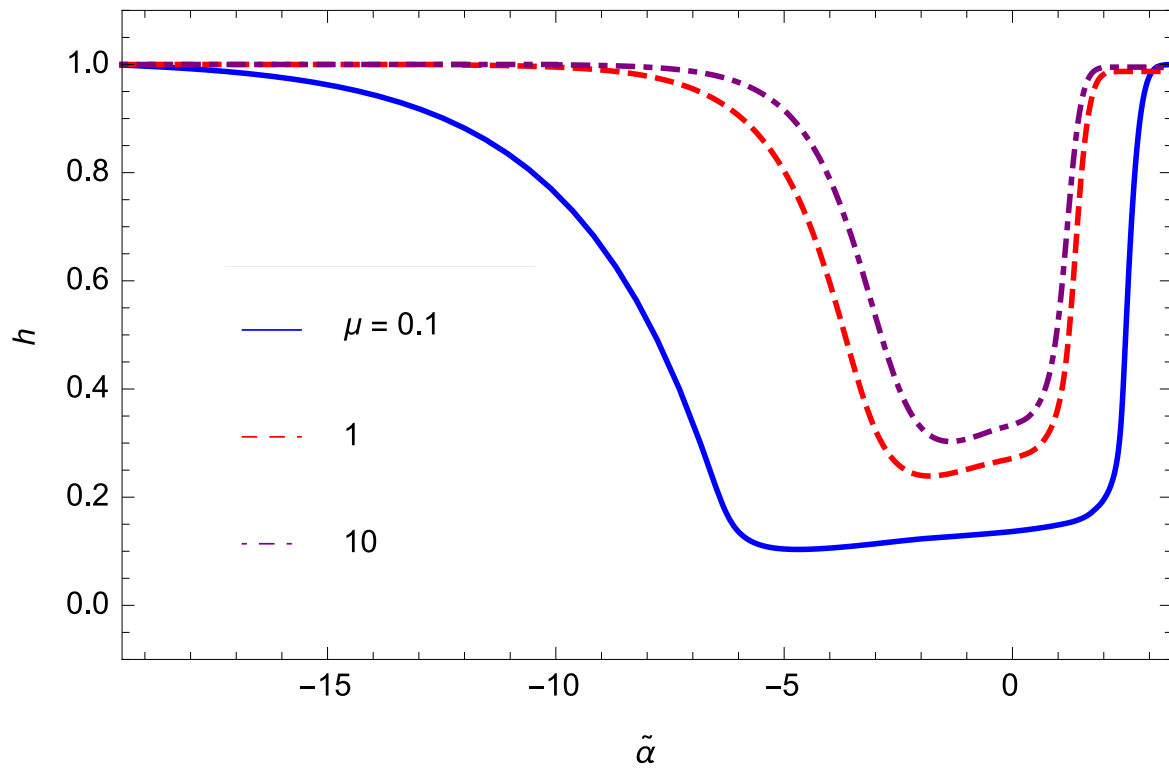


Figure 7.6: The solution to equation (7.27), which gives the number density of photons observed in the comoving frame, for the same set of parameters as in Figure 7.4. The radiation number density roughly follows that of the scatterers.

specifically, however, we find that values of  $\mu$  greater than unity cause the boundary layer thickness to decrease, but not appreciably. On the contrary, a value of  $\mu$  only marginally less than one results in a significant widening of the boundary layer. This dependence is ultimately related to the compressibility of the fluid and the relation between that compressibility and the sound speed of a radiation-dominated gas (see discussion below).

## 7.4 Discussion

The plots of the previous subsection demonstrate how radiation viscosity affects the boundary between a fast-moving flow and its surroundings under the two-stream approximation. Our analysis generalizes the treatment of Arav & Begelman (1992) by permitting the jet velocity to be relativistic and by incorporating the enthalpy of the radiation in the momentum equation. Our results are similar to those found by Arav & Begelman (1992) (compare, e.g., their Figure 3 to our Figures 7.1 and 7.2); there are, however, a few notable differences.

For one, our boundary layer thickness, given by equation (8.7), differs from that of Arav & Begelman (1992), who found  $\delta^2 \sim e' / (\rho_0'^2 \kappa v_j z)$ . In addition to the Lorentz factor contained in ours, their boundary layer thickness has an additional factor of  $e' / \rho_0'$ , meaning that, in the non-relativistic limit, our results do not agree. This discrepancy arises from the fact that, while we compared the lowest-order terms in  $\delta$  to the inviscid terms in the gas energy equation to obtain our boundary layer thickness, they compared the viscous term to the inertial term – the one proportional to  $\rho'$  – in the  $z$ -component of the momentum equation to obtain theirs. Because they ignored the enthalpy of the radiation, the inertial term was the only inviscid term present in the momentum equation, making it the only one available to balance the viscous part. However, if one does not ignore the radiative contribution to the momentum equation, one can now equate the viscous terms to either the term proportional to the mass density or the one proportional to the enthalpy. Because the density equals zero at  $\alpha = 0$ , there is always some location at which the enthalpy term exceeds the inertial term, making it more reasonable to equate the former to the viscous contribution than the latter. If one follows this route, one recovers our ordering for the boundary layer thickness.

The second difference is that their solutions depend on the square of the Mach number,  $M^2 \equiv v^2/c_s^2$ , where  $c_s^2 = 4e'/(9\rho'_0)$  is the non-relativistic sound speed. Our solutions, on the other hand, depend on both the jet velocity  $v_j$  and the ratio  $\mu = e'/\rho'_0$ , which is proportional to the non-relativistic sound speed. One reason for this difference arises from the discrepancy between our definitions of the boundary layer thickness. Another is due to the fact that our solutions included the enthalpy of the radiation; had Arav & Begelman (1992) included this term, factors of the sound speed would have arisen in their  $z$ -momentum equation. Finally, our solutions also depend on the value of the jet velocity – not just the ratio of the jet speed to the sound speed – because we included all relativistic effects, meaning that the speed of light now plays a role in determining the evolution of the system.

Our solutions show that, for fixed  $\mu$ , the thickness of the boundary layer is approximately independent of the jet Lorentz factor, which is due to the competition between the scaling of the fiducial boundary layer thickness  $\delta \propto 1/\sqrt{\Gamma_j}$  (see equation (8.7)) and the viscous heating. Specifically, a larger  $\Gamma_j$  results in a smaller  $\delta$  and a greater shear; this shear increases the specific entropy  $s' \propto e'/(e')^{4/3}$  and, since the pressure is a constant, this increase in the entropy implies a decrease in the density of scatterers which widens the boundary layer.

Figures 7.4, 7.5, and 7.6 show how the solutions for the velocity, density of scatterers, and density of photons vary for a fixed jet Lorentz factor (we chose  $\Gamma_j = 25$ ) but for a variable  $\mu$ . Increasing  $\mu$  relative to  $\mu = 1$  tends to slightly decrease the boundary layer thickness, while decreasing the value of  $\mu$  relative to  $\mu = 1$  dramatically increases the thickness. This behavior arises from the fact that the viscous heating, which decreases the density of scatterers and widens the boundary layer, is effective when the gas is compressible. The compressibility of the fluid, however, is only important when the flow velocity is supersonic, and we can show that the sound speed of the gas is (Chapter 6)

$$c_s = \frac{2}{3} \sqrt{\frac{\mu}{1 + 4\mu/3}}, \quad (7.31)$$

which, noting that  $e' = 3p'$ , where  $p'$  is the radiation pressure, correctly reduces to  $c_s \simeq \sqrt{4p'/(3\rho')}$  in the limit  $\mu \ll 1$  and  $c_s \simeq 1/\sqrt{3}$  in the limit  $\mu \gg 1$ . Thus, when  $\mu \ll 1$ , the location of the sonic point extends farther into the ambient medium, resulting in a widening of the boundary layer. On the other hand, when  $\mu \gg 1$ , the sonic point approaches the jet, but only slightly due to the fact that the sound speed approaches a constant as  $\mu \rightarrow \infty$ . In fact, based on this reasoning, we expect our solutions to be independent of  $\mu$  in the large  $\mu$  limit, which is indeed reflected in equation (7.20).

The densities of scatterers and photons both decrease within the boundary layer. This behavior has two interesting consequences. First, the lower number density of scatterers means that the optical depth is lower in the boundary layer. We are therefore able to see farther into the medium along lines of sight that probe regions of high shear. Second, because the energy density of the radiation stays unchanged as we traverse the media, the average energy per photon increases, resulting in a harder spectrum within the boundary layer.

Equation (8.10) shows that the radiation energy density, and hence the pressure, is constant across the boundary layer, which is ultimately a statement of the causal connectedness of the jet. This means, equivalently, that the boundary layer thickness  $\delta y$  can be traversed by a sound wave in less time than it takes the jet material to cross the distance  $\delta z$ . Since the transverse sound speed is related to the isotropic sound speed by  $c_{s\perp} = c_s/\Gamma_j$ , we find that the boundary layer thickness  $\delta$  must satisfy  $\delta \lesssim c_s/\Gamma_j$ . When this inequality is no longer satisfied, equation (8.10) no longer holds, and we must include more terms in all of the boundary layer equations that account for changes in the pressure.

The solution for  $g$  equals zero at  $\alpha = 0$  which, as we mentioned, can be determined by inspecting the asymptotic ( $\xi \rightarrow 0$ ) limit of equation (7.21). This feature was also found by Arav & Begelman (1992), and can be understood physically by noting that, when the jet and the ambient medium initially interacted, the surface separating them served as a discontinuity in velocity, resulting in an infinite shear and entropy generation. Although the solutions presented here illustrate the time-steady state of the system after radiation viscosity has smoothed out the discontinuity,

the infinite entropy along the contact discontinuity persists and drives the density to zero. Mathematically, this behavior is ultimately due to the fact that  $f(0) = 0$ , which itself came from the requirement that there be no mixing at the surface separating the jet and the external environment. This boundary condition is necessary to ensure that the two media retain their respective identities and underlies the two-stream assumption, and it allows us to prescribe different asymptotic properties of those media.

## 7.5 Summary and conclusions

We applied the relativistic equations of radiation hydrodynamics in the viscous limit to the two-stream boundary layer, expanding on the past work of Arav & Begelman (1992). These equations are applicable as long as changes in the fluid quantities are small over the mean free path of a photon.

An interesting feature of the solutions presented here is the depression in the number density of scatterers within the boundary layer separating the jet and the ambient medium, which is consistent with the findings of Arav & Begelman (1992). We also showed that the number density of photons  $N'$  roughly tracks the density of scatterers, reaching a minimum towards, but not at, the contact discontinuity. Therefore, observers viewing a relativistic outflow with lines of sight that probe regions of high shear see farther into the outflow and they also see a higher energy per photon, and hence a harder spectrum.

Our solutions show that the physical boundary layer thickness does not depend strongly on the jet Lorentz factor  $\Gamma_j$ , which results from a competition between viscous heating and the scaling of the fiducial boundary layer thickness  $\delta \sim 1/\sqrt{\Gamma_j}$ . The dependence of our solutions on  $\mu$  arises from the fact that the change in entropy of the flow is related to its compressibility, which is most important where the outflow velocity is supersonic. Since the sound speed scales as  $c_s \sim \sqrt{\mu}$  when  $\mu \lesssim 1$ , the point at which the outflow becomes subsonic extends farther into the ambient medium when  $\mu$  is small, resulting in a widening of the boundary layer. When  $\mu$  becomes larger than one, however, the sound speed does not increase much, asymptotically approaching  $1/\sqrt{3}$ , meaning that

the sonic point only slightly approaches the jet, yielding a marginal decrease in the boundary layer thickness.

A number of assumptions about the nature of the jet and its surroundings are built in to the two-stream solutions presented here. Specifically, we adopted a two-dimensional, plane-parallel geometry for the flow and its surroundings, and we demanded that there be no pressure gradient ( $e'(z) = e'_0$ ) in the ambient medium. While these assumptions greatly enhanced the tractability of the problem, they somewhat hinder the astrophysical relevance of the solutions, as no systems likely conform precisely to these restrictions. However, in **local** regions of an outflow, where the radius of curvature is large and the pressure can be considered relatively constant, these solutions may be actualized. Therefore, while the physics of an entire jet-disk system may be poorly modeled by the two-stream scenario, local patches of the outflow, where the geometry can be treated as locally flat and the pressure gradient is small, are likely well-described by the solutions presented here.

The two-stream solutions could be applied to relativistic, radiation dominated jets, such as those that appear during super-Eddington TDEs, the event **Swift** J1644+57 being one such case. The event **Swift** J2058+05, observed shortly after **Swift** J1644, is another source that has been interpreted as a jetted TDE (Cenko et al., 2012). A comparison between the models presented here and these sources could provide valuable information concerning their progenitors and the properties of the jets themselves. The application of these models to long GRBs could likewise prove fruitful, potentially yielding, for example, information concerning the Lorentz factor of the jet, the stellar progenitor, and the direction of the line of sight between the observer and the source.

These models may also be applicable to jetted X-ray binary systems, or “microquasars” (Mirabel & Rodríguez, 1999; Fender et al., 2004, 2009). For example, Arav & Begelman (1993) applied their non-relativistic, radiation-viscous solution (Arav & Begelman, 1992) to the source SS 433 (Fabrika, 2004; Begelman et al., 2006a). Since the jets of SS 433 are mildly relativistic, their speeds being  $v_j \simeq 0.26 c$  (Margon & Anderson, 1989), including the relativistic terms arising from the treatment presented here may place new constraints on the properties of those jets and the surrounding envelope.

Finally, quasi-stars – protogalactic gas clouds supported by an accreting black hole – may also contain jets (Begelman et al., 2006a, 2008; Czerny et al., 2012). Since the power radiated by the black hole at the center of a quasi-star supports the overlying gaseous envelope, the mass of the envelope greatly exceeding that of the hole, the black hole accretes supercritically by several orders of magnitude. The jets launched from these systems are therefore radiation-dominated, and as they propagate through the quasi-star envelope, radiation-viscous effects likely dominate the interaction between the two media. Applying the solutions presented here to these systems could then yield information about the properties of these jets and the role they may have played during the epoch of galaxy formation.

One drawback to these models and their physical application, however, is that they require that the jet and ambient medium be separated by a contact discontinuity, which results in the non-physical vanishing of the density of scatterers at the interface. Furthermore, this prevents the jet from entraining ambient material; while this is not particularly problematic for the two-stream problem, in which the jet is considered infinite in extent, realistic jets have a finite width and total momentum, meaning that the entrainment of ambient material will cause a decrease in the outflow velocity with  $z$  that cannot be captured with the two-stream treatment.

In a companion paper (Coughlin & Begelman, 2015), we investigate a different type of viscous boundary layer – the free-streaming jet model. This model treats the entire system, jet and ambient medium, as a single fluid, which removes the need for a contact discontinuity and allows the density to remain non-zero throughout the boundary layer. We also show that the entrainment of ambient material causes an overall slowing of the outflow.

## Chapter 8

### Viscous boundary layers of radiation-dominated, relativistic jets. II. The free-streaming jet model

Particles, magnetic fields, and radiation all contribute to the propulsion of relativistic jets, though the relative contribution of each is still an open matter of debate. In certain situations, however, the mechanism responsible for launching the jet operates simultaneously with the release of a large amount of energy in the form of radiation, making it likely that photons dominate the bulk energetics. This scenario occurs, for example, during the super-Eddington phase of jetted tidal disruption events (TDEs), such as **Swift** J1644+57 (Burrows et al., 2011; Zauderer et al., 2011) and **Swift** J2058+05 (Cenko et al., 2012). Radiation-dominated jets should also be present in the collapsar picture of long gamma-ray bursts (GRBs; Rees & Meszaros 1992; Woosley 1993; Meszaros & Rees 1993; MacFadyen & Woosley 1999; Piran 2004), where the energy released in the form of gamma-rays is ultimately derived from accretion onto a black hole, the associated accretion luminosity exceeding the Eddington limit of the hole by more than ten orders of magnitude. In both of these cases, the propagation of the radiation-dominated jet is modulated by the presence of a radiation pressure-supported environment; for super-Eddington TDEs, this environment is in the form of a highly inflated, quasi-spherical torus of fallback debris (Chapter 5), while a “cocoon” of shocked jet material (Morsony et al., 2007; López-Cámara et al., 2013) and the overlying stellar envelope itself (Matzner, 2003; Woosley & Bloom, 2006) serve as the confining medium for GRBs.

In the previous chapter (Chapter 7) we presented a model that describes the viscous interaction of a radiation-dominated, relativistic jet with its surrounding medium. In that analysis we

treated the jet and its surroundings as two separate fluids, interacting with one another via small anisotropies in the comoving radiation field that are explicitly accounted for in the equations of radiation hydrodynamics in the viscous limit. This two-stream approximation, in agreement with the non-relativistic analysis of Arav & Begelman (1992), demonstrates the manner in which the shear between the two fluids carves out a region of low density material within the boundary layer between them. We also deduced the dependence of the boundary layer thickness on the asymptotic properties of the jet and the ambient medium.

These models also show, however, that the contact discontinuity separating the jet and its surroundings, necessary for maintaining their respective identities, results in the likely unphysical vanishing of the density of scatterers along that surface of separation. The contact discontinuity also prevents the jet from entraining ambient material; since the jet in the two-stream model we considered had an infinite amount of momentum, any entrainment or lack thereof is formally inconsequential to the evolution of the system. However, realistic jets – those with finite extent – will almost certainly engulf more material as they expand into their surroundings; because the total amount of momentum in the system, which is realistically finite, must be conserved, that entrainment will then result in an overall deceleration of the outflow that cannot be captured in the two-stream model.

In view of these unphysical properties of the two-stream treatment – the vanishing of the mass density of scatterers along the contact discontinuity and the lack of entrainment – we present here an alternative boundary layer scenario to describe the interaction of a relativistic, radiation-dominated jet with its surroundings. This “free-streaming jet” model, which has a well-known counterpart in the non-relativistic, incompressible limit (see Chapter 10, Section 12 of Kundu & Cohen 2008), assumes that the jet is injected through a narrow opening into a static, homogenous medium, and that far enough from that opening the entire system can be modeled as a single fluid that is independent of the details at the injection point. By considering the jet and the ambient medium as one fluid we obviate the need for a contact discontinuity, which we demonstrate allows the density of scatterers to remain finite throughout the flow and for the jet to entrain material.

In section 2 of this paper we present the equations of radiation hydrodynamics in the viscous limit. Section 3 uses those equations to analyze the free-streaming jet model, and we demonstrate the existence of approximate self-similar solutions in the limit that the interaction between the jet and the ambient medium is concentrated in a thin boundary layer. In section 4 we discuss the implications of our model and make comparisons to the two-stream scenario, and in section 5 we conclude and consider the application of the free-streaming jet model to super-Eddington TDEs, GRBs, and other astronomical sources.

## 8.1 Governing equations

When changes in fluid quantities over the mean free path of a photon are small, radiation behaves like an effective viscosity and transfers momentum and energy between neighboring fluid elements. The precise form of the viscosity can be determined by investigating the general relativistic Boltzmann equation, which was done in Chapter 6 for the case where Thomson scattering dominates the interactions between the photons and scatterers in the fluid rest frame. In this limit, we found that the relativistic equations of radiation hydrodynamics for a cold gas (gas pressure much less than the gas rest mass density and radiation pressure) are (see equation (49) of Chapter 6; see also Chapter 7):

$$\begin{aligned} \nabla_\mu \left[ \left\{ \rho' + \frac{4}{3} e' \left( 1 - \frac{10}{9} \frac{1}{\rho' \kappa} \nabla_\alpha U^\alpha \right) \right\} U^\mu U^\nu \right] + \frac{1}{3} g^{\mu\nu} \partial_\mu e' - \frac{8}{27} \nabla_\mu \left[ \frac{e'}{\rho' \kappa} \Pi^{\mu\sigma} \Pi^{\nu\beta} \left( \nabla_\sigma U_\beta + \nabla_\beta U_\sigma + g_{\beta\sigma} \nabla_\alpha U^\alpha \right) \right] \\ - \frac{1}{3} \nabla_\mu \left[ \frac{e'}{\rho' \kappa} \left( \Pi^{\mu\sigma} U^\nu + \Pi^{\nu\sigma} U^\mu \right) \left( 4U^\beta \nabla_\beta U_\sigma + \partial_\sigma \ln e' \right) \right] = 0. \quad (8.1) \end{aligned}$$

Here the speed of light has been set to one, Greek indices range from 0 – 3,  $\rho'$  is the fluid rest frame mass density of scatterers,  $e'$  is the fluid rest frame radiation energy density,  $\kappa$  is the scattering opacity (in units of  $\text{cm}^2 \text{g}^{-1}$ ),  $g_{\mu\nu}$  is the metric of the spacetime,  $\nabla_\mu$  is the covariant derivative,  $U^\mu$  is the four-velocity of the flow, and  $\Pi^{\mu\nu} = U^\mu U^\nu + g^{\mu\nu}$  is the projection tensor. The Einstein summation convention has been adopted here, meaning that repeated upper and lower indices imply summation. This equation also shows, in agreement with previous findings (Blandford et al., 1985;

Loeb & Laor, 1992), that the coefficient of dynamic viscosity,  $\eta$ , for an optically-thick, radiation-dominated gas is

$$\eta = \frac{8}{27} \frac{e'}{\rho' \kappa}. \quad (8.2)$$

We will also write down the gas energy equation, obtained by contracting equation (8.1) with the four-velocity  $U_\nu$ , which gives (see equation (50) of Chapter 6)

$$\begin{aligned} \nabla_\mu (e' U^\mu) + \frac{1}{3} e' \nabla_\mu U^\mu &= \frac{4}{3} \frac{10}{9} \nabla_\mu \left[ \frac{e'}{\rho' \kappa} U^\mu \nabla_\alpha U^\alpha \right] + \frac{8}{27} \frac{e'}{\rho' \kappa} \left( \nabla_\sigma U_\beta + \nabla_\beta U_\sigma + g_{\sigma\beta} \nabla_\alpha U^\alpha \right) \Pi^{\mu\sigma} \nabla_\mu U^\beta \\ + \frac{1}{3} \Pi^{\mu\sigma} \nabla_\mu \left[ \frac{e'}{\rho' \kappa} \left( 4U^\beta \nabla_\beta U_\sigma + \partial_\sigma \ln e' \right) \right] &+ \frac{1}{3} \frac{e'}{\rho' \kappa} \left( 4U^\beta \nabla_\beta U_\sigma + \partial_\sigma \ln e' \right) \left( 2U^\mu \nabla_\mu U^\sigma + U^\sigma \nabla_\mu U^\mu \right). \end{aligned} \quad (8.3)$$

To close the system, we require that the normalization of the four-velocity be upheld and that particle flux be conserved:

$$U_\mu U^\mu = -1, \quad (8.4)$$

$$\nabla_\mu \left[ \rho' U^\mu \right] = 0. \quad (8.5)$$

Equations (8.1) and (8.3) – (8.5) constitute six linearly independent equations for the six unknowns  $U^\mu$ ,  $e'$ , and  $\rho'$ .

In addition to the energy density of the radiation,  $e'$ , one can also calculate the number density of photons by requiring that the number flux,  $F^\mu$ , be conserved. One can show (Chapter 6) that the equation  $\nabla_\mu F^\mu = 0$  becomes, in the viscous limit,

$$\nabla_\mu \left[ N' U^\mu \right] = \nabla_\mu \left[ \frac{1}{\rho' \kappa} \left( \frac{10}{9} N' U^\mu \nabla_\sigma U^\sigma + N' U^\alpha \nabla_\alpha U^\mu + \frac{1}{3} \Pi^{\mu\sigma} \nabla_\sigma N' \right) \right], \quad (8.6)$$

where  $N'$  is the rest-frame number density of photons. Once we solve the equations of radiation hydrodynamics for the four-velocity of the fluid and the mass density of scatterers, we can solve

equation (8.6) for the number flux of photons.

The goal of the next two sections is to apply equations (8.1) and (8.3) – (8.6) to the boundary layers established between fast-moving jets and their ambient media. For a more thorough discussion of the nature of the equations of radiation hydrodynamics in the viscous limit, we refer the reader to Chapter 6.

## 8.2 Jetted boundary layer

In this section we consider the problem where a narrow stream of material is continuously injected into a plane-parallel, static, ambient medium, known as the free-streaming jet problem. If the Reynolds number of the outflow is high, the transition between the stream of material and the external environment will be confined to a thin layer, permitting the use of a boundary layer approximation.

The basic setup is similar to that of the two-stream problem (see Chapter 7), with the motion of the 2-D, plane-parallel injected stream predominantly along the  $z$ -direction, the majority of the variation along  $y$ , no variation or velocity in  $x$ , and the point of injection at  $y = z = 0$ . Now, however, there is no contact discontinuity between the stream and the ambient environment, meaning that the entire system is considered a single fluid. We therefore have less freedom in prescribing the asymptotic characteristics of the jet and the environment; however, this configuration permits mixing between the two media, allowing the outflow to entrain material, which almost certainly occurs in realistic jets.

We can reduce the complexity of equations (8.1) and (8.3) by assuming that the interaction between the jet and the ambient medium takes place over a thin boundary layer of thickness  $\delta y$ , thin in the sense that  $\delta \equiv \delta y / \delta z$  is a small number when  $\delta z$  is a typical length along the jet. In this case,  $\delta$  scales in an identical fashion to that derived for the two-stream boundary layer, which can be determined by comparing leading-order terms in the boundary layer thickness to the inviscid terms in the gas energy equation. Setting the left-hand side of equation (8.3) to  $\sim e' \Gamma_j v_j / z$ , we

find, as in Chapter 7,

$$\delta^2 \sim \frac{1}{\rho' \kappa z \Gamma_j v_j}. \quad (8.7)$$

Here  $v_j$  and  $\Gamma_j = (1 - v_j^2)^{-1/2}$  are the jet velocity and Lorentz factor, respectively, measured at some characteristic length along the jet axis  $z_0$ , and  $\rho'$  is a characteristic density of scatterers throughout the outflow. Due to the fact that the boundary layer thickness is the same, the boundary layer equations governing the outflow are identical to those found in paper I, which can be compactly written as

$$\nabla_\mu \left[ \left( \rho' + \frac{4}{3} e' \right) U^\mu U^\nu \right] + \frac{1}{3} g^{\mu\nu} \partial_\mu e' = \frac{8}{27} \frac{\partial}{\partial y} \left[ \frac{e'}{\rho' \kappa} \frac{\partial U^\nu}{\partial y} \right], \quad (8.8)$$

$$\nabla_\mu \left[ \rho' U^\mu \right] = 0. \quad (8.9)$$

In paper I we dealt with the  $\nu = y$  and  $\nu = z$  components of equation (8.8) and its contraction with  $U_\nu$  – the gas energy equation (8.3). For the free-streaming jet problem, however, it will be more convenient to deal with the  $\nu = y$  component of equation (8.8), the gas energy equation, and the contraction of equation (8.8) with the projection tensor  $\Pi_\nu^z$ , which, as we will see, is the relativistic, viscous counterpart of the Bernoulli equation. Performing a few manipulations, we find that these equations become, respectively,

$$\frac{\partial e'}{\partial y} = 0, \quad (8.10)$$

$$\nabla_\mu \left[ e' U^\mu \right] + \frac{1}{3} e' \nabla_\mu U^\mu = \frac{8}{27} \frac{e'}{\rho' \kappa} \left( \frac{\partial S}{\partial y} \right)^2, \quad (8.11)$$

$$\left( \rho' + \frac{4}{3} e' \right) U^\mu \nabla_\mu S + \frac{1}{3} \Gamma \frac{de'}{dz} = \frac{8}{27} \frac{\partial}{\partial y} \left[ \frac{e'}{\rho' \kappa} \frac{\partial S}{\partial y} \right], \quad (8.12)$$

$$\nabla_\mu \left[ \rho' U^\mu \right] = 0. \quad (8.13)$$

where

$$S = \ln \left( \Gamma v_z + \sqrt{1 + \Gamma^2 v_z^2} \right) = \operatorname{arcsinh}(\Gamma v_z). \quad (8.14)$$

The first of these shows that the radiation energy density, and consequently the pressure, is constant across the boundary layer. In the inviscid limit, equation (8.12) can be transformed to give

$$U^\mu \nabla_\mu \left[ \Gamma \left( 1 + \frac{4 e'}{3 \rho'} \right) \right] = 0, \quad (8.15)$$

which, as we mentioned, is the relativistic generalization of the Bernoulli equation. We will also assume that the ambient energy density is independent of  $z$ , i.e., that  $e'(z) = e'_0$ , with  $e'_0$  a constant.

Because it will be convenient, we will change variables from  $y$  to  $\tau$ , where  $\tau$  is given by

$$\tau \equiv \int_0^y \rho'(\tilde{y}, z) \kappa d\tilde{y}, \quad (8.16)$$

which is related to the optical depth across the boundary layer as measured from the axis. In terms of this variable, equations (8.11) and (8.12) become, respectively,

$$\frac{4}{3} e' U^\mu \nabla_\mu \left( \frac{1}{\rho'} \right) = \frac{8}{27} e' \kappa \left( \frac{\partial S}{\partial \tau} \right)^2, \quad (8.17)$$

$$\left( 1 + \frac{4 e'}{3 \rho'} \right) U^\mu \nabla_\mu S = \frac{8}{27} e' \kappa \frac{\partial^2 S}{\partial \tau^2}, \quad (8.18)$$

where we have used the assumption that  $e'(z) = e'_0$ . It should also be noted that the  $y$ -component of the convective derivative is now with respect to  $\tau$ , not  $y$ , i.e.,

$$U^\mu \nabla_\mu = U^z \frac{\partial}{\partial z} + \rho' \kappa U^y \frac{\partial}{\partial \tau}. \quad (8.19)$$

In the ensuing section we will seek self-similar solutions to these equations.

### 8.2.1 Self-similar approximation

We can immediately solve the continuity equation (8.13) by introducing the stream function  $\psi$  via

$$\Gamma v_z = \frac{\partial \psi}{\partial \tau}, \quad (8.20)$$

$$\rho' \kappa \Gamma v_y = -\frac{\partial \psi}{\partial z}, \quad (8.21)$$

where the factor of  $\kappa$  ensures that  $\psi$  remains dimensionless. In paper I we showed that there exist self-similar solutions for  $\psi$ , the velocity, the comoving density of scatterers and comoving density of photons in terms of the variable  $\alpha = y/\delta y$ , where  $\delta y \sim \sqrt{z}$ . One difference between the two-stream problem and this type of outflow, however, is that we expect the jet to expand into the ambient medium, entraining material in the process. Therefore, as we look farther along the  $z$ -direction, the amount of inertia – predominantly in the form of radiation for the systems that we are considering – contained in the flow will increase. Owing to the conservation of momentum, the  $z$ -component of the velocity should thus be a decreasing function of  $z$ .

In light of this observation, we will assume that the  $z$ -component of the four-velocity scales as

$$\Gamma v_z = \Gamma_j v_j \left( \frac{z}{z_0} \right)^{-m} \frac{df}{d\xi} \equiv \zeta \frac{df}{d\xi}, \quad (8.22)$$

where  $z_0$  is a characteristic length scale in the  $z$ -direction,  $m$  is a positive constant, for brevity we defined  $\zeta \equiv \Gamma_j v_j (z/z_0)^{-m}$ , and  $f$  is a function of the self-similar variable  $\xi \simeq \tau/\delta\tau$ ;  $\delta\tau$  is the characteristic boundary layer thickness in terms of  $\tau$ , which, from equations (8.7) and (8.16) in the previous subsection, is given by  $\delta\tau \simeq \rho' \kappa \delta y$ , or

$$\delta\tau^2 \simeq \frac{\rho' \kappa z}{\Gamma_j v_j}. \quad (8.23)$$

We are most interested in the behavior of the properties of the outflow when the velocities are relativistic, as this is the limit that is most applicable to sources of astronomical interest, and in order for the self-similar nature of our solutions to be upheld, the dependence of our self-similar functions on the bulk properties of the outflow, such as the  $z$ -dependence of the jet Lorentz factor along the axis, should be minimal. A fully self-similar solution is likely impossible here, as the speed of light plays a role in setting a finite scale factor for our solutions and becomes problematic when we try to connect the ultra- and non-relativistic regions of the outflow. We will show, however, that the non-self-similarity of our solutions only affects a small region of the outflow.

In paper I, we showed that the self-similarity of the comoving density of scatterers,  $\rho'$ , was approximately satisfied, i.e., we could find solutions with  $\rho' \sim g(\xi)$ . For the case at hand, then, this assumption implies that  $g$  is independent of  $\zeta$ . This means, however, that the observer-frame density of scatterers, given by  $\rho = \Gamma\rho' \simeq \zeta g$ , can be made arbitrarily large (as  $g$  is independent of  $\zeta$  in the self-similar limit), which is a nonsensical result.

Motivated by this reasoning, we conclude that the comoving density of scatterers is unlikely to be independent of  $\zeta$ . On the contrary, a more reasonable approximation is that the **observer**-frame density of scatterers varies self-similarly. Investigating equations (8.17) and (8.18), we see that the  $\rho'$ -dependent quantity that enters both is the combination  $1 + 4e'/(3\rho')$ . Our expectation that the observer-frame density varies self-similarly then prompts the assumption

$$1 + \frac{4e'}{3\rho'} = \frac{4}{3}\mu\Gamma g(\xi), \quad (8.24)$$

where  $\mu \equiv e'/\rho'_0$ ,  $\rho'_0$  being the density of scatterers in the ambient medium. (Note that we could have simply let  $\rho'\Gamma = g(\xi)$ , but equation (8.24), which is merely a change of variables from the initial assignment  $\rho'\Gamma = g(\xi)$ , will allow equations (8.17) and (8.18) to be written in a more compact form.)

We can determine the value of  $m$ , which controls how rapidly the flow decelerates due to entrainment, by integrating the momentum flux,  $\dot{P} \simeq e'\Gamma^2 v_z^2$  for a radiation-dominated system, over

the entire boundary layer, and requiring that the result be independent of  $z$ . This is equivalent to requiring that the total momentum contained in the outflow be conserved. Integrating  $e'\Gamma^2 v_z^2$  from  $y = -\infty$  to  $\infty$ , using equations (8.22) and (8.24), taking the ultrarelativistic limit and changing variables from  $y$  to  $\xi$ , we find

$$\dot{P} \simeq \left(\frac{z}{z_0}\right)^{\frac{1}{2}-2m} \int_{-\infty}^{\infty} \left(\frac{df}{d\xi}\right)^2 d\xi. \quad (8.25)$$

Since the integral in this equation is a constant that is greater than zero, we find that  $m = 1/4$  if the momentum flux is conserved.

With this value of  $m$ , the  $z$ -component of the four-velocity scales as

$$\Gamma v_z = \Gamma_j v_j \left(\frac{z}{z_0}\right)^{-1/4} \frac{df}{d\xi}, \quad (8.26)$$

and the self-similar variable  $\xi$  is given by

$$\xi = \tau \sqrt{\frac{9\Gamma_j^2 v_j^2}{2\rho'_0 \kappa z_0}} \left(\frac{z}{z_0}\right)^{-3/4}. \quad (8.27)$$

We then find from equation (8.20) that the stream function must satisfy

$$\psi = \sqrt{\frac{2}{9}\rho'_0 \kappa z_0} \left(\frac{z}{z_0}\right)^{1/2} f. \quad (8.28)$$

Equation (8.21) then gives the  $y$ -component of the four-velocity:

$$\rho'_0 \kappa \Gamma v_y = -\sqrt{\frac{2}{9}\rho'_0 \kappa z_0} \left[ \frac{1}{2} \left(\frac{z}{z_0}\right)^{-1/2} f + z_0 \left(\frac{z}{z_0}\right)^{1/2} \frac{\partial \xi}{\partial z} f_\xi \right], \quad (8.29)$$

where, both here and in future equations, a subscripted  $\xi$  on the functions  $f$  and  $g$  denotes differentiation with respect to  $\xi$  and the number of subscripts indicates the number of derivatives, i.e.,  $f_\xi = df/d\xi$ ,  $f_{\xi\xi} = d^2f/d\xi^2$ , etc.

Inserting equations (8.24), (8.26) and (8.29) into equations (8.17) and (8.18), changing variables from  $\tau$  to  $\xi$  and performing a bit of algebra, we find that they become, respectively,

$$-\frac{1}{2}\Gamma f g_\xi = \zeta \left( \left( \frac{\partial S}{\partial \xi} \right)^2 - v_z \frac{\partial^2 S}{\partial \xi^2} \right), \quad (8.30)$$

$$-\frac{1}{4}g \left( (f_\xi)^2 + 2f f_{\xi\xi} \right) = \frac{\partial^2 S}{\partial \xi^2}. \quad (8.31)$$

Now, the solutions we seek for  $f$  and  $g$  should depend only on  $\xi$ , as otherwise our assumption of the self-similarity of those functions breaks down. Because of the complicated dependence of  $S$  on  $\Gamma v_z$ , we see that the solutions will not be self-similar for arbitrary  $\Gamma_j$ . However, in the ultrarelativistic limit, for which  $\Gamma \simeq \Gamma v_z$ , we see that  $S \simeq \ln(\Gamma v_z)$ , and it is apparent that the solutions are indeed self-similar, i.e., the  $\zeta$  dependence of equations (8.30) and (8.31) drops out.

As these equations are third order in  $f$  and first order in  $g$ , we require four boundary conditions to solve them numerically. Since  $\Gamma v_z$  is given by equation (8.26) and it is assumed that  $\Gamma v_z = \Gamma_j v_j (z/z_0)^{-1/4}$  along the axis, our first boundary condition is given by  $f_\xi(0) = 1$ . For the second, we note that the jet axis is the streamline along which the  $y$ -component of the velocity is zero. From equation (8.29), then, we find  $f(0) = 0$  (we will see that  $\partial\xi/\partial z = 0$  at  $\xi = 0$ ). The third boundary condition is obtained by noting that the  $z$ -component of the velocity should approach zero as we proceed into the ambient medium, so that, from equation (8.26), we find  $f_\xi(\infty) = 0$ . Finally, the density of scatterers should approach that of the ambient medium far from the jet center. Equation (8.24) then gives  $g(\infty) = 1 + 3/(4\mu)$ .

As we noted, the truly self-similar limit of equations (8.30) and (8.31) is obtained by setting  $S = \ln(\Gamma v_z)$ , but we encounter an issue with this scaling when we consider the boundary conditions on our flow in the ambient medium. In particular, we expect the outflow velocity to approach zero for  $\xi \gg 1$ ; when the velocity becomes subrelativistic, however,  $\ln(\Gamma v_z) \rightarrow -\infty$ , when in actuality the  $v_z \ll 1$  limit of equation (8.14) is  $S \simeq \ln(1 + \Gamma v_z) \simeq \Gamma v_z \simeq 0$ . Thus, we see that taking the ultrarelativistic limit of equations (8.30) and (8.31) will not result in the solutions matching the

correct boundary conditions far from the jet center.

To correct this problem, we will allow the function  $S$  to take on its full form and treat  $\zeta$  as a constant, which will break the self-similarity of our solutions. However, since our boundary conditions do not depend on the value of  $\zeta$ , the functions  $f$  and  $g$  themselves should be largely independent of that parameter. We therefore expect the assumption of self-similarity to be upheld in the ultrarelativistic ( $\xi \ll 1$ ) and the non-relativistic ( $\xi \gg 1$ ) limits of our solutions, with small deviations from self-similarity in the trans-relativistic regime of the outflow.

To exemplify this point, Figures 8.1 and 8.2 show, respectively, the variation of  $f_\xi$  – the normalized  $z$ -component of the four-velocity – and  $g$  – approximately the inverse of the observer-frame density – in terms of the parameter  $\xi$  for  $\zeta = 4, 10$ , and  $25$ . As we anticipated, the functions for different  $\zeta$  are indistinguishable for  $\xi \ll 1$  and  $\xi \gg 1$ , meaning that the self-similarity is nearly exact in those regions. In between those limits, where the flow is trans-relativistic, the deviations from self-similarity are apparent, though they remain small. Keeping the full form of  $S$  in equations (8.30) and (8.31) therefore preserves well the self-similarity of our solutions and provides a reasonable interpolation between the relativistic and non-relativistic regions of the flow.

The solution for  $g$  approaches infinity as we near the axis, which can be seen by investigating the small- $\xi$  behavior of equation (8.31). Specifically, letting  $f \simeq \xi$ ,  $f_\xi \simeq 1$ ,  $\Gamma \simeq \zeta$ , and  $v_z \simeq 1$ , equation (8.31) can be written as

$$\xi g_\xi + \frac{1}{2}g \simeq -2(f_{\xi\xi,0})^2, \quad (8.32)$$

where  $f_{\xi\xi,0}$  is the second derivative of  $f$  evaluated at  $\xi = 0$ . This equation can be integrated, and we find

$$g \simeq \frac{C}{\sqrt{\xi}} - (f_{\xi\xi,0})^2, \quad (8.33)$$

$C$  being a constant of integration. Since it is roughly proportional to  $1/\rho'$ , the value of  $g$  cannot be negative, meaning that  $C$  must be greater than zero. Therefore, the asymptotic,  $\xi \ll 1$  behavior

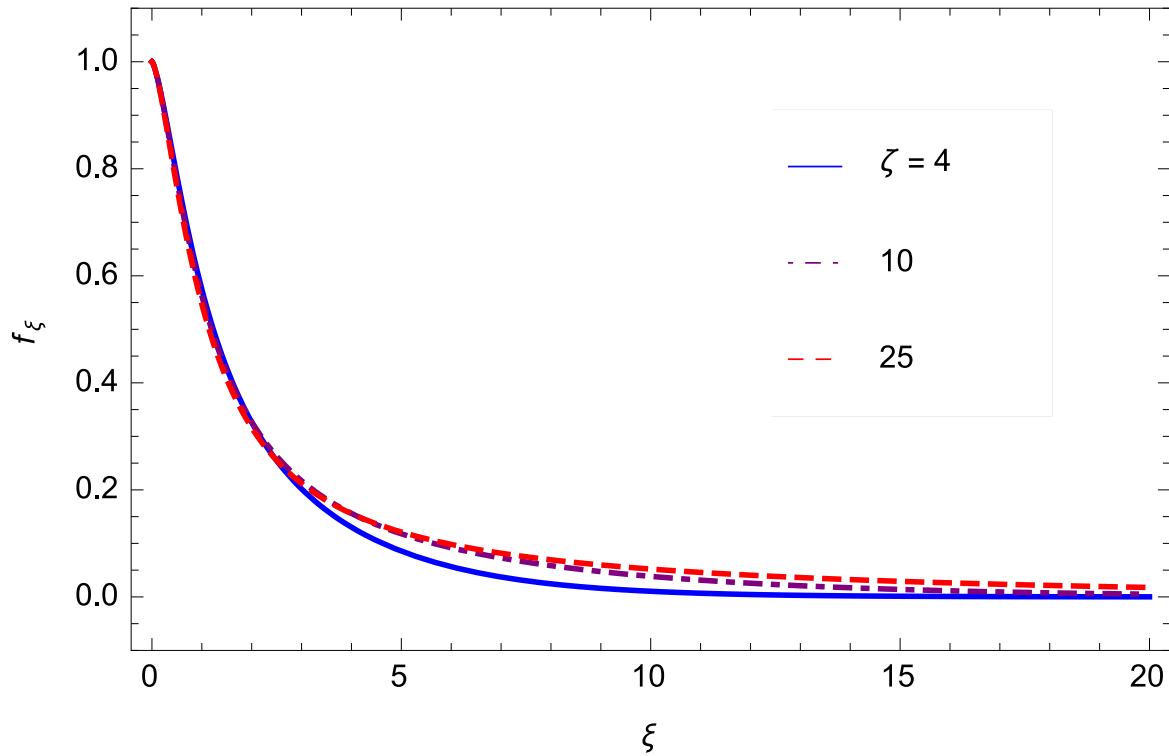


Figure 8.1: The behavior of  $f_\xi$ , which is the normalized  $z$ -component of the four-velocity, with  $\xi$  for  $\zeta = 4$  (blue, solid curve),  $\zeta = 10$  (purple, dot-dashed curve), and  $\zeta = 25$  (red, dashed curve). As expected, the curves are all coincident when  $\xi \ll 1$  and  $\xi \gg 1$ , with a non-self-similar transition (one that depends on  $\zeta$ ) in between those two limits.

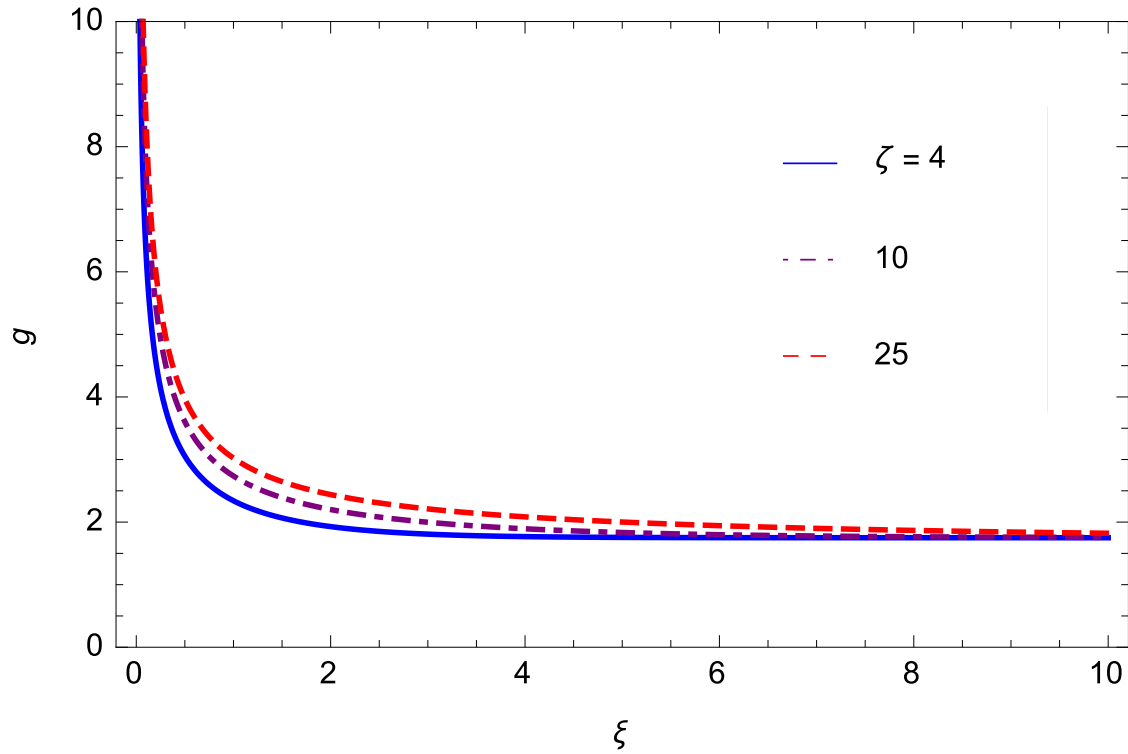


Figure 8.2: The function  $g$ , which is approximately the inverse of the lab-frame density, plotted with respect to  $\xi$  for the same set of  $\zeta$  chosen in Figure 8.1. As was true for  $f_\xi$ ,  $g$  is approximately self-similar close to and far from the jet, with the deviation from self-similarity in the trans-relativistic region being apparent but small.

of  $g$  is  $g \sim 1/\sqrt{\xi}$ .

In addition to the mass density of scatterers and the velocity, we can also calculate the number density of photons,  $N'$ , throughout the boundary layer. As we showed in Chapter 7, the equation of photon number conservation (8.6) becomes, to lowest order in the boundary layer thickness,

$$\nabla_\mu \left( N' U^\mu \right) = \frac{1}{3} \frac{\partial}{\partial y} \left( \frac{1}{\rho' \kappa} \frac{\partial N'}{\partial y} \right). \quad (8.34)$$

Performing a few manipulations, this equation becomes

$$U^\mu \nabla_\mu \left( \frac{N'}{\rho'} \right) = \frac{\kappa}{3} \frac{\partial^2 N'}{\partial \tau^2}. \quad (8.35)$$

As was true for the density of scatterers, we expect the observer frame number density of photons to vary approximately self-similarly, which will be true if we let

$$\frac{N'}{\rho'} = \frac{N'_0}{\rho'_0} h(\xi), \quad (8.36)$$

where  $N'_0$  is the number density of photons in the ambient medium and  $h$  is a dimensionless function.

Inserting this ansatz into equation (8.35) gives

$$-\frac{1}{3} f h_\xi = \zeta \frac{\partial^2}{\partial \xi^2} \left( \frac{h}{\Gamma g - \frac{3}{4\mu}} \right). \quad (8.37)$$

For the boundary conditions on  $h$ , we first require that the number density of photons approach that of the ambient medium in the  $\xi \gg 1$  limit. Equation (8.36) then gives  $h(\infty) = 1$ . For the second condition, return to equation (8.34), integrate both sides from  $y = -\infty$  to  $\infty$ , and require that the derivative of  $N$  vanish in both of those limits. Doing so yields

$$\frac{\partial}{\partial z} \int_{-\infty}^{\infty} N' \Gamma v_z dy = -N' \Gamma v_y \Big|_{-\infty}^{\infty}. \quad (8.38)$$

The right-hand side can be determined by returning to the continuity equation, integrating from  $y = -\infty$  to  $\infty$  and performing a few manipulations to show that  $\Gamma v_\infty \Big|_{-\infty}^{\infty} = -f_\infty$ , where  $f_\infty$  is

the function  $f$  evaluated at infinity. Using the definition of  $N'$  in terms of  $h$ , we find that equation (8.38) becomes

$$\int_{-\infty}^{\infty} h f_{\xi} d\xi = 2 f_{\infty}, \quad (8.39)$$

which serves as our second boundary condition on  $h$ . This integral states that the increase in the number flux of photons occurs at a rate provided by the influx of material at infinity.

The equations derived in this section were all written in terms of the variable  $\xi$ , which is itself a function of  $g$  via equations (8.16) and (8.27). To write the solutions in terms of the physical parameter  $y$ , we can return to equation (8.16), differentiate both sides with respect to  $y$ , rearrange the resulting equation and integrate to yield

$$\int_0^{\xi} \left( \Gamma g - \frac{3}{4\mu} \right) d\tilde{\xi} = y \sqrt{\frac{9 \Gamma_j^2 v_j^2 \rho'_0 \kappa}{2 z_0}} \left( \frac{z}{z_0} \right)^{-3/4} \equiv \alpha, \quad (8.40)$$

where  $\tilde{\xi}$  is a dummy variable of integration. Once we calculate the functions  $g(\tilde{\xi})$  and  $f_{\xi}(\tilde{\xi})$ , this relation can be integrated and solved numerically to yield  $\xi(\alpha)$ . This expression also shows that

$$\left( \Gamma g - \frac{3}{4\mu} \right) \frac{\partial \xi}{\partial z} = \frac{1}{4z} \left( \int_0^{\xi} \frac{\zeta^2 (f_{\xi})^2 g}{\sqrt{1 + \zeta^2 (f_{\xi})^2}} d\tilde{\xi} - 3\alpha \right), \quad (8.41)$$

which we can use in equation (8.29) to give

$$\rho' \kappa \Gamma v_y = \frac{1}{4} \sqrt{\frac{2 \rho'_0 \kappa}{9 z}} \left( \frac{f_{\xi}}{\Gamma g - \frac{3}{4\mu}} \left( 3\alpha - \int_0^{\xi} \frac{\zeta^2 (f_{\xi})^2 g}{\sqrt{1 + \zeta^2 (f_{\xi})^2}} d\tilde{\xi} \right) - 2f \right) \quad (8.42)$$

Equation (8.41) also confirms that  $\partial \xi / \partial z = 0$  when  $\xi = 0$ , which we used in order to determine the boundary condition  $f(0) = 0$ .

## 8.2.2 Solutions

In this section we plot solutions for the outflow velocity, the density of scatterers and the density of photons for various values of  $\mu$  and  $\zeta$ . As was mentioned in the previous subsection, the physical self-similar variable against which we would like to plot our solutions is given by  $\alpha$ .

However, as is apparent from equation (8.40), the definition of  $\alpha$  depends on  $\zeta$ . Therefore, if we are comparing, for example, the outflow velocity of two systems with differing  $\zeta$ , we must incorporate the  $\zeta$  dependence in  $\alpha$  so that the range of physical space that we consider for each solution is the same. For this reason, in this section we will plot our solutions as functions of the variable

$$\tilde{\alpha} \equiv \frac{\alpha}{\zeta} = y \sqrt{\frac{9\rho'_0\kappa}{2z_0}} \left(\frac{z}{z_0}\right)^{-1/2}. \quad (8.43)$$

Figure 8.3 shows the solution for  $f_\xi$ , the normalized  $z$ -component of the four-velocity, for  $\zeta = 4, 10,$  and  $25$ . Since  $\zeta = \Gamma_j v_j (z/z_0)^{-1/4}$ , these values of  $\zeta$  scale approximately linearly with the Lorentz factor until  $z \gg z_0$ . The outflow velocity is maximized at the origin and decays as we move farther into the ambient medium. We see that the width of the boundary layer, loosely defined as the value of  $\tilde{\alpha}$  at which  $f_\xi$  is some fraction of its central value, is nearly unchanged as we modify  $\zeta$ . The average value of the normalized  $z$ -component of the velocity is also slightly larger for larger  $\zeta$ .

Figure 8.4 demonstrates how the normalized, fluid-frame mass density of scatterers varies as we traverse the boundary layer for the same set of parameters chosen in Figure 8.3. Since  $g$  approaches infinity as we near the origin, the mass density of scatterers, related to  $g$  by equation (8.24), equals zero at the origin for all of the solutions, meaning that the center of the jet is evacuated of massive particles. The average comoving density of scatterers across the boundary layer is also lower for larger  $\zeta$ , in accordance with equation (8.24). In Figure 8.5 we plot the normalized number density of photons for the same set of  $\zeta$ . It is evident that the density of photons closely follows the density of scatterers throughout the boundary layer. We see, however, that the density of photons stays above and below the density of scatterers as we move toward and away from the center of the jet, respectively. The photon density also remains finite at the center of the jet.

The  $y$ -component of the three-velocity normalized by  $\sqrt{2/(9\rho'_0\kappa z_0)} \sim \delta$  is illustrated in Figure 8.6 for the same set of  $\zeta$  used in Figure 8.3. For  $\xi > 0$ , each solution initially has a positive  $v_y$ , which shows that the jet material expands away from the axis. The  $y$ -component of the three-velocity then reaches a relative maximum, one which increases slightly for larger  $\Gamma_j$ , before approaching

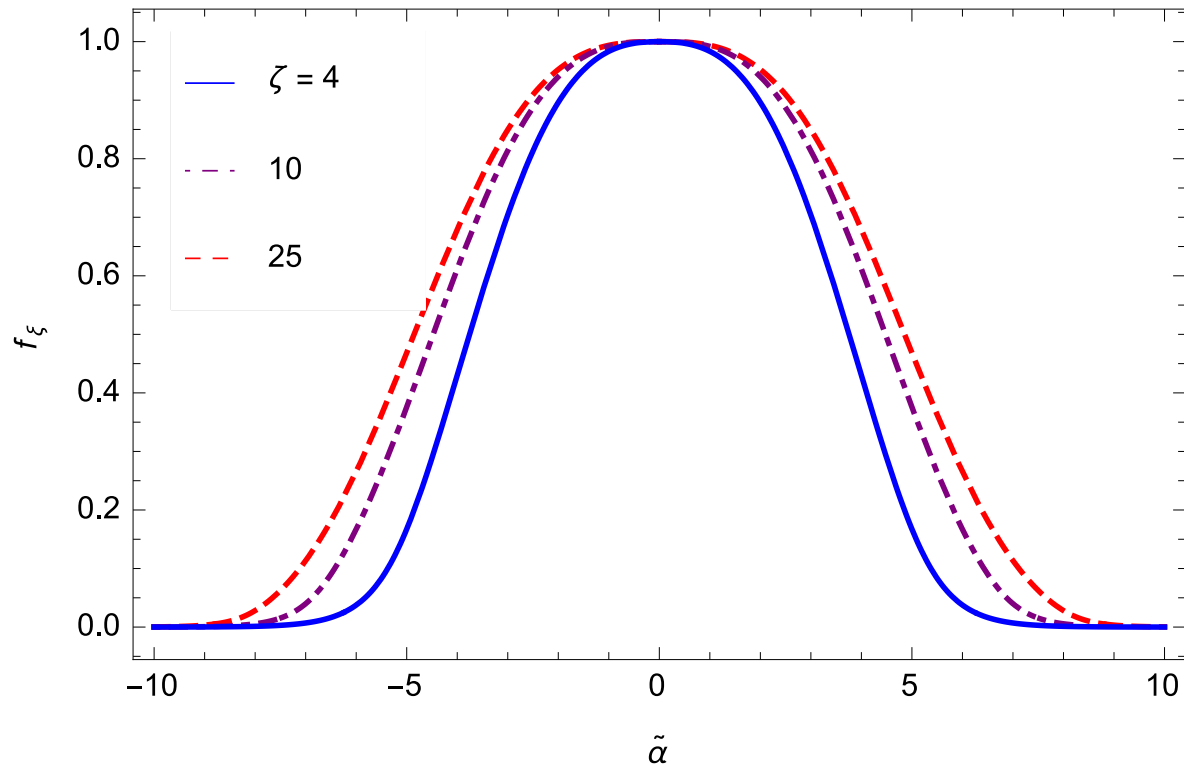


Figure 8.3: The normalized  $z$ -component of the four-velocity ( $f_\zeta$ ) for  $\mu = 1$  and  $\zeta = 4, 10,$  and  $25$  (the solid, blue curve, the dot-dashed, purple curve, and the dashed, red curve, respectively), which, for  $z \simeq z_0$ , correspond to  $\Gamma_j = 4, 10,$  and  $25$ . We see that the width of the boundary layer is nearly unchanged as we alter the value of  $\zeta$ .

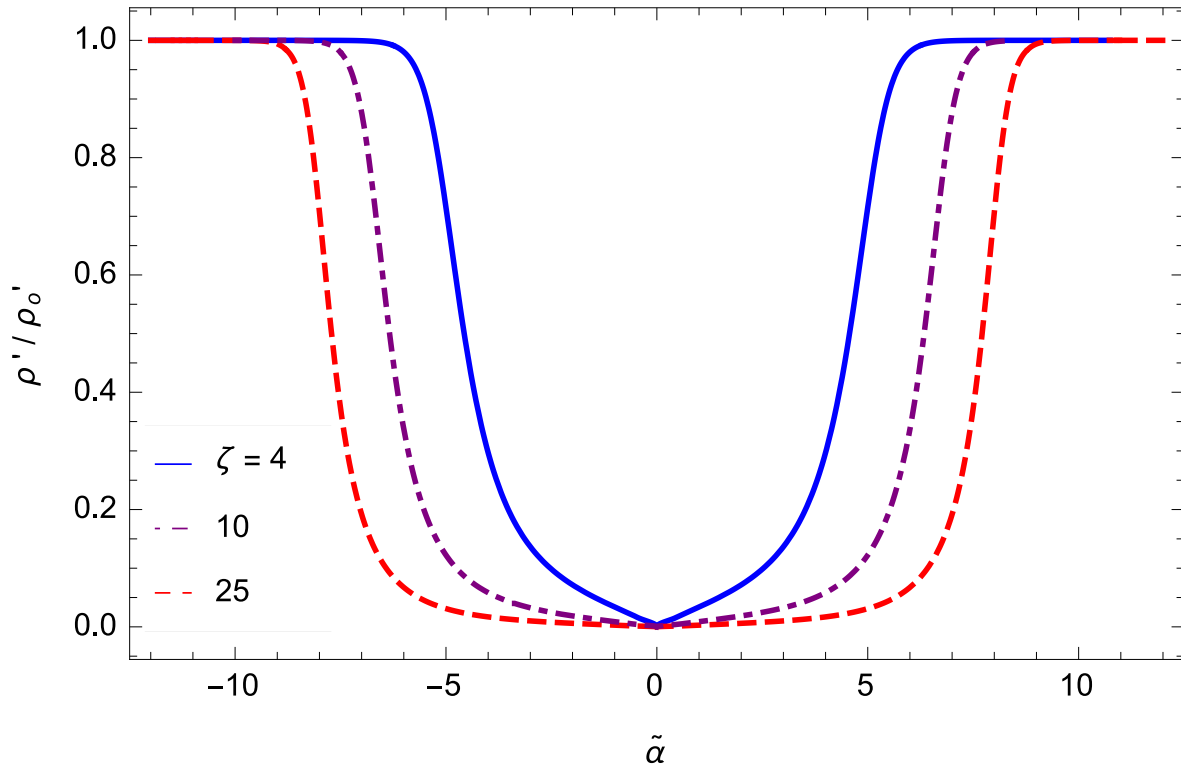


Figure 8.4: The normalized fluid-frame density of scatterers for the same set of parameters used in Figure 8.3. For all solutions the number density of scatterers approaches zero as we near the center of the jet. We see that the average number density of scatterers within the boundary layer is lower for larger Lorentz factors.

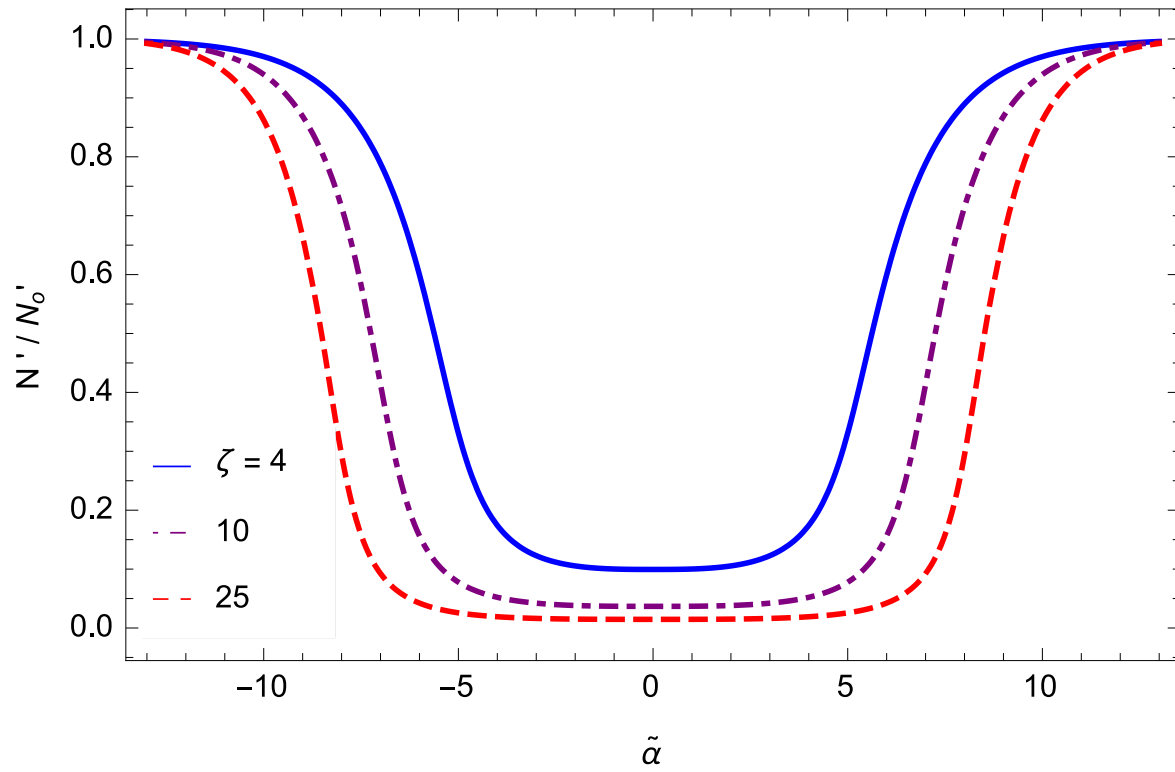


Figure 8.5: The normalized number density of photons for the same set of  $\zeta$  used in Figure 8.3. The photon number density closely follows that of the scatterers.

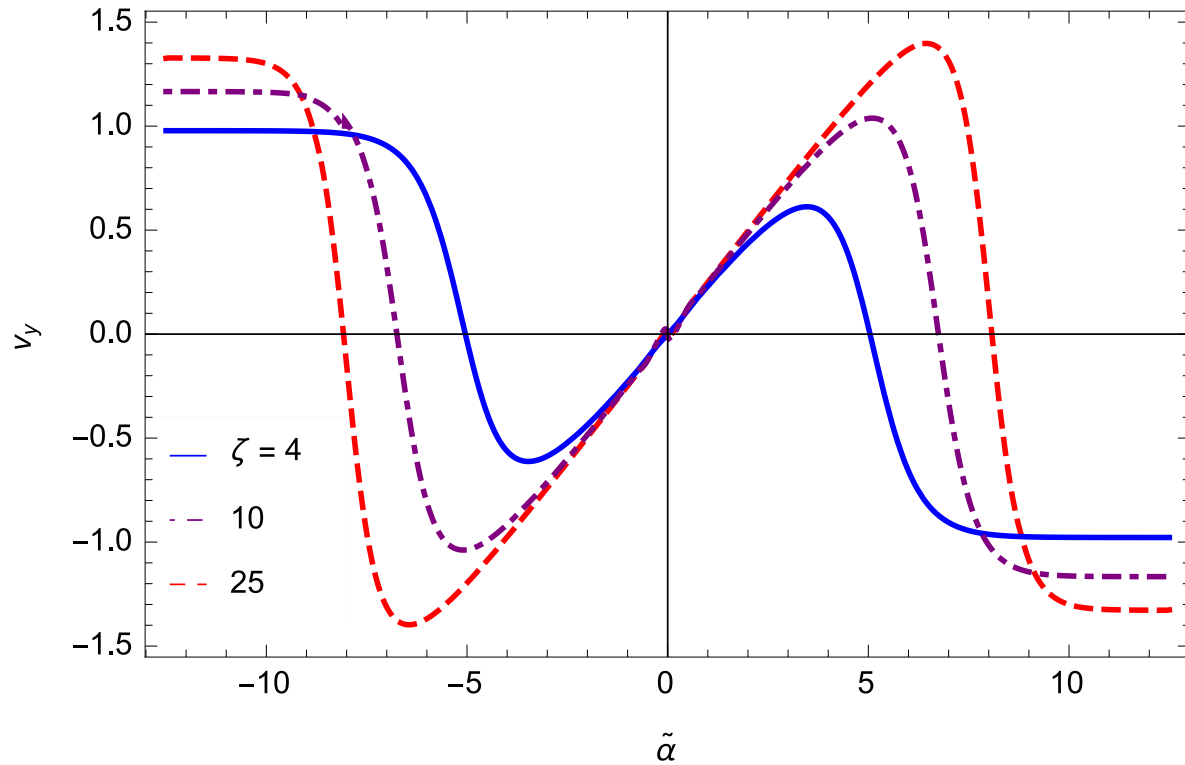


Figure 8.6: The  $y$ -component of the three-velocity normalized by  $\sqrt{2/(9\rho'_0\kappa z_0)}$  (see equation (8.42)) for the same set of parameters used in Figure 8.3. For positive  $\tilde{\alpha}$ , each solution is initially positive and reaches a relative maximum before approaching a negative constant, which shows that the flow expands outwards near the center of the jet and entrains ambient material far from the axis.

a negative, constant value. This behavior is then inverted for negative  $\xi$ . Because the transverse velocity approaches a negative constant for  $\xi > 0$  and a positive constant for  $\xi < 0$ , we see that the jet entrains material from the ambient medium.

Figures 8.7 – 8.10 illustrate how our solutions depend on  $\mu$ . As is apparent, changing the value of  $\mu$  does not drastically alter the qualitative aspects of the functions. We do see, however, that decreasing  $\mu$  from 1 to 0.1 results in a large increase in the boundary layer thickness; on the contrary, changing  $\mu$  from 1 to 10 results in only a slight narrowing of its thickness. It is also evident that a smaller  $\mu$  compared to 1 results in a lower average value of the density throughout the boundary layer and a larger peak in the transverse velocity  $v_y$ .

### 8.3 Discussion

Figures 8.3 – 8.6 demonstrate that the width of the boundary layer is nearly independent of  $\zeta$ , which is the result of the scaling of our boundary layer thickness  $\delta$ . Specifically, note from equation (8.7) that  $\delta$  is given by  $\delta \sim 1/\sqrt{\rho'\Gamma_j}$ . Since our ansatz posited that  $\rho'\Gamma \simeq g$ , with  $g$  a dimensionless function of order unity, and  $\Gamma \simeq \Gamma_j \simeq \zeta$  for  $z \sim z_0$ , the boundary layer thickness is roughly independent of  $\zeta$ .

Figures 8.7 – 8.10 illustrate that a value of  $\mu = 0.1$  causes the boundary layer thickness to increase dramatically compared to  $\mu = 1$ , while setting  $\mu = 10$  causes only a slight narrowing of the width compared to  $\mu = 1$ . This dependence is due to the fact that the viscous heating, which increases the specific entropy by decreasing the density of scatterers (at fixed pressure), is most efficient when the flow is compressible, as is evident from the gas energy equation (8.11). The fluid only becomes compressible, however, when the flow is supersonic, and we can show (Chapter 6) that the sound speed of a radiation-dominated gas is

$$c_s = \frac{2}{3} \sqrt{\frac{\mu}{1 + 4\mu/3}}. \quad (8.44)$$

When  $\mu \ll 1$ , the sound speed reduces to  $c_s \sim \sqrt{\mu}$ , and the location at which the flow becomes

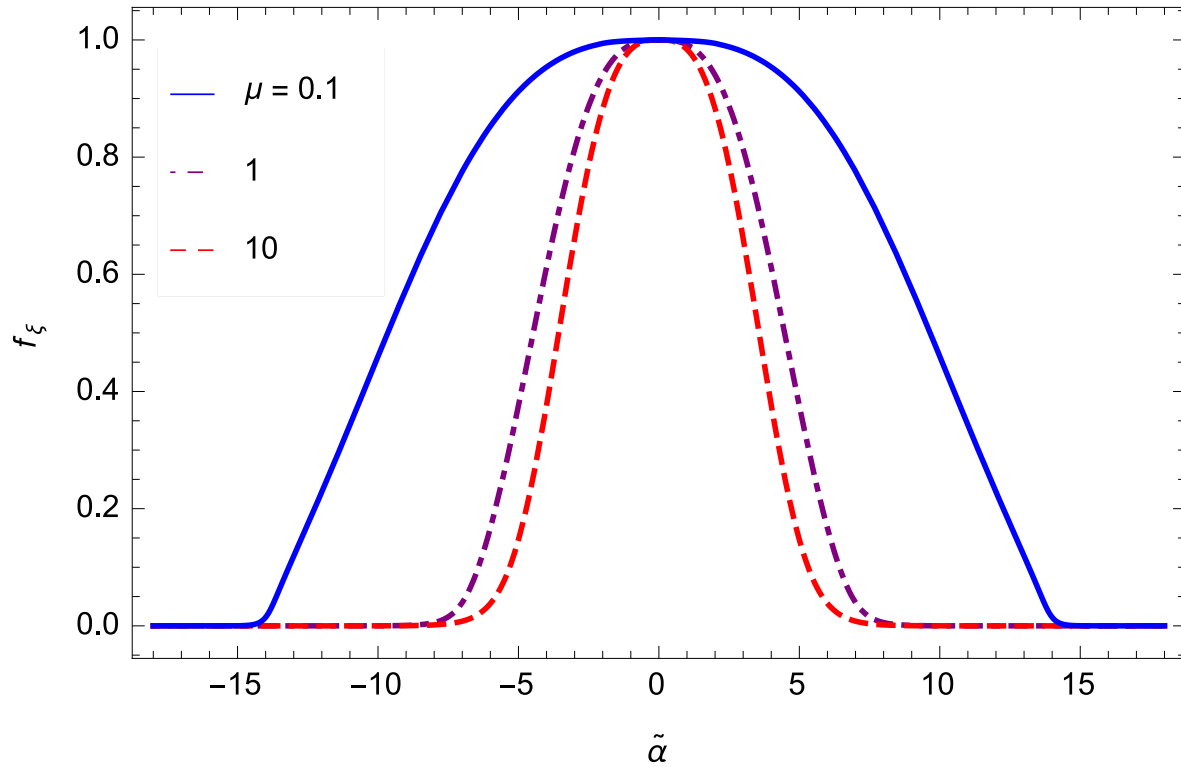


Figure 8.7: The function  $f_\xi$ , which is the normalized  $z$ -component of the four-velocity, for  $\zeta = 10$  and  $\mu = e'/\rho'_0 = 0.1, 1, \text{ and } 10$ , which correspond to the blue, solid curve, the purple, dot-dashed curve, and the red, dashed curve, respectively. Increasing the value of  $\mu$ , we see, has little effect on the solution, while decreasing  $\mu$  drastically widens the boundary layer.

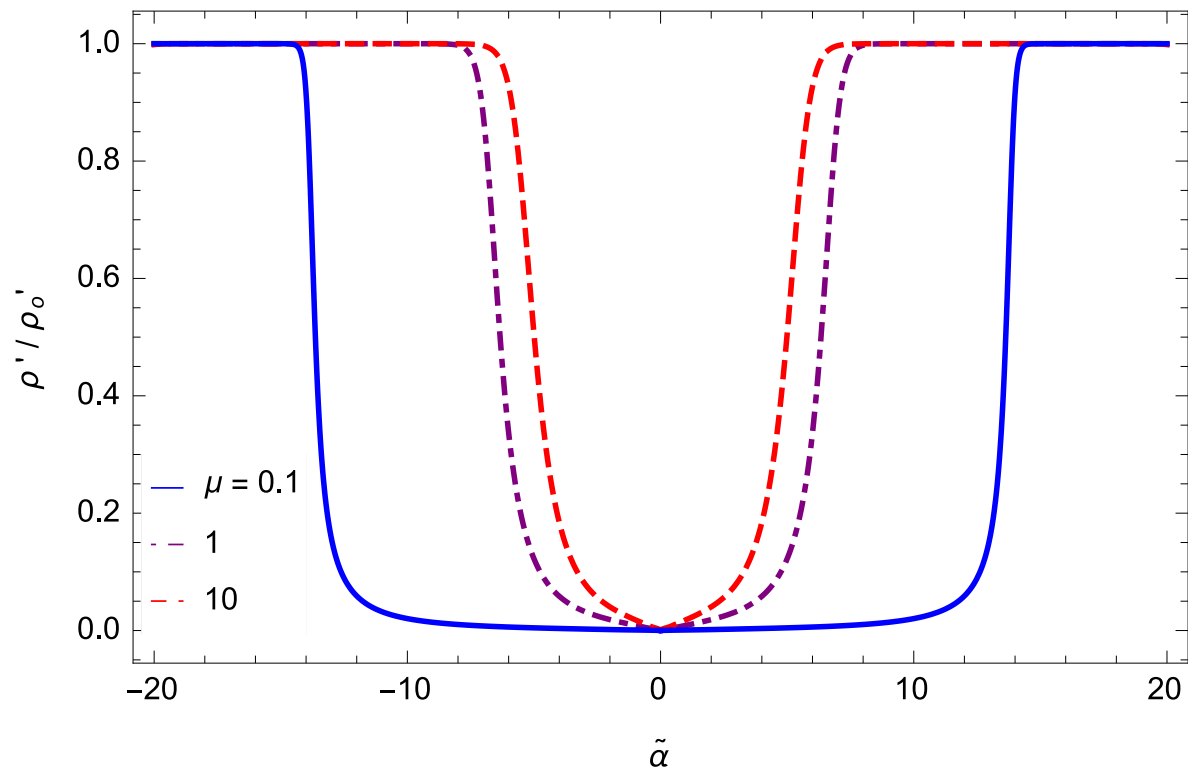


Figure 8.8: The normalized density of scatterers for the same values of  $\mu$  chosen in Figure 8.7. The mean value of the density decreases as  $\mu$  decreases.

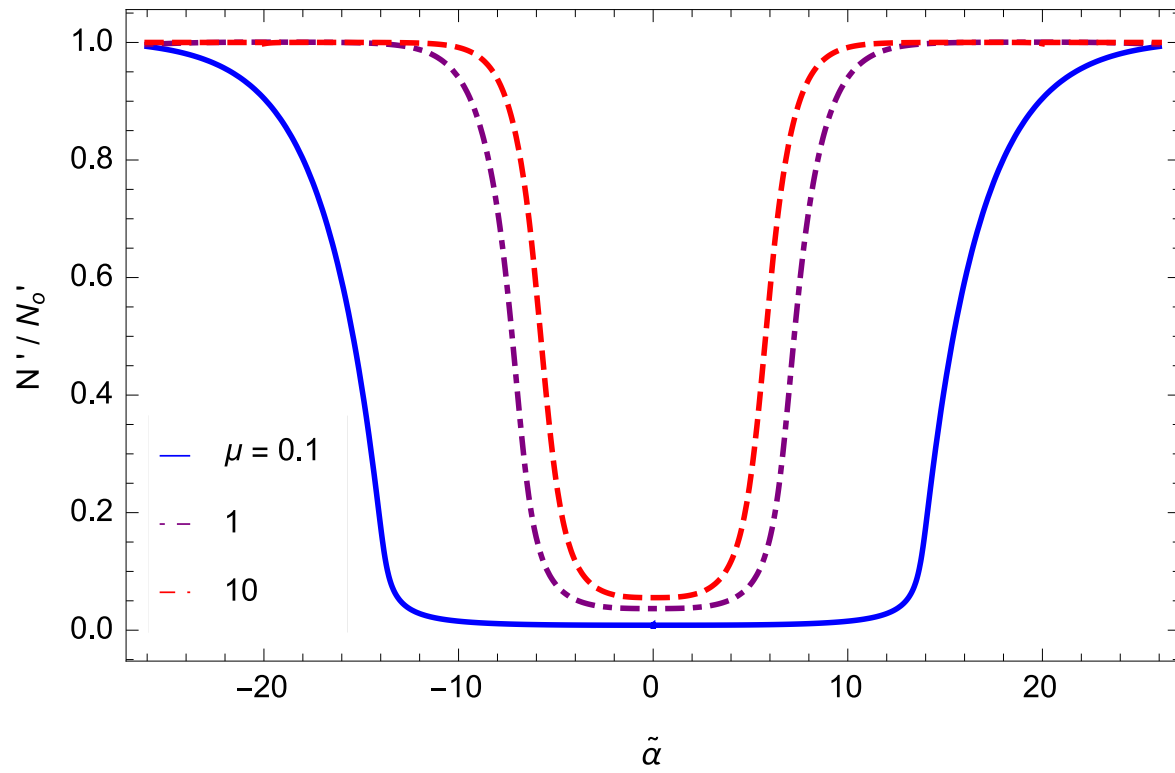


Figure 8.9: The normalized number density of photons for the same set of  $\mu$  chosen in Figure 8.7. This figure demonstrates, as we saw in Figure 8.5, that the density of photons tracks that of the scatterers.

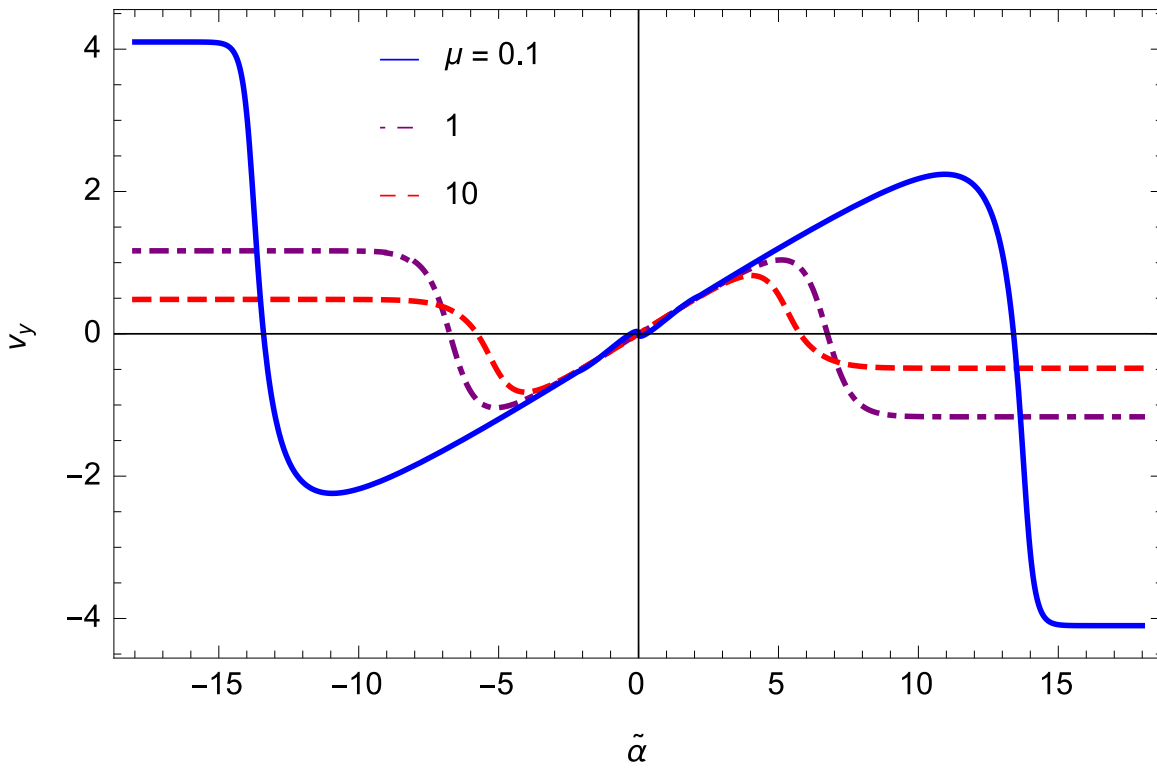


Figure 8.10: The  $y$ -component of the three-velocity, normalized by  $\sqrt{2/(9\rho'_0\kappa z_0)} \sim \delta$ , for the same set of  $\mu$  chosen in Figure 8.7. We see that the relative maximum increases for smaller  $\mu$ .

transsonic extends farther into the ambient medium, widening the boundary layer. Conversely, when  $\mu \gg 1$ , the sound speed approaches a constant  $\simeq 1/\sqrt{3}$ , which results in only a slight narrowing of the boundary layer.

Equation (8.10) shows that the energy density of the radiation, and hence the pressure, is constant across the jet, which is a statement of the causal connectedness of the boundary layer. In order for this equation to remain valid, then, we require that the transverse sound crossing time over the boundary layer thickness  $\delta y$  be less than the time it takes the fluid to traverse the distance  $\delta z$ . Since the transverse sound speed is given  $c_{\perp} = c_s/\Gamma$ , where  $c_s$  is given by equation (8.44), this requirement yields the inequality  $\delta \lesssim c_s/(\Gamma_j v_j)$ . Once this inequality is no longer satisfied, equation (8.10) does not hold, and we must include more terms in equations (8.10) – (8.11) to account for the gradients in the energy density of the radiation.

As we noted in Section 3, the density approaches zero as we near the axis of the jet. Physically, this effect arises from the fact that, for  $z \ll z_0$ , the Lorentz factor grows unbounded and the boundary layer thickness goes to zero. Therefore, the center of the jet originates along a curve of infinite shear and, consequently, infinite entropy. Since the specific entropy scales as  $s' \propto e'/(\rho')^{4/3}$  and  $e'$  is constant across the boundary layer, we see that the density of scatterers must equal zero at the center of the jet.

From Figures 8.6 and 8.10, we see that the  $y$ -component of the velocity initially causes the outflow to expand into its surroundings. When  $|\xi|$  becomes large, however, the directionality of  $v_y$  reverses toward the jet. The outflow therefore entrains material from the ambient medium not only by expanding in the transverse direction, but also by dragging material in from the environment.

Interestingly, the  $y$ -component of the velocity approaches a non-zero, constant value as we move into the external medium. This behavior arises from the fact that the jet is removing material from the system at a rate  $\dot{M} \sim \rho' \Gamma v_z dy \sim z^{1/2}$ , showing that amount of mass excavated from the envelope increases as we move along  $z$ . Therefore, in order to maintain a steady-state, we require a constant influx of material at infinity that can resupply the amount lost due to the jet. This interpretation is substantiated by integrating the continuity equation (8.13) from  $y = -\infty$  to

$y = \infty$ , which shows that the  $y$ -component of the velocity at infinity scales as  $v_{y,\infty} \sim -f_\infty/2$ . The factor of  $1/2$  arises from the fact that the mass loss rate scales as  $\dot{M} \sim \rho' \Gamma v_z dy \propto z^{1/2}$ ; therefore, if one could decrease the mass loss rate to one that was constant in  $z$ , then the  $y$ -component of the velocity would vanish at infinity. Likewise, if one could create a scenario in which  $\dot{M}$  scaled as a **negative** power of  $z$ , then the value of  $v_y$  would maintain an efflux of material at infinity to keep the system from amassing inertia towards the center of the jet (thus violating the steady-state assumption).

The free-streaming jet solutions analyzed in this paper are only valid when the Lorentz factor is relativistic, i.e., when  $\zeta > 1$ . When  $\zeta \ll 1$ ,  $\Gamma \simeq 1$ ,  $\rho' \simeq \rho'_0$ , and we can show that conservation of momentum along the  $z$ -axis results in the scaling  $v_j \sim z^{-1/3}$ ,  $\delta \sim z^{2/3}$ , which agrees with the results of the incompressible, non-relativistic theory (in Chapter 10, Section 12 of Kundu & Cohen 2008, see their discussion at the top of page 383). Therefore, once  $z \gtrsim \Gamma_j^4 z_0$ , the outflow will undergo a non-self-similar transition from the solution presented here to its non-relativistic counterpart.

The free-streaming jet model has observational consequences. For example, the decrease in the density along the jet axis means that observers looking down the barrel of the jet see farther into the outflow. Because  $\Gamma \propto z^{-1/4}$  and  $e = \Gamma^2 e'$ , where  $e$  is the lab-frame radiation energy density, this means that those observers see a higher energy density of photons. Also, those same observers, using the fact that the lab-frame radiation number density is  $N \sim \Gamma N'$ , see an energy per photon of  $e/N \sim \Gamma e'/N'$ . Therefore, not only do the on-axis observers see a more Lorentz-boosted spectrum because they can see deeper into the outflow, their spectrum is also hardened from the fact that  $N'$  is minimized along the axis of the jet (where  $y = 0$  in the figures of Section 3).

### 8.3.1 Comparative notes between the two-stream model (Chapter 7) and the free-streaming jet model

Chapter 7 analyzed how the presence of a radiation pressure-supported envelope affected the propagation of a radiation-dominated, relativistic jet through the two-stream approximation. This approximation treats the jet and its surroundings as semi-infinite, separate fluids, a contact

discontinuity serving as the surface of separation between the two. In contrast, the free-streaming jet solution presented here treats the entire system – the jet and its surroundings – as a single fluid. There is thus no formal distinction between “jet material” and “ambient material,” meaning that no contact discontinuity exists in the system.

By comparing Figure 1 of Chapter 7 and Figure 8.3 of the previous section, we see that the  $z$ -component of the four-velocity at a fixed  $z$  behaves similarly between the two models. Namely, the solution starts at some “jet” velocity, which corresponds to  $y = \infty$  in the two-stream model and to  $y = 0$  in the jet model, and smoothly transitions to a velocity of approximately zero over the extent of a few boundary layer thicknesses. However, the full spatial dependence of the velocity, one that includes variation in the  $z$ -direction, differs drastically between the two models: while the two-stream jet maintains a constant  $\Gamma_j$  along  $z$ , we found here that the  $z$ -component of the four-velocity scales as  $\Gamma v_z \propto z^{-1/4}$ , implying that the overall velocity of the jet slows as we look farther down  $z$ . This behavior arises from the fact that the free-streaming jet can entrain material, this entrainment causing an increase in the inertia contained in the outflow and a resultant decrease in its velocity.

The general behavior of the number densities of scatterers and photons between the models is also similar, which can be understood by comparing Figures 2 and 3 of Chapter 7 to Figures 8.4 and 8.5 of Section 3, respectively. In particular, both densities decrease within the boundary layer separating the outflow and its surroundings, asymptotically approaching their jet values as  $y \rightarrow \infty$  in the two-stream model and as  $y \rightarrow 0$  in the free-streaming jet model. Likewise, each approaches its ambient value as  $y \rightarrow -\infty$  in the two-stream model and as  $y \rightarrow \pm\infty$  in the free-streaming jet model. Although the gross properties of both are similar, one striking difference arises, however, in the behavior of the scatterer density: in the two-stream model, the existence of the contact discontinuity causes the function  $g$ , and hence the density  $\rho'$ , to vanish within the boundary layer (it vanishes specifically at  $y = 0$  – the location of the contact discontinuity). Conversely,  $\rho'$  remains non-zero throughout the boundary layer that connects the jet and its surroundings in the model presented here, and only as we near the center of the jet does the density of scatterers go to zero.

The presence of a contact discontinuity thus results in the likely non-physical vanishing of the massive particles within the boundary layer.

Finally, the scaling of the boundary layer thickness itself differs between the two models. In the two-stream case, we found that  $\delta \propto z^{1/2}$  (see equation (15) of Chapter 7). Therefore, as one looks farther down the  $z$ -axis, the boundary layer that develops between the jet and the ambient environment extends into both media at a rate proportional to  $z^{1/2}$ . Contrarily, equation (8.40) shows that the free-streaming jet boundary layer expands into its surroundings as  $\propto z^{3/4}$  (though this transitions to  $z^{2/3}$  in the non-relativistic limit; see the discussion at the top of page 383 in Chapter 10, Section 12 of Kundu & Cohen 2008). The free-streaming jet boundary layer thus expands more rapidly than does the two-stream solution.

#### 8.4 Summary and conclusions

Employing the equations of radiation hydrodynamics in the viscous limit, which are applicable as long as changes in fluid quantities are small over the mean free path of a photon, we analyzed the dynamics of a relativistic, free-streaming jet under the boundary layer approximation. This approximation, which should be upheld in jets with transverse optical depths substantially greater than one, states that variations in the properties of the outflow are confined to a thin layer of width  $\delta$ , and it allowed us to transform the full set of equations (8.1) – (8.5) into a set of greatly simplified boundary layer equations (8.10) – (8.13).

Perhaps the biggest difference between the two-stream solutions, presented and analyzed in paper I, and the free-streaming jet solutions presented here is in the distinction between the jet and the ambient medium. In the former, the two are considered as distinct, interacting entities, which allows one to specify separately their asymptotic properties. The latter approach, on the other hand, considers the whole configuration as a single fluid.

Because one has more freedom in specifying the properties of the outflow, the two-stream solution has the added benefit of being able to treat scenarios in which the properties of the jet and the ambient medium differ significantly. However, maintaining the distinction between the two

media necessitates the existence of a surface of contact between the two across which no fluid can flow, meaning that the jet cannot entrain ambient material. Furthermore, as was demonstrated in Chapter 7, this boundary condition results in the density formally vanishing at the interface, which is likely non-physical.

By treating the outflow and the environment as one fluid, we demonstrated that entrainment does occur in the radiation-viscous, free-streaming jet solution, which causes the  $z$ -component of the four-velocity of the jet to slow as  $\sim z^{-1/4}$  (this power-law, however, may differ if the adopted symmetry is azimuthal as opposed to planar; see below). These solutions also show that the comoving densities of scatterers and photons decrease dramatically within the boundary layer, with the density of scatterers approaching zero as one nears the center of the jet. Therefore, because observers that look “down the barrel of the jet” can see farther into the outflow, they see a more Lorentz-boosted energy density than those that view the outflow off-axis. They also observe a higher energy per photon, given by  $e/N \simeq e'\Gamma_o/N'$ , both because  $N'$  is minimized along the axis and because  $\Gamma_o$ , the observed Lorentz factor, is larger. Such features are in qualitative agreement with the event **Swift** J1644+57, where such an observer orientation is invoked to explain the X-ray emission (Zauderer et al., 2011).

In addition to super-Eddington TDEs and long GRBs (as well as the relatively new class of “ultra-long” GRBs; Levan et al. 2014) – the two applications considered in the Introduction – the free-streaming jet model could be applied to other sources. As mentioned in Chapter 7, this model may also be relevant to microquasars (Fender et al., 2004) (particularly those that fall in the class of ULX’s; King et al. 2001) such as the object SS 433 (Fabrika 2004; Begelman et al. 2006a; see Arav & Begelman (1993) for an application of the two-stream model to this source). Additionally, a jetted quasi-star – a protogalactic gas cloud supported by a supercritically accreting black hole (Begelman et al., 2006a, 2008; Czerny et al., 2012) – provides another situation in which a radiation-dominated jet propagates alongside a radiation pressure-supported envelope.

The free-streaming jet solution presented here is limited to describing plane-parallel, two-dimensional systems. One consequence of this assumption is that the entrainment of material,

which slows down the jet as  $\Gamma \propto z^{-1/4}$ , happens effectively in one dimension. If, on the other hand, one imposed azimuthal symmetry and described the system in terms of spherical coordinates  $(r, \theta, \phi)$ , which is likely more relevant for realistic jetted systems, the entrainment would occur in two dimensions. Other conditions being equal, the slowing of the jet along the axis would then be more pronounced, i.e., the Lorentz factor would scale as  $\Gamma \propto r^{-p}$  with  $p > 1/4$ .

The other main assumption of the free-streaming jet model presented here is that the energy density of the ambient medium is independent of  $z$ , i.e.,  $e'(z) = e'_0$ . If a pressure gradient were present, this force would tend to accelerate (or, in principle, decelerate) the jet material, offsetting the power-law scaling  $\Gamma \propto z^{-1/4}$ . In fact, one can imagine that if the pressure gradient were strong enough, it could indeed reverse the overall slowing of the jet and cause the outflow to accelerate. If the energy density scaled as  $e' = e'_0(z/z_0)^{-q}$ , which is relevant for super-Eddington TDEs as long as the constant  $q$  satisfies  $q > 3/2$  (Chapter 5), this situation could be actualized near the launch point of the jet.

In an ensuing paper, we plan to compare more quantitatively the predictions made by the free-streaming jet model presented here and the observations of **Swift** J1644+57. We will also extend our analysis to incorporate a spherical geometry – as azimuthal symmetry is almost certainly more relevant for this and other systems than the planar symmetry adopted here – as well as radially-dependent ambient pressure and density profiles.

## Chapter 9

### Conclusions

Tidal disruption events provide information about the properties of the supermassive black holes residing in the centers of galaxies, thereby constraining our models of galaxy growth and the evolution of the Universe. However, our ability to correctly interpret that information hinges on our understanding of the tidal disruption process. This thesis has hopefully conveyed to the reader that this process is incredibly intricate and encompasses a wealth of distinct, physical processes, including the formation of gas streams, the creation of accretion disks, and the launching of relativistic jets.

Sections 2 – 4 analyzed the formation and evolution of tidally-disrupted debris streams, using a combination of analytical and numerical techniques. We showed that, once the stream recedes to large distances from the black hole, the self-gravity of the stream in the radial direction can result in its fragmentation into small-scale, gravitationally bound clumps. The time at which the stream fragments and the properties of the clumps (e.g., their masses and radii) depend on the thermodynamics of the gas, and we performed a suite of simulations to delineate that dependence. Finally, we constructed an analytic model to describe these debris streams, showing that there is a simple, self-similar function that characterizes the velocity profile of these streams and agrees very well with our simulations. We also provided approximate expressions for the density distributions of tidally-disrupted debris streams, and we showed that the effective adiabatic index of the gas must be  $\gamma \geq 5/3$  if the stream is to be gravitationally unstable.

Section 5 presented a new model for the accretion disks that form during the super-Eddington

phase of tidal disruption events. This model assumes that the radiation liberated during the accretion process is trapped by the inflowing material, increasing the specific energy, or Bernoulli parameter, of the accretion disk. Once the Bernoulli parameter approaches zero, the material is only marginally-bound to the black hole, and any further augmentation of the specific energy would effectively unbind the disk. Therefore, once this zero-Bernoulli stage is reached, we postulate that the remaining accretion energy is funneled into two, bipolar jets that remove the accretion energy from the system without destroying the debris disk, the resulting configuration being a zero-Bernoulli accretion (ZEBRA) disk. We showed that the characteristics of the progenitor star and the supermassive black hole completely determine the properties of the resulting ZEBRA flow, and the high pressure and sub-Keplerian angular momentum of the material cause these disks to be “puffed up” into quasi-spherical envelopes with narrow, centrifugally-supported funnels that self-consistently provide exhaust routes for the jets. We made comparisons between the ZEBRA model and the jetted tidal disruption event **Swift** J1644+57, and, based on simple timing arguments, demonstrated that the black hole powering **Swift** J1644+57 must have a mass of  $\sim 10^5 M_\odot$  (assuming the ZEBRA model correctly describes the accretion process).

Sections 6 – 8 investigated the nature of the relativistic jets launched from tidal disruption events. These outflows are unique in that radiation can contribute overwhelmingly to their energy and momentum, and it is thus the photons present in the jet that mediate the interaction between the jet and the ZEBRA envelope. We developed the precise way by which this interaction takes place when the photon mean free path is small, showing from the general relativistic Boltzmann equation that small anisotropies in the comoving radiation field generate an effective viscosity that transfers energy and momentum from the jet to its surroundings (and vice versa). We derived the equations describing this viscous interaction – the general relativistic equations of radiation hydrodynamics in the viscous limit – and applied them to a boundary layer model of the jets produced from tidal disruption events. The boundary layer assumption states that the transition from the jet to the surrounding medium is confined to a thin transition region, which we showed is on the order of the square root of the photon mean free path. These boundary layer models showed

that in the transition from the jet to the surrounding ZEBRA, where the shear is maximized, the number of scatterers decreases dramatically and the photon spectrum hardens. Thus, the angle between the jet axis and the observer angle has important consequences for the inferred properties of the outflow.

## Bibliography

- Abramowicz, M., Jaroszynski, M., & Sikora, M. 1978, *A&A*, 63, 221
- Abramowicz, M. A., Czerny, B., Lasota, J. P., & Szuszkiewicz, E. 1988, *ApJ*, 332, 646
- Abramowicz, M. A., & Fragile, P. C. 2013, *Living Reviews in Relativity*, 16, arXiv:1104.5499
- Arav, N., & Begelman, M. C. 1992, *ApJ*, 401, 125
- . 1993, *ApJ*, 413, 700
- Bade, N., Komossa, S., & Dahlem, M. 1996, *A&A*, 309, L35
- Balbus, S. A., & Hawley, J. F. 1991, *ApJ*, 376, 214
- . 1992, *ApJ*, 400, 610
- Bardeen, J. M., Press, W. H., & Teukolsky, S. A. 1972, *ApJ*, 178, 347
- Barnes, J., & Hut, P. 1986, *Nature*, 324, 446
- Bate, M. R., & Burkert, A. 1997, *MNRAS*, 288, 1060
- Begelman, M. C. 1978, *MNRAS*, 184, 53
- Begelman, M. C., Blandford, R. D., & Rees, M. J. 1984, *Reviews of Modern Physics*, 56, 255
- Begelman, M. C., King, A. R., & Pringle, J. E. 2006a, *MNRAS*, 370, 399
- Begelman, M. C., Rossi, E. M., & Armitage, P. J. 2008, *MNRAS*, 387, 1649
- Begelman, M. C., Volonteri, M., & Rees, M. J. 2006b, *MNRAS*, 370, 289
- Bersier, D., Rhoads, J., Fruchter, A., et al. 2004, *GRB Coordinates Network*, 2544
- Bicknell, G. V., & Gingold, R. A. 1983, *ApJ*, 273, 749
- Blandford, R. D., & Begelman, M. C. 1999, *MNRAS*, 303, L1
- . 2004, *MNRAS*, 349, 68
- Blandford, R. D., Jaroszynski, M., & Kumar, S. 1985, *MNRAS*, 215, 667
- Blandford, R. D., & Payne, D. G. 1982, *MNRAS*, 199, 883

- Blandford, R. D., & Znajek, R. L. 1977, MNRAS, 179, 433
- Blasius, H. 1908, in Tech. Memoranda National Advisory Committee for Aeronautics (English trans.), 1256
- Bloom, J. S., Giannios, D., Metzger, B. D., et al. 2011, Science, 333, 203
- Bogdanović, T., Cheng, R. M., & Amaro-Seoane, P. 2014, ApJ, 788, 99
- Bonnerot, C., Rossi, E. M., & Lodato, G. 2015, ArXiv e-prints, arXiv:1511.00300
- Bonnerot, C., Rossi, E. M., Lodato, G., & Price, D. J. 2016, MNRAS, 455, 2253
- Brockamp, M., Baumgardt, H., & Kroupa, P. 2011, MNRAS, 418, 1308
- Bromberg, O., & Levinson, A. 2007, ApJ, 671, 678
- Brown, G. C., Levan, A. J., Stanway, E. R., et al. 2015, MNRAS, 452, 4297
- Buchler, J. R. 1979, J. Quant. Spec. Radiat. Transf., 22, 293
- Burkert, A., Scharmann, M., Alig, C., et al. 2012, ApJ, 750, 58
- Burrows, D. N., Kennea, J. A., Ghisellini, G., et al. 2011, Nature, 476, 421
- Caderni, N., & Fabbri, R. 1977, Physics Letters B, 69, 508
- Cannizzo, J. K. 1992, ApJ, 385, 94
- Cannizzo, J. K., Lee, H. M., & Goodman, J. 1990, ApJ, 351, 38
- Cannizzo, J. K., Troja, E., & Lodato, G. 2011, ApJ, 742, 32
- Carter, B., & Luminet, J. P. 1982, Nature, 296, 211
- Carter, B., & Luminet, J.-P. 1983, A&A, 121, 97
- Castor, J. I. 1972, ApJ, 178, 779
- Cenko, S. B., Krimm, H. A., Horesh, A., et al. 2012, ApJ, 753, 77
- Chen, X., Gómez-Vargas, G., & Guillochon, J. 2015, ArXiv e-prints, arXiv:1512.06124
- Chen, X., Madau, P., Sesana, A., & Liu, F. K. 2009, ApJ, 697, L149
- Chen, X., & Spiegel, E. A. 2000, ApJ, 540, 1069
- Coles, P., & Lucchin, F. 1995, Cosmology. The origin and evolution of cosmic structure
- Coughlin, E. R., & Begelman, M. C. 2015, ApJ, 809, 2
- Czerny, B., Janiuk, A., Sikora, M., & Lasota, J.-P. 2012, ApJ, 755, L15
- Dado, S., Dar, A., & De Rújula, A. 2008, ApJ, 680, 517
- Debbasch, F., & van Leeuwen, W. A. 2009a, Physica A Statistical Mechanics and its Applications, 388, 1079

- . 2009b, *Physica A Statistical Mechanics and its Applications*, 388, 1818
- Donley, J. L., Brandt, W. N., Eracleous, M., & Boller, T. 2002, *AJ*, 124, 1308
- Eckart, C. 1940, *Physical Review*, 58, 919
- Eggum, G. E., Coroniti, F. V., & Katz, J. I. 1988, *ApJ*, 330, 142
- Evans, C. R., & Kochanek, C. S. 1989, *ApJ*, 346, L13
- Faber, J. A., Rasio, F. A., & Willems, B. 2005, *Icarus*, 175, 248
- Fabrika, S. 2004, *Astrophysics and Space Physics Reviews*, 12, 1
- Fender, R. P., Belloni, T. M., & Gallo, E. 2004, *MNRAS*, 355, 1105
- Fender, R. P., Homan, J., & Belloni, T. M. 2009, *MNRAS*, 396, 1370
- Ferrarese, L., & Merritt, D. 2000, *ApJ*, 539, L9
- Frail, D. A., Kulkarni, S. R., Sari, R., et al. 2001, *ApJ*, 562, L55
- Frank, J. 1978, *MNRAS*, 184, 87
- Frank, J., & Rees, M. J. 1976, *MNRAS*, 176, 633
- Fruchter, A. S., Thorsett, S. E., Metzger, M. R., et al. 1999, *ApJ*, 519, L13
- Fynbo, J. P. U., Watson, D., Thöne, C. C., et al. 2006, *Nature*, 444, 1047
- Gafton, E., & Rosswog, S. 2011, *MNRAS*, 418, 770
- Galama, T. J., Vreeswijk, P. M., van Paradijs, J., et al. 1998, *Nature*, 395, 670
- Gebhardt, K., Bender, R., Bower, G., et al. 2000, *ApJ*, 539, L13
- Gezari, S., Basa, S., Martin, D. C., et al. 2008, *ApJ*, 676, 944
- Gezari, S., Chornock, R., Rest, A., et al. 2012, *Nature*, 485, 217
- Giannios, D., & Metzger, B. D. 2011, *MNRAS*, 416, 2102
- Gillessen, S., Genzel, R., Fritz, T. K., et al. 2012, *Nature*, 481, 51
- Goldreich, P., & Schubert, G. 1967, *ApJ*, 150, 571
- Guillochon, J., Loeb, A., MacLeod, M., & Ramirez-Ruiz, E. 2014a, *ApJ*, 786, L12
- Guillochon, J., Manukian, H., & Ramirez-Ruiz, E. 2014b, *ApJ*, 783, 23
- Guillochon, J., McCourt, M., Chen, X., Johnson, M. D., & Berger, E. 2015, *ArXiv e-prints*, arXiv:1509.08916
- Guillochon, J., & Ramirez-Ruiz, E. 2013, *ApJ*, 767, 25
- Guillochon, J., Ramirez-Ruiz, E., Rosswog, S., & Kasen, D. 2009, *ApJ*, 705, 844

- Halpern, J. P., Gezari, S., & Komossa, S. 2004, *ApJ*, 604, 572
- Hansen, C. J., Kawaler, S. D., & Trimble, V. 2004, *Stellar interiors : physical principles, structure, and evolution*
- Harrison, E. R. 1977, *Vistas in Astronomy*, 20, 341
- Hayasaki, K., Stone, N., & Loeb, A. 2013, *MNRAS*, 434, 909
- Hayasaki, K., Stone, N. C., & Loeb, A. 2015, *ArXiv e-prints*, arXiv:1501.05207
- Hills, J. G. 1988, *Nature*, 331, 687
- Hiscock, W. A., & Lindblom, L. 1985, *Phys. Rev. D*, 31, 725
- Hsieh, S.-H., & Spiegel, E. A. 1976, *ApJ*, 207, 244
- Hu, W., & Dodelson, S. 2002, *ARA&A*, 40, 171
- Hubber, D. A., Goodwin, S. P., & Whitworth, A. P. 2006, *A&A*, 450, 881
- Ivanov, P. B., & Novikov, I. D. 2001, *ApJ*, 549, 467
- Ivezic, Z., Tyson, J. A., Abel, B., et al. 2008, *ArXiv e-prints*, arXiv:0805.2366
- Jaroszynski, M., Abramowicz, M. A., & Paczynski, B. 1980, *Acta Astron.*, 30, 1
- Jiang, Y.-F., Stone, J. M., & Davis, S. W. 2014, *ApJ*, 796, 106
- Johri, V. B., & Sudharsan, R. 1988, *Physics Letters A*, 132, 316
- Kamble, A., Misra, K., Bhattacharya, D., & Sagar, R. 2009, *MNRAS*, 394, 214
- Kasen, D., & Ramirez-Ruiz, E. 2010, *ApJ*, 714, 155
- Kelley, L. Z., Tchekhovskoy, A., & Narayan, R. 2014, *MNRAS*, 445, 3919
- Khatri, R., Sunyaev, R. A., & Chluba, J. 2012, *A&A*, 543, A136
- Kim, S. S., Park, M.-G., & Lee, H. M. 1999, *ApJ*, 519, 647
- King, A. R., Davies, M. B., Ward, M. J., Fabbiano, G., & Elvis, M. 2001, *ApJ*, 552, L109
- Knierman, K., Knezek, P. M., Scowen, P., Jansen, R. A., & Wehner, E. 2012, *ApJ*, 749, L1
- Kochanek, C. S. 1994, *ApJ*, 422, 508
- Kohler, S., & Begelman, M. C. 2012, *MNRAS*, 426, 595
- . 2015, *MNRAS*, 446, 1195
- Kohler, S., Begelman, M. C., & Beckwith, K. 2012, *MNRAS*, 422, 2282
- Komissarov, S. S. 2006, *MNRAS*, 368, 993
- Komossa, S. 2015, *Journal of High Energy Astrophysics*, 7, 148

- Komossa, S., & Greiner, J. 1999, *A&A*, 349, L45
- Komossa, S., Halpern, J., Schartel, N., et al. 2004, *ApJ*, 603, L17
- Kozłowski, M., Jaroszynski, M., & Abramowicz, M. A. 1978, *A&A*, 63, 209
- Krawczynski, H., & Treister, E. 2013, *Frontiers of Physics*, 8, 609
- Kundu, P. K., & Cohen, I. M. 2008, *Fluid Mechanics: Fourth Edition* (Academic Press)
- Lacy, J. H., Townes, C. H., & Hollenbach, D. J. 1982, *ApJ*, 262, 120
- Landau, L. D., & Lifshitz, E. M. 1959, *Fluid mechanics*
- Lazzati, D., Morsony, B. J., & Begelman, M. C. 2007, *Philosophical Transactions of the Royal Society of London Series A*, 365, 1141
- Lee, W. H., & Ramirez-Ruiz, E. 2007, *New Journal of Physics*, 9, 17
- Levan, A. J., Tanvir, N. R., Cenko, S. B., et al. 2011, *Science*, 333, 199
- Levan, A. J., Tanvir, N. R., Starling, R. L. C., et al. 2014, *ApJ*, 781, 13
- Levermore, C. D. 1984, *J. Quant. Spec. Radiat. Transf.*, 31, 149
- Levermore, C. D., & Pomraning, G. C. 1981, *ApJ*, 248, 321
- Li, L.-X., Narayan, R., & Menou, K. 2002, *ApJ*, 576, 753
- Lima, J. A. S., & Waga, I. 1990, *Physics Letters A*, 144, 432
- Lindquist, R. W. 1966, *Annals of Physics*, 37, 487
- Lodato, G., King, A. R., & Pringle, J. E. 2009, *MNRAS*, 392, 332
- Lodato, G., & Price, D. J. 2010, *MNRAS*, 405, 1212
- Lodato, G., & Rossi, E. M. 2011, *MNRAS*, 410, 359
- Loeb, A., & Laor, A. 1992, *ApJ*, 384, 115
- Loeb, A., & Ulmer, A. 1997, *ApJ*, 489, 573
- López-Cámara, D., Morsony, B. J., Begelman, M. C., & Lazzati, D. 2013, *ApJ*, 767, 19
- MacFadyen, A. I., & Woosley, S. E. 1999, *ApJ*, 524, 262
- MacLeod, M., Guillochon, J., & Ramirez-Ruiz, E. 2012, *ApJ*, 757, 134
- Magorrian, J., Tremaine, S., Richstone, D., et al. 1998, *AJ*, 115, 2285
- Maiolino, R., & Rieke, G. H. 1995, *ApJ*, 454, 95
- Margon, B., & Anderson, S. F. 1989, *ApJ*, 347, 448
- Markoff, S., Nowak, M. A., & Wilms, J. 2005, *ApJ*, 635, 1203

- Markwardt, C. B., Marshall, F. E., Smith, E. A., Strohmayer, T. S., & Swank, J. H. 2011, *The Astronomer's Telegram*, 3251
- Martin, R. G., Nixon, C., Armitage, P. J., Lubow, S. H., & Price, D. J. 2014a, *ApJ*, 790, L34
- Martin, R. G., Nixon, C., Lubow, S. H., et al. 2014b, *ApJ*, 792, L33
- Matzner, C. D. 2003, *MNRAS*, 345, 575
- McKinney, J. C., Tchekhovskoy, A., Sadowski, A., & Narayan, R. 2014, *MNRAS*, 441, 3177
- Meszáros, P., & Rees, M. J. 1993, *ApJ*, 405, 278
- Metzger, B. D., Giannios, D., & Mimica, P. 2012, *MNRAS*, 420, 3528
- Mihalas, D., & Mihalas, B. W. 1984, *Foundations of radiation hydrodynamics*
- Miller, J. M., Kaastra, J. S., Miller, M. C., et al. 2015, *Nature*, 526, 542
- Milosavljević, M., Merritt, D., & Ho, L. C. 2006, *ApJ*, 652, 120
- Mirabel, I. F., & Rodríguez, L. F. 1999, *ARA&A*, 37, 409
- Misner, C. W., & Sharp, D. H. 1965, *Physics Letters*, 15, 279
- Morsony, B. J., Lazzati, D., & Begelman, M. C. 2007, *ApJ*, 665, 569
- Mundell, C. G., Kopač, D., Arnold, D. M., et al. 2013, *Nature*, 504, 119
- Munier, A. 1986, *Phys. Rev. D*, 33, 2111
- Narayan, R., & Yi, I. 1994, *ApJ*, 428, L13
- Nealon, R., Price, D. J., & Nixon, C. J. 2015, *MNRAS*, 448, 1526
- Nixon, C., King, A., Price, D., & Frank, J. 2012a, *ApJ*, 757, L24
- Nixon, C. J., King, A. R., & Price, D. J. 2012b, *MNRAS*, 422, 2547
- Ohsuga, K. 2007, *PASJ*, 59, 1033
- Ohsuga, K., Mineshige, S., Mori, M., & Kato, Y. 2009, *PASJ*, 61, L7
- Ohsuga, K., Mori, M., Nakamoto, T., & Mineshige, S. 2005, *ApJ*, 628, 368
- Okuda, T. 2002, *PASJ*, 54, 253
- Okuda, T., Teresi, V., Toscano, E., & Molteni, D. 2005, *MNRAS*, 357, 295
- Paczynski, B., & Abramowicz, M. A. 1982, *ApJ*, 253, 897
- Paczyński, B., & Wiita, P. J. 1980, *A&A*, 88, 23
- Panaitescu, A. 2007, *MNRAS*, 380, 374
- Phinney, E. S. 1989, in *IAU Symposium*, Vol. 136, *The Center of the Galaxy*, ed. M. Morris, 543

- Piran, T. 2004, *Reviews of Modern Physics*, 76, 1143
- Piran, T., Svirski, G., Krolik, J., Cheng, R. M., & Shiokawa, H. 2015, *ApJ*, 806, 164
- Piro, L., Massaro, E., Perola, G. C., & Molteni, D. 1988, *ApJ*, 325, L25
- Price, D. J., & Federrath, C. 2010, *MNRAS*, 406, 1659
- Price, D. J., & Monaghan, J. J. 2007, *MNRAS*, 374, 1347
- Pugliese, D., Montani, G., & Bernardini, M. G. 2013, *MNRAS*, 428, 952
- Qian, L., Abramowicz, M. A., Fragile, P. C., et al. 2009, *A&A*, 498, 471
- Racusin, J. L., Liang, E. W., Burrows, D. N., et al. 2009, *ApJ*, 698, 43
- Rees, M. J. 1988, *Nature*, 333, 523
- Rees, M. J., & Meszaros, P. 1992, *MNRAS*, 258, 41P
- Reipurth, B., & Bally, J. 2001, *ARA&A*, 39, 403
- Saxton, C. J., Soria, R., Wu, K., & Kuin, N. P. M. 2012, *MNRAS*, 422, 1625
- Sądowski, A., Narayan, R., McKinney, J. C., & Tchekhovskoy, A. 2014, *MNRAS*, 439, 503
- Sądowski, A., Narayan, R., Tchekhovskoy, A., & Zhu, Y. 2013, *MNRAS*, 429, 3533
- Seguin, F. H. 1975, *ApJ*, 197, 745
- Shakura, N. I., & Sunyaev, R. A. 1973, *A&A*, 24, 337
- Shen, R.-F., & Matzner, C. D. 2014, *ApJ*, 784, 87
- Shiokawa, H., Krolik, J. H., Cheng, R. M., Piran, T., & Noble, S. C. 2015, *ApJ*, 804, 85
- Sikora, M. 1981, *MNRAS*, 196, 257
- Stone, J. M., & Norman, M. L. 1994, *ApJ*, 433, 746
- Stone, N., & Loeb, A. 2012, *Physical Review Letters*, 108, 061302
- Stone, N., Sari, R., & Loeb, A. 2013, *MNRAS*, 435, 1809
- Stone, N. C., & Metzger, B. D. 2014, *ArXiv e-prints*, arXiv:1410.7772
- Strubbe, L. E., & Quataert, E. 2009, *MNRAS*, 400, 2070
- . 2011, *MNRAS*, 415, 168
- Tauber, G. E. 1978, *Ap&SS*, 57, 163
- Tchekhovskoy, A., Metzger, B. D., Giannios, D., & Kelley, L. Z. 2014, *MNRAS*, 437, 2744
- Tejeda, E., & Rosswog, S. 2013, *MNRAS*, 433, 1930
- Thomas, L. H. 1930, *The Quarterly Journal of Mathematics*, 1, 239

- Truelove, J. K., Klein, R. I., McKee, C. F., et al. 1997, *ApJ*, 489, L179
- Turner, N. J., Stone, J. M., Krolik, J. H., & Sano, T. 2003, *ApJ*, 593, 992
- Ulmer, A. 1999, *ApJ*, 514, 180
- Walker, M. A. 1990, *ApJ*, 348, 668
- Warren, S. J., & Hewett, P. C. 1990, *Reports on Progress in Physics*, 53, 1095
- Waxman, E., Kulkarni, S. R., & Frail, D. A. 1998, *ApJ*, 497, 288
- Weinberg, S. 1971, *ApJ*, 168, 175
- Woosley, S. E. 1993, *ApJ*, 405, 273
- Woosley, S. E., & Bloom, J. S. 2006, *ARA&A*, 44, 507
- Zauderer, B. A., Berger, E., Margutti, R., et al. 2013, *ApJ*, 767, 152
- Zauderer, B. A., Berger, E., Soderberg, A. M., et al. 2011, *Nature*, 476, 425

## Appendix A

### Non-self-similar ZEBRA solutions

Blandford & Begelman (2004) demonstrated that, if the angular momentum is distributed in a quasi-Keplerian fashion, i.e.  $\ell^2 \propto GMr \sin^2 \theta$ , then there exist self-similar solutions for the pressure and the density throughout the disk. Here we wish to demonstrate that the converse of this statement, namely “If the pressure and density fall off in a self-similar manner, then the angular momentum is quasi-Keplerian,” is also true. In the process we will find the general solution for the density, pressure, and angular momentum distributions of ZEBRA flows in a Keplerian potential.

As a reminder, the momentum and Bernoulli equations governing the ZEBRA flow are

$$\frac{1}{\rho} \frac{\partial p}{\partial r} = -\frac{GM_h}{r^2} + \frac{\ell^2 \csc^2 \theta}{r^3}, \quad (\text{A.1})$$

$$\frac{1}{\rho} \frac{\partial p}{\partial \theta} = \frac{\ell^2 \csc^2 \theta \cot \theta}{r^2}, \quad (\text{A.2})$$

$$-\frac{GM_h}{r} + \frac{\ell^2 \csc^2 \theta}{2r^2} + \frac{\gamma}{\gamma - 1} \frac{p}{\rho} = 0. \quad (\text{A.3})$$

Now make the following auxiliary definitions:

$$\frac{\ell^2 \csc^2 \theta}{r^2} = \frac{GM_h}{r} f(r, \theta), \quad (\text{A.4})$$

$$p(r, \theta) = \frac{GM_h}{r} h(r, \theta). \quad (\text{A.5})$$

Inserting these definitions into (A.1), (A.2), and (A.3), we find the following differential equation for  $h$ :

$$\frac{1}{\gamma-1}h(r, \theta) + r\frac{\partial h}{\partial r} = \frac{1}{2}\frac{\partial h}{\partial \theta}. \quad (\text{A.6})$$

The solution to this partial differential equation may be found most simply by separating variables. Doing so, we obtain

$$h(r, \theta) = r^{-\frac{1}{\gamma-1}} \int_0^\infty c(\lambda)(r \sin^2 \theta)^\lambda d\lambda. \quad (\text{A.7})$$

Here  $\lambda$  is the arbitrary constant obtained from the separation of variables technique, and  $c(\lambda)$  is the constant of integration which is, in general, a function of  $\lambda$ . The total solution, capable of being matched to arbitrary boundary conditions, is then a sum of the eigensolutions appropriate to a single  $\lambda$  (if  $\lambda$  takes on a discrete set of values, the integral becomes a sum and  $c(\lambda) \rightarrow c_\lambda$ ). The range of  $\lambda$  has been chosen in hindsight to be consistent with the restriction that the square of the angular momentum and the density both be positive.

Using (A.7), we can readily determine expressions for the density, pressure, and angular momentum, which we find to be

$$\rho(r, \theta) = r^{-\frac{1}{\gamma-1}} \int_0^\infty \left(\lambda + \frac{\gamma}{\gamma-1}\right)c(\lambda)(r \sin^2 \theta)^\lambda d\lambda, \quad (\text{A.8})$$

$$p(r, \theta) = GM_h r^{-\frac{\gamma}{\gamma-1}} \int_0^\infty c(\lambda)(r \sin^2 \theta)^\lambda d\lambda, \quad (\text{A.9})$$

$$\ell^2(r, \theta) = 2GM_h r \sin^2 \theta \frac{\int_0^\infty \lambda c(\lambda)(r \sin^2 \theta)^\lambda d\lambda}{\int_0^\infty \left(\lambda + \frac{\gamma}{\gamma-1}\right)c(\lambda)(r \sin^2 \theta)^\lambda d\lambda}. \quad (\text{A.10})$$

We are now in a position to prove the statement at the beginning of this appendix: if we require the density or pressure to vary self-similarly, then  $c(\lambda) = c'\delta(\lambda - \lambda')$ , where  $c'$  is a constant independent

of  $\lambda$  and  $\delta(x)$  is the Dirac delta function. Inserting this relation for  $c(\lambda)$  into (A.10), we find

$$\ell^2(r, \theta) = \frac{2\lambda}{\lambda + \frac{\gamma}{\gamma-1}} GM_h r \sin^2 \theta, \quad (\text{A.11})$$

which agrees with the result in section 2.2 if we let  $\lambda = n - 3/2 + 1/(\gamma - 1)$ . The angular momentum distribution of a self-similar flow is therefore quasi-Keplerian. Furthermore, even if  $c(\lambda)$  is not a delta function, the functional dependence of the angular momentum is the Keplerian solution multiplied by a ratio of integrals, with each of those integrals having the same leading power of  $r$ . For this reason the dominant behavior of the angular momentum will always be Keplerian.

## Appendix B

### Non-zero Bernoulli parameter

One of the tenets upon which much of our previous analysis rests is that the Bernoulli parameter is exactly zero. Here we would like to investigate the consequences of letting  $B$  become negative, meaning that the disk is more than marginally bound; this situation may occur if the jet turns on before enough energy is pumped into the debris disk. We will also examine the case where  $B > 0$ , and we will show that this regime is associated with a wind.

Assuming that we can still regard  $B$  as roughly constant, then  $\nabla B = 0$ , and the gyrotropic nature of the flow in the disk is preserved (see Section 2). The fluid and Bernoulli equations are now

$$\frac{1}{\rho} \frac{\partial p}{\partial r} = -\frac{GM_h}{r^2} + \frac{\ell^2 \csc^2 \theta}{r^3}, \quad (\text{B.1})$$

$$\frac{1}{\rho} \frac{\partial p}{\partial \theta} = \frac{\ell^2 \cot \theta \csc^2 \theta}{r^2}, \quad (\text{B.2})$$

$$-\frac{GM_h}{r} + \frac{\ell^2 \csc^2 \theta}{2r^2} + \frac{\gamma}{\gamma - 1} \frac{p}{\rho} = B, \quad (\text{B.3})$$

where we have written the Bernoulli parameter as  $B$ , with  $B$  a negative number. We can generalize our analysis in the previous appendix to include non-zero  $B$ . The resultant self-similar solutions

for the angular momentum, density, and pressure are

$$\ell^2 = a \left( \frac{GM_h}{r} + B \right) r^2 \sin^2 \theta, \quad (\text{B.4})$$

$$\rho = \rho_0 \left( \frac{\frac{GM_h}{r} + B}{\frac{GM_h}{r_0} + B} \right)^{\alpha + \frac{1}{\gamma-1}} \left( \frac{r^2}{r_0^2} \right)^\alpha (\sin^2 \theta)^\alpha, \quad (\text{B.5})$$

$$p = \beta \rho_0 \left( \frac{GM_h}{r} + B \right) \left( \frac{\frac{GM_h}{r} + B}{\frac{GM_h}{r_0} + B} \right)^{\alpha + \frac{1}{\gamma-1}} \left( \frac{r^2}{r_0^2} \right)^\alpha (\sin^2 \theta)^\alpha. \quad (\text{B.6})$$

Here our notation is consistent with that in section 2, i.e.  $a$ ,  $\alpha$ ,  $n$ , and  $\beta$  retain their original definitions. We see that a disk with finite binding energy differs in its radial structure from that considered previously only in regions where  $GM_h/r \sim |B|$ , with the angular dependence completely unaltered. Therefore, our analysis in sections 2-4 concerning the properties of the disk is largely incorrect only if  $GM_h/|B| < R$ .

To determine when and if this inequality is satisfied, let us assume that the inverse is true, i.e.  $R < GM_h/|B|$ , so that the results from the preceding sections are almost correct. Then we can approximate the outer radius by the expression in section 3. We then find, in order for our neglect of the Bernoulli parameter to be permissible, that  $B$  must satisfy

$$|B| < \frac{GM_h}{\left( \frac{\kappa y}{4\pi c} \mathcal{M} \sqrt{GM_h} \beta \sqrt{a} (3-q) \right)^{2/5}}. \quad (\text{B.7})$$

For our current models, the right-hand side of (B.7) takes on values that are on the order of  $\approx 10^{17}$ . To see if this number is consistent with our neglect of finite binding energy, we can further specify the Bernoulli parameter by recalling the gravitational potential energy of the disk and its relation to the star, which implies  $B = -\delta(GM_*/R_*)(M_h/M_*)^{1/3}$ , where  $\delta$  is a numerical factor. Inserting numbers into (B.7), we find that our assumptions in sections 2-4 are correct if  $\delta \lesssim 1$ . As we have argued, the shock heating and energy generation in the inner regions of the disk are thought to raise the Bernoulli parameter, so that  $\delta \lesssim 1$  should be satisfied in nearly all cases. However, for larger

black hole masses or larger progenitors, the binding energy, and hence the Bernoulli parameter, will increase, and the assumption of  $B \approx 0$  may start to break down.

By changing the sign of  $B$ , we obtain the solutions for positive-Bernoulli disks. As anticipated, these models yield finite pressure, density, and angular momentum at infinity, confirming our suspicions that positive-Bernoulli disks produce winds. In fact, if  $B$  becomes too large, the density again approaches a power law but with  $2\alpha$  replacing  $-q$ . In this limit we can show that, for  $q$  that leave the density finite at the poles, all solutions predict an energy that increases as we go out in radius. These two physically meaningless conclusions lead us to the assertion that positive  $B$  solutions do not describe wind-less disks, and hence are not appropriate to our modeling of the debris disks produced by tidal disruption events.